Galaxy Evolution
and the redshift desert

Ralf Kotulla
2010

Galaxy Evolution and the Redshift Desert

Ralf Christian Kotulla

**submitted to the University of Hertfordshire
in partial fulfilment of the requirements of the degree of
Doctor of Philosophy**

09 July 2010

Hier kommt der Text unten links hin

Contents

Contents

Acknowledgement

At this point I first of all want to thank my family and in particular my parents Klaus and Ulli for their constant support during the past 29 years and especially during my study times.

I want to extend this thank to my scientific family: Uta, without your help, encouragement, insight and all our discussions this thesis would not exist and I would have missed a really wonderful time.

Jay, I really loved the time I spend over in Madison and our chats and morning coffees always made my day and gave me inspiration and the encouragement to continue, even when things didn't go as smoothly as I had wished. Peter,

Abstract

Chapter *1*

Introduction

Modern astronomers can roughly be sorted into two categories: Those dealing with stars and their evolution, and those working on galaxies and their formation and evolution. As the title of this thesis is "Galaxy evolution and the redshift desert" I clearly belong to the second group, and so I first want to give an introduction on what galaxies are, why we are interested in them and in particular what the motivation for this present thesis is.

In the following we will use both terms Milky Way and Galaxy (with capital G) when we mean our own galaxy, while galaxy (with small g) means galaxies in general
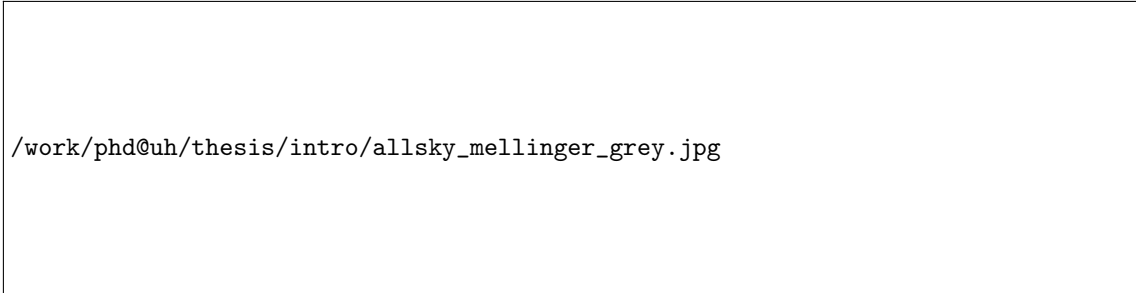
1.1 The history of galaxy research in a nutshell

The term galaxy originates from the *galaxias*, the greek word for "milky" which refers to the milky appearance of of our own galaxy, the Milky Way. While in the ancient greece this appearance was believed to have mythological origins, philosophers soon started to link the Milky Way to stars in the sky. However, not until 400 years ago when Galileo Galilei first pointed his early telescope at the night sky could we attribute the milky glow we can see in clear nights to an assembly of myriads of stars too faint for the naked eye to resolve (Galilei, 1610).
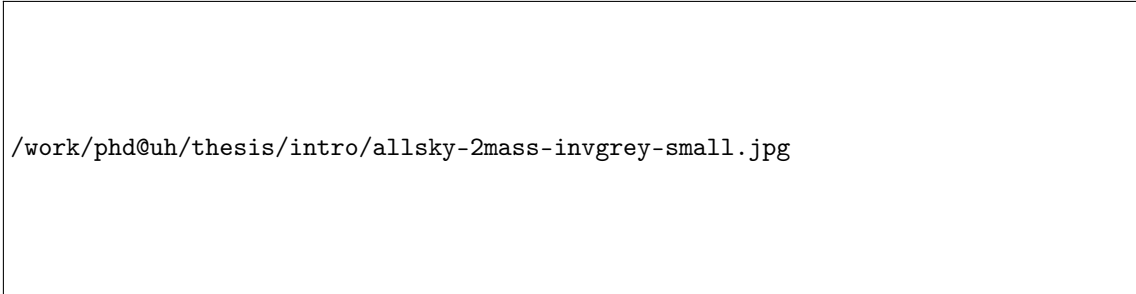
Over time more and more substructure was found to be part of the Milky Way, ranging from stellar associations consisting of only a few stars to clusters of stars with several tens to hundreds of stars to the magnificent globular clusters containing tens of thousands and up to millions of stars. With the advent of the first photographic observations (e.g. . as part of the Bonner Durchmusterung [Argelander, 1859-1903], and later the National Geographic Society – Palomar Observatory Sky Surveys [Wilson (1952)]), later photo-electric detectors and, at the present, Charged Coupled Devices (CCDs, as used e.g. in the Sloan Digital Sky Survey, Gunn et al. (1998)) that allowed to reliably derive the brightnesses or magnitudes of stars as well as their colours, astronomers started to learn more about how stars evolve by comparing the colour-magnitude diagrams of these star clusters. Furthermore star clusters allow to study stellar evolution from birth to death and also the distribution of stellar masses, the Initial Mass Function. This holds up to the present day, when ever better quality observations taken with both ground-based and space-borne telescopes constantly challenge our understanding of the stellar powerhouses.

While the study of stars dates back at least to the stone-age as indicated by early astronomical observing sites such as Stonehenge and archaeological artifacts such as the Nebra star disk, the study of galaxies is a significantly younger field of research. Early observations of galaxies by pioneers such as Charles Messier and William Herschel denominate them as "nebulae" or "spiral nebulae" in the believe that these nebulae are part of our own Milky Way. Only in the early 1920's a number of astronomers (Hubble, 1929b; Opik, 1922; XXX missing reference XXX, 2035) independently derived the distance to the great Andromeda nebula and found it to well exceed estimates of the size of our own Milky Way, confirming that many of these nebulae are indeed "island universes" outside our own Galaxy. The Milky Way, its companion the Andromeda galaxy and local galaxies in general are of immeasurable value to astronomers: Their proximity allows for detailed in-depth studies of the physical processes at work, and the fossile records of their formation and evolution uncovered by these studies allows a detailed view into the very distant past when the universe was still in its infancy.

In the same decade, it was Edwin Hubble and his co-workers to find a "A relation between distance and radial velocity among extra-galactic nebulae" (Hubble 1929a, also see Hubble & Humason 1931, 1934). This work laid the foundation for all later studies of galaxies, as it offers a possibility to determine the distance to any galaxy for which we can estimate a velocity via its redshift. While the common practice of deriving redshifts from identified emission- and/or absorption lines in spectra works extremely well for nearby and therefore reasonably bright galaxies, this approach gets increasingly difficult for more distant and faint galaxies. We will come back to some of these difficulties XXX.

```
/work/phd@uh/thesis/intro/allsky_mellinger_grey.jpg
```

```
/work/phd@uh/thesis/intro/allsky-2mass-invgrey-small.jpg
```

Figure 1.1: All-sky images of our Milky Way in the optical (top panel) and the near-infrared by 2MASS (lower panel). Images courtesy of Axel Mellinger (optical) and 2MASS/IPAC/Caltech (near-infrared).

1.2 Our Milky Way

As mentioned above we know since four centuries that our Milky Way is made out of stars, that at least in part conglomerate in star clusters and are aligned in an elongated, flat structure that we observe as the Milky Way. A closer look brings up more features, such as large patches of lower stellar density that are obscured by dust. These features can be clearly seen in the top panel of Fig. 1.1, showing an all-sky optical image of the Milky Way. The same region taken in the NIR by the 2 Micron All-Sky Survey (2MASS, Skrutskie et al., 2006) can pierce through this dust and reveal the true structure of our Milky Way, shown in the lower panel of Fig. 1.1. In addition to the disk that we recognise as "Milky Way", our Galaxy also contains a bulge, a central, spheroidal component.

A more abstract version of these figures is given in Fig. 1.2, showing the four major components of our Milky Way: Bulge, thin and thick disks and halo. Most of the gas and dust are concentrated into a thin disk, and therefore the thin disk also marks the location where most young stars are formed. These young stars show a wide range of stellar masses that can, for masses comparable to our sun's mass and above, be well described by a power-law (Salpeter, 1955; Kroupa, 2001; Chabrier, 2003), with many more low-mass stars being formed than high-mass stars. This initial mass function (IMF) is found to show very little variation within and across different galaxies, but this might not hold for extreme environments, and a range of authors have begun to investigate these issues (e.g. Weidner & Kroupa, 2006; Boissier et al., 2007; Meurer et al., 2009). Chapter 8 present the results of such a study, looking in detail at the properties of the IMF in the relatively nearby galaxy Arp 78.

Of particular interest for the evolution of galaxies are the massive stars. Their high masses lead to high luminosities, making them sign-posts for active, ongoing star formation out to large distances. They also use up their hydrogen fuel supply rather quickly within only several million years (e.g. Bertelli et al., 1994; Marigo et al., 2008) and then end their life in a supernova explosion, returning a significant fraction of their mass and in particular the end-products of their nuclear burning processes in form of heavier elements (e.g. Woosley & Weaver, 1995) back to the surrounding inter-stellar medium (ISM). This process leads to a chemical enrichment of
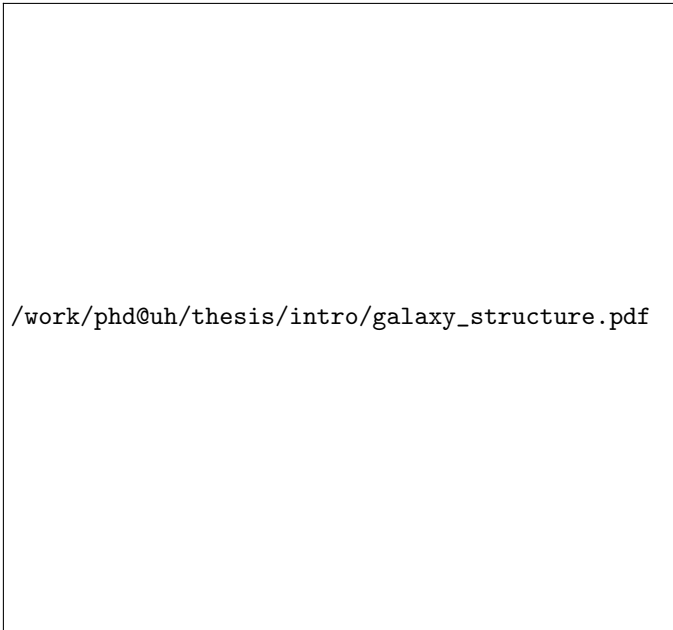
Figure 1.2: Sketch of the structure of our Milky Way: A thin disk, embedded into a thick disk, a central bulge and a surrounding stellar halo.

the gas that can then cool and form new stars, and it is the details of this enrichment process that can be used to reconstruct past star formation in our and external galaxies.

The thin disk is embedded in a more extended structure, the thick disk. The main difference, in addition to different scale heights between the disks, is, that stars in the thick disk are older than stars in the thin disk, and as the gas they were formed out of in the past has undergone less enrichment, they have lower metallicities (e.g. Ak et al., 2007). In the centre of our Galaxy we have the bulge, a roughly spherical structure that consists of old and therefore red stars. All these three components, thin disk, thick disk and bulge, are in turn embedded into a large halo. Stars in the halo are among the oldest and most metal-poor stars we can find in the Galaxy (e.g. Ivezić et al., 2008), and so are the stars in the globular clusters that also inhabit the halo (Harris, 1996). This suggests that the stars in the halo were the very first to be formed very early in the history of the universe and shortly after the Big Bang (Eggen, Lynden-Bell, & Sandage, 1962; Salaris & Weiss, 2002; De Angeli et al., 2005; Marín-Franch et al., 2009; Marks & Kroupa, 2010).

This structure and their respective stellar populations they are made out of also imply different formation scenarios: The stellar halo and bulge formed very early on in a relatively short period of time, with stars in the thick disk following shortly after that. The stars in the thin disk, on the other side, form over an extended period of time until the present day. These different star formation histories determine the integrated light of the galaxy at each moment of time and also have a share in determining its subsequent evolution, and it is this very evolution that astronomers strive to decipher.

1.3 Hubble and the galaxy types

Now that we have discussed the structure and stellar populations of our own Milky Way in some detail, we will have a closer look at the variety that nearby galaxies have to offer.

Edwin Hubble was among the first trying to bring some order into the plethora of galaxy morphologies we observe in the very nearby universe alone. His classification (Hubble, 1926), that was later refined and expanded by de Vaucouleurs (1959, 1963), is shown in Fig. 1.3. In his "Tuning Fork" galaxies are classified morpholgically on the basis of the prominence of the central bulge and the existence and appearance of spiral arms. Galaxies showing a smooth, featureless

Figure 1.3: Hubble's tuning fork to classifiy galaxies into early-type, elliptical galaxies, lenticular galaxies as link to the late-type, spiral galaxies. Depending on the presence of a central bar spirals are classified as regular or barred spirals. Image courtesy: NASA and ESA, adopted by the author.

appearance and round or ellipsoidal shapes are called ellipticals or E-type galaxies. The suffix attached to their type (e.g. E3) gives their apparent axis-ratio. For historical reasons, elliptical and lenticular galaxies are often referred to as early-type galaxies, whereas spiral galaxies, occupying the right-hand side of the tuning fork, are labelled as late-type galaxies. Located at the interlink between ellipticals and spirals are the lenticular galaxies. Their light is dominated by the central bulge, but they also show signs of a stellar disk, but both bulge and disk are smooth.

Unlike ellipticals late-type galaxies show a spiral-like structure of two or more separate arms in their optical images. Different spiral types, ranging from Sa through Sc, again classified as early-type and late-type spirals, are classified by a range of interrelated features such as the prominence of their central bulge, the bulge-to-disk or bulge-to-total (light) ratio (increasing from Sa-Sc) or arm pitch angle (more tightly wound arms for the Sa's to looser arms for Sc's). In addition to these spiral arms spirals can also contain a bar, a central elongated structure. de Vaucouleurs (1959) later added two more spiral classifications: Sd galaxies are pure disks, and do not contain any bulges, while Sm-type galaxies show neither bulge nor a definite spiral structure, linking them to the Irregular galaxies.

The sequence from early-type ellipticals to late-type spirals also involves a continuum in both colours and, as a proxy of stellar mass, absolute luminosities in the sense that earlier-type galaxies are in general brighter and redder then later-type galaxies. This can naturally be explained with the stellar population mix causing the light: As in the Milky-Way, stars in bulges are on average older than stars in disks. Furthermore early-type galaxies do not show signs of significant ongoing star formation (they are sometimes also referred to as "red and dead"), while in particular later-type spirals have ongoing star formation as shown by UV and Hα emission, originating in H$_{II}$regions surrounding hot and short-lived massive stars. In addition to this purely morphological Hubble sequence we can therefore define an analogous spectral sequence, using spectral features instead of morphology. As morphologies are only discernible for relatively nearby galaxies, these spectral types will become important in the course of this thesis when it comes to modelling more distant galaxies, their spectra and spectral evolution with time.

/work/phd@uh/thesis/intro/tadpole.jpg

/work/phd@uh/thesis/intro/m51.jpg

/work/phd@uh/thesis/intro/antennae.jpg

/work/phd@uh/thesis/intro/mice2.jpg

Figure 1.4: A small subset of interacting galaxies, observed with the Hubble Space Telescope. Top: Tadpole Galaxy (courtesy of NASA and B. Preston [STScI]); middle left: M51 (courtesy of NASA, ESA, S. Beckwith and the Hubble Heritage Team); middle right: Antennae (courtesy of Brad Whitmore [STScI] and NASA); bottom: The Mice (courtesy of NASA, H. Ford [JHU] et al, the ACS Science Team, and ESA).

Despite all its successes in bringing some order into the zoo of galaxy shapes, the Hubble Tuning Fork as shown in Fig. 1.3 misses several important galaxy classes. The first classes contains dwarf galaxies, the by far most frequent galaxy type. Dwarf galaxies, only defined to have low luminosities as compared to the "normal" Hubble types, again can be separated into early-type dwarfs (dwarf ellipticals [dE], dwarf spheroidals [dSph]) and late-type dwarf Irregulars (dIrrs) and Blue Compact Dwarf Galaxies (BCDGs). Galaxies with active nuclei (active galactic nuclei, AGN), powered by accreting black holes at their centres, are another distinct class with several sub-classes too numerous to be detailed here, but these AGN are often hosted by otherwise unremarkable galaxies on the Hubble scheme.

The last group not described by any regular Hubble type are irregular galaxies. This group contains morphologically irregular galaxies like XXX or the Magellanic clouds in the direct vicinity of the Milky Way. It also contains galaxies in the process of merging with a second galaxy (e.g. M51), with (tidal) arms (e.g. the Antennae NGC4038/39, the Tadpole Galaxy UGC10214 or The Mice NGC4676; also see Fig. 1.4), or the like. Their peculiar shapes are often caused by gravitational interactions with a nearby companion. These interactions dramatically affect all of the galaxies' properties. For instance, a merging of two galaxies not only combines the light of both

/work/phd@uh/thesis/intro/2MASS_LSS_inverted3.jpg

Figure 1.5: 2MASS image of our Milky Way and its surrounding environment, showing galaxies in the local group and the nearby large scale structure consisting out of a range of galaxy clusters.
Image courtesy: Tom Jarrett (IPAC/Caltech).

progenitors, but forms a remnant with a different morphology (typically of earlier type), possibly featuring a large extended tidal structures such as tails, ripples and shells (Toomre & Toomre, 1972; Heyl et al., 1994; Barnes & Hernquist, 1996; Mihos & Hernquist, 1996; Weil & Hernquist, 1996; Cox et al., 2006, but also see Springel & Hernquist, 2005). If at least one of the galaxies contained some gas, this gas can be stirred up during the interaction and trigger a starburst (e.g. Mihos & Hernquist, 1996), a short phase of enhanced star formation [SF] activity. This starburst also increases the luminosity of the galaxy, making it visible out to large distances or redshifts, and also leads to very blue colours and spectra as consequence of the immense number of newly formed massive stars. The enhanced SF also leads to a increased formation rate of massive star clusters (Larsen, 2002; Bastian, 2008), and this young star cluster population can then serve as witnesses of the galaxy's eventful past, allowing to reconstruct its formation history. In the framework of this thesis, this approach has successfully been applied to the nearby lenticular galaxy NGC 4570, a member of the Virgo galaxy cluster (see Fig. 1.5), and the details and results from this project are given in Chapter XXX.

In Fig. 1.5 we show the 2MASS all-sky image of the Milky Way and its surrounding large-scale structure. The image clearly shows that our Galaxy, together with the Large and Small Magellanic clouds (LMC/SMC), the Andromeda Galaxy M31 and the Triangulum Galaxy M33 form the Local Group with an extent of $\approx$ 1Mpc. At larger distances the large-scale structure is dominated by a range of galaxy clusters, with the Virgo and Fornax clusters being the closest in the northern and southern hemisphere, respectively.

Galaxy clusters add a whole new perspective on the evolution of galaxies. Galaxies in the field evolve mostly isolated or at most undergo few interactions with nearby companions. Galaxy clusters keep forming and growing by accretion of field galaxies. Galaxies in clusters, however, live in swarm of numerous other, close-by galaxies. They feel the deep gravitational potential caused by luminous and dark matter in the cluster. Furthermore, they interact with the hot, ionised gas that forms the intra-cluster medium (ICM). These interactions can affect the evolution of a galaxy in a number of ways: As it travels through the cluster, the ICM interacts with the

Figure 1.6: Small cutouts from the Hubble Ultra Deep Field, illustrating the immense number of galaxies found in each small patch of sky. It also clearly shows the variety of shapes these galaxies have, ranging from spirals similar to the local universe (e.g. in the top right panel) to small and scraggy (several examples in the lower right panel). Image Courtesy: NASA, ESA, S. Beckwith (STScI) and the HUDF Team

gas within the galaxy, leading to gas-loss due to ram-pressure stripping. As the gas-reservoir diminishes, star formation can no longer be sustained and the galaxy is slowly transformed into a red and dead early type galaxy. On the other hand frequent and fast fly-by interactions with nearby galaxies also disturb the gas within the galaxy and are able to shred of stars in the outskirts. As this process primarily destroys the disk but leaves the bulge, located deeper within the galaxy's gravitational well, unaffected, it also leads to the transformation of late-type into early-type galaxies. Both ram-pressure stripping and galaxy-galaxy interactions can also trigger a starburst as long as a galaxy is still gas-rich. All these processes together obviously account for a significant transformation of an originally spiral-rich field galaxy population with lots of gas and ongoing SF to an ultimately E- and in particular S0-rich cluster galaxy population with little gas and SF. In Chapter XXX and XXX we present a study aimed to explain a certain type of galaxies that are observed in a particular state of this transformation process: Their spectra show strong balmer absorption lines, robust signs of rigorous recent SF, but no emission lines that would indicate ongoing SF.

1.4 The high(er) redshift universe

Now moving our view to more distant galaxies, such as first done in the Hubble Deep Field and later the Hubble Ultra Deep Field (Fig. 1.6), we see that more and more galaxies show signs of active star formation, as indicated by the presence of emission lines and/or blue colours. Furthermore the number of galaxies that show signs of interactions (see, e.g. , the galaxies just towards the lower right of the centre of the top-left panel or the blue, clumpy galaxies in the bottom right panel of Fig. 1.6) increases as we look back in time towards earlier phases of the

Figure 1.7: Snapshots of a small region of the Millennium simulation (Springel et al., 2005) at four different ages of 0.21 Gyr (top left), 1.0 Gyr (top right), 4.7 Gyr (bottom left) and 13.7 Gyr (bottom right).
Image courtesy: V. Springel et al.

universe. This suggests that galaxies are likely to be formed bottom-up, by hierarchical merging of small, more dwarfish galaxies that slowly built up the large galaxies we observe in the local universe.

Further evidence for this scenario comes from large cosmological N-body simulations, such as the Millennium simulation (Springel et al., 2005). These simulations start from initial conditions derived from the cosmic microwave background (CMB), the oldest signature of the Big Bang that is currently observable, and can successfully reproduce a large number of observations in the local universe. However, one important caveat of these simulations so far is that they only include dark matter, and although this means they account for the bulk of the mass in the universe, they still lack the level of detail necessary to fully reproduce the wealth of data we can observe today. Fig. 1.7 shows snapshots of a small region in the Millennium simulation at four different times, ranging from very early (210 Myr) after the Big Bang in the top left, 1 Gyr (top right), and 4.7 Gyr (bottom left), to the present day (13.7 Gyr) in the bottom right.

To overcome this drawback and in order to make these simulations comparable to observations of the "ordinary", non-dark matter observed in the form of stars and galaxies, several groups have developed semi-analytical models of galaxy formation (White & Frenk, 1991; Kauffmann et al., 1993; Cole et al., 1994, 2000b; Bower et al., 2006; De Lucia & Blaizot, 2007; Lacey et al., 2008; Fontanot et al., 2009). These combine the information on the merging and building of dark matter halos from the cosmological simulations with descriptions for star formation, fueling of the central AGNs, and their resulting feedback processes on the gas in and around the galaxies (see Fig. 1.8 for an illustration of this process). These models use recipes for gas cooling, SF, AGN growth and feedback from both in as much agreement as possible with observations in the relatively local universe. They include a number of free parameters that need to be adjusted

Figure 1.8: Comparison of the underlying dark matter distribution (left panel) and the visible galaxy population (right panel) inhabitating in this distribution for one galaxy cluster in the Millennium simulation. The colours ranging from blue to red correspond to the stellar population age of the galaxy from young to old.
Image courtesy: V. Springel et al.

and their validity has to be extracted far into the early universe.

In the first five chapters of this thesis we describe, as a complementary approach, a comprehensive study of the evolution of various types of galaxies, starting from the relatively nearby universe and extending out to redshifts at which the universe was still young, less than 10 per cent of its current age. Our study is based in the largest ever observed sample and uses relatively simple and thouroughly tested stellar population models. These models nowadays are looking back on a long and successful history started by (Tinsley, 1967, 1968, 1972), subsequently improved and refined (Bruzual, 1983; Guiderdoni & Rocca-Volmerange, 1987; Matteucci & Tornambe, 1987; Fritze et al., 1989; Bressan et al., 1994; Fritze & Gerhard, 1994a; Prantzos et al., 1994; Fioc & Rocca-Volmerange, 1997; Portinari et al., 1998; Silva et al., 1998; Leitherer et al., 1999; Bruzual & Charlot, 2003; Anders & Fritze, 2003; Pipino & Matteucci, 2004; Kotulla et al., 2009) and are now widely applied throughout the astrophysical community. They all have in common that they generally assume simple description of the SFH of a galaxy, and then synthesize the emitted light from a distribution of stellar masses, stellar evolution data and observed and/or theoretical stellar spectral libraries. A detailed description of the model underlying many of the results in this thesis is given in Chapter 2.

1.5 The redshift desert and photometric redshifts

As mentioned above the star formation activity in galaxies in general increases towards higher redshifts. However, this trend does not continue back to very young ages, as galaxies at these early epochs were significantly less massive and, although very gas-rich, only started their SF activity. The cosmic star formation history as measured by the star formation rate density shows a peak roughly at redshift $z = 2$ when the universe was $\approx 1/5$ of its current age (Madau et al., 1996, 1998; Blain et al., 1999; Hartwick, 2004; Juneau et al., 2005; Reddy et al., 2008). This epoch furthermore overlaps with the epoch of maximum QSO activity, a measure for the growth rate of galaxies (Schmidt et al., 1995; Pei, 1995; Fan et al., 2001; Babbedge et al., 2006; Brown et al., 2006; Richards et al., 2006). Unfortunately, this redshift range is hard to access with current instruments on large telescopes: In order to obtain a redshift from an observed spectrum one needs to identify spectral features, most commonly emission lines. Most of the strongest features

in the rest-frame optical spectral range are, for a redshift 2 galaxy, shifted into the near-infrared and hence beyond the sensitivity range of optical spectrographs, the workhorses of modern extragalactic research. At the same time, emission lines in the far-ultraviolet are not redshifted far enough to reach into the optical window.

These mostly technical challenges gave rise to the term "redshift desert", as very few galaxies with spectroscopic redshifts in the redshift range from $z = 1 \ldots 2.5$ were known. In the recent past efforts using NIR spectrographs on large telescopes (e.g. Erb et al., 2003) or optical instruments that reach into the near-UV (see, e.g. , Steidel et al., 2004, for an overview) have partly overcome these difficulties, opening the door to this truely remarkable phase in the evolution of our universe. Towards very high redshifts, spectra become both rare and often of low quality, as, owing to their redshift, the flux of the spectrum is decreased by a factor $(1 + z)^{-1}$. This, in combination with the distances to these galaxies, causes them to be very faint. Tremendous integration times on the largest telescopes are therefore required to even detect these galaxies at $z = 5 - 7$, let alone to spread out their light over many detector elements as done in spectroscopy.

This difference in required telescope time can be nicely demonstrated with the 2 sq.deg. Cosmic Evolution Survey (COSMOS)[1]: Imaging in 5 broadband-, 13 narrowband- and 3 narrow-band filters took "consumed" a total 22 nights on SUBARU, a 8 m telescope on Mauna Kea, yielding photometry for ≈ 2 million galaxies, allowing for photometric redshifts with accuracies as good as 1%. The spectroscopic follow-up, zCOSMOS, obtained spectra for a total of 37500 galaxies – less than 2% of the photometric sample, and with limiting magnitudes $4 - 5$ magnitudes brighter than what was reached with imaging – using 68 nights of VLT (same telescope aperture, 8 m) telescope time. On top of all that comes the fact that spectroscopy does not always yield a redshift (for instance in the case the galaxy lies in the redshift desert), losing a certain fraction of precious telescope time. **XXX Absolute flux calibration? Better than 10% for spectroscopy possible? XXX** Admittedly, some science questions can only be answered with spectroscopy (dynamics and detailed abundance ratios are just two examples), but for many science questions the photometric redshift approach is by far the more efficient one.

In addition to these challenges, redshift furthermore stretches the wavelength by a factor $(1 + z)$ such that, with current instrumentation, only a very short rest-frame part of the spectrum can be observed at a time. As a consequence, redshifts and galaxy properties such as SF rates are often derived from just one single strong emission line, with considerable risk of misidentification. The potential magnitude of this effect was demonstrated by Fernández-Soto et al. (2001) who find that even in the best and most thoroughly checked redshift surveys 3% and possibly upto 14% of spectroscopic redshifts are incorrect, be it due to misidentified lines, blended objects or faulty acquisition at the time of the observations, and we will present one such case below.

In the present thesis these difficulties of deriving redshifts and physical parameters are overcome by using a method that is becoming increasingly popular at a time where large astronomical surveys, partly using dedicated survey telescopes, observe fainter and fainter galaxies in rapidly growing numbers: Instead of using spectral features such as emission and/or absorption lines to determine a precise redshift, I obtain a *photometric* redshift. I compare the overall spectral shape, the spectral energy distribution, to a grid of galaxy templates that cover a wide range in redshift, and assign each galaxy with the spectral type and redshift of its best-matching template. For this purpose I developed – from scratch – a completely new photometric redshift code, called **GAZELLE** . It is tailored to work with **GALEV** models that include the full spectral and chemical evolution of galaxies, and not only derive redshifts as many other codes do, but also extract the physical information from the observed photometry, fully and consistently accounting for the often mutually dependent uncertainties. As dataset I compiled the largest ever catalog from a large number of individual surveys covering more than a dozen deep fields, all with a large wavelength basis covering at least the optical and near-infrared. For a large fraction of my sample the covered spectral range extends even further than that, from far-ultraviolet at 0.15μm

---

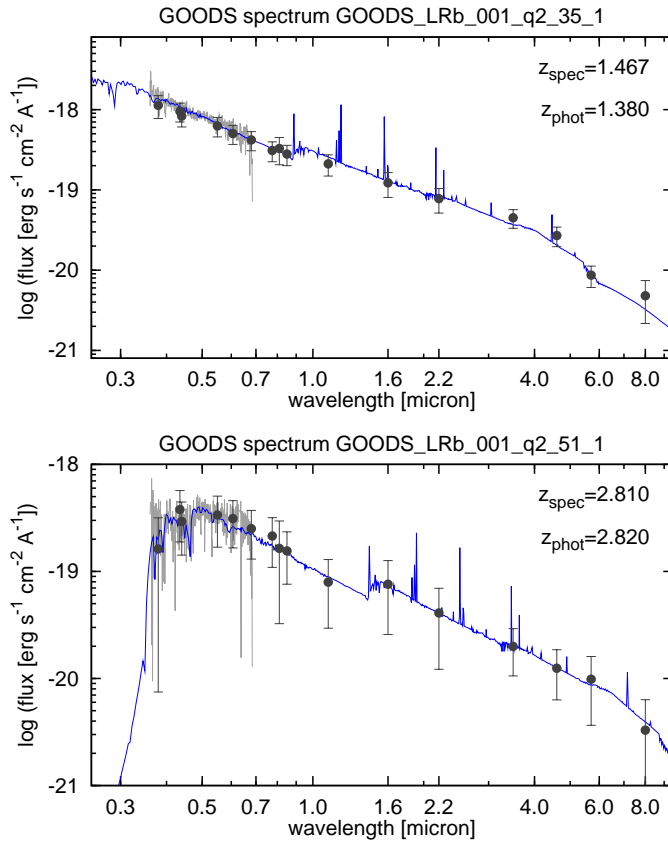[1]data taken from the COSMOS website, http://cosmos.astro.caltech.edu

Figure 1.9: Example spectra for two galaxies at either side of the redshift range covered by the "redshift desert". Observed spectra are shown as grey lines, observed photometric datapoints and their respective uncertainties are shown with black circles; the blue solid line shows the best-fit spectrum obtained via the photometric redshift fitting.

Spectroscopic redshift identification in both cases is based on the location of absorption lines.

to the mid-infrared at 8.0μm, a range that is totally unheard of when it comes to spectroscopy, with exception of a handful selected and very nearby objects. With this data at hand I can now efficiently constrain the type and redshift ranges for each of the galaxies.

The power of this photometric approach and a comparison to several observed spectra is shown in the following Figs. 1.9, 1.10, and 1.11.

Fig. 1.9 shows, as grey line, the spectra of two galaxies at either side of the redshift desert, $z = 1.4$ and $z = 2.8$, taken from the spectroscopic follow-up study of the GOODS-South field, executed using the Visible Multi Object Spectrograph (VIMOS) on the Very Large Telescope (VLT) at the European Southern Observatory (Balestra et al., 2010). For comparison I also show the photometry from the FIREWORKS catalog (Wuyts et al., 2008) as black data points, and the spectrum corresponding to the best-fit to that photometry. The details on the data and the used method are given in Chap. **??**. This figure shows very clearly the two effects described above: The observed spectral range only covers a narrow rest-frame wavelength window from $1400 - 2800$ Å (upper panel) and $950 - 1800$ Å (lower panel). Unfortunately, this wavelength region is devoid of strong emission features, so that for these two galaxies the redshifts were established based on absorption lines. This, however, is only feasible from high signal-to-noise ratio spectra, limiting its application to the very brightest galaxies. These in turn are generally the least representative of the underlying population (e.g. consider brightest cluster galaxies as representatives of the galaxy population in the local universe) , heavily biasing conclusions based on these "tip-of-the-iceberg galaxies".

Now turning our focus to the photometric data for these two galaxies. I show the photometry in 16 bands, covering the observed near-UV through to the mid-infrared at 8.0μm. These cover nearly the complete rest-frame far-UV to rest-frame near-infrared. This allows a significantly better determination of the galaxy type, which in turn impacts on the dust extinction and hence
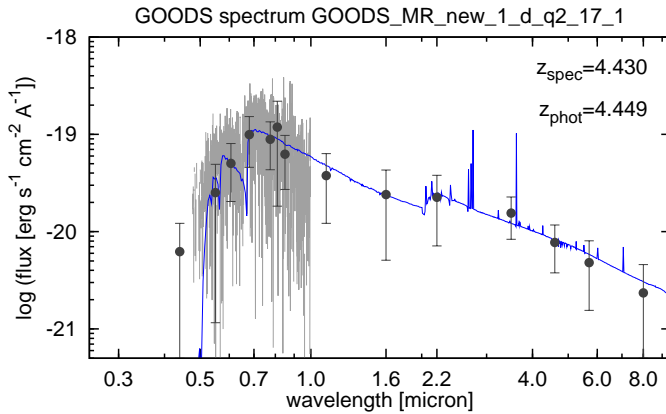
Figure 1.10: Same as Fig. 1.9, but for a higher redshift galaxy at $z = 4.43$.

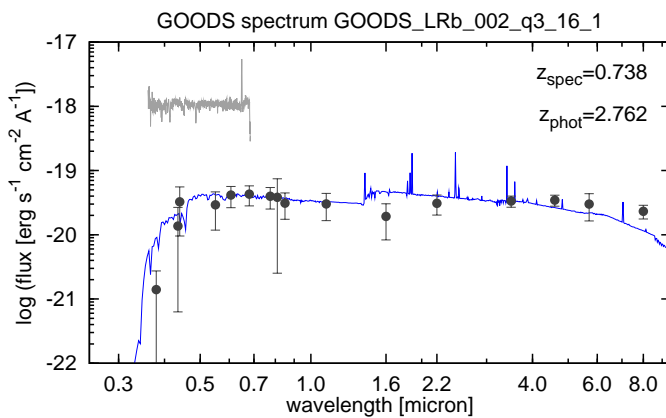Spectroscopic redshift determined based on the position of the Lyman Break.

Figure 1.11: Same as Fig. 1.9, but for a case with discordant spectroscopic and photometric redshifts. For the observed spectrum, the redshift is supposedly based on the detection of the Mg IIλ2798 and [O II]λ3727 lines.

the dust-corrected star formation rate, stellar mass, and age of the stellar population than the spectroscopic data alone.

The next Fig. 1.10 shows the observed spectrum of a galaxy at redshift $z = 4.43$, significantly beyond the redshift desert that forms the core of this thesis, but not less interesting. It is obvious that the quality as measured by the signal-to-noise ratio is considerably lower than what I presented in the previous figure. The spectrum only covers the immediate vicinity of the Lyman-α line at $\lambda_{\rm rest} = 1216$ Å, which allowed for a redshift determination based on the position of the Lyman-break. However, based on the spectrum alone I would not dare to extract any physical information from this spectrum beyond the redshift and maybe a star formation rate (if the dust content can be specified based on the UV slope). On the other hand, using the available photometry alone also allowed for an accurate redshift estimation, differing from the spectroscopic redshift by only $\Delta z = 0.019$, corresponding to a relative error $\Delta z / (1 + z_{\rm spec}) = 3.5 \times 10^{-3}$, more than sufficient for most scientific application. On top of that, analysis of the photometry with **GAZELLE** also yields a galaxy type, i.e. a star formation history, a stellar mass, star formation rate, stellar population age, metallicities, etc.

So far I have presented three cases where my photometric redshifts agree with the available spectroscopic data, but due to the longer wavelength coverage of the photometric data allows to extract more physical information about the galaxy. I therefore present in Fig. 1.11 a case where both cases are in stark disagreement, with $z_{\rm spec} = 0.738$ and $z_{\rm phot} = 2.762$.

Unlike all the previous plots, for this case the absolute normalisation of the observed spectrum does not agree with the photometry for this object, suggesting that the spectrum and the photometry refer to two different objects. This can, e.g. , result from errors during acquisition when the spectrograph slit is misplaced, during data reduction when slits are confused or misidentified,

or because of blending of multiple nearby sources. Although these errors are likely to be rare, they pose a significant risk if not properly accounted for. Furthermore, the redshift measurement is claimed to be based on the location of the Mg II ($\lambda_{\rm rest} = 2798$ Å, $\lambda_{\rm obs}(z = 0.738) = 4862$ Å) and [O II] ($\lambda_{\rm rest} = 3727$ Å, $\lambda_{\rm obs}(z = 0.738) = 6477$ Å) lines. Detailed visual inspection of the spectrum reveals the first line (Mg II) to detected marginally at most, while the second ([O II])is undetected altogether, making this redshift classification, despite its claim to be "secure" – or, in the authors words, "high quality, i.e. several emission lines and strong absorption features are well identified" (Balestra et al., 2010) – everything but that.

In this context I particularly want to emphasise one aspect already noted in the Fernández-Soto et al. (2001) study mentioned earlier: Unlike **GAZELLE** , a range of photometric redshift codes use empirical templates instead of model templates, arguing that these better represent true galaxy spectra. In many cases, these "empirical" templates are constructed from photometry and the corresponding observed galaxy spectra, often available for a small number of comparably bright galaxies. Therefore, even a few mis-identified galaxy spectra have a significant negative effect, not only on the resulting photometric redshift but in particular the results and conclusions based on these redshifts. To a somewhat smaller degree this also applies to the extrapolation of templates to regions of the parameter space, either in redshift, colour range or apparent magnitudes, that are not covered by the template set. This applies in particular to galaxies in the redshift desert, i.e. with redshifts $z = 1.4 - 2.5$, where spectroscopic redshifts in large numbers and covering a representative fraction of the colour space (most galaxies in the redshift desert, e.g. , are star-forming, *blue* galaxies, allowing to derive redshift from the Lyman-α line; up until today there are only very few spectra of *red* galaxies in this redshift range), are still hard to come by. All these reasons reinforced the decision to use not only photometric redshifts, but photometric redshifts based on model templates that not only include all known types of galaxies (with exception of AGNs), but also fully account for the effects of galaxy aging, emission lines and especially sub-solar metallicities.

1.6 Outline of this thesis

This thesis is structured into XXX chapters. After this initial introduction shortly presenting previous work that sparked the idea and layed the foundation for this thesis I will present the models I developed and used for most of my work, the methods I were using to analyse the data and the conclusions I have drawn. I finish this thesis (Chapter 9) with a short summary of the conclusions and give a short outlook on how I plan to build up on and extend the work done so far. I also attached in Appendix A a pictorial description of my models, and in Appendix B a list of further publications I was part of in addition to my own thesis-related work.

1.6.1 GALEV evolutionary synthesis models: Code, input physics and web-interface

In Chapter 2 (published as Kotulla et al., 2009) I present the basis of this thesis, our **GALEV** evolutionary synthesis models. The **GALEV** code allows to model spectra, magnitudes and colours, and physical properties, such as stellar and gaseous masses, metallicities, stellar population ages, based on a small number of input parameters. The most crucial parameters that determine the evolution of our simulated galaxies are the star formation history, i.e. the variation of the star formation rate with time, and the stellar initial mass function, i.e. the relative number of stars of different masses. For this modelling process **GALEV** uses a range of input physics such as data for stellar evolution from stellar isochrones, stellar yields from nucleosynthesis calculations and stellar spectra from theoretical stellar libraries.

GALEV is the ideal tool for the science of this thesis, as it features two components that discriminate it from similar codes such as the de-facto "industry standard" from Bruzual & Charlot

(2003): By using the input physics listed above for a wide range of metallicities it includes a detailed treatment of the chemical evolution in a self-consistent way, fully accounting for the increasing initial abundances of successive stellar generations. It furthermore includes emission lines that also very strongly with metallicity and are a significant contributor to broad- and in particular narrow-band filters whenever the galaxy is actively forming stars and hence contains a population of massive, young stars.

I detail the input physics that is currently used and also explain how the code works. In order to be able to model galaxies both in the local and the distant universe, **GALEV** models have to be calibrated, and I demonstrate this calibration process that allows us to simultaneously reproduce spectra and colours, stellar masses, star formation rates, metallicities and mass-to-light ratios for typical galaxies of a range of spectral Hubble types. Once calibrated on local galaxies **GALEV** can – for any desired choice of the cosmological parameters – also be used to describe galaxies out to the highest redshifts, consistently accounting not only for the cosmological, but also for the evolutionary corrections appropriate for every individual galaxy type. In addition to the applications presented in the course of this thesis I give several examples on how **GALEV** can be and has been very successfully used to study galaxies at a range of redshifts. To facilitate the access to our models I also created a web-interface that, at the time of writing and after just over one year of public access, allowed more than 150 researchers around the globe to run 1500 models with user-defined parameters, and the details of this web-interface are also given. I conclude the first chapter with a summary and a list of things I plan to improve or that already are in preparation in collaboration with Peter Anders as second active GALEV developer.

1.6.2 Evolutionary synthesis modelling of galaxies from nearby to high redshifts

In Chapter 3 I present the model grid, computed with our **GALEV** models, that will serve as a theoretical foundation of large parts of the remainder of my thesis. My model grid contains five undisturbed models representing the spectral galaxy types E and Sa through Sd, all using the chemically consistent treatment distinguishing **GALEV** from other codes. The term "undisturbed" means that these galaxies are described by a smooth star formation history and do not undergo any starburst of star formation truncation events. These models are supplemented by a large number of models undergoing a starburst, followed by a full or partial truncation of star formation in the aftermath of the burst. Starbursts in this model grid are characterized by three parameters: The time of the onset or peak of the burst, the decline time of the exponential decay of the SFR during the burst, and the burst strength, i.e. the fraction of the gas-mass available at the onset of the burst that is converted into stars during the burst.

I detail the evolution of spectra with time and redshift and remark on some interesting findings from this modelling alone. For instance, even in the extreme case that a galaxy formed all its stars in an instant at very high redshift, it would take until redshift $z \approx 3$ for its spectrum to become similar to a spectrum of an old elliptical galaxy in the early universe, explaining why the search for this type of galaxies has not turned up any reliable candidates. I also particularly emphasize the impact of evolutionary effects, i.e. the younger ages of galaxies in the early universe, and of sub-solar metallicities on the spectra and spectral energy distributions of galaxies. Both effects increasingly make galaxies brighter and bluer, leading to biased ages, masses and star formation rates if not properly taken into account. I also show the evolution of the gas-to-total mass fraction with time and redshift, and explain how accounting for this gas can help to understand the observed discrepancy between stellar and dynamical masses at high redshifts.

Then I present the grid of starburst models and the evolution of their (specific) star formation rates and chemical enrichment, and show that these models agree remarkably well with observations from several authors. The following analysis of the spectral evolution of starburst models revealed, amongst other, that even a small mass-percentage of young stars are sufficient to dominate the integrated spectrum at nearly all wavelengths. If not accounted for, this can lead

to stellar masses that are underestimated by a factor of a few and up to a factor of 20-50 in the most extreme cases. The colour evolution of our models revealed, that – as expected – ongoing, active starbursts are necessary to successfully and do reproduce the full range of blue colours observed out to high redshifts. On the other hand, post-starburst galaxies, i.e. galaxies for which the starburst has occured a while ago and that have only little or no ongoing star formation, successfully explain the very red colours observed in galaxies at intermediate and high redshift even in the absence of additional dust reddening. Passive aging of these post-starburst galaxies then defines a curve of maximum redness, again in excellent agreement with observations. I finish this chapter with a short summary and an outlook to possible applications of this model grid, some of which are presented in the following chapters.

1.6.3 Confronting model predictions with observations

In the following chapter (Chapter 4) I compare model predictions for the evolution of colours, spectra and physical parameters like stellar masses, star formation rates and, as far as available, metallicities to observations. As observational dataset I use results compiled from a large number of publications. The aim is to establish a framework for comparing and linking the various galaxy populations culled by each of the various colour selection criteria put forward by different authors.

I start with Lyman Break Galaxies, blue and hence actively star-forming galaxies at redshifts $z = 1.5 - 3$, in the heart of the redshift desert, that are selected via their UGR colours. My grid of **GALEV** models successfully reproduces their colour evoution over the full redshift range and confirms that only actively star-forming galaxies with low dust reddenings ($E(B - V) \lesssim 0.2$) fulfill the selection criteria in the targeted redshift range, with only small contributions from nearby late-type galaxies. From their colours and observed magnitudes as a function of redshift I conclude that Lyman Break Galaxies are likely progenitors of low-mass ellipticals or early-type spirals, and indeed this is confirmed by their stellar masses, star formation rates and metallicities. This interpretation, of course, only holds in the case of undisturbed evolution, i.e. without interactions with other galaxies after the epoch of observation. Should interactions occur these would lead to a galaxy, which in the local universe has an earlier type than what I predict from my models.

BzK galaxies, named after the filters used for their selection criteria, also target the redshift desert at $z = 1.4 - 2.5$. Using my model grid I can confirm the originally empirical colour selection, but I also find some contamination from higher-redshift galaxies up to $z = 3$. Again I find good agreement with **GALEV** predictions for E- and Sa-type galaxies based on observed stellar masses, SFRs and near-solar metallicities. The starburst galaxies in my grid furthermore explain the observed trend of an upper boundary to the star formation rate as function of stellar mass, as well as comparably low-mass galaxies with extreme star formation rates.

Extremely Red Objects, another class of colour-selected galaxies, as I show and is observationally found to consist of two sub-groups, either dusty starbursts or genuinely red galaxies with old stellar populations. Roughly one third of the latter is found to have strong Hδ absorption lines indicating violent recent star formation activity. This is nicely explained by the post-starburst models in my grid.

Distant Red Galaxies have recieved significant interest from various groups in the recent past. Based on the physical parameters that I derive for these galaxies from the comparison with GALEV models, I conclude that they are progenitors of local ellipticals. Surprisingly, both dusty starbursts and passive galaxies that fulfil the colour selection criteria require very similar stellar masses to yield the same observed K-band flux, despite the tremendous differences in the intrinsic stellar population. From my model grid I could derive a polynomial fit that allows to derive a stellar mass from a given redshift and K-band magnitude, nearly independent of galaxy type.

In all cases, I confirm the colours selection criteria derived by various independent methods with my GALEV models. For several cases my models even allow to pinpoint the origin of

contamination by galaxies outside the targeted redshift range, allowing to extend and refine the criteria in cases with photometry in additional bands.

I conclude the chapter with a short discussion of Luminous Red Galaxies, that are among the most massive galaxies in the universe, and a concluding summary.

1.6.4 Photometric redshifts and the metallicity bias

As mentioned already in the introduction, most of the galaxies we observe in modern astronomical surveys are too faint to be studied spectroscopically. Consequently, the only way to extract even the simplest information, the distance or redshift, from them is to rely on photometric redshifts. This technique works very well and reliable for brighter galaxies where additional spectroscopic data is available to calibrate magnitudes and templates (also see Chap. **??** XXX). At faint magnitudes, the realm of low-mass and hence low-metallicity galaxies, things are not that simple. In Chap. 5 I use my own photometric redshift code **GAZELLE** , presented in detail in Chap. **??**, to study, how sub-solar metallicities impact the obtained photometric redshifts.

For that purpose I simulate observations by taking model data of our chemically consistent, undisturbed galaxy models, change their stellar mass, add some dust extinction and finally finish it off by adding noise to simulate observational uncertainties. I then analyse these mock observations with a matched set of templates that account for these sub-solar metallicities and once again with a template set that only uses solar metallicity models. While the matched set, as expected, returns the correct redshift, the solar metallicity template set also yields redshifts with comparable uncertainties, but those are biased towards too low values. This bias depends on the chosen set of filters, the galaxy type and also on dust extinction, and can reach values of up to 50% of the actual value. It also particularly affects relatively low redshift galaxies for which even small redshift errors lead to large errors in the inferred physical parameters.

1.6.5 Semi-analytical models on the test-bench

tbc

1.6.6 Star clusters in nearby galaxies: Witnesses of an eventful past

Chapter 7 extends a common technique of age-dating star clusters via broad-band colours to a new kind of galaxy, in our case the lenticular galaxy NGC 4570 in the Virgo cluster. The biggest challenge in age-dating star clusters, or in our case globular clusters, is the age-metallicity degeneracy, i.e. disentangling reddening due to older ages, higher metallicities and, to some degree, dust extinction.

In the present case I solved this challenge by obtaining very deep K-band photometry using the ESO New Technology Telescope on La Silla, Chile. In combination with archival HST photometry in the F435W and F850LP bands this gave me the necessary wavelength basis to disentangle ages and metallicities. Extinction turned out to be low for this case, so that for this galaxy photometry in these three filters was sufficient for our purpose. Globular cluster candidates were then selected based on their physical sizes I obtained from the HST data. I pioneered the K-band observing technique, that allowed me to obtain an age, mass and metallicity, all with their respective uncertainties, for each individual object, yielding a sample of 63 trustworthy globular cluster candidates.

Their age and metallicity distribution revealed a large population of old and mostly metal-poor clusters, in agreement with findings in our own Milky Way and other nearby galaxies. However, it also revealed an almost equally large population of massive clusters with ages of only $1 - 2$ Gyr and near solar metallicities. The only plausibly way to explain this young and metal-rich

population is by a merger. From the information we derived for the star clusters we can even extract more information about the merger: To match the ages of the clusters it must have occured $1 - 2$ Gyrs ago, and must have involved at least on gas-rich galaxy to have enough fuel to trigger the starburst that formed these clusters. From the metallicity of the clusters we can furthermore estimate the Hubble type of this progenitor to be Sb or Sc. Earlier Sa-type galaxies do not have enough gas left, while later types are too metal-poor to explain the near-solar cluster metallicities. Although this Chapter only gives results from our pilot-study of one galaxy, it clearly demonstrates the feasibility and power of this novel technique. This opens the door to reconstruct the evolution of galaxies in the early universe from the age and metallicity distribution of the globular cluster populations in galaxies we find in our cosmic neighbourhood.

This pilot study has established the "astroarcheological" analysis of star cluster populations around unsuspicious local galaxies as a powerful method to infer violent starbursts in their distant past. Only starbursts accompanying gas-rich mergers are powerful enough to leave - after 2 or more Gyrs – rich populations of star and/or globular clusters. Star cluster analysis are the only way to identify multiple generations of starbursts, as studies of the integrated light or even colour-magnitude diagrams of the most nearby galaxies, only allow to reconstructed the evolution back to the most recent starburst. In this respect, this new method, that is applicable to all galaxies up to Virgo- and, with the advent of the next generation of space telescopes such as the James Webb Space telescope, out to Coma cluster-distances, opens up an important complementary approach to the direct analysis of high-redshift galaxies.

1.6.7 How universal is the stellar initial mass function? A test-case

Chapter 8, published in Kotulla et al. (2008b), takes a closer look at one of the most crucial and influential parameters in galaxy evolution, the stellar initial mass function (IMF). Its importance arises from the fact that small changes to the IMF, for instance a change to the slope of its powerlaw, or a variation in the mass fraction of low-mass and hence low-luminosity stars, not only affects the amount of light emitted per unit stellar mass, but also changes the rate of chemical enrichment and energy input into the interstellar medium (via the mass fraction of short-lived high-mass stars), and, e.g. for star clusters, also affects the dynamical evolution.

Several authors (e.g. Weidner & Kroupa, 2006; Meurer et al., 2009) have recently predicted a change in the high-mass slope of the IMF in under-dense regions. The underlying assumption there is, that under-dense regions form preferentially low-mass star clusters, and these low-mass clusters are observed and, on statistical arguments, expected to only contain stars up to a certain limiting mass that depends on the mass of the host cluster. This would lead to an IMF that is either truncated at the high-mass end, or, alternatively, has a steeper slope in the sense that they contain fewer high-mass stars than expected from their number of low-mass stars. For very young clusters this can be tested by comparing the luminosity in the UV, which is dominated by relatively low-mass stars down to a few solar masses, to the luminosity in Hα, a proxy for the flux of ionizing photons primarily emitted by stars more massive than 20M$_\odot$.

To test this scenario I took very deep Hα narrow-band data of a nearby galaxy Arp 78 and extending to far beyond the "optical" radius of this galaxy at the WIYN 3.5m telescope on Kitt Peak (USA). After a very careful data reduction and continuum subtraction necessary to obtain good sensitivity for the extremely faint line emission I determined the star formation rate from Hα. For comparison I also obtained a SFR from the far-UV flux measured on archival data taken with the GALEX space telescope, and find that, within the associated large uncertainties, both values agree. After careful consideration of age- and dust effects that might affect our findings I conclude that the very low density tidal structure around Arp 78 can be described by a "normal" Salpeter-like IMF and does not show signs of truncation or steepening. This clearly rules out the modified IMF theories as described above at least for this galaxy, and similar observations for a larger sample, some of which I already have acquired during a second WIYN observing run, will be required to draw more generally applicable conclusions.

GALEV evolutionary synthesis models
I. Code, input physics and web-interface

Ralf Kotulla, Uta Fritze, Peter Weilbacher, and Peter Anders
Monthly Notices of the Royal Astronomical Society 396, 462 (2009)

Abstract:

GALEV evolutionary synthesis models describe the evolution of stellar populations in general, of star clusters as well as of galaxies, both in terms of resolved stellar populations and of integrated light properties over cosmological timescales of ≥ 13 Gyr from the onset of star formation shortly after the Big Bang until today.

For galaxies, **GALEV** includes a simultaneous treatment of the chemical evolution of the gas and the spectral evolution of the stellar content, allowing for what we call a chemically consistent treatment: We use input physics (stellar evolutionary tracks, stellar yields and model atmospheres) for a large range of metallicities and consistently account for the increasing initial abundances of successive stellar generations.

Here we present the latest version of the **GALEV** evolutionary synthesis models that are now interactively available at **http://www.galev.org**. We review the currently used input physics, and also give details on how this physics is implemented in practice. We explain how to use the interactive web-interface to generate models for user-defined parameters and also give a range of applications that can be studied using **GALEV** , ranging from star clusters, undisturbed galaxies of various types E ... Sd to starburst- and dwarf galaxies, both in the local and the high-redshift universe.

2.1 Introduction

GALEV (short for GALaxy EVolution) evolutionary synthesis models have been developed over many years. They were published in several steps and under a variety of first author names, reflecting the number of students who have contributed their respective shares to the development. **GALEV** models include the spectral evolutionary synthesis of a stellar population with arbitrary star formation history on the basis of the time evolution of the stellar population in the Hertzsprung-Russell diagram, as well as a detailed chemical evolution model for the ISM in terms of a large number of individual element abundances. **GALEV** models have a wide range of application from star clusters (SCs) to resolved nearby galaxies, to more distant galaxies observed in terms of integrated spectra and photometry, all through galaxies at high redshifts.

Previous applications cover the range from star clusters, normal galaxies E, . . . Sd, dwarf galaxies with and without starbursts, tidal dwarf galaxies, interacting and merging galaxies with their major starbursts, galaxy transformation processes in galaxy clusters, high redshift galaxies with and without starbursts and post-starbursts and damped Lyman-α absorbers. An early attempt at coupling **GALEV** evolutionary synthesis models into a cosmodynamical structure formation simulation was presented in Contardo et al. (1998).

GALEV models are now widely used throughout the community. To facilitate access to the latest developments we here present a user-friendly and customized web-interface. It allows access to already available models for the evolution of star clusters of various metallicities, and galaxies of all types both in terms of their time evolution for comparison with observations in the Local Universe and in terms of their redshift evolution. Furthermore it allows the user to run new models for specific applications.

The philosophy for **GALEV** models is to keep them simple with as small a number of free parameters as possible, and have them predict a large range of observational properties, which – in comparison with observations – constrain the few free parameters. At the present stage, **GALEV** models are 1-zone models without spatial resolution and without any dynamics included. Future prospects are the consistent inclusion of dust detailing absorption and reemission as a function of gas content, metallicity and galaxy type, and the coupling with a dynamical model for stars and gas, including a star formation criterion and an appropriate feedback description, to cope with spatially resolved galaxy data.

2.2 The GALEV code: An overview

2.2.1 Evolutionary synthesis for star clusters and galaxies

Our **GALEV** evolutionary synthesis models have many properties in common with the evolutionary synthesis codes from other groups, e.g. BC03 (Bruzual & Charlot, 2003), PEGASE (Fioc & Rocca-Volmerange, 1997) and Starburst99 (Leitherer et al., 1999), just to name a few, in that all these codes trace the evolution of the stellar population in terms of integrated spectra and/or colours for simple and composite stellar populations.

In contrast to evolutionary synthesis, *stellar population synthesis* (e.g. O'Connell, 1976, 1980) or *differential synthesis* (e.g. Pickles, 1985a,b; Pickles & Visvanathan, 1985) attempts to find the best linear combination of stellar spectra from some library to fit an observed galaxy spectrum . This approach usually achieves very good fits but is limited to a *status quo* description and has difficulties to prove the uniqueness of its solutions. The existence of a stellar Initial Mass Function (IMF) and some continuous Star Formation History (SFH) can be imposed as boundary conditions via Lagrangian multipliers. The major advantages of the population synthesis approach are that it can give valuable first guesses for unknown SFHs and that it allows for unexpected solutions.

All *evolutionary synthesis* models, on the other hand, have to assume a stellar IMF and a SFH, i.e. the time evolution of the SFR for the galaxy. They use stellar evolutionary tracks or isochrones that have to be complete in terms of all relevant stellar evolutionary stages.

Both methods need stellar spectral libraries that also have to be complete in terms of stellar effective temperatures T_{eff}, surface gravities $\log(g)$, and metallicities [Fe/H].

GALEV models are available for a range of stellar IMFs, including Salpeter (1955), Kroupa (2001), and Chabrier (2003). Other choices of the IMF can easily be customized.

For the case of a simple stellar population (SSP), i.e. a star cluster, the SFH is a δ-function, meaning that all stars are formed in a single timestep. **GALEV** models for SSPs of different metallicities (Kurth et al., 1999; Schulz et al., 2002; Anders & Fritze, 2003; Lilly & Fritze, 2006) were shown to well reproduce observed colours and spectral indices of star clusters as function of age and metallicity. They also show a pronounced non-linearity at metallicities close to and above the solar value. Important results include the findings that any colour-to-age or index-to-age calibration/transformations are only valid *at one metallicity* and that any colour-to-metallicity or index-to-metallicity calibration/transformations are only valid *at a given age* (cf. Schulz et al., 2002), and that extrapolating observational relations beyond their calibration range lead to significantly misleading results.

In Anders & Fritze (2003) we demonstrated the importance of nebular emission lines and continuum for young stellar populations and showed that they can account for as much as $50-60\%$ of the flux in broad-band filters, in particular at low metallicities.

For the description of undisturbed galaxies, SFHs have been determined for normal average galaxies of types E, S0, Sa, Sb, Sc, Sd (cf. Sect. 2.5.2), that, in combination with a Salpeter IMF extending from a lower mass limit of 0.1 $M_\odot$ (roughly the hydrogen burning limit) to an upper mass limit around $70-120$ $M_\odot$, depending on the set of isochrones (cf. Sect. 2.3.1) selected, provide agreement with average observed galaxy properties in terms of colours, spectra, luminosities, abundances, and gas content. We stress that our galaxy types are meant to denote *spectral types* and we caution that the one-to-one correspondence between spectral and morphological types observed in the Local Universe might not hold to arbitrarily high redshifts.

While in terms of spectral evolution of the integrated light of galaxies (or star clusters) our models are comparable to other evolutionary synthesis models, they go beyond those in that they also allow to describe and analyze resolved stellar populations in terms of colour-magnitude diagrams (CMDs) and in that they self-consistently describe the chemical evolution of the ISM in galaxies together with the spectral evolution of the stellar populations (for the latter see Sect. 2.2.3), allowing to realistically account for the coexistence of stellar subpopulations of different metallicities observed in local galaxies.

Most of the aforementioned capabilities are not entirely new. Models of the photometric evolution of galaxies date back to Tinsley (1967, 1968, 1972), the first spectroscopic models appeared roughly a decade later (Bruzual, 1983; Guiderdoni & Rocca-Volmerange, 1987). Models of the chemical evolution of galaxies (e.g., Truran & Cameron, 1971; Tinsley, 1972; Matteucci & Padovani, 1993) were capable of taking the increasing enrichment of subsequent stellar populations into account when computing colours (see also, e.g., Matteucci & Tornambe, 1987; Fritze et al., 1989), spectra (e.g., Bressan et al., 1994; Fritze & Gerhard, 1994a; Fioc & Rocca-Volmerange, 1997; Pipino & Matteucci, 2004) and line indices (e.g., Weiss et al., 1995; Bressan et al., 1996). Silva et al. (1998) were the first to include a radiative transfer code into their model and could hence extend the wavelength coverage into the (far-)infrared. However, only very few models (e.g., Prantzos et al., 1994; Portinari et al., 1998) exist that take the metallicity dependence of stellar yields into account and hence merit to be called *chemically consistent*. Those, unlike **GALEV** presented here, mainly focus on the metallicity distribution in the solar neighbourhood and only derive a detailed chemical evolution but no spectral or photometric evolution.

2.2.2 Chemical evolution of galaxies

Modeling the chemical evolution of galaxies starts from a gas cloud with given initial (e.g. primordial) abundances and given mass. A modified version of Tinsley's equations (Tinsley, 1968), including detailed stellar yields, is solved to study the chemical enrichment history of galaxies of different spectral types. This requires knowledge of stellar yields, i.e. production rates of different elements and isotopes, including contributions from SN Ia, as well as stellar lifetimes as function of stellar mass *and metallicity*, that can be taken from nucleosynthesis and stellar evolution models, respectively.

Closed-box models can be compared to models with specified in- and outflow rates and abundances. We follow the chemical evolution of a large number of chemical elements H, He, ... Fe, fully accounting for the time delay between SF and the return of material in stellar winds, PNe, and SNe.

2.2.3 Chemically consistent GALEV models for galaxies

Combining the chemical evolution of ISM abundances and the spectral evolution of the stellar population thus allows for what we call a chemically consistent treatment of both the chemical evolution of the ISM and the spectral evolution of the stellar population in galaxies: we use input physics (stellar evolutionary tracks, model atmospheres, stellar lifetimes and yields) for a large range of metallicities and consistently account for the increasing initial abundances of successive stellar generations.

Broad stellar metallicity distributions have been reported for the Milky Way disk (Rocha-Pinto & Maciel, 1998a), bulge (Sadler et al., 1996; Ramírez et al., 2000), and halo (Ak et al., 2007), as well as for the nearby elliptical galaxy NGC 5128 (Harris et al., 1999; Harris & Harris, 2000).

Depending on the SFH of the respective galaxy type and eventually its infall rate, stars of different ages within a galaxy will have different metallicities and obey an age-metallicity relation determined by their galaxy's SFH.

An important consequence of this coexistence of stars with different ages and metallicities is that stars of different metallicities and different ages dominate the light in different wavelength regions. It has severe implications for metallicity indicators defined in different wavelength regimes, which cannot be expected to trace one and the same stellar metallicity. It also affects some widely used SF indicators and modifies, e.g., the calibrations for SFRs from Hα or [OII] fluxes, as well as from FUV luminosities (cf. Bicker & Fritze, 2005).

Our **GALEV** code can model the spectral and chemical evolution of galaxies with arbitrary IMF and SFH over cosmological timescales, from the very onset of SF all through a Hubble time. In combination with a cosmological model we can follow the redshift evolution of galaxies from the early universe until today (Bicker et al., 2004). It also allows to directly study the impact of evolutionary corrections as well as of the chemically consistent treatment as compared to using solar metallicity input physics only (cf. Kotulla & Fritze, 2009).

2.2.4 Colour magnitude diagrams

Despite simplifications the CMDs are valuable tools to study systematic effects of SFH recovery from observations. Fritze & Lilly (2007) and Lilly & Fritze (2008) investigated the accuracy of recovering SFHs from CMDs as a function of the ages of various subpopulations. In addition, they compared their results with the accuracies of recovering SFHs from integrated spectra, multi-band photometry, or Lick indices. These systematic studies are essential for more distant unresolved stellar populations. Moreover, since synthetic CMDs can be calculated in any desired filter combinations, they can be used to optimize observational strategies with respect to the optimal filter combination, e.g. to disentangle ages and metallicities of young, intermediate-age or old stellar populations.
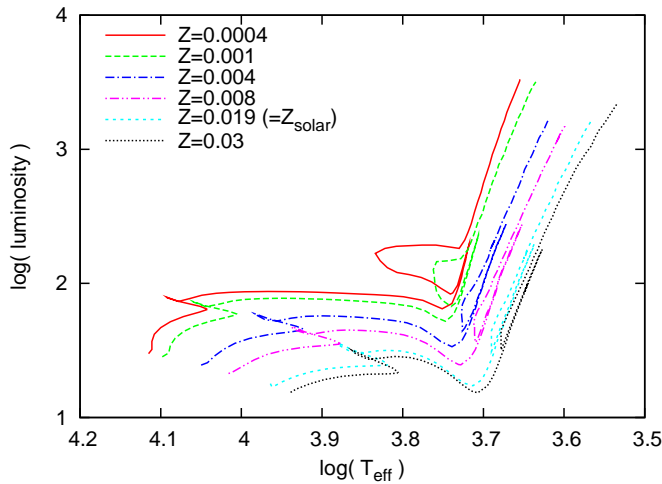
Figure 2.1: Stelar evolutionary tracks of a $2\,M_\odot$ star for different metallicities ranging between $Z = 0.0004 = 1/50\,Z_\odot$ and $Z = 0.03 = 1.5\,Z_\odot$.

2.3 Input physics

In the following sections we will review the input physics we use for our **GALEV** models.

2.3.1 Stellar evolutionary tracks and/or isochrones

Data for stellar evolution can be taken either from isochrones or stellar evolutionary tracks, both having their advantages and disadvantages. **GALEV** models currently use the most recent consistent set of theoretical isochrones from the Padova group (Bertelli et al., 1994, ff) for five different metallicities $[\mathrm{Fe/H}] = (-1.7; -0.7; -0.4; 0.0; +0.4)$ and include the TP-AGB phase, the importance of which was shown in Schulz et al. (2002). In order to be able to fully account for emission lines we also include the Zero Age Main Sequence (ZAMS) into our models. The isochrone for this ZAMS includes stars up to $120\,M_\odot$ and is created from the unevolved first data points of the stellar evolutionary tracks. For more details we refer the reader to Bicker & Fritze (2005).

In Fig. 2.1 we show stellar evolution tracks for a $2\,M_\odot$ star for 6 different metallicities ranging from $Z = 0.0004 = 1/50\,Z_\odot$ to $Z = 0.03 = 1.5\,Z_\odot$ (Girardi et al., 2000). The general shape remains unchanged with changing metallicity, but low-metallicity tracks are shifted towards increasing luminosities and higher effective Temperatures, i.e. towards the top left in the Hertzsprung-Russell diagram. This behaviour is the same for stars of all masses, in the sense that with decreasing metallicity stars become more luminous and their spectra shift towards higher effective temperatures. It is therefore crucial to include those effects to obtain a consistent picture of galaxy evolution.

2.3.2 Library of stellar spectra

In principle, every library of stellar spectra – observed or theoretical – can be used, provided it is complete in terms of stellar T_{eff}, $\log(g)$, and $[\mathrm{Fe/H}]$. **GALEV** assigns spectra to stars in the isochrones according to each star's metallicity, effective temperature T_{eff} and surfce gravity $\log(g)$, normalising the spectra with the star's luminosity (for details see Sect. 2.4.1). So far, **GALEV** uses the BaSeL library of model atmospheres from Lejeune et al. (1997, 1998), originally based on the Kurucz (1992) library. The wavelength coverage spans the range from the XUV at $\lambda \approx 90\,\text{Å}$ to the FIR at $\lambda = 160\,\mu\mathrm{m}$, with a spectral resolution of $20\,\text{Å}$ in the UV-optical and $50 - 100\,\text{Å}$ in the NIR range. We remind the reader that there are significant contributors other
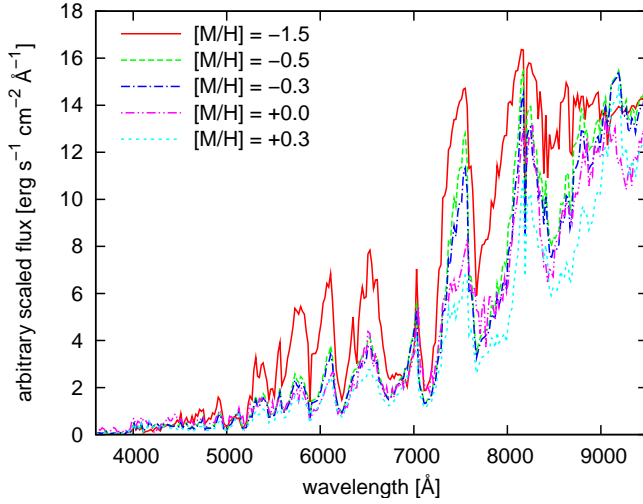
Figure 2.2: Stellar spectra from the Lejeune library for a star with identical $T_{eff} = 3000$K and $\log g = 4.0$, but different metallicities from $[M/H] = -1.5 \ldots + 0.3$.

than starlight (e.g. PAHs, thermal emission from cold dust) at wavelengths beyond the K-band, that are not currently included in our models. This wavelength range should hence be used with caution.

Stellar spectra are heavily influenced by metallicity due to the increased absorption line strength (e.g. for Fe-lines) and line-blanketing with increasing abundances. In Fig. 2.2 we show the example of a cool star ($T_{eff} = 3000$K, $\log g = 4.0$) from the above mentioned BaSeL library. The effects of metallicity are stronger for cool stellar atmospheres where molecular absorption by VO, TiO, NH_4, H_2O etc. plays a larger role (Allard et al., 2000; Kučinskas et al., 2006).

2.3.3 Gaseous emission: lines and continuum

In addition to the stellar absorption spectra we also compute line and continuum emission from gas ionized by hot massive stars.

We do not take the ionizing photons from the stellar spectral library, but instead use the tabulated values from Schaerer & de Koter (1997) for N_{LyC} as a function of stellar effective temperature, radius, and metallicity. They yield much better agreement with observations as well as with recent results from expanding non-LTE, line-blanketed models atmosphere calculations by Smith et al. (2002).

We can then compute the total flux emitted by the gas per unit wavelength as

$$F_\lambda = \frac{\gamma_\lambda(T)}{\alpha^{(2)}(T)} N_{LyC} = \frac{c}{\lambda^2} \frac{\gamma_\nu(T)}{\alpha^{(2)}(T)} N_{LyC} \tag{2.1}$$

with the speed of light c, electron temperature $T = 10\,000$ K, and total recombination coefficient $\alpha^{(2)}(10\,000\,\text{K}) = 2.575 \times 10^{-13}\,\text{cm}^3\,\text{s}^{-1}$ (Aller, 1984). The gas continuum coefficients are then computed for $T = 10\,000$ K following Ercolano & Storey (2006) that contains an algorithm to compute the bound-free radiation for hydrogen and helium (γ_{HI}, γ_{HeI}, and γ_{HeII}). The H I two-photon emission coefficient γ_{H2p} is taken from Nussbaumer & Schmutz (1984) and for the free-free emission γ_b we use the formula from Brown & Mathews (1970) and compute the Gaunt factors using the algorithm from Hummer (1988). All γ-factors are summed to form the final:

$$\gamma_\nu = \gamma_b + \gamma_{H2p} + \gamma_{HI} + \frac{n_{He^+}}{n_{H^+}} \gamma_{HeI} + \frac{n_{He^{++}}}{n_{H^+}} \gamma_{HeII}. \tag{2.2}$$

For the densities of the helium He I and He II ions relative to H I we use values typical for H II regions in galaxies (Ercolano, private communication), 0.0897 and 1.667×10^{-4} for He I and He II, respectively. The final isochrone spectra are not very sensitive to slight changes in these values.

The line strengths of the hydrogen lines are computed using atomic physics and the emission rate of ionizing photons N_{LyC} from O- and early B-stars. From the number of ionizing photons, N_{LyC}, we compute the flux in the Hβ line using

$$f(H\beta) = 4.757 \times 10^{-13} \text{erg} \times N_{LyC}. \tag{2.3}$$

Assuming Case B recombination for a pure hydrogen cloud with $T_e = 10\,000$ K (Osterbrock & Ferland, 2006), we can then derive the line strengths of all other hydrogen lines. Line strengths for heavier elements are computed using metallicity-dependent line-ratios relative to Hβ. For metallicities [Fe/H] ≥ -0.4 those are taken from the Stasińska (1984) photoionization models, adopting typical Galactic values of $T_e = 8100$ K and $n_e = 1$ cm^{-3} for electron temperature and density. For lower metallicities, we use observed line ratios from Izotov et al. (1994, 1997) and Izotov & Thuan (1998). These are supposed to include systematic changes in T_e, n_e and the ionizing radiation field in lower metallicities environments (cf. Anders & Fritze, 2003). Note that we do not include detailed radiation transfer calculations (as, e.g., in Garcia Vargas & Diaz, 1994; Ferland et al., 1998; Ercolano et al., 2003), hence we caution the user to use line-ratios for detailed line diagnostics. We correct the gaseous emission for small amounts of dust within the H II regions by reducing the ionizing flux by 30% if the gaseous metallicity is near solar, i.e. for [Fe/H] ≥ -0.4. For lower metallicities we use the full ionizing flux since those environments are essentially dust-free (Mezger, 1978). We do not account for yet unknown amounts of dust depletion of heavy elements within the H II regions. However, in the case of low-metallicity galaxies these effects are already included in the observed line-ratios.

Note that we do not account for internal self-absorption of Lyman continuum photons within the H II regions or the surrounding galaxy, since the fraction of flux leaking out of these regions is still a matter of ongoing debate (see, e.g., Ferguson et al., 1996; Castellanos et al., 2002; Fernández-Soto et al., 2003; Inoue et al., 2005; Siana et al., 2007; Wise & Cen, 2009).

Depending on application, our models can include both continuum and line emission, continuum emission only or no gas emission at all. In Krüger et al. (1995) and Anders & Fritze (2003) we showed that in the case of Blue Compact Dwarf galaxies and in young and metal-poor SSPs, gaseous emission can contribute as much as 60% to the flux in broad-band filters. Emission lines are the dominant contributors in the optical, whereas continuum emission dominates in the NIR.

Combining the effects of higher luminosities and higher effective temperatures with the effects of longer lifetimes of high-mass stars at low metallicities has a profound impact on the spectrum of galaxies. All three factors lead to bluer colours, higher overall luminosities and as a further aspect significantly stronger gaseous emission, i.e. gaseous continuum and line emission.

In Fig 2.3 we show the gaseous emission spectra for isochrone spectra at an age of 4 Myr and for 5 metallicities from $1/50\,Z_\odot$ to $2.5\,Z_\odot$. The first notable aspect is the overall emission line strength that is higher by a factor of about 10 comparing the two extreme cases. But also the individual line ratios change significantly, i.e. the ratio between Hα (6563 Å) and [N II] (6583 Å) (Hα/[NII] $\approx$ 48 at low metallicity and $\approx$ 7 for solar metallicities). This extreme ratio is directly affected by the lower nitrogen abundance at low metallicity. Other line ratios, e.g. [O II] (3727 Å) to [O III] (5007 Å) also change due to the more intense radiation field coming with the low metallicity environment.

2.3.4 Lick stellar absorption indices

Since the resolution of the Lejeune et al. (1997, 1998) library is not sufficient to calculate Lick absorption indices directly from the spectra, **GALEV** models use the empirical calibrations
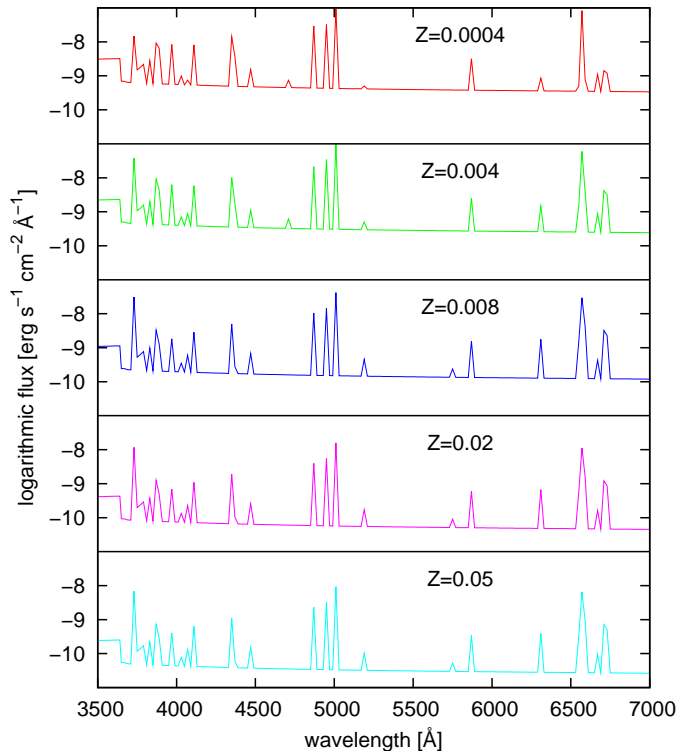
Figure 2.3: Emission line spectrum of the 4 Myr isochrone for 5 different metallicities ranging between $Z = 0.0004$ ([Fe/H] = -1.7) and $Z = 0.05$ ([Fe/H] = $+0.4$).

presented by Gorgas et al. (1993), Worthey et al. (1994) and Worthey & Ottaviani (1997). From those, **GALEV** calculates the fluxes in the Lick indices for every star, sums them up for the entire stellar population at every timestep to yield integrated index fluxes and, in combination with continuum fluxes from the integrated absorption line spectra, the respective index equivalent widths (Kurth et al., 1999; Lilly & Fritze, 2006). **GALEV** at the present stage includes the following Lick indices: $H\delta_A$, $H\gamma_A$, $H\delta_F$, $H\gamma_F$, CN_1, CN_2, Ca4227, G4300, Fe4383, Ca4455, Fe4531, Fe4668, $H\beta$, Fe5015, Mg_1, Mg_2, Mgb, Fe5270, Fe5335, Fe4506, Fe5709, Fe5782, NaD, TiO_1, and TiO_2 (see Trager et al., 1998, and references therein for all index definitions).

2.3.5 Stellar yields

To model the chemical enrichment histories of galaxies, **GALEV** uses stellar yields for a large number of individual elements (H, He, Li, Be, B, C, N, O, F, Ne, Na, Mg, Al, Si, P, S, Cl, Ar, K, Ca, Sc, Ti,V, Cr, Mn, Fe, Co, Ni, Cu, Zn, Ga, Ge) from Woosley & Weaver (1995) for massive stars and from van den Hoek & Groenewegen (1997) for low-mass stars of various metallicities. Stellar lifetimes are taken from the isochrones. There is a minor inconsistency in doing so, since Woosley & Weaver (1995) used models without mass-loss, while current isochrones in general account for mass-loss. However, since yields are only available for a very coarse metallicity grid this does not significantly affect the resulting chemical evolution. **GALEV** also includes type Ia SN yields for the carbon deflagration white dwarf binary scenario (W7) from Nomoto et al. (1997). See Lindner et al. (1999) for a detailed description of the chemically consistent chemical evolution aspects of **GALEV** .

2.3.6 Ejection rates and remnant masses

One of the central input parameters for **GALEV** is the time-dependent ejection rates necessary to compute the chemical evolution of galaxies. Those rates are derived from the initial stellar
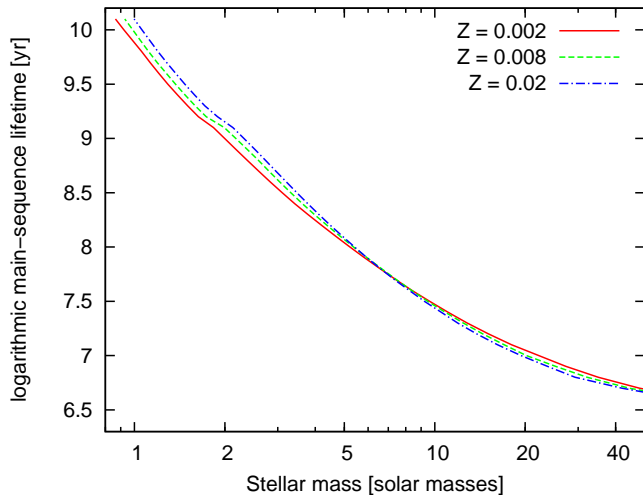
Figure 2.4: Main-sequence lifetimes as function of initial stellar mass for three different metallicities.

masses $M_\star$ and the remaining remnant masses m_R. For stars with masses $M_\star \geq 30\,M_\odot$ the remnant is assumed to be a black hole of $m_{BH} = 8.0\,M_\odot$, with the remaining mass being returned to the ISM; stars with initial masses of $30\,M_\odot \geq M_\star \geq 6.0\,M_\odot$ result in a neutron star of mass m_{NS} given by Nomoto & Hashimoto (1988):

$$m_{NS}[M_\odot] = 1.02 + 3.6363 \times 10^{-2}(M_\star/M_\odot - 8.0)M_\odot;$$

For the mass range of $6.0\,M_\odot \geq m_\star \geq 0.5\,M_\odot$, for which the stellar remnant is a white dwarf, we use a fit to the data points of Weidemann (2000):

$$m_{WD}[M_\odot] = 0.444 + 0.0838(M_\star/M_\odot);$$

This, combined with the extrapolation of the NS relation down to $6\,M_\odot$, provides a better matched connection between the two mass ranges. while being compatible with the slightly steeper slope derived by Kalirai et al. (2008). However, as the remnant is only used to derive the mass returned to the ISM during its lifetime and death, the exact transition point from neutron star to white dwarf is of minor importance.

Stars with masses $m_\star \lesssim 0.5M_\odot$ have lifetimes in excess of a Hubble time and negligible winds, hence do not return any material to the ISM.

In Fig. 2.4 we show the main-sequence lifetimes of stars as function of initial mass for three different metallicities from $Z = 0.002 = 1/10\,Z_\odot$ to $Z = 0.02 = Z_\odot$, based on data from Marigo et al. (2008) for $M_\star < 7\,M_\odot$ and Bertelli et al. (1994) for $M_\star > 7M_\odot$. Low-mass stars live longer at high metallicities, while high-mass stars have longer lifetimes for lower metallicities; stars with masses $\approx 3 - 4\,M_\odot$ have roughly the same lifetimes independent of metallicity (see Fig. 2.4). The $20M_\odot$ star for example has a 10% increased lifetime at $Z = 1/10\,Z_\odot$ as compared to $Z = Z_\odot$.

2.3.7 Filter functions and magnitude systems

GALEV includes a large number of filter functions to be convolved with the model spectra in order to avoid uncertainties associated with transformations between filter systems. It also provides the option to choose the desired magnitude system Vegamag, ABmag, and STmag to be directly comparable to observations and avoid transformations between different magnitude systems. Magnitudes in the Vegamag systems are defined to have magnitude zero for an A0V star; we use the Vega-spectrum from the Lejeune et al. (1997, 1998) library combined with the flux calibration from Bohlin & Gilliland (2004) as our standard star. AB magnitudes (Oke, 1974; Bohlin &

Gilliland, 2004) are derived from the monochromatic flux f_ν such that $m_{AB} = -2.5 \log(f_\nu) + 48.6$ if f_ν is measured in $erg\, s^{-1}\, cm^{-2}\, Hz^{-1}$; a colour of 0 in the AB magnitude means that the object emits constant flux per unit *frequency* interval; analogous to the above, colours of 0 in the ST magnitude systems mean constant emitted flux per unit *wavelength* interval. The zeropoint has been chosen such that a source with $f_\lambda = 3.63 \times 10^{-9} erg\, s^{-1}\, cm^{-1\, -1}$ has $m_{ST} = 0\, mag$ in all filters.

Our current database contains filters from all major telescopes and instruments, including all HST instruments (including WFC3), many ESO instruments, and all common filter sets like Johnson/Cousins, Strömgren, Washington, and SDSS. However, note that due to the wide wavelength sampling of 20 of the current spectral library, narrow-band filters cannot be adequately supported at this stage.

2.3.8 Dust extinction

To account for extinction and reddening due to interstellar dust, **GALEV** also implements the most commonly used empirical extinction laws from Calzetti et al. (2000) and Cardelli et al. (1989). The earlier was derived from actively star-forming galaxies and describes a relatively gray extinction without the 2175 bump, characteristic for the latter extinction law. For the Cardelli law we assume a mean extinction parameter of $R_V = A(V)/E(B-V) = 3.1$, characteristic for relatively quiescent galaxies. Although models exists that offer a more detailed treatment of dust extinction and in some cases dust emission (see, e.g., Silva et al., 1998; Popescu et al., 2000; Cunow, 2001, 2004; Dopita et al., 2005; Möllenhoff et al., 2006; Piovan et al., 2006a,b), the major drawback of these models is that they in general require assumptions on the geometry and spatial distribution of dust, gas and stars. However, the aim of **GALEV** is to describe the spectrum of the average represantation of each galaxy type, making if difficult to compare these two approaches.

2.3.9 Cosmological model

GALEV can also be coupled to a cosmological model to describe the evolution of galaxies as function of redshift. For this purpose we have to convert ages into redshifts and vice versa. In its current version we implemented a flat cosmology ($\Omega_K = 0$). The choice of the local Hubble constant H_0, the density parameters Ω_M and Ω_Λ (with the additional constraint $\Omega_M + \Omega_\Lambda = 1$) and the galaxy formation redshift z_{form} then completely determine the galaxy age as function of redshift. Because of the short time interval between e.g. $z = 12$ and $z = 5$, the exact value of z_{form} has very little impact, hence we choose an intermediate value of $z_{form} = 8$ as our default.

2.3.10 Intergalactic attenuation

To correctly describe spectra of higher redshift galaxies one has to include the absorption shortwards of the Lyman-α line due to intervening neutral hydrogen clouds. For that reason **GALEV** implements the description for the average attenuation effect as function of redshift following Madau (1995) and covering the range $0 \leq z \leq 7$.

2.4 Program structure

The actual modeling process with **GALEV** can be divided into three steps:

1. In the first step **GALEV** convolves the isochrones of each age-metallicity combination with the specified IMF, normalized to $1\,M_\odot$. It then assigns a spectrum from the stellar library to each star on each isochrone and computes the integrated isochrone spectrum. Then the gaseous continuum emission and emission lines are added to the young isochrone spectra. Using the yield tables and stellar remnant masses described in Sect. 2.3.5 with stellar lifetimes from the isochrones, **GALEV** also derives the gas and metal ejection rates needed for the chemical evolution.

2. In the second step **GALEV** computes the chemical and spectral evolution of the desired stellar population. For each timestep the current isochrone spectra are weighted with the SFH. The contributions from older SF episodes are obtained by integration over all past timesteps. The required interpolations in age and metallicity are described below. **GALEV** thus calculates the time evolution of the integrated spectrum and its resulting line strength (i.e. Lick-) indices of a simple (SSP, star cluster) or composite (galaxy) stellar population, including the gaseous emission where appropriate. From the ejection rates and the available gas mass **GALEV** calculates the new gaseous metallicity that will be used for stars born during the next timestep.

3. In the last step **GALEV** converts the integrated spectra into magnitudes in a large number of filters. Given a list of requested filters it convolves the spectra with the filter functions and applies zero-points to yield absolute magnitudes for each timestep. It can alternatively be combined with a cosmological model to yield apparent and absolute magnitudes as function of redshift. If requested it also accounts for dust extinction using observed extinction laws and, in the context of cosmological evolution, also for the attenuation by intergalactic neutral hydrogen.

This process is also explained in a more vivid step-by-step explanation in appendix A.

2.4.1 Computation of isochrone spectra

A crucial step is the assignment of stellar spectra from the library to the points describing the isochrones. Since the available stellar parameters T_{eff} and $\log(g)$ in the library often do not match those required by the isochrones, **GALEV** has to interpolate between them in both T_{eff} and $\log(g)$. For a given combination of T_{eff} and $\log(g)$ this is done as follows:

1. Find up to four spectra bracketing the required values in both T_{eff} and $\log(g)$.

2. Interpolate the spectra to the required value of T_{eff} in each pair of lower (upper) values of $\log(g)$, yielding two new interpolated spectra with the correct T_{eff} and different $\log(g)$. An important factor during this interpolation is the weighting of the spectra with each star's luminosity given by the isochrone. We choose to use the integrated luminosity in the Johnson-V or Bessell-H-band, depending on the temperature of the star given by T_{eff}. The original approach to normalize all stars in the V-band turned out to be insufficient for cool giants with only little flux in the optical. A "cool giant" in this context is defined by $T_{\text{eff}} \leq 3500\,\text{K}$ and $\log(g) \leq 3.5$.

3. The spectrum for the required value of $\log(g)$ is then obtained by interpolation between the two spectra with the right T_{eff}, again weighting with each star's respective luminosity.

For the very hot stars ($T_{\text{eff}} > 50\,000\,\text{K}$), the BaSeL stellar library does not provide spectra. In those cases we extend the spectral library by approximating the missing stellar spectra with black-body spectra of the requested temperatures. The validity of this approximation for wavelengths longwards of $\lambda \approx 230$ is supported by only minor differences between pure black-body and true spectra from both observations (Gauba et al., 2001) and modelling (Rauch, 2003) of very hot central stars of planetary nebulae.

In a final step, all isochrone spectra are normalized to a distance of $10\,\text{pc}$, and are given in units of $\text{erg s}^{-1}\,\text{cm}^{-2}\,^{-1}$.

2.4.2 Interpolation of isochrone-spectra and integration of galaxy spectra

One important aspect of **GALEV** is how to interpolate between the isochrone spectra of different ages and metallicities, in other words how to map the coarse grid of isochrones available onto the finer grid needed for galaxies. **GALEV** here interpolates logarithmically between ages and linearly between metallicities expressed as $\log(Z) \sim [Fe/H]$. During their very early stages the gaseous metallicities of galaxies are lower than the metallicity of the lowest metallicity isochrone with $[Fe/H] = -1.7$. For stars born at these stages, we chose to use the lowest metallicity isochrone to avoid the uncertainties in an extrapolation to lower metallicities. The same is done for stars born from gas with a metallicity higher than the highest metallicity isochrone. For these stars we use the highest metallicity isochrone available with $[Fe/H] = +0.4$.

2.5 Calibration of the GALEV models and comparison to observations

We stress that with the input physics as outlined above, a stellar IMF with lower and upper mass limits chosen and total mass of the galaxy or star cluster specified, **GALEV** models provide the time evolution of spectra, luminosities, and colours *in absolute terms*. The same holds true for the gas content and the chemical enrichment of galaxies. *No a posteriori* gauging is applied.

The only exception is the cosmological context for galaxies: before luminosities and magnitudes of redshifted galaxies are calculated, the B-band model luminosities after a galaxy age corresponding to redshift z = 0.0044 (i.e. the redshift of the Virgo cluster) in the chosen cosmological model are scaled to the average observed B-band luminosity of the respective galaxy type in the Virgo cluster (cf. Sect. 2.5.2).

In the following we present as an overview the comparison of **GALEV** models for star clusters and for normal galaxy types E, Sa . . . Sd with observations and refer to previous papers for more details.

2.5.1 Star clusters

The colours from U through K predicted by **GALEV** models for SSPs or star clusters at an age of $\sim 12 - 13$ Gyr are in very good agreement with the respective observed colours for a large set of M31 and Milky Way globular clusters (Barmby et al., 2000; Barmby & Huchra, 2000) at their respective metallicities (cf. Schulz et al., 2002). Small deviations in the U- and B-bands can be explained by the existence of Blue Straggler stars (likely products of stellar mergers) in the dense cores of GCs, which can make significant contributions at those short wavelengths (Xin et al., 2007; Xin & Deng, 2005; Cenarro et al., 2008), but are not included in our models yet, as standard isochrones exist for non-interacting single stars only. Further contaminants in the blue-to-UV region are Blue Horizontal Branch stars (Schiavon et al., 2004; Dotter et al., 2007) and to a lesser degree even Cataclysmic Variables and low-mass X-ray binaries in the far-UV range (Rich et al., 1993; Dieball et al., 2007).

As shown in Kurth et al. (1999) and Lilly & Fritze (2006), Lick indices for SSPs as calculated by **GALEV** agree well with Galactic and M31 globular cluster data as compiled by (Harris, 1996) in his online catalog[2].

GALEV models for star clusters also show good agreement at an evolutionary age of $\sim 12 - 13$ Gyr with the empirical calibrations for colours $(B - V)$ and $(V - I)$ versus metallicity [Fe/H] for old Galactic and M31 globular clusters, as e.g. given by Couture et al. (1990) and Barmby et al. (2000) over the metallicity range $-2.3 \leq [Fe/H] \leq -0.5$ of these clusters. They also show,
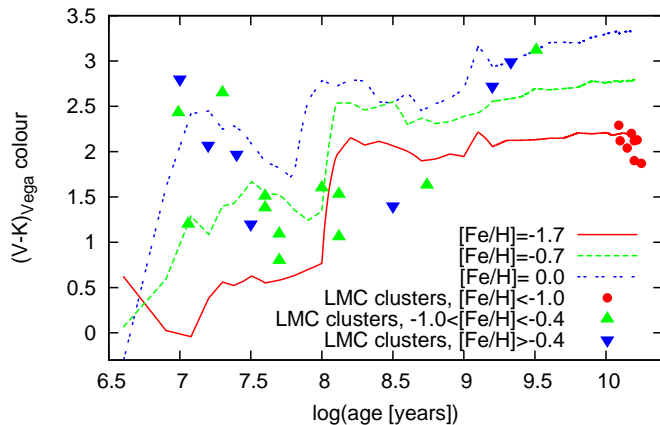
---

[2]http://physwww.physics.mcmaster.ca/~harris/mwgc.dat

Figure 2.5: Evolution of the V-K colour of our SSP models with metallicities of [Fe/H] = −1.7 (red, solid line), [Fe/H] = −0.7 (green, dashed), and [Fe/H] = 0.0 (blue, dash-dotted). We also plot the data (ages from Mackey & Gilmore (2003), colours from Persson et al. (1983)) for 35 clusters in the Large Magellanic Cloud for comparison.

however, significant deviations from a linear extrapolation of these empirical relations towards higher metallicities, and they also show that the empirical relations are only valid for the *old* globular clusters for which they have been derived. Models can, of course, be used to study the behaviour of colour – metallicity relations for any colour and as a function of time (cf. Schulz et al., 2002, for details).

In Figure 2.5 we plot the evolution of three SSP models with different metallicities ranging from the lowest available value of [Fe/H] = −1.7 to the solar value [Fe/H] = 0.0. For comparison we also show V-K colours from Persson et al. (1983) for star clusters in the Large Magellanic Cloud, colour-coded according to their metallicity as derived from CMDs Mackey & Gilmore (2003). Our models are able to not only reproduce the full range of observed colours, but also match the colour-evolution of each metallicity subpopulation if accounted for typical uncertainties of 0.4 dex in the age-determination. For the old and metal-poor globular clusters our predicted V-K colours are in good agreement with observations.

As shown in Lilly & Fritze (2006), **GALEV** models for SSPs also agree, after $12 − 13$ Gyr of evolution with empirical calibrations of Lick indices vs. [Fe/H]. However, they also show that *all metal-sensitive indices are also age-dependent* and that the famous *age-sensitive H_β and H_γ indices are also metal-dependent* to some extent (see also Thomas et al., 2003; Korn et al., 2005). Hence, the empirical calibrations of Mg_2, Mgb, etc. vs. [Fe/H] are valid only for *old* (i.e. > 10 Gyr) globular clusters.

Empirical calibrations for colours or Lick indices vs. metallicity or age should therefore not be used for star clusters or globular clusters for which it is not a priori clear that their properties fall within the range of the calibrating Galactic clusters. Instead a full set of colours and/or indices in comparison to an extended grid of models covering the full parameter space, allows for independent and accurate determinations of both ages and metallicities (cf. Sect. 2.8.1).

2.5.2 Galaxies

By default, all our **GALEV** models for galaxies use a Salpeter IMF (Salpeter, 1955) with lower and upper mass limits of $0.1\,M_\odot$ and $100\,M_\odot$, respectively.

The star formation histories, i.e. the time evolution of the star formation rates, of the different spectral galaxy types E and Sa to Sd are *the* basic parameters of **GALEV** and, in fact, of any kind of evolutionary synthesis models. In Fig. 2.6 we show SFHs for galaxies of different types from E through Sd, assuming the same total (i.e. stars and gas) mass M_{tot} of $10^{10}\,M_\odot$ for all of them. These SFHs are in good agreement with chemical and spectrophotometric findings from Sandage (1986).
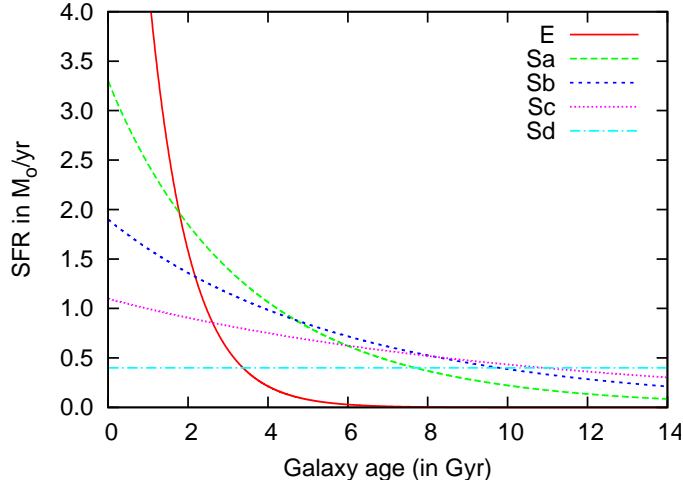
Figure 2.6: Star formation histories for the five different galaxy types E and Sa through Sd. Absolute numbers are normalized to a total galaxy mass of $10^{10} M_{\odot}$.

For the elliptical model we use an exponentially declining SFR

$$\Psi(t) = \frac{M_{\text{tot}}}{\alpha} \times \exp(-t/\tau) \tag{2.4}$$

with an e-folding time $\tau = 1\,Gyr$ and $\alpha = 8.55 \times 10^8$ yr.

For spectral types S0 and Sa through Sc the SFR is tied to the evolving gas content as given by

$$\Psi(t) = \beta \times \frac{M_{\text{gas}}(t)}{10^9}, \tag{2.5}$$

with efficiency parameters β decreasing from early to later spiral types, $\beta = 1.0\,\text{yr}^{-1}$ for S0, $\beta = 0.33\,\text{yr}^{-1}$ for Sa, $\beta = 0.19\,\text{yr}^{-1}$ for Sb, and $\beta = 0.11\,\text{yr}^{-1}$ for Sc galaxies.

Sd model galaxies are described by a constant SFR:

$$\Psi(t) = \psi_0 \times \frac{M_{\text{tot}}}{10^{10}} = \text{const}, \tag{2.6}$$

where $\psi_0 = 0.4\,M_{\odot}\,\text{yr}^{-1}$.

For *closed-box models*, these parameters α, β, ψ_0, and τ are the only free parameters. We do *not* require additional parameters such as infall of gas or outflow in galactic winds to reproduce observations. Note that all these SFH parameters are independent of galaxy mass. We therefore do not reproduce mass-metallicity or colour-magnitude relations for galaxies of identical spectral types.

These SFHs are very similar in *all* evolutionary synthesis models (cf. e.g. Bruzual & Charlot, 2003; Fioc & Rocca-Volmerange, 1997). In detail, we adjust the SFH for the chemically consistent **GALEV** models as to match, after a Hubble time of evolution (i.e. $\approx 13\,\text{Gyr}$ for our assumed concordance cosmology with $H_0 = 70\,\text{km}\,\text{s}^{-1}\,\text{Mpc}^{-1}$, $\Omega_M = 0.30$ and $\Omega_\Lambda = 0.70$), the observed

- average integrated colours from UV through NIR,
- average gas fractions,
- average metallicities,
- average present-day SFRs,
- average mass-to-light ratios, and
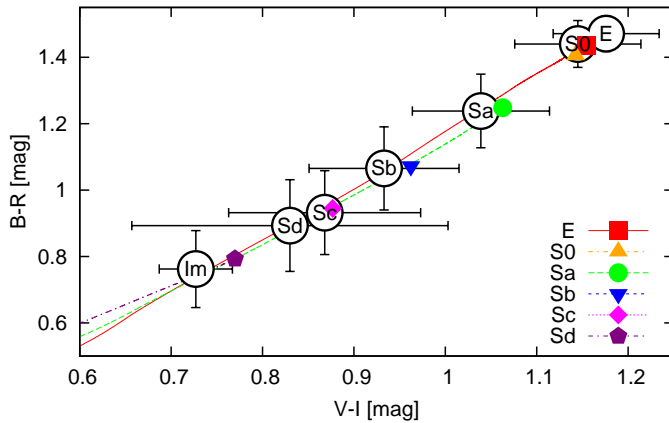- template UV – optical spectra

Figure 2.7: Evolution of galaxies of different types E through Sd in the (B-R)–(V-I) colour-colour-plane. Colours after 13 Gyr are plotted with large symbols. We also show colours for typical galaxies (large circles around galaxy type) taken from Buta et al. (1995) and Buta & Williams (1995).

of the respective spectral types as detailed below. All these observational constraints together very neatly define the average SFHs of undisturbed galaxies E, Sa, Sb, Sc, Sd and tightly constrain the few parameters describing them for a given IMF.

We stress that **GALEV** and all other evolutionary synthesis models with their respective SFHs are meant to describe *spectral types* of galaxies. And we caution that while in the Local Universe and for undisturbed galaxies a clear one-to-one correspondence is observed between spectral and morphological types, it is an open question how far back in time this correspondence might hold.

Gas fraction: The above described parameters have been tuned to reproduce the typical gas fractions observed in local galaxies (e.g. Read & Trentham, 2005). We use gas contents, defined as fractions of gas relative to the total (gas+stars) mass, of $M_{gas}/M_{tot} = 0.0$ for E-models, 0.05 for Sa, 0.15 for Sb, 0.30 for Sc, and 0.55 for Sd models, respectively.

Colours: With these parameters being fixed, we compare a wide range of model-predicted colours from near-UV to near-IR to values from the literature. Our (B-V) colours, e.g. of 0.86 (E), 0.78 (Sa), 0.64 (Sb), 0.56 (Sc), and 0.43 (Sd) compare very well with the ranges found in the RC3 catalog of de Vaucouleurs et al. (1995), listing mean colours of $(B - V) = 0.89^{+0.17}_{-0.53}$ (E), $0.74^{+0.25}_{-0.35}$ (Sa), $0.66^{+0.22}_{-0.47}$ (Sb), $0.51^{+0.22}_{-0.50}$ (Sc), and $0.44^{+0.22}_{-0.18}$ (Sd).

Spectra: In Fig. 2.8, we compare our model spectra to local templates for the galaxy types E, Sa, Sb, Sc, Sd from the catalog of Kennicutt (1992). As can be seen from those plots, the observed spectra for all spectral galaxy types from old passive ellipticals through the actively star forming Sd galaxies are well reproduced. Although our spectra (here using Lejeune's library) have a lower spectral resolution than the observed templates, they nonetheless reproduce all features, like absorption and emission lines. In the lower part of each plot we also show relative differences between model and template spectra. Deviations are generally smaller than differences between different galaxies of the same type, confirming the good agreement. Small differences for the emission lines originate in different spectral resolutions of templates and model spectra. Note that due to our chemically consistent treatment **GALEV** models can reproduce the Sd template spectrum with our Sd model at an age of 13 Gyr. This is a notable difference to all other evolutionary synthesis models that can only reproduce Sd template spectra with younger models of ages $4 - 6$ Gyr (cf. Bruzual & Charlot, 1993).

Metallicities: As mentioned above **GALEV** models calculate the time evolution not only of individual element abundances but also of the global ISM metallicity Z. After $\sim$ 13 Gyr of evolution (for details on the evolution as function of age or redshift see Bicker et al. (2004) or Kotulla & Fritze (2009)), our models reach ISM abundances of $Z_E = Z_\odot$, $Z_{Sa} = 1.5 Z_\odot$, $Z_{Sb} = 0.8 Z_\odot$, $Z_{Sc} = 0.5 Z_\odot$, and $Z_{Sd} = 0.25 Z_\odot$. Those metallicities are in good agreement with
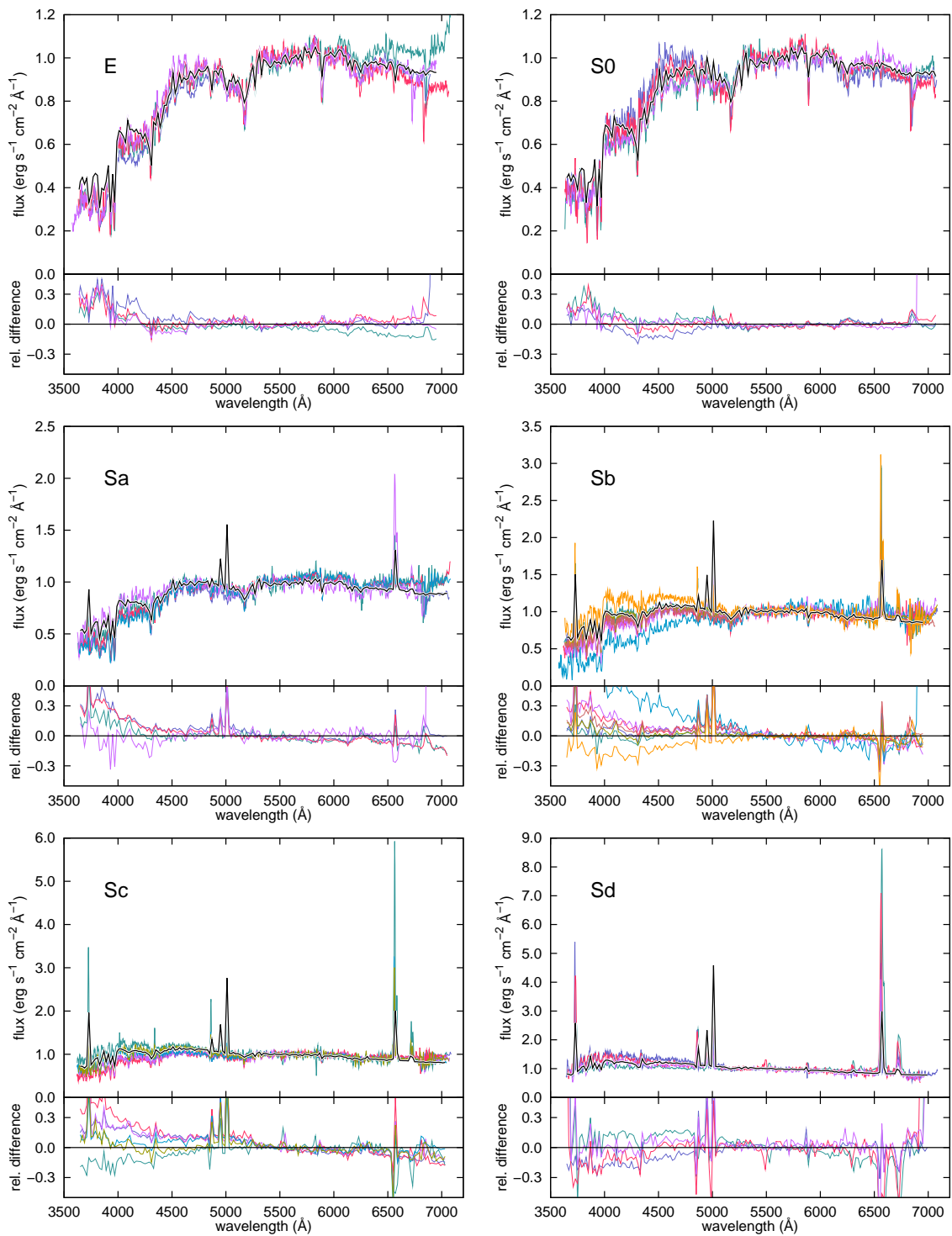
Figure 2.8: Comparison of model spectra of different types (top row: E and S0, middle row Sa and Sb, bottom row Sc and Sd) with observed template spectra from Kennicutt (1992). The black solid lines show the spectrum of **GALEV** models at an age of 12.8 Gyr, the coloured lines show spectra of several template galaxies of each respective type. In the lower part of each plot we also show relative differences between the **GALEV** spectra and each template spectrum.

typical ISM abundances, as measured at $1\,\mathrm{R_{eff}}$, the effective or characteristic radius, of spiral galaxies of various types (Oey & Kennicutt, 1993; Ferguson et al., 1998a; van Zee et al., 1998). Note that our models aim to represent the *typical L* or M* galaxy of each spectral type*. Galaxies of different masses within the same spectral type are known to have slightly different metallicities, as described by the mass-metallicity or luminosity-metallicity relations (Skillman et al., 1989; Tremonti et al., 2004; Kewley & Ellison, 2008). As stated before, these relations are currently not accounted for by **GALEV** standard models. However, the user is free to choose parametrizations of the SFHs as a function of galaxy mass (as, e.g., in Bressan et al., 1994) that reproduce these relations.

Star formation rates: GALEV models predict the following present-day SFRs Ψ_p in $[\mathrm{M_\odot\,yr^{-1}}]$ for the different spectral galaxy types: $\Psi_p \approx 0$ for E, $\Psi_p = 0.65$ for Sa, $\Psi_p = 0.4$ for Sb, $\Psi_p = 0.47$ for Sc, and $\Psi_p = 0.13$ for Sd galaxies. These numbers are in agreement with the average star formation rates of 0.22, 0.32 ± 0.2, 0.33 ± 0.14, and $0.09 \pm 0.03\,\mathrm{M_\odot\,yr^{-1}}$ for Sa to Sd galaxies from Kennicutt (1983). We caution that the smooth SFHs in **GALEV** and other evolutionary synthesis models certainly are simplifications; real galaxies will in general experience fluctuations in their SFRs around these mean values. For the Milky Way, Rocha-Pinto et al. (2000) showed on the basis of individual stellar ages and abundances that the mean global SFH indeed fell nicely between those of our Sb and Sc models, with fluctuations of a factor of 2 on timescales of 100 Myr. Such fluctuations around the mean, however, do not significantly affect the long-term evolution.

Mass-to-light ratios: Using the stellar mass assembled after ~ 13 Gyr and the absolute V-band luminosity, we compute the V-band mass-to-light ratios. The results are: $\mathrm{M/L_V(E, Sa, Sb, Sc, Sd)} = 11.8, 8.2, 5.9, 4.5, 3.0$, respectively. These include a factor that we call *fraction of visible mass* (FVM) and that accounts for the fraction of mass locked up in sub-stellar objects like brown dwarfs, planets, etc. This factor is set to FVM=0.5 in **GALEV** models, implying that only half the star formation rate forms luminous stars, while the remaining half is locked up in non-luminous objects (cf. Bahcall et al., 1992). Only with this FVM=0.5 can agreement with observed average M/L ratios (Faber & Gallagher, 1979; Bell & de Jong, 2001; Read & Trentham, 2005) be achieved together with agreement in colours, spectra, and chemical abundances. Note that FVM does not include remnants of stellar evolution like white dwarfs, neutron stars or black holes; those are considered separately as part of stellar evolution.

Introducing the FVM parameter does not only affect the mass-to-light ratios but also has an impact on the chemical evolution with in turn impacts on most other derived parameters. A Salpeter IMF with mass-limits of 0.1 and $100\,\mathrm{M_\odot}$ would lock up 60% of the mass in long-lived stars with $\mathrm{M} \leq 1\,\mathrm{M_\odot}$, with the remaining 40% progressing the chemical enrichment of the galaxy. However, by applying a FVM=0.5 we half this fraction of stars with $\mathrm{M} \geq 1\,\mathrm{M_\odot}$ so that now only 20% of stars return their ejecta at the end of their lives, with the majority of mass being locked up. This concept to slow down the chemical enrichment is a common feature of many codes, but comes with different names, e.g. as free parameter $(1 - \xi)$ in Portinari et al. (1998).

Luminosity normalization With the SFHs as given above and a Salpeter IMF, **GALEV** models calculate the time evolution of spectra and luminosities in absolute terms as a function of the total mass, initially all in gas. Colours, of course, are independent of galaxy mass as **GALEV** models assume the SFH of each galaxy type to be independent of galaxy mass (see Fig. 2.6). Chemical ISM abundances are also determined by this SFH *and* by the absolute level of SFRs in relation to the mass in the initial gas reservoir. Spectral fluxes and luminosities on the other hand are mass-dependent. If models of undisturbed galaxies are to be compared to observations of individual galaxies, it is important to calibrate their absolute luminosities to the observed ones, thereby also calibrating their (gaseous + stellar) masses and their SFRs.

Before we can compare models to distant galaxies, we need to calibrate their apparent magnitudes in the Johnson B-band against average observed magnitudes of the respective spectral galaxy types in the Local Universe. The average observed apparent luminosities of the different

galaxy types in the Virgo cluster are given by Sandage et al. (1985a,b) to be $m_B(E) = 10.20$, $m_B(S0) = 12.60$, $m_B(Sa) = 11.95$, $m_B(Sb) = 12.90$, $m_B(Sc) = 12.83$, and $m_B(Sd) = 13.95$. The correction factors to match the computed and observed luminosities are then also applied to all mass-dependent model parameters, i.e. to stellar and gaseous masses, SFRs, etc.

2.5.3 Disturbed galaxies: Starbursts & SF truncation

In addition to the undisturbed galaxies above with their smooth and monotonically decreasing SFRs, **GALEV** can also describe the evolution of galaxies encountering fast changes in their SFR, e.g. a starburst with significantly enhanced star formation rate, or a truncation or strangulation of the star formation rate on some shorter or longer timescale, respectively. This allows us to study not only the spectral but also the chemical evolution of galaxies that experience starbursts or a quenching of their normal SFR, as they can occur e.g. during galaxy-galaxy interactions or mergers or in the course of the various transformation processes discussed for field galaxies that fall into galaxy clusters. We recall that **GALEV** models only deal with effects on the SFRs of galaxies and should be viewed as complementary to dynamical models describing the morphological transformations eventually related to these processes. Both starbursts and SF truncation/strangulation require additional free parameters. The first of these is the time of onset t_b, i.e. the age at which a previously undisturbed galaxy begins to feel changes in its SFR. Starbursts are described by a prompt increase in SFR followed by an exponential decline on some given timescale τ_b, that typically is of the order of a few hundred Myr for normal-size galaxies and of order $10^5 - 10^6$ yr for dwarf galaxies.

Across the literature, a number of different definitions for the strength of a burst are in use. The strength of a burst is either described by the amount of stars formed during the burst as compared to the stellar mass at the beginning or at the end of the burst or by the amount of all gas available at t_b that is transformed into stars during the burst, equivalent to the star formation efficiency (SFE) of the burst. We prefer the latter definition and define the burst strength via the star formation efficiency of the burst:

$$\text{SFE(burst)} = \frac{\text{stellar mass formed during burst}}{\text{gas mass available at onset of burst}} \tag{2.7}$$

This definition limits burst strengths to be within the range $0 \ldots 1$ and gives, at the same time, a measure of the global SF efficiency during the burst. Please note that since the burst strength depends on the amount of gas available at the onset of the burst, bursts of the same strength but occuring at different times and/or in galaxies of different types do not necessarily form the same amount of *stars*. E.g. a strong burst in an old and gas-poor Sa galaxy will form a much smaller mass of new stars than a weak burst early in the life of a gas-rich Sd galaxy. All burst strengths can only be determined at the end of the bursts. Before the end of the burst only lower limits can be estimated.

A truncation or strangulation of the SFR, e.g. as a galaxy falls into a galaxy cluster and has its H I stripped by ram pressure, is described either by an abrupt termination of SF or an exponential decline of the SFR on a timescale τ_b. After a burst or after SF truncation/strangulation, **GALEV** models can have SFRs going either exponentially to zero or to some constant low level.

2.6 The web interface

We present the new web interface that enables everyone to run her or his model of choice in a fast, easy to learn and easy to use, and comfortable way over the internet. The interface can be found at

http://www.galev.org

Using a web interface enables us to impose some checks previous to program execution dealing with the most serious and frequently occuring problems. For the user this has the important advantage of always having the latest version at hand, including the most up-to-date input physics like isochrone sets and stellar libraries.

2.6.1 How to use the web-interface

The web-interface consists of four steps: Two for the input of the model parameters and the requested output, one for parameter checking and at last the actual running of the program on the web-server.

Principal model parameters

On the first page the user has to decide which type of model (s)he wants to run. Those defining parameters are

1. **Galaxy type**: choose between the most common types E, S0, and Sa to Sd for undisturbed galaxies, for which the parameters described in Sect. 2.5.2 will be used. In addition we offer *free* types, defining the shape of the SFH as described by eqs. 2.4–2.6. We also offer instantaneous burst (SSP) models, as well as completely definable SFHs. For the latter mode the user has to specify a file with SFRs as function of time in the next step.

2. **Burst**: we currently offer three possibilities: *No burst*, i.e. an undisturbed galaxy, a *Burst* with given strength, duration, and exponentially declining SFR, beginning at some time t_b and *SF Truncation* with the SFR declining exponentially to zero on some specified timescale, again from time t_b on.

3. Number of filters for which magnitudes are to be computed.

If the user chooses to run a standard model for an undisturbed galaxy, i.e. an elliptical or spiral galaxy, then **GALEV** in the following uses the parameters described in Sect. 2.5.2. For all other cases, i.e. either user-defined galaxy types or models with burst/truncation, the parameters will be entered in the following step.

Model configuration

Depending on the choices from the previous page the user might not have all possible parameters to choose from; only the ones required for the specified model type will be shown. Those are:

1. We offer a set of **Initial Mass Functions (IMF)**, namely from Salpeter (1955) and Kroupa (2001), both using the Lejeune (Lejeune et al., 1997, 1998) stellar atmosphere library. Further IMF shapes (e.g. Chabrier, 2003) and different sets of stellar libraries are in preparation. In a future release we plan to also allow the user to choose customized IMFs; this feature, however, will be limited to SSP models (i.e. for star clusters).

2. **Gaseous emission** can be switched off or on, and the user can choose to include only continuum emission or both continuum and line emission. In fixed metallicity models, the gaseous emission is evaluated for the respective metallicity, in the chemically consistent case, it is calculated appropriately as described in Sect. 2.3.3.

3. The **metallicity**: choose between *chemically consistent* models, i.e. those including all enrichment effects described above, or a model with metallicity fixed to one of the following values $[Fe/H] = -1.7, -0.7, -0.4, 0.0, +0.4$.

4. The **galaxy type** is shown as a reminder, but cannot be changed here any more. To change the type the user has to go back to the first step.

5. **Galaxy mass** is another free parameter, mainly used for normalization. We do not include a mass-metallicity relation of any kind, so this parameter has no impact on the resulting colours. Note that when **GALEV** is combined with a cosmological model to e.g. obtain apparent magnitudes, the model galaxy mass can optionally gets rescaled to match, after a Hubble time, the average B-band luminosity of local galaxies of the respective type in Virgo.

6. **SFH parameters**: if (and only if) one of the free models has been chosen, then the variables α (normalization for the SFR of an elliptical model), τ (e-folding timescale of an elliptical model), β (factor of proportion for spiral models), and ψ_0 (constant SFR of an Sd model) can be freely chosen by the user. The meaning of those parameters is explained in more detail in Sect. 2.5.2. If in the previous step the user requested the SFH to be read from a file this will be specified here. We caution the reader to carefully study the web-output from **GALEV** , since depending on the chosen parameters there might be problems, e.g. a SFR exceeding the amount of gas that is available.

7. If the user wants to compute a galaxy featuring a **burst** or SF **truncation**, then (and only then) he/she has to specify the time of the onset of the burst, expressed in years after galaxy formation and the e-folding timescale for the decline of the SFR during the burst. While those two parameters are common to both truncation and burst, only in the latter case one also needs to supply a burst strength. Following our definition of the burst-strength in Sect. 2.5.3 (eq. 2.7), this specifies the fraction of gas available before the burst that is to be converted into stars during the burst. If one instead wants to specify the SFR at the very onset of the burst, $SFR(t = t_b)$, those two numbers can be converted into each other by $b = SFR(t = t_b) \times \tau_b / M_{\text{gas}}(t = t_b)$.

8. **GALEV** currently supports two different **extinction** laws that can be applied to the spectra, the Calzetti et al. (1994) law for starburst galaxies, and the Cardelli et al. (1989) Milky Way extinction law, using the standard value of $R_V = 3.1$. To compute colours for different extinction values, the user can specify a maximum E(B-V) value and a step-size. The output (see below) will then include multiple files, one for each extinction value in the requested range.

9. **Cosmological parameters** need to be specified to model the evolution of galaxies with redshift. The user can choose Hubble constant H_0, Ω_M, and Ω_Λ, while Ω_K is fixed to 0. To convert ages into redshifts the user also has to select a formation redshift z_{form}, so that the age of the galaxy is given by $age(z) = t_H(z) - t_H(z_{\text{form}})$ with t_H being the Hubble time at redshifts z and z_{form}. Note that the modeling process is terminated at a galaxy age of 16 Gyr. A choice of cosmological parameters leading to a galaxy age of more than 14 Gyr (e.g. too low a Hubble constant) hence results in an error-message, so that no colours will be computed for this case.

10. Although **GALEV** offers a full range of different output options (see below), not all the numbers will be actually needed for any specific application. The user can therefore use the section **Output parameter** to restrict the output, leading to faster execution and smaller downloads.

11. To compute magnitudes from the spectra the user can choose from a large list of **filter functions** and also specify the magnitude system on which magnitudes are to be based (Vega, AB or ST magnitudes) For each filter a different magnitude system can be chosen. This eliminates the uncertainties involved in any *a posteriori* transformations between different systems.

We also offer an extensive online help giving examples for different parameters and how they affect the resulting SFH.

Output

In the following we will describe which outputs are available and also how they are computed.

1. The **integrated spectra for each timestep** are the most important output, since from those all magnitudes and redshifted spectra are derived.

2. Convolving the spectra with the appropriate filter functions and applying the appropriate zeropoints gives us the **magnitudes** of the model as a function of time.

3. **GALEV** also delivers the most useful diagnostic data for each timestep, such as current **stellar and gaseous mass**, **star formation rates**, **ISM metallicity**, and ionizing flux N_{LyC}.

4. After applying a cosmological model to convert galaxy age into redshift (assuming a formation redshift) we can compute the redshifted galaxy spectrum, that includes all evolutionary effects. We also apply the intergalactic attenuation from Madau (1995) to account for absorption of flux shortwards of Lyα by intervening neutral hydrogen clouds.

5. Convolving those redshifted spectra with filter functions FF($\check{}$) and adding the bolometric distance modulus gives us apparent magnitudes with and/or without attenuation, that then can be used e.g. for comparison with observed SEDs to derive photometric redshifts or ages and metallicities.

6. From the data described above we can derive cosmological corrections due to the shifting of the filter functions to shorter restframe wavelengths (k-corrections) and evolutionary corrections (e-corrections). Those corrections are computed as follows:

$$k(z) = -2.5 \times \log \frac{\int_0^\infty f(t = t_0, z, \lambda) \times \text{FF}(\lambda) d\lambda}{\int_0^\infty f(t = t_0, 0, \lambda) \times \text{FF}(\lambda) d\lambda} \tag{2.8}$$

$$e(z) = -2.5 \times \log \frac{\int_0^\infty f(t = t(z), z, \lambda) \times \text{FF}(\lambda) d\lambda}{\int_0^\infty f(t = t_0, z, \lambda) \times \text{FF}(\lambda) d\lambda} \tag{2.9}$$

where $f(t, z, \lambda)$ is the flux at wavelength λ of a galaxy of age t at redshift z, t_0 the current age of the universe (which depends on the specified cosmological parameters), and FF(λ) a filter function.

Parameter checking and execution

As a third step in the modeling process we perform a quick check to ensure that all required parameters are given and correspond to valid combinations. The page also displays all given parameters to allow the user to check the input, and eventually perform corrections by going back to the previous page. However, the tests performed are just basic validity tests and do not ensure that the computed model makes physical sense.

In the fourth and last step, after the user has made sure that all input is correct, we create all files necessary for the actual modelling. The execution of the **GALEV** program takes several minutes to run. We urge all users to carefully read through the given output to check if everything ran smoothly.

Directly after **GALEV** has created all spectra, it computes the magnitude evolution as a function of time or redshift in all filters requested, again taking a few minutes to complete.

For compatibility reasons all output is given as human-readable ascii-files, with values aligned in columns that are separated by spaces, so that the files can be easily analysed and/or plotted. The resulting files are then automatically combined and compressed into one archive (.tar.gz) file, that can be downloaded. Each archive also contains a small ReadMe file listing the content of each file. The meaning of individual columns are specified at the beginning of each file.

2.6.2 Upcoming features of the web-interface

In its current version the web-interface supports the most frequently used **GALEV** features like computing spectra and colours. Further features, like the computation of Lick indices or colour magnitude diagrams are currently in the process of being adapted and implemented into the webpage and will be accessible online in the near future.

2.7 Future prospects

In the near future (Weilbacher et al. 2009, in prep.) we will offer further stellar libraries, e.g. Munari et al. (2005) and Coelho et al. (2005), to be able to compute high-resolution spectra for comparison with modern spectroscopic surveys. Those libraries have higher spectral resolution and shorter wavelength coverage but are not colour-corrected in the way Lejeune et al. (1997, 1998) did for the Kurucz spectra to reproduce the observed colours of stars from the UV through the NIR over the full range of effective temperatures.

One drawback of current galaxy evolutionary synthesis models is that they do not include a self-consistent treatment of dust absorption and reemission. One factor contributing to this difficulty are geometric effects and dependencies of dust masses and properties on gas content, chemical abundances and eventually even radiation field. Early attempts to consistently include dust absorption as a function of gas content and [Fe/H] in collaboration with D. Calzetti were encouraging (cf. Möller et al., 2001) and showed that every undisturbed galaxy goes through a phase of maximum extinction of $E(B-V) \sim 0.4$. The redshift of this maximum $E(B-V)$ phase is determined by the interplay between decreasing gas content and increasing metallicity. The predicted values at high-redshift $z \approx 3$ (equivalent to a galaxy age of ≈ 2 Gyr) agree well with observations from Steidel et al. (1999), Shapley et al. (2001) and Colbert et al. (2006).

Another aspect is the coupling of **GALEV** to a dynamical model (SPH + N-body + SF + feedback) to cope with increasingly available data from Integral Field Units allowing spatially resolved spectroscopy. Our early attempt to couple **GALEV** models for single stellar generations with a cosmological structure formation simulation by M. Steinmetz was encouraging (cf. Contardo et al., 1998) and showed that this approach is feasible. The simulated HST images of a galaxy at different redshifts showed fairly good agreement with observations but ultimately failed to reproduce the correct local disk sizes and parameters. A better and more detailed description of feedback seems to be required. This can only be obtained from an extensive comparison between model results and resolved galaxy observations. The key issue is to have a correct criterion for SF and a correct description of feedback on the relevant scales and over the full range of SF activity – from the lowest levels in the farthest outskirts of galaxies to the highly clumped and clustered SF in the strongest starbursts.

2.8 Applications

GALEV models have a wide range of applications from star clusters and resolved stellar populations of nearby galaxies through integrated properties of galaxies up to the highest redshifts. A fair number of them have been explored so far, many of them hand in hand with refinements or special features added to the models. Here we briefly recall a few of them to illustrate the various features of **GALEV** .

2.8.1 Star clusters

The simplest stellar systems to study with **GALEV** are star clusters, so-called simple stellar populations (SSPs) where all stars are formed essentially within one timestep and with the

same chemical abundances. **GALEV** models describe the time evolution of SSPs with different metallicities, including the gaseous emission during early evolutionary stages and as appropriate for their respective metallicity. They can also incorporate extinction within the clusters' parent galaxy on the basis of empirical extinction laws from Calzetti et al. (1994) or Cardelli et al. (1989).

Using our AnalySED tool (Anders et al., 2004b,a), we can compare observations in widely spaced broad-/medium-band filters to a grid of **GALEV** models and derive physical cluster parameters such as ages, masses, metallicity, and extinction between the cluster and the observer If one of the parameters can be externally constrained (e.g. dust-free environment, or metallicity previously determined from spectroscopy) observations in at least 3 bands are required, otherwise at least 4 bands are needed. As a large number of star clusters can usually be covered by a single set of observations, this is a very efficient way to study statistically significant cluster samples.

As shown both in studies based on artificial star clusters and on star clusters with ages and metallicities derived independently from CMDs, accuracies in age determination of $\Delta age/age \leq 0.3$ and in metallicity determinations of $\Delta[Fe/H]/[Fe/H] \leq 0.2$ are achievable, preferably if both a short-wavelength band (U or B) and a NIR-band are included (Anders et al., 2004a; de Grijs et al., 2003a; de Grijs & Anders, 2006). The U-band is crucial for accurate age-dating, and a NIR-band (H or K) for accurate abundances. We successfully applied these models in Anders et al. (2004b) to the interpretation of the young star cluster systems in the starburst dwarf galaxy NGC 1569, in Anders et al. (2007) to the analysis of the star clusters in the interacting Antennae galaxies (NGC 4038/39), and in Kotulla et al. (2008a) to the derivation of ages and metallicities of the globular clusters in the Virgo S0 galaxy NGC 4570.

2.8.2 Colour-magnitude diagrams

One special feature of **GALEV** is its ability to compute colour-magnitude diagrams (CMDs) in any desired passband combination. This is possible not only for SSPs or instantaneous bursts, but also for composite stellar populations with complex SFHs. This has successfully been used to identify the best possible passband combination to disentangle age and metallicity effects in star clusters in various age ranges (cf. Fritze et al., 2006).

In Fritze & Lilly (2007) we compared the SFH obtained from the CMD with those obtained from the integrated spectrum, from Lick index measurements and from multi-band photometry in their respective accuracies and limitations. The basic result was that none of the methods allows to look back beyond a recent burst or some recent phase of enhanced SFR, and that all methods face very similar accuracy limitations at look-back times beyond ~ 1 Gyr. Only within the most recent Gyr, CMD analysis achieves the most detailed SFHs (cf. Lilly & Fritze, 2005b,a). The importance of this kind of comparative investigation lies in the fact that CMD analyses can only be done for the resolved stellar populations within the nearest Local Group galaxies. All attempts to explore the SFHs of more distant galaxies have to rely on integrated spectra and, for the most distant ones, on integrated photometry only.

2.8.3 Undisturbed galaxies

In Bicker & Fritze (2005) we used **GALEV** models to study the effects of the chemical evolutionary state of galaxies on their star formation rate indicators (Hα, [OII], NUV and FUV luminosities) and found that *all of them* significantly depend on metallicity, with errors in the worst cases of up to factors of a few, confirming previous observational evidence (e.g., Jansen et al., 2001; Hopkins et al., 2003; Kewley et al., 2004).

In Schulz et al. (2003) study the time and redshift evolution of bulge-to-disk light ratios in different wavelength bands by assuming a short timescale for SF for the bulge component $\Psi_{bulge} \sim exp(-t/1\,Gyr)$ and a constant SFR for the disk component $\Psi_{disk} \sim$ constant. The

integrated spectral and photometric evolution of different spiral galaxy types was then obtained by adding up the bulge and disk components in mass ratios so as to give, after a Hubble time of evolution, the observed average B-band bulge-to-disk light ratios for the respective spiral types Sa through Sd. This study showed a significant wavelength dependence of the bulge-to-disk light ratios in agreement with observations by Eskridge et al. (2002). This has implications for galaxy classification in different redshift intervals. It also opens a new possibility to explore bulge formation scenarios and bulge formation redshifts by comparing bulge-to-disk light ratios measured in different bands.

Starbursts in Blue Compact Dwarf Galaxies

Starbursts were first investigated with **GALEV** models in the context of Blue Compact Dwarf Galaxies (BCDGs) in a series of papers by H. Krüger (Krüger et al., 1991, 1992, 1993; Krüger & Fritze, 1994; Krüger et al., 1995). These authors investigated a sample of BCDGs with optical and NIR photometry in order to derive their burst strengths and the age of their underlying stellar population. The main results we want to recall here are that even very weak ongoing bursts can completely dominate the light in the optical, in particular at the low metallicities $Z_\odot/50 \ldots Z_\odot/5$ typical for BCDGs. An underlying old galaxy component can only be detected in the NIR and was found for every BCDG of our sample. Very accurate age-dating was possible for those BCDGs which showed a 4600 bump caused by WR-stars in their spectra. Burst strengths were found to be of the order of a few percent only, when defined in terms of stellar mass increase. They were also shown to systematically decrease with increasing galaxy mass, where the latter included the important mass contributions of H I. This result is in agreement with expectations on the basis of the stochastic self-propagating SF scenario put forward by Gerola & Seiden (1978) and Seiden & Gerola (1979).

2.8.4 Interacting galaxies and mergers

In Fritze & Gerhard (1994a,b) we studied a grid of starburst models with bursts of various strengths occurring in Sa, ..., Sd spirals at different ages in their spectral, photometric and chemical evolution and then analyzed the starburst in the gas-rich massive spiral-spiral merger NGC 7252. We found this burst to have started about $600 - 900$ Myr ago and to have been stronger by $1 - 2$ orders of magnitude than those in BCDGs. The bulk of information available for this galaxy even allowed us to estimate the SF efficiency on the basis of a comparison of the stellar mass formed during the burst.

Our conservative estimate for the overall SF efficiency (see equation 2.7) during this interaction-induced starburst indicated a very high value SFE ≥ 0.35 (Fritze & Gerhard, 1994a,b; Fritze & Burkert, 1995), again about two orders of magnitude higher than any SFE measured for molecular clouds in the Milky Way or the Magellanic Clouds, and high enough to allow for the formation of a new generation of globular clusters (cf. Brown et al., 1995; Li et al., 2004). **GALEV** models indicated that NGC 7252 at present still features a low-level ongoing SFR of $\sim 3\,M_\odot\,yr^{-1}$ in its centre, powered for $\sim 50\,\%$ by gas set free at present from dying burst stars and for $\sim 50\,\%$ by H I falling back onto the main body from the tidal tails. Both of these gas delivery rates will decrease over the next $1 - 3$ Gyr. Depending on whether the SFR will cease completely or continue at some very low level, NGC 7252 will spectrally evolve into an elliptical or S0 galaxy over the next $1 - 3$ Gyr. Already at present, NGC 7252 features an $r^{1/4}-$ light profile across a radial range of ~ 14 kpc, if azimuthally averaged (Schweizer, 1982a).

Independent confirmation for the unexpectedly high value found for the SFE in NGC 7252 came from the detection of a rich population of massive compact star clusters with ages in agreement with the global starburst age which, in turn, is in agreement with dynamical merger ages from N-body + SPH simulations (e.g. Hibbard & Mihos, 1995). Spectroscopy of the brightest clusters confirmed their metallicities to be between $Z_\odot/2$ and $Z_\odot$, as expected if they formed out of

the gas pre-enriched in Sc-type spirals – with some evidence for a moderate amount of self-enrichment during the burst on the basis of their slightly enhanced [ff/Fe] ratios. In Fritze & Burkert (1995) we estimated that the number of clusters with masses in the range of Galactic globular cluster (GC) masses that formed in the burst and survived until the present is of the same order of magnitude as the number of GCs present in two average-luminosity Sc-type spirals before the merger. Hence, this spiral-spiral merger will, after the fading of the post-starburst and after the fading and dissolution of the tidal features, evolve into an elliptical or S0 galaxy with a normal GC specific frequency. GCs of age $0.5 \ldots 1$ Gyr have already survived the most critical phase in their lives, the infant mortality and early mass loss stages, and stand fair chances to survive for many more Gyr (cf. Lamers et al., 2005; Bastian & Goodwin, 2006; Parmentier & Fritze, 2009).

In de Grijs et al. (2003b) we used **GALEV** SSP models to analyze the luminosity-weighted ages pixel-by-pixel on ACS images of the interacting galaxies Tadpole and Mice and studied their star cluster populations. A surprising result was that about 35 % by mass of all recent SF went into the formation of star clusters in both galaxies, not only across the main bodies of both galaxy systems but all along their very extended tidal tails.

In Temporin & Fritze (2006) we applied **GALEV** models to investigate the SF and starburst histories of galaxies in a very compact group of galaxies on the basis of multi-band photometry and spectra and in Wehner et al. (2006) we studied the SF activity and its history in the extended tidal debris surrounding the starburst galaxy NGC 3310.

Tidal Dwarf Galaxies

Not only star clusters can form in the low-density environments of tidal tails but sometimes even star-forming objects with masses in the range of dwarf galaxies: so-called Tidal Dwarf Galaxies (TDGs), or better TDG candidates. In Weilbacher & Fritze (2001) and Weilbacher et al. (2002, 2003b,a) we analyzed the first reasonably sized sample of TDGs and found that they all contain a stellar population inherited from the spiral disk out of which the tidal tail has been torn, together with a significant young stellar population that must have been formed *in situ* within the tidal tail after it had been ejected. A characteristic feature of TDGs is that they do not follow the luminosity-metallicity relation of dwarf galaxies but all have similar metallicities characteristic of the H ɪɪ region abundances in spiral disks.

Again it turned out that optical observations alone are not sufficient to disentangle the mass contributions of the inherited versus the starburst components. Even a 90 % mass fraction in the inherited component can be entirely hidden in the optical by an ongoing burst that only makes up for 10 % of the mass. Only in optical-NIR colours can the inherited component be detected that is not entirely old but contains the mix of stellar ages present in the disk before the tidal tail was thrown out.

2.8.5 Galaxy transformation in groups and clusters

A variety of scenarios are discussed in the literature to explain the transformation of the spiral-rich field galaxy population into the S0-/dSph-/dE-rich galaxy population observed in rich galaxy clusters at low redshift. The following processses have been proposed: High-speed disruptive galaxy-galaxy interactions called harassment, interactions between galaxies and the dense hot Intracluster Medium (ICM), and enhanced merging within infalling groups. All of these scenarios are observed to be at work in a number of individual cases. Their relative importance, their timescales, transition stages, and end products, however, are not known yet. All of these transformation processes both affect the morphological appearance of galaxies and – via their SF histories – their spectral properties. How the timescales for morphological transformation and spectral transformation relate to each other in the various scenarios and environments

is not clear to date. Removal of gaseous halos, outer, and inner H I disks leads to SF strangu-lation on long timescales or to SF truncation on shorter ones. Destabilization of disks through encounters or shocks as well as mergers within infalling groups may lead to starbursts. We explored aspects related to the spectral transformation of galaxies through all these scenarios and investigated which scenarios in which type of progenitor galaxy and at which evolutionary stage can lead to the observed luminosity and colour ranges of S0 galaxies by implementing SF strangulation/truncation on different timescales with and without preceding starbursts into **GALEV** models in Bicker et al. (2002). In Falkenberg et al. (2009a,b) we extended the models to also include the evolution of the D4000 and Hδ Lick indices into the **GALEV** models for galaxy transformation and investigated under which conditions the so-called E+A-, or k+a-, and the Hδ-strong galaxies (cf. Poggianti et al., 2004; Dressler et al., 2004) are formed, what is the lifetime of this respective phase, what is the colour and luminosity of the galaxy in this transition stage and what is the end-product.

2.8.6 High redshift galaxies and photometric redshifts

If coupled to a cosmological model, **GALEV** can be used to study the evolution of galaxies from the very onset of SF in the early universe until today. Accounting for the significantly sub-solar metallicities observed at high redshifts – in particular when dealing with intrinsically faint galaxies that dominate in deep field surveys – allows us to determine more accurate photometric redshifts, as compared to those obtained with solar-metallicity models only (Kotulla & Fritze, 2009) or observed templates (Kotulla 2009, *in preparation*).

In Fritze & Bicker (2006) we examined starbursts and their respective post-starburst stages across a wide range of redshifts with the surprising result that dust-free models in their long post-burst phases after strong starbursts at high redshifts can get the colours and luminosities of Extremely Red Objects (EROs) as e.g. observed in the K20-survey (cf. Daddi et al., 2002; Cimatti et al., 2002a,b).

Only when we also include – in addition to our set of undisturbed models E, Sa, ..., Sd – the very blue starburst phases and also their *extremely red postburst phases* can we reproduce the full range of colours observed e.g. in the Hubble Deep Fields (Kotulla & Fritze 2009, in preparation). In Fig. 2.9 we show the F606W-Ks (approx. V-K) colour evolution for a set of undisturbed models E, and Sa through Sd, and for models with major starbursts (burst strengths chosen to consume 70% of the in each case available gas) occurring at different ages in a previously undisturbed Sb galaxy. A comparison to the photometric galaxy catalog of Fernández-Soto et al. (1999) for the HDF shows that **GALEV** models can describe the full colour range, even without any dust. Note that dust certainly plays a role in ongoing starbursts but not any more during postburst stages. Apparently, as observed in the local Universe, galaxies use up and destroy part of their dust in starbursts, while the rest is blown away by the end of the burst.

2.8.7 Redshift evolution of ISM abundances: spiral models vs. DLAs

The SFHs of our closed-box model galaxies were constrained by requiring agreement after $12-13$ Gyr of evolution not only with observed spectrophotometric properties of the various galaxy types but also with their gas content and ISM abundances (cf. Sect. 2.5.2). While this en-sures agreement at the present stage it needs not necessarily imply agreement over the entire evolutionary path. Some subtle interplay between SFR and infall rate, e.g., could lead to the present-day agreement after ages of disagreement. Infall rates are very hard to constrain from a comparison with spectrophotometric properties alone. They can, however, be constrained by comparing chemical abundances. It is therefore of prime interest to compare the redshift evolu-tion of ISM abundances to observations of high-redshift galaxies.
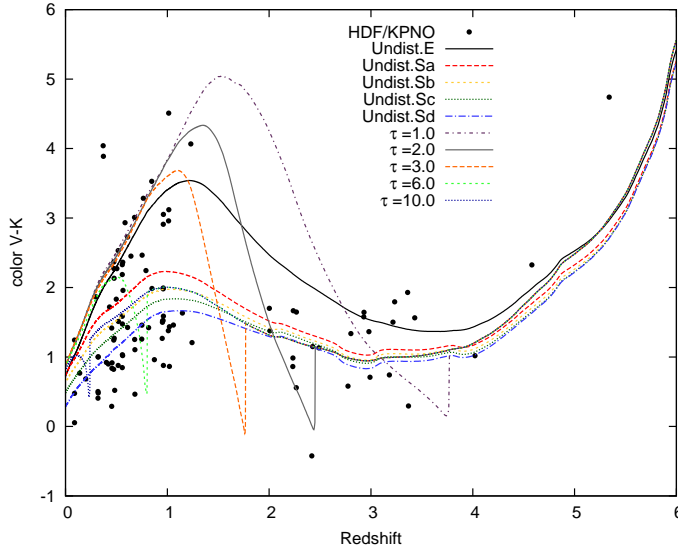
Figure 2.9: V-K colour as function of redshift for five undisturbed spectral types E and Sa through Sd. Extremely blue colours are found during active starbursts, while extremely red colours can be reached during the postburst phases of early starbursts, here shown for galaxy ages of 1, 2, 3, 5, and 10 Gyr.

Transforming the time evolution of ISM abundances into a redshift evolution only requires the one-to-one transformation between galaxy age and redshift that is given by any set of cosmological parameters (see. Sect. 2.3.9)

Damped Lyman-α absorbers (DLAs) are a particular class of absorption systems, usually observed in the line-of-sight of quasars, with damping wings on the Lyman-α line due to the high column densities of neutral hydrogen of $N(HI) \geq 10^{21}\,cm^{-3}$ in the absorbers. The damped Lyman-α line is always accompanied by a number of low-ionisation heavy element lines, many of which are the dominant ionisation states in those absorbers. DLAs are most easily observed in the redshift range $z \sim 2$ to $z > 4$ and have been proposed to be potential progenitors of present-day spiral disks: Their $H\,I$ column densities are similar to those in local gas-rich disks and their gas content, derived from rotational velocities of the order $100\ldots200\,km\,s^{-1}$, is similar to gaseous plus stellar masses in local spirals. In Lindner et al. (1999) we compared the redshift evolution of our spiral galaxy models, calculated in a chemically consistent way with stellar yields for a large number of elements and 5 different stellar metallicities to the first reasonably sized set of Keck HIRES abundances for DLAs from the literature. We found surprisingly good agreement for all the different abundances over the entire observed redshift range with our closed-box models.

Studying the impact of various amounts of infall showed that it was not possible to accommodate more than a moderate amount of infall, increasing the total mass from redshift 2 until the present by not more than a factor ~ 2, without losing agreement with either the spectral or the chemical properties or both, no matter how we tuned the SFH. We hence concluded that from a chemical evolution point of view DLAs might well be the progenitors of present-day spiral galaxies of all types Sa ... Sd and that those are reasonably well described by closed-box or moderate-infall models. This implies that DLAs have already almost all the mass of present-day spirals – albeit almost completely in the form of $H\,I$ gas. **GALEV** models indicated low stellar masses and low luminosities for DLA galaxies, in agreement with the large number of non-detections/upper limits. Mass estimates from rotation velocities derived from detailed modeling of asymmetries detected in some DLA profiles confirmed our mass predictions (cf. Wolfe et al., 2005). **GALEV** models also predicted a change in the DLA galaxy population from high to low redshift and showed that the DLA phenomenon can be understood as a normal transition stage in the life of every spiral. During their enrichment process to higher metallicities they convert their gas reservoir into stars, therefore get increasingly gas-poor so that above a certain metallicity they drop out of DLA samples due to too low a gas content (cf. Lindner et al., 1999, for more information). This is in agreement with observations that show the lowest redshift DLA galaxies to be low-luminosity late-type or irregular galaxies.

2.9 Summary

This paper presents the **GALEV** evolutionary synthesis models for star clusters, undisturbed galaxies and galaxies with starbursts or/and star formation truncation now available on the web at

http://www.galev.org

We describe the input physics currently used, that will continuously be updated.

For a number of different stellar IMFs, the spectral evolution of star clusters of metallicities in the range $-1.7 \leq [\mathrm{Fe/H}] \leq +0.4$ can be calculated, and a large number of filter systems are available for the photometric evolution as well as the full set of Lick absorption indices.

GALEV features a unique combination of characteristics that allow for what we call a *chemically consistent modelling* of the chemical evolution of the ISM together with the spectral evolution of the stellar component.

This means that the initial abundances of every stellar generation are accounted for by using input physics (stellar evolutionary tracks, stellar model atmospheres, gaseous line and continuum emission, stellar lifetimes, yields and remnant masses) appropriate for the increasing initial abundances present at the formation time of successive stellar generations. This chemically consistent modeling accounts for the observed broad stellar metallicity distributions in local galaxies as well as for the increasing importance of subsolar abundances in local late-type and low luminosity galaxies and in high redshift galaxies.

Galaxy models can be calculated either in the chemically consistent way or for some fixed metallicity upon request. Models give spectra, emission line strengths and Lick absorption features, photometric quantities for a large number of filter systems, and chemical abundances, gaseous and stellar masses, star formation rates, etc. in their time evolution for normal galaxies, galaxies with starbursts or/and star formation truncation as specified by the user or for user customized star formation histories.

If a cosmological model is selected, all quantities are also provided in their redshift evolution, fully accounting for evolutionary and cosmological corrections and including the attenuation by intergalactic neutral hydrogen.

We present the models, the input physics they use, their calibrations, the web interface and some examples of selected applications for illustration and we discuss current limitations and future prospects.

Acknowledgement

Galaxies to the redshift desert and beyond I. Evolutionary synthesis modelling

Ralf Kotulla

Abstract:

Evolutionary synthesis models are a ideal tool to study the formation and evolution of galaxies with respect to their stellar populations. Here we present an extensive grid of chemically consistent **GALEV** evolutionary synthesis models that include the spectral and chemical evolution of galaxies in a chemically consistent way, i.e. accounting for the increasing initial abundances of successive stellar generations.

Our model grid contains undisturbed E and Sa-Sd type galaxies as well as a wide range of models undergoing starbursts of various strengths and at different times and also includes the subsequent post-starburst phases for these galaxies. For each model we trace star formation rates, stellar and gaseous masses, metallicities and the evolution of spectra and magnitudes for a wide range of filters from the formation in the early universe until today. Our models include both evolutionary and cosmological corrections as well as the attenuation by intergalactic HI.

Our main findings are: **a)** At redshifts $z \gtrsim 3$ all galaxy spectra look alike and very similar to starburst spectra; **b)** evolutionary corrections are crucial for all kinds of studies with extreme values reaching up to -12 mag; **c)** even weak bursts can completely dominate the galaxy spectrum, leading to significantly underestimated galaxy ages and masses if not taken into account properly; **d)** post-starburst phases are extremely important since they last considerably longer than starburst phases; **e)** post-starbursts even with relatively recent bursts result in galaxy spectra very similar to that of local ellipticals and define a narrow, maximally red postburst sequence as function of redshift;

All model data, i.e. spectra, magnitudes, cosmological and evolutionary corrections for a wide range of filters as well as star formation rates, stellar and gaseous masses, and metallicities, are available online at http://www.galev.org. A comparison to multi-wavelength photometric observations of a wide range of high redshift galaxies from the bluest Lyman Break Galaxies to Extremely Red Objects is the subject of a companion paper.

3.1 Introduction

Most of our current knowledge on galaxy formation and evolution originates from observations of the electromagnetic spectrum emitted by galaxies at a range of redshifts and hence look-back times. This holds in particular for studies of the optical and near-infrared light emission that is dominated by stars. Over the years a wide range of tools have been developed to derive star formation histories (SFHs), i.e. the evolution of star formation rates (SFRs) with time or redshift. For local galaxies ($D \lesssim 10\,\text{Mpc}$) that can be resolved into individual stars colour-magnitude diagrams analyses are the most effective way (Smecker-Hane et al., 2002; Aloisi et al., 2007). Determination of ages and metallicities of star clusters (Hempel et al., 2003; Anders et al., 2004b, 2007; Pasquali & Castangia, 2008; Kotulla et al., 2008a; Beasley et al., 2008) extends the range to larger distances ($D < 100\,\text{Mpc}$). For all galaxies further away we purely have to rely on studies of the integrated light. Common approaches in this case are the comparison of the full spectrum or spectral indices to predictions of either Simple Stellar Populations (SSPs) (e.g. Pickles, 1985a,b; Howell, 2005; Tojeiro et al., 2007), models with constant or exponentially declining star formation rates (Shapley et al., 2004, 2005; Erb et al., 2006b; Chen et al., 2009), or combinations of both approaches (Kauffmann et al., 2003; Salim et al., 2005; Erb et al., 2006b; Pozzetti et al., 2007). The main drawback of all those approaches is that they are only viable for the most massive galaxies at each redshift that are bright enough for spectroscopy. Typical intermediate and low-mass galaxies at larger distances or cosmological redshifts, however, that dominate the number counts are beyond the limits of modern spectrographs. Studies of statistical samples hence have to rely on photometric data alone and their intrinsic properties can only be derived by comparison to models of galaxy evolution.

This applies in particular to galaxies in the so-called redshift desert from $z = 1.4$ to $z = 2.5$ (Steidel et al., 2004). Galaxies in this redshift range lack strong emission lines in the optical window that is most easily accessed by optical spectroscopy, requiring either UV-sensitive spectrographs to obtain redshifts from Lyman-α, or NIR spectroscopy to access the rest-frame optical emission lines. However, the cosmic epoch corresponding to this redshift desert is of particular interest since it not only encompasses a doubling in the age of the universe but also marks the peak of cosmic star formation activity and hence mass assembly and chemical enrichment (Madau et al., 1996, 1998; Blain et al., 1999; Hartwick, 2004; Juneau et al., 2005; Reddy et al., 2008), as well as the peak of bright QSO activity (Schmidt et al., 1995; Pei, 1995; Fan et al., 2001; Babbedge et al., 2006; Brown et al., 2006; Richards et al., 2006).

Evolutionary synthesis models such as **GALEV** (Bicker et al., 2004; Kotulla et al., 2009), GALEXEV (Bruzual & Charlot, 2003), and PEGASE (Fioc & Rocca-Volmerange, 1997) among many others are an ideal utility to model galaxy evolution and enable a more detailed insight into the properties of these galaxies. They allow to track the evolution of a wide range of physical parameters such as spectra, luminosities, and, if also gas is considered in the modelling, relative gas fractions and metallicities.

One of the crucial requirements for the photometric study of any galaxy population at cosmologically significant redshifts is the knowledge of cosmological (k-) corrections to compensate for the shift in filter response curves relative to the intrinsic spectrum. This filter-dependent k-correction can be obtained relatively easily from observed (Humason et al., 1956; Oke & Sandage, 1968; Coleman et al., 1980; Frei & Gunn, 1994; Assef et al., 2008) or model spectra (Bruzual, 1983; Poggianti, 1997; Bicker et al., 2004). Evolutionary corrections, i.e. corrections describing the intrinsic evolution due to stellar evolution and a change in the stellar population mix, on the other hand are much harder to derive from observations, although there were some attempts (e.g. Sandage, 1961, 1988), but can easily be computed from evolutionary synthesis models for which the evolution of all their respective predicted quantities is known exactly (Tinsley, 1970; Bruzual, 1983; Poggianti, 1997; Bicker et al., 2004).

Events that dramatically change the intrinsic properties of galaxies and that can easily be studied with evolutionary synthesis models are starbursts, i.e. short phases of enhanced star formation,

with the strongest ones most likely triggered by a merger of two gas-rich galaxies. Observational studies of this topic (Hibbard & van Gorkom, 1996; Murphy et al., 2001; Laine et al., 2003; Rossa et al., 2007) mostly have to rely on a sample of galaxies in different stages of the merging process, rendering the identification of typical vs. peculiar features a difficult task. Evolutionary synthesis, however, enables a much easier approach and also allows to explore the whole parameter space without observational restrictions. This becomes even more relevant for studies targeting galaxies in the early universe, where galaxy densities were much higher and subsequently galaxy mergers appeared more frequently (Carlberg et al., 1994; Le Fèvre et al., 2000).

The detailed knowledge about both quiescent and starbursting modes of galaxy formation and evolution is crucial for studies of galaxy populations in the high-redshift universe. An unbiased comparison to observations furthermore requires that models are able to reproduce the wide range of galaxy evolution scenarios found in observations and as accurately as possible describe true galaxies, i.e. they have to include not only the spectral but also the chemical evolution of galaxies as well as the additional emission from gas ionized by young stars.

For this purpose we here present a large grid of **GALEV** evolutionary synthesis models, including undisturbed galaxies as well as of galaxies encountering bursts at different stages during their evolution over a Hubble time from the onset of star formation shortly after the Big Bang until the present. We present their spectral and chemical evolution and show the impact of evolutionary corrections and sub-solar metallicities. For the models with burst we also demonstrate the impact of varying burst time, duration and strength on the resulting galaxy spectrum. This grid provides an insight into the evolution and transformation of galaxies, aiming at establishing links between the different galaxy populations found both locally and at high redshift.

This paper is organized as follows: After a description of our **GALEV** models (Sect. 4.2) we present the evolution of spectra (Sect. 3.3) and spectral energy distributions (SEDs, Sect. 3.4). Sect. 3.5 describes the evolution of galaxies undergoing a starburst, which is followed by a summary in Sect. 4.8.

In a companion paper (Kotulla, 2009b, hereafter Paper II) we will apply our results from our modelling to empirically derived colour selection criteria and compare observationally derived physical properties (masses, star formation rates and metallicities) of galaxies at a range of redshifts to predictions obtained with our models.

3.2 Chemically Consistent galev models

Our chemically consistent **GALEV** evolutionary synthesis models allow us to model galaxies with arbitrary star formation histories (SFHs). The models not only take formation of stars from gas and the subsequent stellar evolution into account, but also compute the chemical evolution of the galaxy. We use this chemical enrichment history (CEH) to assign to each stellar generation spectra, yields, and lifetimes appropriate for their particular initial metallicity, thus allowing for what we call "chemically consistent" treatment.

As shown in Kotulla & Fritze (2009), appropriately accounting for sub-solar metallicities stellar (sub-)populations becomes increasingly important towards higher redshifts, in particular when analysing deep field multi-band imaging data that give access to intrinsically faint galaxies.

All our models start from a gas cloud of primordial abundances and fixed mass, that determines the total mass of the galaxy at all times; we consider the "closed box" approximation and hence do not include any infall or outflows during the lifetime of the galaxy, and also assume perfect and instantaneous mixing. We use the most recent stellar isochrones from the Padova group, including the thermal-pulsing AGB phase (Bertelli et al., 1994) and convolve them with a Salpeter (1955) initial mass function with stellar masses ranging from $0.1\,\mathrm{M_\odot}$ to $100\,\mathrm{M_\odot}$. To each point in this synthetic colour-magnitude diagram we assign a spectrum from the Lejeune et al. (1997, 1998) library; integration over all masses then yields an integrated isochrone spectrum for each

age. **GALEV** then multiplies the specified SFH with the spectrum for each age and integrates to get the galaxy spectrum for each time-step.

Using a concordance cosmological model with $H_0 = 70\,\mathrm{km\,s^{-1}\,Mpc^{-1}}$, $\Omega_M = 0.30$, $\Omega_\Lambda = 0.70$ (Spergel et al., 2007; Komatsu et al., 2009) we assign a redshift to each galaxy age, assuming that all galaxies started forming stars at redshift $z_{form} = 8$. This formation redshift is in agreement with current evidence for the epoch of reionization between $z = 6$ and $z = 10$ (Becker et al., 2001; Fan et al., 2006). Note that small changes to the formation redshift as suggested by Noeske et al. (2007b) do not significantly affect our results, since the properties of local galaxies do not change much with the small changes in age imposed by formation redshifts varying between $z = 6$ and $z = 10$.

We then redshift each spectrum, apply the intergalactic attenuation according to Madau (1995) and convolve each spectrum with the specified set of filters to yield the observed apparent magnitudes. These then include both the cosmological and evolutionary corrections. We recall that our models refer to *spectral types of galaxies* and caution that the one-to-one correspondence between spectral and morphological galaxy types observed in the local universe might not hold out to arbitrarily high redshifts.

3.2.1 The model set

Our basic set of models consists of the spectral types E and Sa through Sd. The E model is described by an exponentially declining SFR with an e-folding timescale of $1\,\mathrm{Gyr}$; the Sa-, Sb-, and Sc-models have SFRs proportional to their current gas mass with factors of proportionality decreasing towards later types; the Sd-model has a constant SFR. All our models are calibrated to reproduce typical colours from UV to NIR, gas content and abundances of local galaxies of their type. For a detailed comparison we refer the reader to Kotulla et al. (2009).

This set of models, however, fails to reproduce the bluest and reddest colours observed in current deep fields. For this reason we supplement the basic set with a set of galaxies encountering strong bursts at various ages. For those cases the assumption of a "closed box" model is most likely not justified, since starbursts are generally triggered by external factors such as galaxy interactions. We therefore use input physics, mainly stellar evolution data and spectra, for a metallicity fixed to half the solar value (Heavens et al., 2004). All burst models start as an undisturbed Sb-model, and encounter a burst that transforms 75% of the gas remaining at the onset of the burst into stars. The time of the onset of burst is varied from $0.5\,\mathrm{Gyr}$ to $10\,\mathrm{Gyr}$ in steps of $0.5\,\mathrm{Gyr}$. At every redshift, these 20 burst models cover the range from a starting burst, an ongoing burst, a young and an old postburst model, and they successfully reproduce the full range of observed colours.

3.2.2 Comparison to semi-analytic models of hierarchical galaxy formation

Current cosmological simulations (e.g. Springel et al., 2005, 2008) generally find that galaxies evolve hierarchically, meaning that small building blocks form first and subsequently merge to form increasingly massive galaxies. There has been considerable progress with semi-analytical models using a combination of first principles combined with empirical relations in order to model the evolution of galaxies in this hierarchical formation scenario (Kauffmann et al., 1999; Cole et al., 2000b; De Lucia et al., 2004; Bower et al., 2006; Croton et al., 2006; De Lucia & Blaizot, 2007; Lacey et al., 2008; Fontanot et al., 2009)

At first glance our approach to model individual galaxies via the time evolution of their star formation history seems in contradiction to this scenario as it does not include the build-up of galaxy mass by a number of major and/or minor mergers. However, the main goal of this paper is to first present how *average* galaxies evolve *without* major mergers; these are described later in

the context of models with starbursts. In semi-analytical models minor mergers are assumed to mostly replenish the gas reservoir that is available to fuel star formation (Kauffmann et al., 1999; Croton et al., 2006). This effectively slows down the gas consumption and increases the SFR which we assume to be proportional to the gas-mass. If significant amounts of gas get accreted this can transform the galaxy into a galaxy of later spectral type. A galaxy starting as Sa-type model would then, for example, be gradually converted into an Sb- or even Sc-type galaxy and hence also follow the evolution of this later galaxy type.

Major mergers, i.e. mergers of two galaxies with roughly equal masses $m_1 : m_2 \leq 1 : 3$ (Kauffmann et al., 1999), on the other hand, convert all available gas into stars and combine these newly born stars with the previously existing stars into a central bulge component. This scenario is similar to our models including a strong starburst as described in Sect. 3.5 where we assume that galaxies consume most (75%) of the available gas in a exponentially declining burst. We compare different burst decline times as well as different burst times and burst strengths to study how these affect the resulting colour evolution. We also computed some models with non-zero SF after the burst to study the effects of gas-accretion onto a passively evolving galaxy, often referred to as "frosting" (Trager et al., 2000, 2008; Allanson et al., 2009).

We again stress that we aim at describing the *average* representation of a galaxy of a given type and not, as consequence of an intentionally limited set of input parameters, the full range of variations that can be found observationally. This approach also validates our use of analytical SFHs instead of an full evaluation of merging histories that generally differs from galaxy to galaxy. However, if averaged over large numbers of galaxies, these merging histories – even in the case of elliptical galaxies with their generally complex histories – closely resemble our analytical SFHs (De Lucia et al., 2006). Observational reconstructions of SFHs of elliptical galaxies (e.g. , Gavazzi et al., 2002; Heavens et al., 2004) confirm this result.

Another key component that can dramatically change the spectral shape of a galaxy is reddening due to dust. Semi-analytical models generally assume the dust to be closely related to some observed parameter such as the B-band luminosity (Kauffmann et al., 1999). While this parameterized approach is a well-working simplification, it is still unclear how to describe the evolution of dust reddening from first principles. This is mostly due to the large number of contributing factors such as unknown geometry and inclination, the way dust is distributed relative to stars, changes of the dust contribution with metallicity and radiation field, just name a few. We therefore decided to create models without dust attenuation and instead treat the amount of dust as a free parameter that can be constrained observationally with SED fitting techniques. We stress again that the observation of the *full* SED should allow to very precisely analyse the contribution of dust reddening of galaxies versus reddening by passive star formation as show by GALEV models (see Sect. 5.4 and Fig. 10 in Paper II).

In these respects we offer an alternative and complementary approach to the aforementioned hierarchical galaxy formation models in that we do not model each galaxy or dark matter halo individually but offer a more detailed inview on several aspects of galaxy evolution.

3.3 Spectral modeling

3.3.1 Impact of evolution on spectra

In Fig. 3.1, we present spectra for three different galaxy types E (upper panel), Sa (central panel) and Sd (lower panel) representing three very different star formation histories at four different galaxy ages of t = 0.9 Gyr, t = 2.6 Gyr, t = 5.1 Gyr and t = 12.8 Gyr, corresponding to redshifts of $z = 0$, $z = 1$, $z = 2$, and $z = 4$, respectively.

The evolution of the constant SFR Sd-model in the lowest panel is dominated by the accumulation of low-mass, long-lived stars that dominate the light emission at long wavelengths
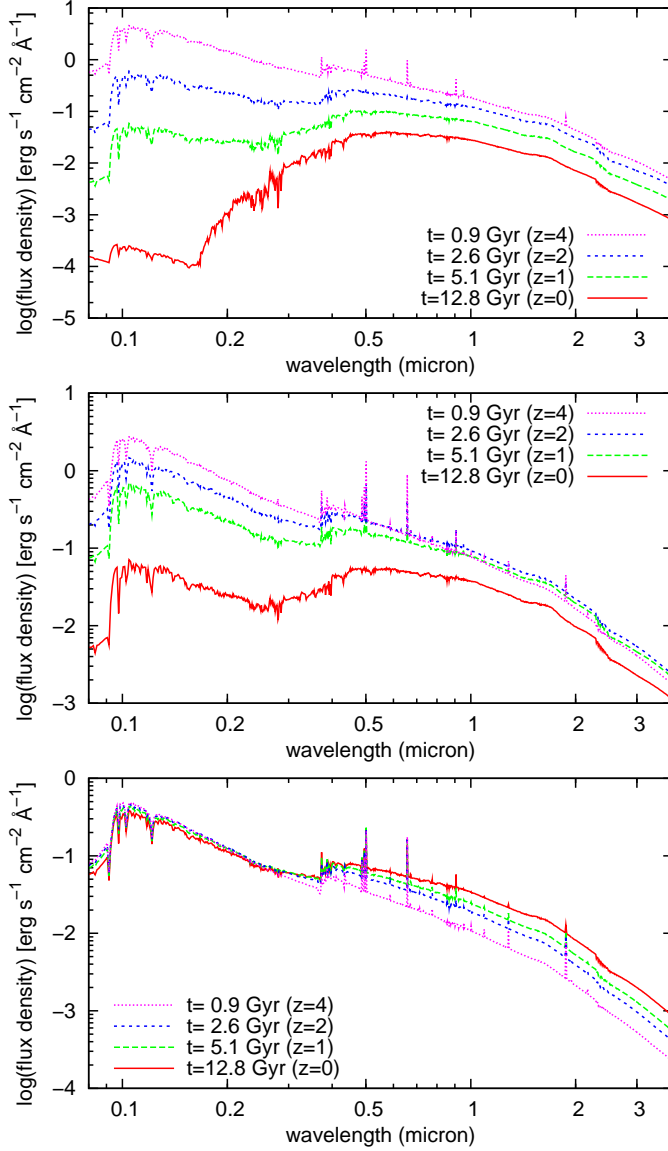
Figure 3.1: Spectra for the spectral types elliptical (top panel), Sa (central panel) and Sd (lower panel) at four different ages of 12.8, 5.1, 2.6 and 0.9 Gyr, corresponding to redshifts z=0, z=1, z=2, and z=4.

$\lambda \geq 4000$. The constant SFR of this galaxy model leads to an almost constant light output at UV wavelengths that is dominated by young, massive, short-lived stars, remains constant. Small differences are attributed to the metallicity increasing over time (see below)

In the case of the Sa- and even more so for the E-model, the increasing SFR towards higher redshifts or younger ages has a dramatic impact on the overall spectral shape. The rest-frame UV of the Sa-model increases by a factor of $\gtrsim 20$ from $z = 0$ to $z = 4$. The optical light emission increases only by a factor of ≈ 3 and is mostly driven by the lower mass-to-light ratios of the younger populations.

For the E-model with its rapidly declining SFR, evolution plays an even greater role. The rest-frame UV emission that is very low at $z = 0$ relative to the flux longwards of 4000 increases by a factor of 10^4, the rest-frame optical by a factor of ≈ 10 from $z = 0$ to $z = 4$.

Comparing all the spectra for E-, Sa and Sd-models at redshift $z = 4$ clarifies another aspect that is shown more clearly in Fig. 3.2. With increasing redshift galaxies look more and more alike, and at very high redshifts they all look like a starburst galaxy observed in the local universe. This, however, is not surprising if one takes a closer look at the star formation rates as function of redshift: At redshift $z = 4$ (corresponding to a galaxy age of 0.9 Gyr), the typical L^* elliptical
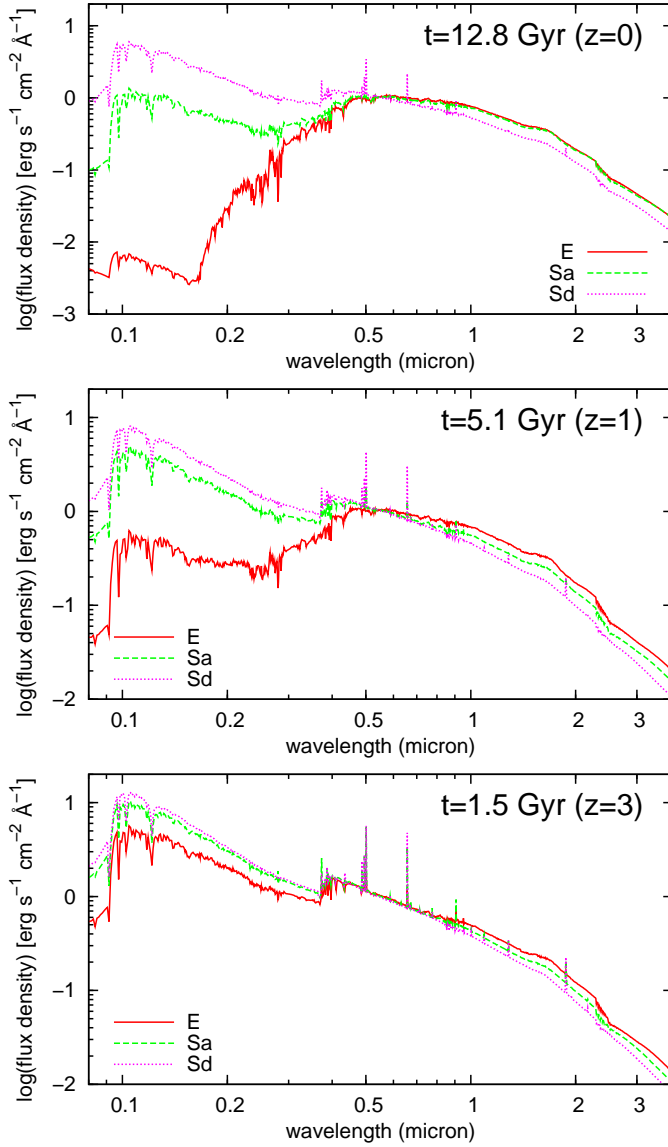
Figure 3.2: Comparison of spectra for three different spectral types E, Sa and Sd for three different ages of 12.8 Gyr (top panel), 5.1 Gyr (middle panel) and 1.5 Gyr (lower panel), corresponding to redshifts z=0, z=1 and z=3. All spectra are normalized to have unit flux at 0.55micron.

galaxy has a SFR of $180 \, M_\odot yr^{-1}$, or a specific star formation rate sSFR = SFR/M_{stars} = $8.2 \times 10^{-10} \, yr^{-1}$. An L^* Sa-model for comparison, has a SFR of $\approx 14 \, M_\odot \, yr^{-1}$ and a sSFR of $1.15 \times 10^{-9} \, yr^{-1}$, only 40 % higher than that of the E-model (also see Figs. 3.7 and 3.8).

This naturally explains the unsuccessful searches for high-redshift "red and dead" ellipticals, i.e. galaxies with predominantly old stellar populations and only little ongoing SF at redshifts z $\gtrsim$ 3 (van Dokkum et al., 2003; Franx et al., 2003; Grazian et al., 2006; Conselice et al., 2007; Quadri et al., 2007b). It also explains the observational evidence for the need of starburst templates for photometric redshifts (e.g. Coe et al., 2006) and the findings of larger fractions of star-forming galaxies towards higher redshifts (e.g. Dye et al., 2008). In a very simplistic estimation we assume that all stars are formed at the same time and that this population has to be $\geq$ 1.5 Gyr old to feature a spectrum similar to that of an passive galaxy. Assuming a formation redshift of $z = 8$ we only can expect to observe this red and dead galaxy population at $z \leq 3$. For more realistic assumptions of SF being spread out over a longer timescale, red and passive galaxies are not expected above even lower redshifts.

Our model SFRs compare well to SFRs deduced for Lyman Break Galaxies (LBGs) at redshift z = 3, as e.g. from Shapley et al. (2001). Their "old" galaxies are described by star formation ages in
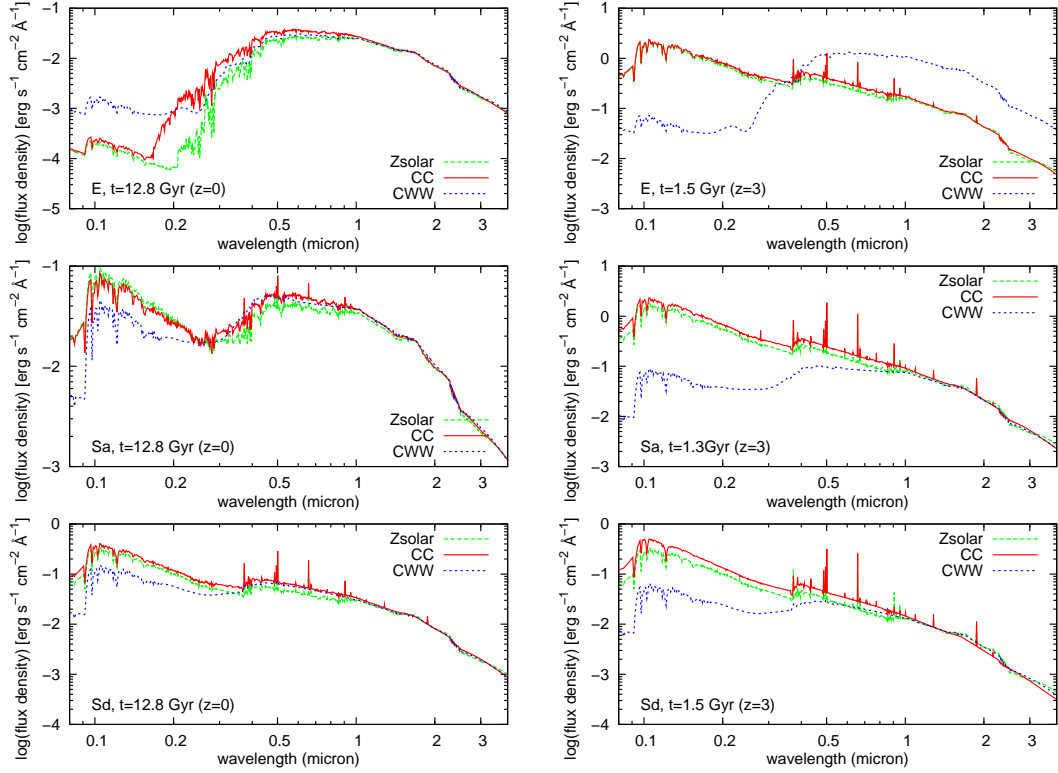
Figure 3.3: Spectra for an E-type (top panels), Sa-type (middle panels) and Sd-type model (lower panel) for two different ages 12.8 Gyr (z=0, left panels) and 1.5 Gyr (z=3, right panels), modeled chemically consistent (red lines) and with fixed to solar metallicity (green lines). Shown for comparison are local templates (blue lines) from Coleman, Wu, & Weedman (1980).

excess of 1 Gyr, stellar masses $> 10^{10}\,M_\odot$ and SFRs $> 30\,M_\odot yr^{-1}$. A typical elliptical (Sa) galaxy at this redshift has an age of 1.5 Gyr, a stellar mass of $3 \times 10^{11}\,M_\odot$ ($2 \times 10^{10}\,M_\odot$) and a SFR of $\approx 100\,M_\odot\,yr^{-1}$ ($11\,M_\odot\,yr^{-1}$). Hence already our undisturbed models can successfully reproduce the SF properties of this LBG population. Their "young" LBG population with stellar population ages $\leq 35\,Myr$, however, can either be explained by a massive starburst happening shortly before that redshift or by a formation redshift closer to redshift $z = 3$. This later possibility has been studied in detail by Noeske et al. (2007b,a) in the context of staged galaxy formation. A detailed comparison with observations is the topic of Paper II.

3.3.2 Evolutionary effects

In Fig. 3.3, we compare spectra with evolution (shown in red) to local observed templates from Coleman, Wu, & Weedman (1980) without evolution. While our models and the observed templates match very well at redshifts $z = 0$ (left column), they are very different at higher redshifts, e.g. at redshift $z = 3$ (right column in Fig. 3.3). By redshift $z = 3$, the elliptical model has changed completely, and now shows a very prominent peak in the UV due to the strong ongoing star formation. Also the peak in the optical has shifted, so that the optical continuum spectrum now very much resembles the spectrum of an A-star without the deep Balmer absorption lines. The spectrum of the Sa-model at redshift $z = 3$ also has a much more prominent rise in the UV shortwards of the 4000 break. Emission lines in the optical are now much stronger than for local galaxies. Least affected by evolution is the Sd-type spectrum. Its UV part has remained almost constant; the optical, however, at higher redshift has a much stronger rise to the blue, since cooler, long-lived low-mass stars with relatively red colours only had little time to accumulate and hence are much less abundant at younger ages than it is the case for local galaxies.

The comparison of the redshifted model spectra that account for evolutionary effects with red-shifted local galaxy template spectra (e.g. those from Coleman, Wu, & Weedman, 1980) very clearly shows the importance of evolutionary corrections that can only be obtained from evolutionary synthesis modeling. They become increasingly important towards higher redshifts (i.e. younger galaxy ages) and, as expected, are more important for early-type galaxies that have seen strong changes in their SFR than for late-type galaxies with their comparably constant SFRs.

3.3.3 Impact of sub-solar metallicities on spectra

A crucial, although frequently neglected, parameter to describe galaxies, and high redshift galaxies in particular, is their metallicity. This can be measured either as ISM abundances from emission lines (e.g. Kewley & Dopita, 2002; Tremonti et al., 2004; Nagao et al., 2006) or as stellar abundances from stellar absorption line features, such as e.g. Lick indices (Worthey et al., 1994; Lilly & Fritze, 2006). Bicker & Fritze (2005) showed that using solar metallicity calibrations to derive the SFR of sub-solar metallicity galaxies overestimates the true SFR by a factor of up to two and underestimates ages by the same factor. Such low-metallicity environments are found not only in local late-type spirals, irregular and dwarf galaxies, but in most if not all normal high-redshift galaxies.

In Fig. 3.3, we also compare models of three different spectral types at two different redshifts, one computed using our chemically consistent approach taking the chemical evolution into account, and one using a metallicity fixed to the solar value. We furthermore show how observed, local galaxy templates would look like at those redshifts. Those represent the case without any evolution, neither in terms of metallicity nor in terms of their stellar population age.

At redshift $z = 0$ our models match the observed templates very well; this is expected since we use local templates to calibrate our models. The mismatch shortwards of $\approx 0.3 \mu m$ can arise from two reasons: The observed models might contain some dust, that absorbs UV-flux at those wavelengths, but is not included in our models; or our model galaxy has a higher SFR and hence higher UV luminosity than the observed template galaxy.

With one exception (our Sa-type model at $z = 0$), the chemically consistent models predict a significantly higher flux at UV- and optical wavelength and comparable fluxes longwards of the rest-frame H-band at $\lambda \approx 1.5 \mu m$. This higher luminosity translates into a lower mass-to-light ratio and hence an overestimation of the mass of the galaxy. In addition to this metallicity effect the application of mass-to-light ratios derived from local, and hence old and relatively metal-rich, galaxy templates to galaxies in the distant universe results in an even larger overestimation, as can be seen from the blue curves in Fig. 3.3.

Metal-poor stars are not only brighter but also hotter than their equal-mass solar-metallicity counterparts. Sub-solar metallicities thus lead to bluer SEDs. Not taking this properly into account results in photometric redshifts being significantly underestimated (Kotulla & Fritze, 2009). Furthermore the strength of emission lines as well as line ratios depend heavily on metallicity with sub-solar metallicities generally resulting in stronger emission lines (Bicker & Fritze, 2005; Kotulla et al., 2009). This has recently been studies by Schaerer & de Barros (2009).

3.4 Spectral Energy Distributions

Although spectra carry more information then magnitudes (e.g. about dynamics), they are very difficult to obtain for distant, faint galaxies. For that reason one is frequently constrained to rely on coarsely sampled spectral energy distributions (SEDs) from broadband photometry. We therefore present in the following the imprint that evolution and chemical evolution make on SEDs, constructed from photometry from UV to NIR, using Bessell U, B, V, R, I and 2MASS-like

J, H, and K filters. The data for a wide range of filters can be obtained from our website at http://www.galev.org.

In addition to intrinsic parameters like galaxy type and mass, there are three cosmological parameters involved in calculating the observed magnitude of a galaxy at a given redshift: **a)** The bolometric distance modulus to account for the increasing distance; **b)** the k-correction that describes the change in brightness due to the moving position of the filter with respect to the galaxy's rest-frame system; and **c)** the evolutionary correction, originating from the look-back time, i.e. describing the fact that we see a distant galaxy in an earlier evolutionary state. While distance modulus and k-correction are straightforward to include, the evolutionary correction, however, can only be properly modelled using evolutionary synthesis models, and *generally depend on the adopted cosmology, the filter function and the galaxy type, i.e. its SF history.*

3.4.1 Evolutionary and cosmological corrections

A comparison of evolutionary (e-) and cosmological (k-) corrections for three different spectra types E, Sa, and Sd and for two different filters g and K is shown in Fig. 3.4. Both correction factors can be derived from the spectra as follows:

$$k_i(z) = -2.5 \log \left(\frac{\int_0^\infty f(t_0, z, \lambda) \times \mathrm{FF}_i(\lambda) \times \mathrm{ATT}(z, \lambda) d\lambda}{\int_0^\infty f(t_0, 0, \lambda) \times \mathrm{FF}_i(\lambda) d\lambda} \right)$$

$$e_i(z) = -2.5 \log \left(\frac{\int_0^\infty f(t_z, z, \lambda) \times \mathrm{FF}_i(\lambda) d\lambda}{\int_0^\infty f(t_0, z, \lambda) \times \mathrm{FF}_i(\lambda) d\lambda} \right)$$

where $f(t, z, \lambda)$ is the flux of a galaxy of age t at redshift z and wavelength λ. FF_i means the relative sensitivity of the observing system, i.e. the combination of atmosphere, relative filter transmission function and detector efficiency. $t_0 = t(z = 0) - t(z_{\mathrm{form}})$ is the age of the galaxy today, $t_z = t(z) - t(z_{\mathrm{form}})$ the age of the galaxy at redshift z and $t(z)$ the age of the universe at redshift z. $\mathrm{ATT}(z, \lambda)$ describes the intergalactic attenuation due to intervening neutral hydrogen.

A complete set of cosmological and evolutionary corrections for a wide range of filters can be downloaded from our group webpage at http://www.galev.org.

For the g-filter the k-correction of the E-type model is rising nearly linear with redshift to reach a plateau of $k_g \approx 8$ mag from $z = 2.5$ upwards. This tremendous k-correction comes from the fact that local galaxies only emit very little flux at UV wavelengths, so that the blueshift of the filter response relative to the rest-frame spectrum results in a decreasing observed flux. Without any further corrections a typical L^* E-type galaxy would have an apparent magnitude of $m_g = 33$ mag at redshift $z = 2.5$ and would hence be undetectable in even today's deepest surveys. The fact that indeed galaxies are observable to very high redshifts is due to the evolutionary corrections. As shown e.g. in Fig. 3.1 and 3.3, ellipticals at high redshifts are not the "old and passive" ellipticals observed locally, but rather violently star-forming, as much and even more than today's starburst galaxies, well comparable e.g. to the Antennae (NGC 4038/39). Over the same redshift range $z = 0 \ldots 2.5$ the evolutionary correction for the E-type model reaches a maximum of -10 mag, making it brighter by a factor of $10\,000$ and as a consequence easily observable in current deep fields. The slightly negative slope of the combined e+k correction counterbalances the rising distance modulus leading to an almost constant magnitude over a wide redshift range. In the K-band the k-correction is much less pronounced, being slightly negative until $z \approx 4$ and rising slowly afterwards; the evolutionary correction again is much stronger, rising almost linearly by -1 mag per unit redshift, so that the combined e+k correction reaches $(e + k)_K \approx -4$ mag at $z = 4$ and beyond. If, as predicted by the hierarchical scenario, galaxies were not yet fully assembled at high redshift, this will directly impact the e-corrections. For a galaxy that only contained a fraction f of its mass at redshift z, the corresponding e-corrections has to be reduced by $2.5 \log(f)$. This, however, is likely to counterbalance the evolutionary corrections in only the most extreme cases.
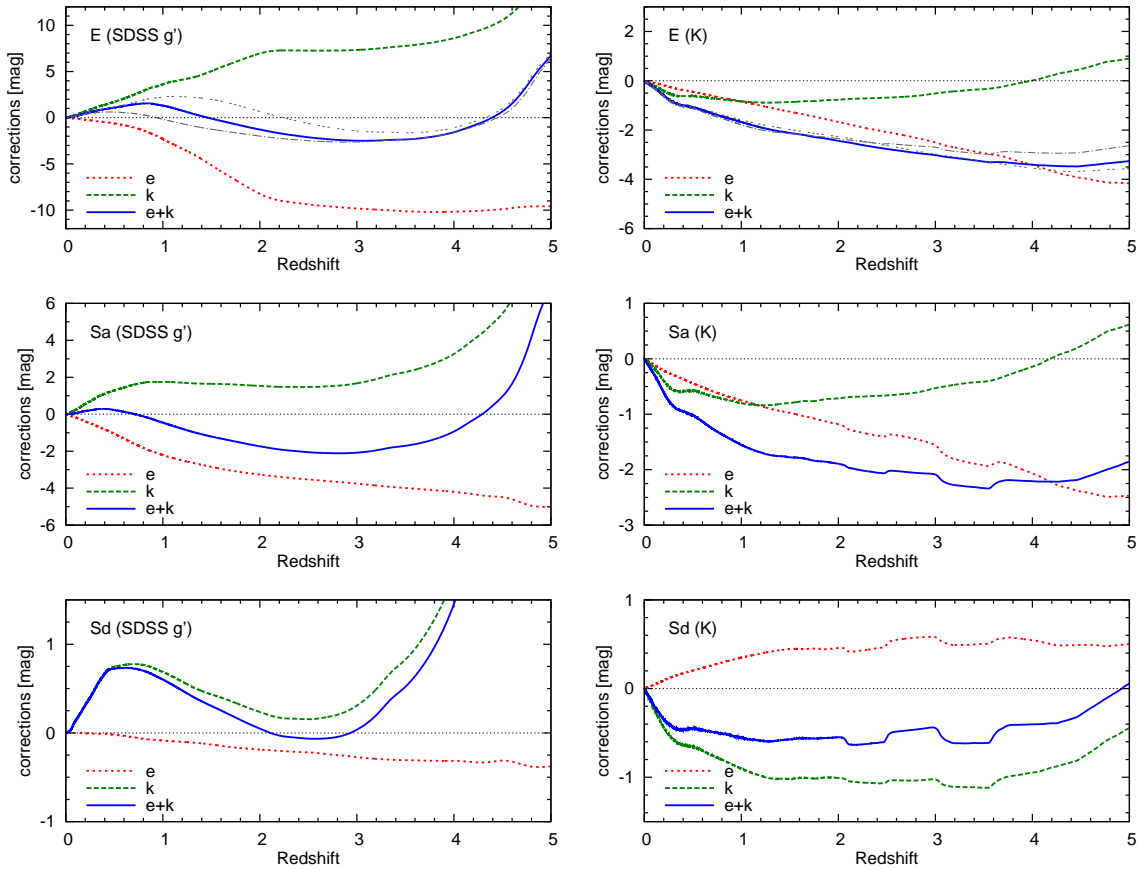
Figure 3.4: Comparison of evolutionary (e-) and k-corrections for three different spectra galaxy types E (top panel), Sa (middle panel), and Sd (lower panel), for two different filters SDSS g' (left) and K (right); e-corrections are shown with red lines, k-corrections in green and the sum, e+k, in blue. k-corrections also include the effects of intergalactic attenuation. Note the widely different scales on each of the plots. Bumps in the curves are due to nebular line emission. In the top panel we also show e+k corrections for two models with exponentially declining SFRs, but with decline times of 0.5 (double dashed) and 2 Gyr (dot-dashed), i.e. half and twice the decline time of our standard E-model.

For the Sa-type galaxy the g-band k-correction quickly rises to $k \approx 2\,\text{mag}$ at $z = 1$ and stays almost constant until the Lyman break reaches into the filter at $z \approx 3.0$. Again this faintening is completely reversed by evolutionary corrections of more than $-4\,\text{mag}$ at this redshift, resulting in a negligible combined correction until $z \approx 0.8$ and a maximum of $-2\,\text{mag}$ shortly before the Lyman-break moves into the filter. In the K-band the behaviour is similar to that of the E-type, with e-corrections rising roughly linearly by $-0.5\,\text{mag}$ per unit redshift. This effect is even enhanced by a negative k-correction of $-0.8\,\text{mag}$ at $z = 1$, so that from $z = 1$ until the highest redshifts the combined e+k correction is roughly $-2\,\text{mag}$.

The Sd-galaxy has a completely different characteristic compared to the types described above. In the g-band the e-correction is slightly negative with a maximum value of only $0.4\,\text{mag}$. The k-correction has a maximum at $z = 1$, coincident with the local minimum shortwards of the 4000-break moving through the filter, followed be a decline back to 0 at redshift $z = 3$ when the Lyman-alpha emission line moves into the filter. In the K-band k-corrections reach a maximum in the range $z = 1 \ldots 3.5$, with much smaller values of only $0.2\,\text{mag}$ at higher redshifts. e-corrections are slightly positive, up to $+0.4\,\text{mag}$, originating in a declining number of low-mass stars, that did not have enough time to accumulate at these high redshifts. Note, however, that independent of those e+k corrections the bolometric distance modulus combined with the low luminosity of those galaxies prevents them from being detected in current deep surveys at redshifts beyond $z = 1 - 2$.

3.4.2 Impact of sub-solar metallicity on SEDs

To study the impact of sub-solar metallicities on integrated magnitudes, we subtract SEDs of our chemically consistent (CC) models from their counterparts with fixed to solar metallicity. The results for the three types E, Sa, and Sd, and a range of redshifts are shown in Fig. 3.5. In this figure negative values mean that the chemically consistent and in generally sub-solar galaxy model is brighter than the model computed using fixed to solar metallicity, but otherwise identical parameters, in particular identical masses and star formation histories.

The outcome of this comparison is that our CC models are on average brighter in all filters by about -0.3 mag or 30 %, compared to their solar metallicity counterparts. One exception is the E-type model at redshifts $z = 1 - 2$. In this range the youngest stars are indeed formed with slightly super-solar metallicities, yielding a lower UV-flux and also weaker emission lines than the solar metallicity model. For more details on the detailed chemical evolution of the different spectral types we refer the reader to Bicker et al. (2004) and Kotulla & Fritze (2009).

As mentioned earlier, lower metallicities result in higher overall luminosities (also see Bicker & Fritze (2005) and Kotulla & Fritze (2009)). If this is not taken into account and solar metallicity calibrations are used instead, this leads to an overestimation of galaxy masses by the same factor, i.e. 30 % for masses derived from NIR magnitudes as e.g. the K-band, but up to factors of 2 if masses for high-redshift galaxies are derived from optical magnitudes alone. This does not yet take into account the younger age of the stellar populations in high-redshift galaxies that have significantly lower mass-to-light ratios than observed in galaxies in the local universe. This younger age and lower mass-to-light ratio adds on to the mass overestimate from the neglect of metallicities.

3.4.3 Gas fractions vs. redshift

In our models we treat galaxies as closed-boxes, i.e. as closed entities that have a fixed total mass that initially is completely gaseous and subsequently gets transformed from gas into stars according to the chosen SFH. The upper panel in Fig. 3.6 shows how the gas-fraction, i.e. the fraction of mass in gas relative to the total mass, evolves with redshift. All galaxies start forming stars at redshift $z = 8$, so at this time the gas-fraction is one. With decreasing redshift the stellar mass increases, leading to a decreasing gas-fraction. The slope of the curve depends on the galaxy type: Early type galaxies such as our E-type model form stars very rapidly and hence reach very low gas-fractions very early at high-redshift. Our spiral models have SFRs proportional to the available gas mass with factors of proportionality decreasing towards later types, i.e. from Sa to Sd (see Kotulla et al., 2009, for details). Late type spirals therefore consume their gas reservoir very slowly, leading to high gas-fractions over most of their lifetime.

This fraction of mass still present in gas has to be taken into account in any comparison between photometric and dynamical masses. Dynamical masses contain all the matter in the galaxy, i.e. stars, gas, and dark matter, while photometric masses only measure the light-producing stellar content. Note that our models are calibrated (via the fraction of visible mass parameter, see Kotulla et al. (2009) for details) to match the mass-to-light ratios of local galaxies and hence include the dark matter contained within the optical radius in their mass budgets. Since dynamical masses are mostly derived from line-widths of emission and/or absorption lines they only trace the dynamical mass within the optical radius and can consequently be directly compared without the need for additional corrections.

In the lower part of Fig. 3.6, we show the mass correction factor as a function of redshift, i.e by which factor photometric and dynamical masses differ simply due to the presence of optically invisible gas. Since this correction factor is very closely related to the gas-fraction, it also depends on the galaxy type and redshift, ranging from values of a few to more than an order of magnitude.
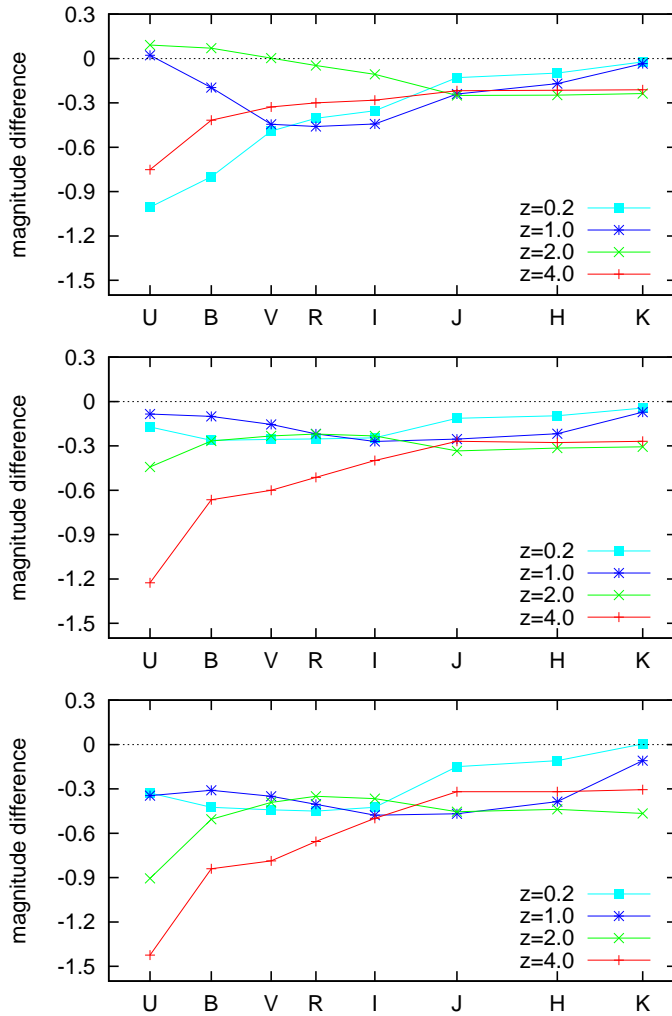
Figure 3.5: Magnitude differences between the chemically consistent (CC) and solar metallicity models for several filters from U through K for different models of an elliptical (top panel), Sa (central panel) and Sd (lower panel) at four different redshift z=0.2, z=1, z=2, and z=4. Positive values mean the CC model is fainter, at negative values the CC model is brighter than the solar metallicity model.

For comparison we also show data from Erb et al. (2006b) and Daddi et al. (2008) who derived dynamical masses from Hα line widths and gas masses from CO lines respectively. Stellar masses in both cases were derived from fitting the observed SED models with galaxy models. The results are in good agreement with our model predictions, with early-type spirals giving the best overall fits.

3.5 Starburst and post-starburst templates

To reach bluer and redder colours than those reached by our undisturbed models we supplement our grid with an extended set of models presented in Fritze et al. (2006). The full model-set now includes 42 starburst models including their respective extremely red post-burst phases. The starburst models start as a galaxy of spectral type Sb and encounter an burst at galaxy ages from 0.1 to 13.0 Gyr in steps of typically 0.5 Gyrs, but increasingly smaller steps for the earlier bursts. A burst is characterized by an gaussian-shaped increase of SFR on a timescale of 125 Myr, followed by an exponential decline with an e-folding time 250 Myr. The burst time corresponds to the time of maximum SFR. We assume the SFR after the burst to asymptotically drop to zero, i.e. the SF is truncated as a consequence of the burst. This is physically motivated either by feedback processes directly related to the SF activity during the burst, i.e. by supernovae expelling the gas in form of galactic winds (e.g. Strickland et al., 2004; Westmoquette et al.,
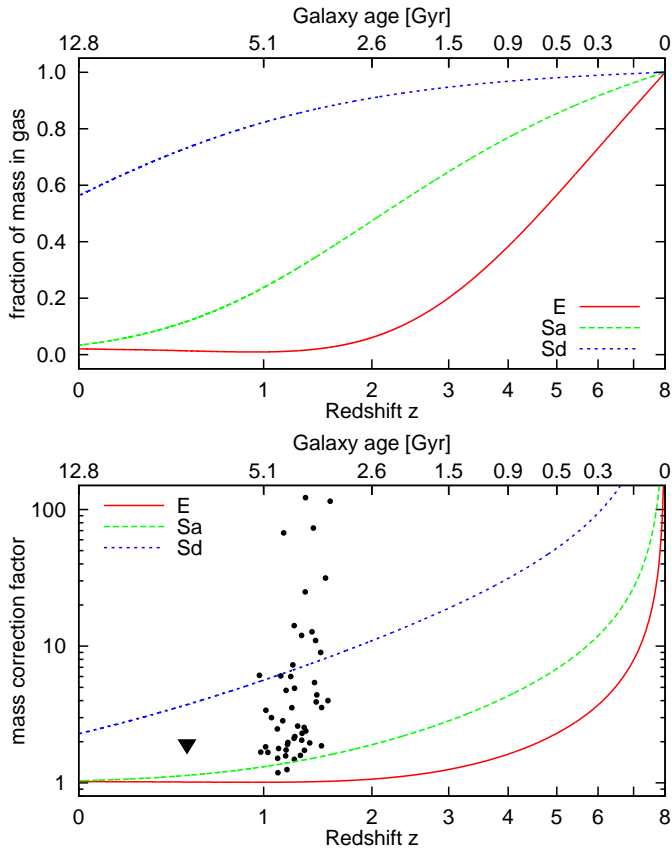
Figure 3.6: Top panel: Fractions of mass in gas relative to total mass for three different models as a function of redshift. Bottom panel: Photometric-to-dynamical mass correction factor for the same models shown in the top panel. The data points are observed data from Erb et al. (2006b) (small circles) and Daddi et al. (2008) (triangle). In both panels we give the corresponding galaxy age on the top axis.

2008) or heating it to high temperatures (e.g. Kay et al., 2002), or more indirect means such as AGN feedback (e.g. Silk & Rees, 1998; Schawinski et al., 2007; Reuland et al., 2007). We relax this assumption in Sect. 3.5.8 where we also investigate several models with incomplete truncation, i.e. a burst remnant with some ongoing, low-level SF.

Strong starburst are likely to be triggered by external encounters like mergers, so that the assumption of a closed-box models underlying our chemically consistent models would not hold in these cases. We therefore fix the metallicity of the input physics that goes into all burst models, in particular stellar evolution and stellar spectra, to half the solar value (also see Sect. 3.5.2).

3.5.1 Star formation rates

In Fig. 3.7 we show the evolution of SFR for a small selection of our burst models with varying peak-SFR times at galaxy ages of 0.5, 2.0 and 7.0 Gyr. The star formation rate during the burst depends on the remaining gas-mass at that onset time of the burst and is chosen in such a way that during the burst 75 per cent of the available gas is transformed into stars (e.g. Mihos & Hernquist, 1996). For this reason bursts occuring at younger galaxy ages have higher initial SFRs than later bursts, since the reservoir of gas within the progenitor galaxy gets constantly consumed by the quiescent SF activity.

For a total galaxy mass, i.e. the sum of stellar and gaseous masses, of $10^{10} \, \mathrm{M_\odot}$ typical SFRs during the burst have values of a few to a few tens of solar masses per year. However, there are two main factors influencing these values, namely the galaxy mass and the decline time. In our description of the burst strength the peak SFR during the burst, $\psi(t_B)$ is given by

$$\psi(t = t_B) = bs \times \frac{f_{\mathrm{Gas}} \times M_{\mathrm{total}}}{\tau_B} \tag{3.10}$$
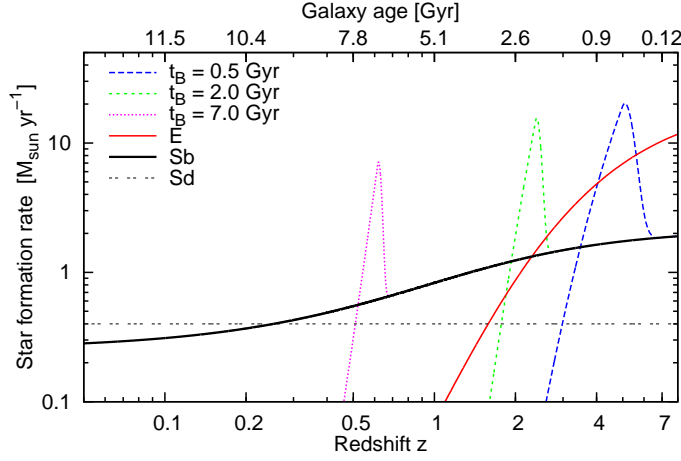
Figure 3.7: Star formation rates as a function of redshift for three different burst models with SFRs reaching their peak at galaxy ages varying between 0.5 Gyr and 7.0 Gyr . In all cases the progenitor is of Sb-type (shown for comparison as black solid line) and all galaxies have total (stars + gas) masses of $10^{10}\,M_\odot$. The solid red line shows the SFR of our E-type model, also normalized to the same total mass. The top axis gives the corresponding galaxy age.
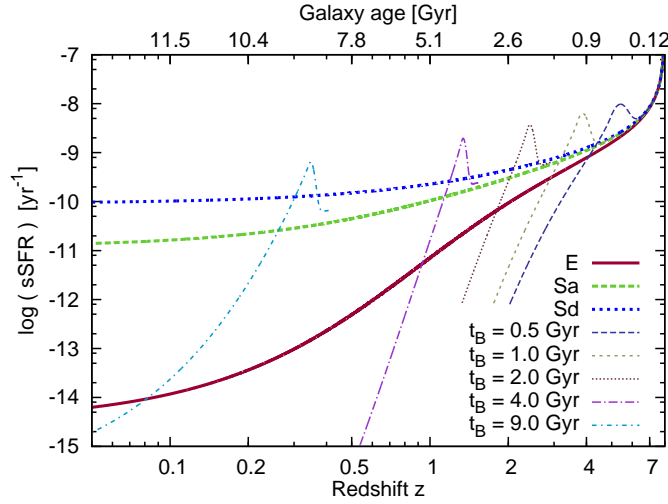

Figure 3.8: Specific star formation rates (sSFRs, see text for definition) for a range of undisturbed models (thick lines) and starburst models (thinner lines). Starburst models are only shown for ages after the onset of the burst. The top axis gives the corresponding galaxy age.

where bs is the burst strength, f_{Gas} the fraction of mass available as gas, M_{total} the total galaxy mass and τ_B the decline time of the burst. Massive star bursts with SFRs of hundreds of $M_\odot\,yr^{-1}$ as found in e.g. Ultra-Luminous InfraRed Galaxies (ULIRGs) or Sub-mm galaxies (Chapman et al., 2004; Greve et al., 2005; Schinnerer et al., 2008) hence can be explained by bursts in massive galaxies undergoing bursts with short decline times. Short decline times arise naturally from the compactness of the star formation regions, as found in both simulations (Mihos & Hernquist, 1996) and observations (e.g. Greve et al., 2005).

As consequence of the quiescent SF in the yet undisturbed galaxy the gas-to-total mass fraction f_B is constantly decreasing with time. This leads to slight variations in stellar mass as $z = 0$, with models encountering later bursts having higher masses.

In Fig. 3.8 we show the redshift evolution of specific SFRs (sSFRs), defined by

$$sSFR(t) = \frac{SFR(t)}{M_{stars}(t)} \tag{3.11}$$

for a range of models. sSFRs are a valuable tool because they are independent of the galaxy's stellar mass. At very high redshift ($z \gtrsim 7$) sSFRs reach extreme values because the still extremely young galaxies did not yet assemble a significant stellar mass (note that we assume a formation redshift of $z_{form} = 8$). With increasing age the sSFR decreases due to the decrease in SFR combined with the increase in stellar mass. During the bursts, and for early bursts in particular,
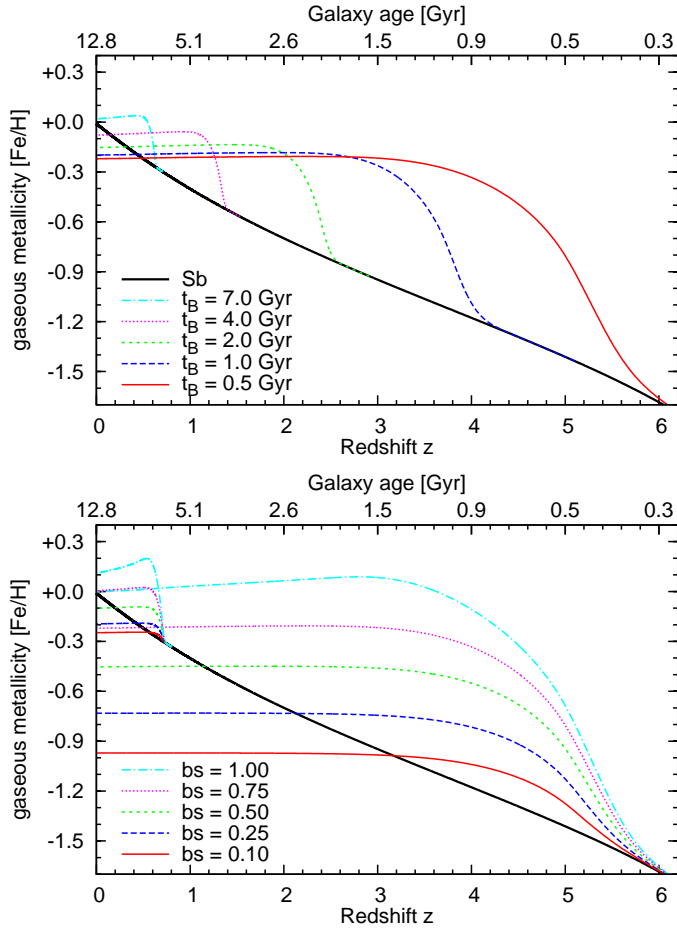
Figure 3.9: Top panel: Chemical enrichment histories for a range of burst models as function of burst time. All bursts start as undisturbed Sb-type model and encounter burst with a burst-strength of 0.75, i.e. 75% of their available gas-mass at the onset time of the burst gets converted into stars. Bottom panel: Similar to above, but for varying burst-strengths for one early (burst at galaxy age of 0.5 Gyr) and one late burst (6.5 Gyr). The black solid lines in both plots marks the evolution of the Sb-type progenitor. The top axis gives the corresponding galaxy age.

sSFRs can reach values of $10^{-9} - 10^{-8}\,\mathrm{yr}^{-1}$, which is comparable to galaxies at their peak of star formation. In the aftermath of the bursts sSFRs decline very quickly due to the assumed truncation of SF as consequence of the burst.

Daddi et al. (2007) used deep UV through Mid-IR data to derive sSFR for a large sample of galaxies out to redshift $z = 2$ and found a decrease in sSFR from $z = 2$ to $z = 1$ by a factor 3.7 and by a factor of 27 to $z = 0$, very similar to more recent findings by Pannella et al. (2009). These values are in excellent agreement with results from our model grid which, in the case of an Sa model, predicts a decrease by 2.8 and 26 for the respective redshift ranges. Later galaxy types show a more shallow decrease with redshift, but are too faint at high-redshifts to significantly contribute to the overall sample and hence have little impact on the results.

3.5.2 Chemical enrichment

The top panel of Fig. 3.9 shows the evolution of the ISM abundances for a part of our model grid as a function of redshift. All galaxies start as undisturbed Sb-type galaxies (shown as black solid line). During the burst the metallicity in the gas-phase rises very rapidly due to the metal-rich ejecta of Type-II supernovae mixed into the ISM. In the late phases of the burst ≈ 1 Gyr after the burst started the metallicity remains roughly constant and reaches roughly solar enrichment levels $[\mathrm{Fe/H}] \simeq 0$. However, a significant fraction of the stars are formed shortly after the burst started and hence will have sub-solar metallicities, confirming our assumptions to use half-solar metallicity spectra for the spectral modelling.

In the lower panel of Fig. 3.9 we present the chemical evolution for two selected models with one early (at a galaxy age of 0.5 Gyr) and one late (galaxy age of 6.5 Gyr) burst, but varying burst
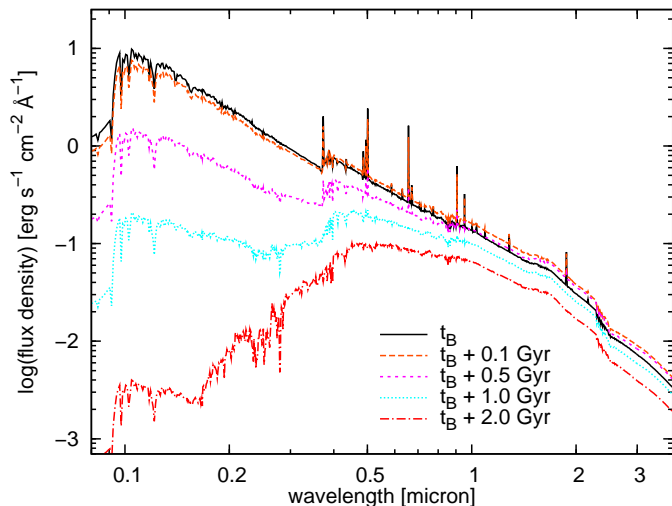
Figure 3.10: Spectra of a starburst galaxy, starting as a Sb-type model and encountering a strong (burst strength 75%) burst after 4 Gyr. Ages range from directly at the peak of the burst to late postburst phases.

strengths from 10 to 100 per cent. Weak bursts followed by SF truncation result in relatively metal-poor galaxies with metallicities of $10 - 30\%$ of solar. Strong bursts with $bs \geq 0.5$ on the other hand produce the near-solar metallicities typical for local early-type galaxies. Furthermore late bursts reach generally higher levels of enrichment despite the fact that they produce a smaller amount of stars during the burst. The reason for this is again the slow quiescent SF in the undisturbed host galaxy that very effectively enriches the host galaxy's ISM.

3.5.3 Spectral evolution of starburst models

In Fig. 3.10 we show the spectrum of a model with a burst starting at a galaxy age of $t_B = 4.0$ Gyr at 5 different times from the onset of the burst to a late postburst phase 2 Gyr after burst onset. At the very beginning of the burst the SFR reaches it maximum, leading to a very blue continuum from the Lyman break all the way through NIR. At this time the emission line strength, a measure for the SF activity during the last few Myr, reaches its maximum. The UV luminosity, however, continues to increase with time due to the accumulation of longer-lived (≈ 100 Myr) and UV-bright intermediate mass stars. 0.5 Gyr after the peak of the burst the luminosity shortwards of the 4000 break starts to decrease significantly, while the ongoing built-up of stellar mass leads to a maximum brightness in the optical and NIR. 1 Gyr into the burst the strength of the Balmer (absorption) lines reach their maximum strength, leading to the so-called E+A phenomenom (e.g. Zabludoff et al., 1996; Dressler et al., 1999; Tran et al., 2003; Goto, 2007; Yamauchi et al., 2008; Falkenberg et al., 2009a,b). At later times the spectral evolution is dominated by the passive aging of the stellar populations, gradually turning the spectrum into an early-type galaxy spectrum.

In Fig. 3.11 we compare the spectra of burst models with bursts starting at different galaxy ages. All spectra show the galaxy spectrum directly at the peak of the burst, i.e. in the moment of maximum SFR; this moment does not necessarily need to be the moment of maximum luminosity (see above). For the bursts occuring at very young ages (0.5 and 1.0 Gyr) the spectra are completely dominated by the young population, there are no significant contributions from an older population yet. For the two intermediate cases with onset times of 2.5 and 5.0 Gyr the galaxy has had enough time to accumulate low mass stars, leading to a increased luminosity in the optical-NIR. For those two and in particular the model with a late burst after 10 Gyrs, the galaxies do not become as UV-bright as in the case of early bursts. This is due to our definition of the burst strength, which measures the amount of stars formed relative to the available gas reservoir before the burst. Since the underlying host galaxy continuously forms stars, the available gas-mass (see Fig. 3.6) and with it the peak SFR (see Fig. 3.7) decreases with increasing burst onset times. For the latest burst the optical-NIR region does not reach the luminosities of
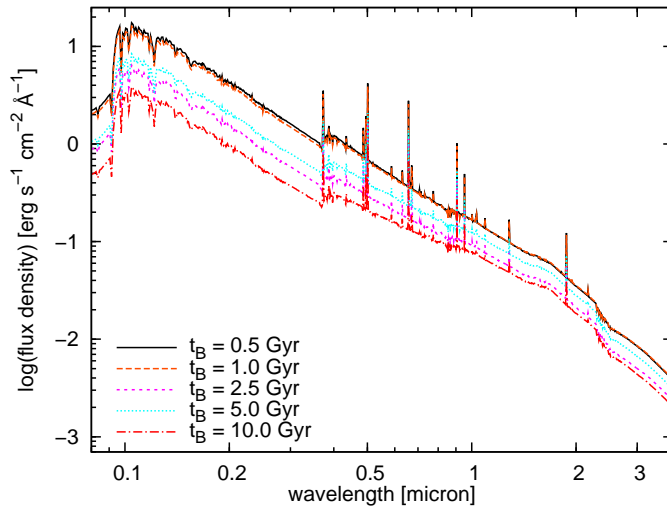
Figure 3.11: Comparison of spectra of burst models at the moment of maximum SFR for different onset times from 0.5 to 10 Gyr.
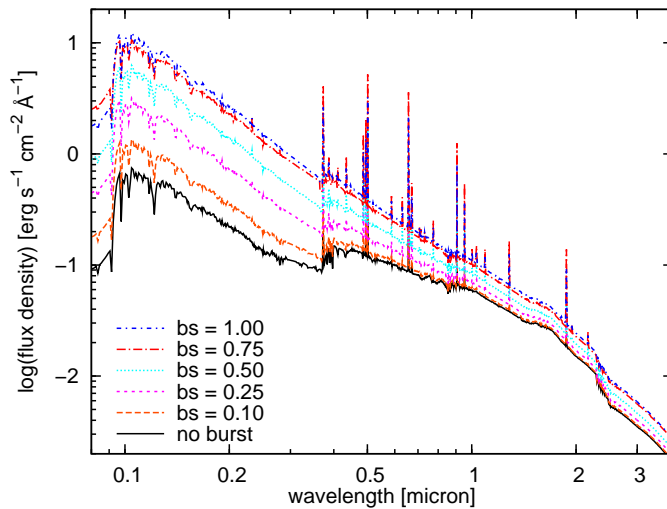

Figure 3.12: Comparison of spectra of burst models with identical onset times of 5 Gyr, but different burst strengths *bs* between 0.1 and 1.0.

the earlier bursts, since for this model the dominating SF episode early in the life of the galaxy has faded due to stellar evolution.

Fig. 3.12 compares spectral shapes shortly (20 Myr) after the peak of burst for a wide range in burst strengths from $bs = 0.1$ to $bs = 1.0$. Weak bursts $bs = 0.1$ mainly increase the UV part of the spectrum with their relative higher star formation rate. The optical and NIR, however, remains essentially unchanged. With increasing burst strengths $bs \gtrsim 0.25$ the young burst stars also significantly increase the flux in the longer passbands. *The overall spectrum for those cases is hence determined by the burst, although the mass fraction of young stars formed during the burst relative to the underlying, older population is still very small ($\approx$ 2% in the case of $bs = 0.25$).* For even stronger bursts the integrated galaxy spectrum is completely dominated by the young population despite their low mass fraction compared to the underlying host, so that the spectrum, compared to the case of weaker bursts, only changes in luminosity, but not in shape.

This can lead to significant uncertainties in the derived stellar masses. Fitting a very young population with its low mass-to-light ratio underestimates the stellar mass by a factor of a few.
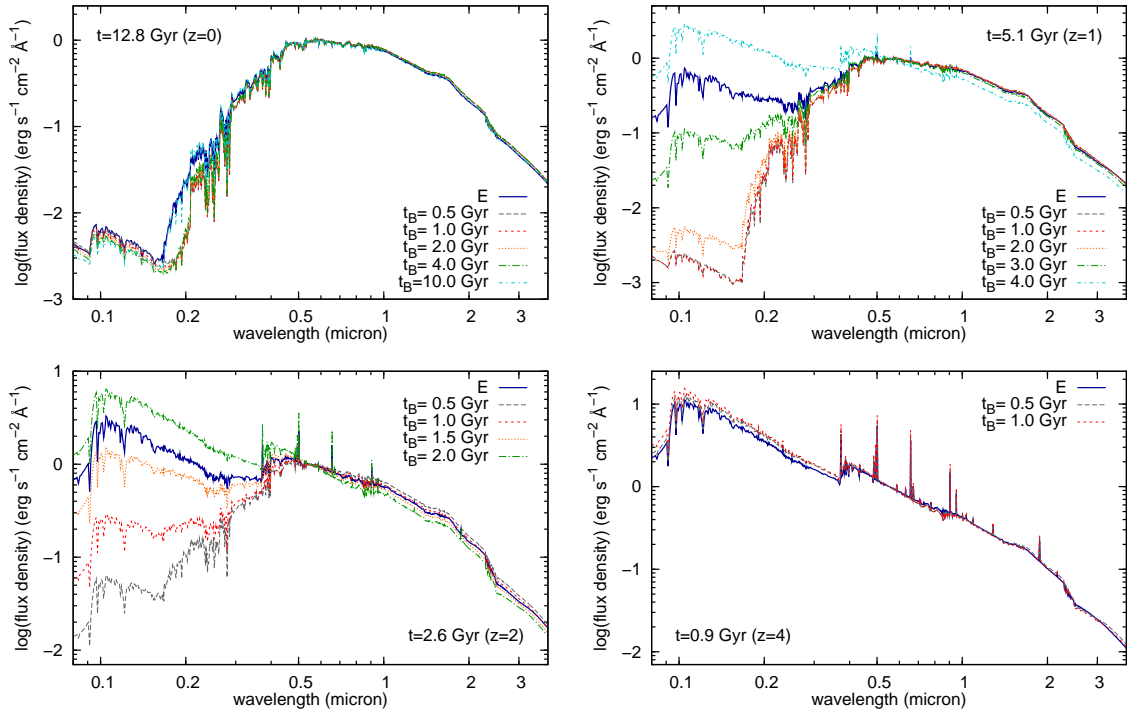
Figure 3.13: Spectra for bursts occuring at different galaxy ages for different redshifts $z = 0, 1, 2,$ and 4. The number of spectra shown decreases with increasing redshift, because at higher redshift some galaxies are not old enough, so they did not yet encounter the burst. All spectra are normalized by their flux at 0.55 micron.

3.5.4 Comparison of postburst to elliptical galaxies

In Fig. 3.13 we compare spectra of (post-)burst galaxies to that of our E-type model. The main difference is that the E-type galaxy is formed in a monolithical collapse, with a purely exponentially declining SFR and e-folding timescale of 1 Gyr. Postbursts, however, formed a significant fraction of their stars in an exponentially declining burst at later times (depending on burst model), but with an e-folding time of only 250 Myr.

As can be seen from the top-left panel of this figure there is very little difference between all the burst-models. While this is not surprising for the early bursts that are dominated by a very old population just as the E-type model, not even our latest burst after $t_B = 10.0$ Gyr, i.e. only 2.8 Gyr ago in our adopted cosmology, can be differentiated from the E-type model. This agrees with studies of local merger remnants, that not only have spectra and accordingly colours like old ellipticals, but also $r^{1/4}$ light profiles typical for bulges and ellipticals (e.g. Schweizer, 1982b, 1996; Wright et al., 1990; Hibbard & Yun, 1999; Rothberg & Joseph, 2004).

The most effective way to discriminate between the two formation paths is to use independent tracers of star formation such as globular clusters (GCs). Deriving ages and metallicities for a representative sample of GCs then allows to reconstruct individual bursts of SF that otherwise can not be disentangled from integrated light studies alone (Ashman & Zepf, 1992; West et al., 2004; Fritze, 2004; Brodie & Strader, 2006). However, this approach requires to break the age-metallicity degeneracy and hence was only successfully applied to a small sample of nearby galaxies (Puzia et al., 2002; Kissler-Patig et al., 2002; Hempel et al., 2003, 2007; Larsen et al., 2005; Kotulla et al., 2008a).

3.5.5 Colour evolution of burst models

The colour evolution of those models is shown in Fig. 3.14. For reasons of clarity we did not include all models, with more intermediate models skipped at lower redshift. Note that
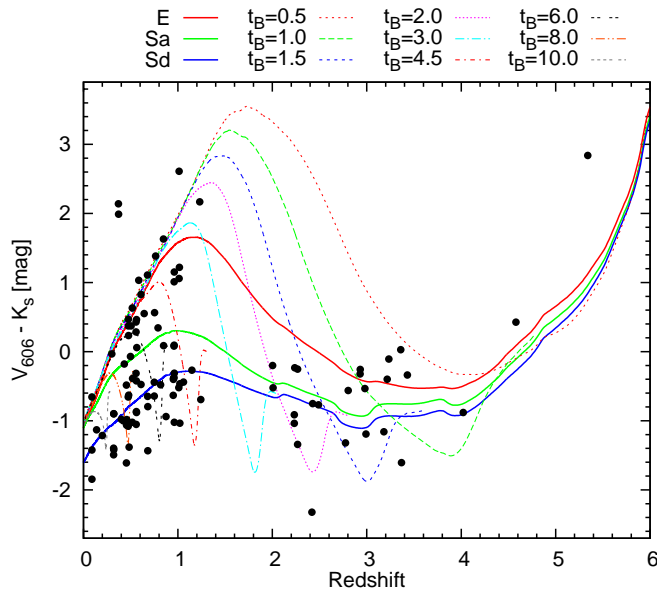
Figure 3.14: V-K colour evolution of a subset of models (for reasons of clarity) used to derive the photometric redshifts. Undisturbed models are shown with thick, solid lines, and burst models with dashed lines. Black points are galaxies from the catalog of Fernández-Soto et al. (1999). All magnitudes are given in the AB-system.

although our model grid spans similar steps for the time of the onset of the burst, the steps in redshift space get increasingly smaller towards lower redshifts; due to cosmic time dilation a fixed redshift interval at low redshift corresponds to a larger time-span than an equal sized redshift interval at high redshift.

From the very beginning of the burst, the galaxy becomes very blue due to the high SFR. After $\approx 0.5\,\mathrm{Gyr}$ or two e-folding times the colour returns to the value before the burst. During this first phase until $\approx 1\,\mathrm{Gyr}$ after the burst the galaxy becomes brighter by $1.5 - 4\,\mathrm{mag}$, depending on filter and galaxy age at the onset of the burst (i.e. the amount of gas converted into stars). This relatively short blue and bright phase is followed by a longer phase of $\approx 2.5\,\mathrm{Gyr}$ where the galaxy becomes increasingly red and very faint in the rest-frame UV and, to a lesser degree, optical, before it finally settles down on the red postburst sequence described below (see also Fritze & Gerhard, 1994a). From that moment on the decreasing absolute magnitude due to passive aging of the galaxy's stellar population is compensated by the decreasing distance modulus.

Not all bursts have the same effect on the colour evolution. At very high redshift the galaxy hardly becomes bluer during the violent early burst phases, since its young stellar population is very blue anyway. The maximum blueing during a burst happens in bursts at intermediate redshift. At high redshifts galaxy colours are red due to redshift and not due to the age of their stellar populations, that intrinsically are very blue. At lower redshifts the available gas-mass has decreased considerably, and with it the maximum amount of new stars that can form during the burst.

The phase of maximum redness in the aftermath of a burst also occurs at intermediate redshifts around z $\approx$ 2; the maximum colour reached gets redder with bursts happening earlier in the lifetime of the galaxy. In general, galaxies reach their extremely red phases $\approx 1.5 - 3\,\mathrm{Gyr}$ after the peak of the burst. At that time their spectra are dominated by a large number of A-type stars, while the majority of their bolometric luminosity is emitted by intermediate mass (M $\approx 3\,\mathrm{M_\odot}$) stars in their extremely bright but cool and hence very red TP-AGB phase.

The redshift range covered by the very red phases depends on the starting time of the burst. Very early bursts ($t_B = 0.5\,\mathrm{Gyr}$) lead to extremely red phases with $(V - K_{\mathrm{AB}} > 2$ over the large redshift interval $z = 2.4 - 1$. Later bursts reach this phase for only a very short interval (e.g. $z = 1 - 1.4$ for $t_B = 2\,\mathrm{Gyr}$) or not at all (if $t_B > 3\,\mathrm{Gyr}$). Note that independent of the time of the burst the extremely red phase with $V - K > 4$ ends at z $\approx$ 1. Hence $(V - K)_{\mathrm{AB}} > 4$ can be taken as a colour criterion to preselect galaxies at z $\geq$ 1.

A detailed analysis of this finding and a comparison with observations is the topic of Paper II.
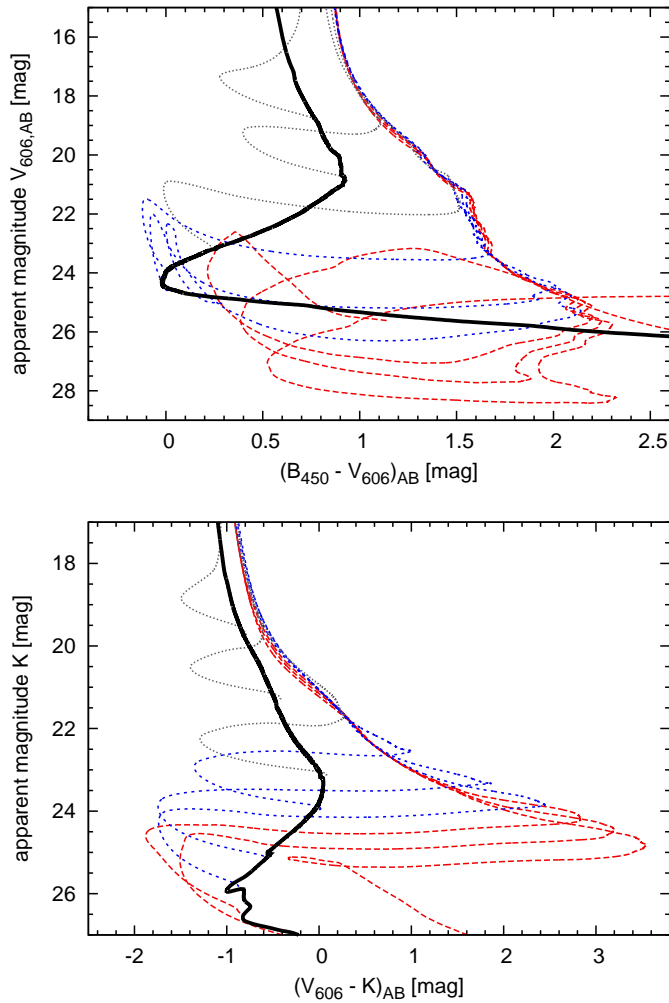
Figure 3.15: B-V (upper panel) and V-K (lower panel) colour evolution of all galaxy models in our model grid. The thick solid line gives the colour of the Sb-type progenitors for comparison. All magnitudes are given in the AB system. Red lines show early bursts with $t_B = (0.5, 1.0, 1.5)$ Gyr, blue are bursts at intermediate ages ($t_B = (2.0, 3.0, 4.5)$) and shown in grey are late bursts with $t_B = (6.0, 9.0, 11.0)$ Gyr.

3.5.6 Universal red postburst sequence

At $z < 1$ all early burst models join the colour evolution of the undisturbed E-type galaxy, later bursts reach this colour sequence roughly 1.5 Gyr after the onset of their respective bursts. This is not only valid in the case of the $V - K$ colour. In Fig. 3.15 we demonstrate the evolution of all burst models in the $B - V$ and $V - K$ colour magnitude planes.

All galaxies start forming stars as a Sb-type galaxy at redshift $z = 8$ and encounter a strong ($bs = 0.75$) burst after $0.5 - 10$ Gyr in steps of 0.5 Gyr. At the time of the onset of the burst they get both brighter and bluer, moving to the left and top in both panels of Fig. 3.15. In the B-V case they then become fainter and red, making a turn back to the lower right, crossing the position of the undisturbed Sd-type model ≈ 0.5 Gyr after the beginning of the burst. Once reaching reddest colours at the very right they join the envelope that we call the "red postburst sequence". In the $V - K$ plane galaxies also become brighter and bluer, but they do *not* become fainter in their transition phase to the red postburst sequence. Finally they also join into an enveloping postburst sequence.

3.5.7 Evolutionary corrections for burst galaxies

Fig. 3.16 shows evolutionary corrections for a subset of our burst grid in three different filters u, i, and K (top, middle and bottom panel, respectively). It is obvious that, although the overall
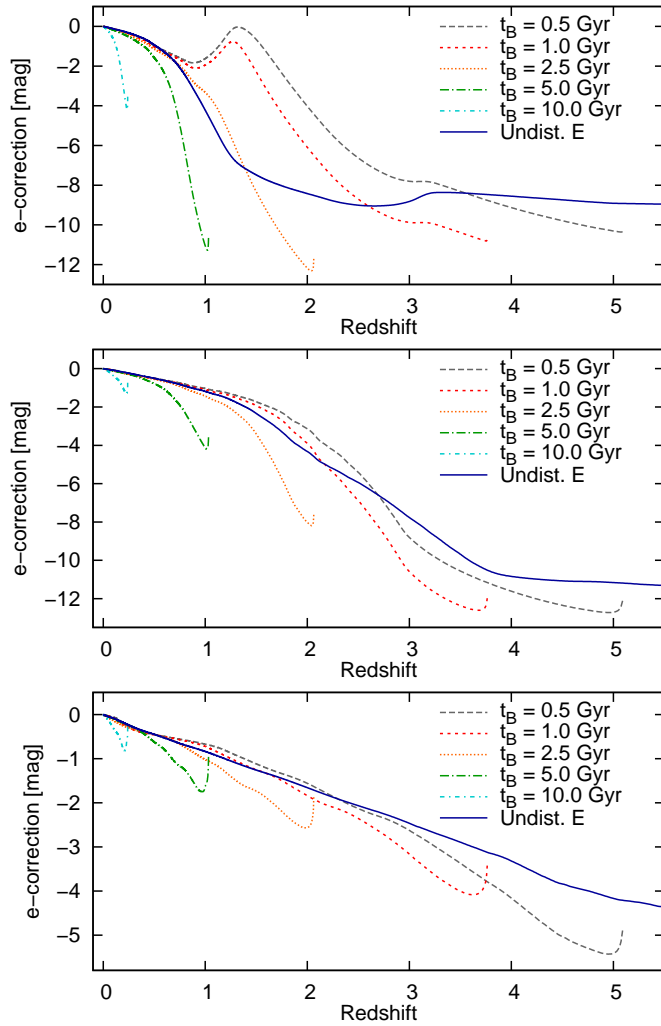
Figure 3.16: Evolutionary corrections for several selected burst models with different burst onset times for three filters U (top panel), I (middle panel) and K (bottom panel). For comparison we also show the evolutionary corrections for an E-type model with exponentially declining star formation rate.

shape is similar for the different models and to a lesser degree even among the filters, there are significant differences between them. For both optical filters u and i the corrections reach peak values of $\approx -10 \ldots -13$ mag (corresponding to a factor $\times 10^5$ in luminosities), making it possible to observe those galaxies out to the highest redshifts. These phases of maximum brightness are followed by a relative fast decline towards lower redshifts owing to the decline of SF combined with stellar evolution.

Note that all burst models have k-corrections very similar to that of the undisturbed E-type galaxy because the spectra of all postburst models at redshift z = 0 are very similar to the spectrum of an undisturbed E-type model (see top left panel in Fig. 3.13). This means that the evolutionary corrections of our burst models shown in Fig. 3.16 can be directly compared with the e-corrections of the E-type model.

3.5.8 Models with bursts and remaining SF after the burst

One scenario that is predicted by structure formation simulations but was not yet covered is the case where a post-starburst accretes gas and restarts star formation. To study this case we modelled galaxies with exponentially declining bursts as described before, but with a SFR proportional to the available gas-mass. For simplicity, the constant of proportionality was chosen to be identical with the one of the progenitor before the burst. The choice of a different value does not significantly affect our results.
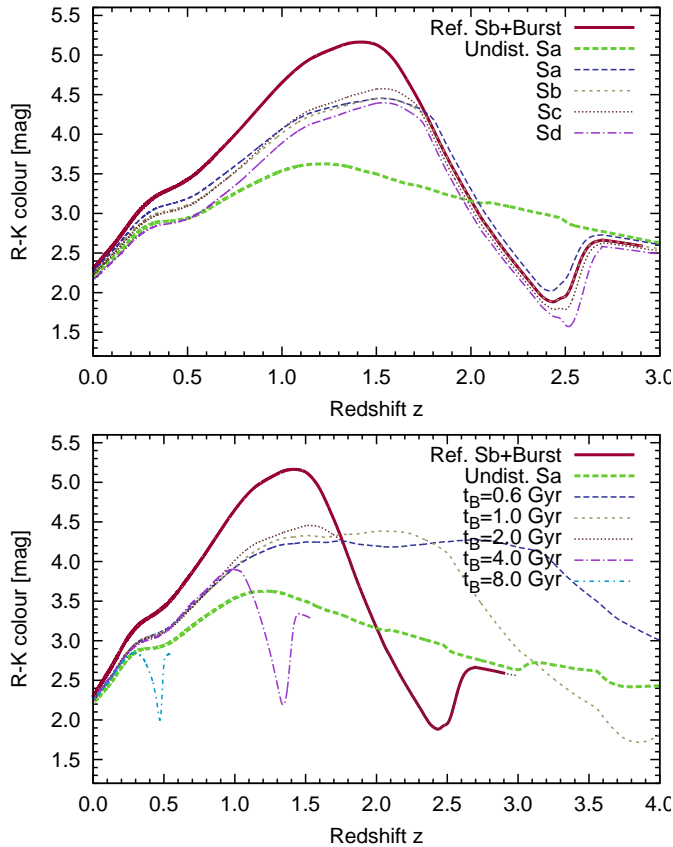
Figure 3.17: $R - K$ colour evolution of models with bursts and remaining SF during the post-starburst phase for different progenitor types Sa to Sd (top panel) and different times of burst onset $t_B = 0.6 - 8.0$ Gyrs (bottom panel). The red solid line shows a model with Sb-type progenitor, a burst at a galaxy age of 2 Gyr and complete shutdown of SF after the burst as a reference with previous plots. The thick green line shows the colour evolution of our undisturbed Sa-type model.

In the top panel of Fig. 3.17 we show the colour evolution in $R - K$ for several models with fixed peak time of $t_B = 2.0$ Gyr for which we varied the progenitor type from Sa to Sd. As expected, we find only small variations with progenitor type since all galaxies are still gas-rich and actively star-forming at this early stage. The comparison with a reference model with complete truncation of SF during the post-starburst phase and identical time of burst shows that the originally found very red colours are no longer reached as a consequence of the small fraction of young stars.

The comparison of different burst times $t_B = 0.6 - 8.0$ Gyr for a fixed progenitor type (Sb) is shown in the bottom panel of Fig. 3.17. In the post-starburst phase starting ≈ 0.5 Gyr after the peak of the burst, all models have indistinguishable colours due to their similar recent SFHs. At low redshifts $z \lesssim 0.5$, these colours coincide with the colours of an undisturbed Sa-type model. In a more general case for arbitrary progenitor types we find that a burst with subsequently remaining low-level SF yields a remnant galaxy that is approximately one spectral type earlier than the progenitor, e.g. transforming an Sd progenitor into an Sc remnant.

3.6 Summary and outlook

Evolutionary synthesis models are an established tool to study both physical properties and spectra of galaxies over cosmological times from the big bang until the present. We used our chemically consistent **GALEV** code to create a large grid of models for both undisturbed galaxies as well as galaxies undergoing a starburst event at some stage of their evolution. For each of these models we trace stellar and gaseous masses, star formation rates, metallicities and spectra as a function of age and redshift.

We find that all galaxies from early-type ellipticals to late-type spirals have very similar spectra in the early universe, despite their significantly different spectra in the local universe. The reason for their look-alike spectra are high specific star formation rates, naturally explaining why searches for "red and dead" ellipticals are unsuccessful at redshifts beyond z = 3.

For each model we also compute cosmological and evolutionary corrections. These corrections enable a comparison of galaxies at different redshifts. Accurate evolutionary corrections are of paramount importance for all studies of high-redshift galaxies since they heavily impact on both observed magnitudes and colours and hence are able to completely alter their spectra and SEDs.

We also compare models that account for increasing abundances of successive stellar populations to models assuming a fixed, solar metallicity for all stars. Galaxies with subsolar metallicities can be brighter than their solar-metallicity counterparts by up to $\gtrsim$ 1mag depending on galaxy type, filter, and redshift. Neglecting this metallicity evolution of galaxies can have a profound impact on both masses and star formation rates derived for high-redshift galaxies.

However, even including both e- and k-corrections does not allow us to describe all observed properties with our model grid. For this reason we added a number of galaxies encountering strong starbursts. During these starbursts models reach the observed very blue galaxy colours, while becoming extremely red in their late postburst phases. This extended model grid can cope with the extremely wide range of star formation rates found among high-redshift galaxies from Lyman Break Galaxies all through sub-millimeter galaxies. A detailed comparison is given in Paper II.

We furthermore find that even small mass contributions from young stars of the order of a few per cent can outshine a massive underlying host galaxy, leading to significantly underestimated ages and stellar masses. In their late phases, all postburst models have similar colours that only depend on redshift and hence form a narrow red post-starburst sequence, similar to the well-known colour-magnitude relation. All postburst models and even models with relatively recent bursts less than 3 Gyrs ago reach metallicities at z = 0 near the solar value and also have spectra very similar to those of local elliptical galaxies. In case star formation is not completely halted after the burst, but continues at an rate proportional to the remaining gaseous masses, the remnant is one spectral type earlier than the burst progenitor.

All models presented here (spectra, SEDs, e- and k-corrections for a wide range of filters, star formation rates, stellar and gaseous masses, and metallicities) are freely available at http://www.galev.org. Models with different parameters can also be created using the same URL. For more details see Kotulla et al. (2009).

In a companion paper (Kotulla, 2009b) we use the models presented here and compare them to the observed properties of galaxy population selected by relatively simple colour criteria, showing that our models can reproduce all these criteria. Our models furthermore are in excellent agreement with typical masses, star formation rates and metallicities derived from optical and near-infrared spectroscopy, further emphasizing the value of this grid for a wide range of studies of galaxies from nearby to the redshift desert and beyond to the highest redshifts.

Based on these encouraging results we will in a next step combine the results from our modeling described in this paper with our new photometric redshift code GAZELLE and then apply this combination to a large sample of galaxies from a number of deep fields. This will give us not only accurate redshifts, but also physical parameters for a large number of galaxies over a range of redshifts and hence grant us a deeper insight into galaxy formation and evolution.

Galaxies to the redshift desert and beyond
II. Comparison to observations

Ralf Kotulla

Abstract:

In a companion paper, we presented evolutionary synthesis models for undisturbed E and Sa-Sd type galaxies as well as a wide range of starbursts and post-starburst models. For each model we trace star formation rates, stellar and gaseous masses, metallicities and the evolution of spectra and magnitudes for a wide range of filters, from the formation in the early universe until today. We furthermore include both evolutionary and cosmological corrections.

Here we show that this model grid is able to describe currently used colour selection criteria for Lyman Break Galaxies (LBGs), BzK galaxies, Extremely Red Objects (ERO) and both Distant and Luminous Red Galaxies (DRG, LRG) not only in terms of colours, but also with respect to stellar masses, gas fractions, star formation rates and metallicities. Our main findings are: **a)** We not only confirm the original LBG/BM/BX colour selections, but based on masses, SFRs and metallicities identify LBGs as the most likely progenitors of local early type spiral galaxies and low-mass ellipticals. **b)** Our model grid correctly confirms the BzK colour selection, but also points out a class of post-starburst galaxies that are missed by this colour selection. We correctly explain the observed range of masses, SFRs and metallicities. **c)** By including post-starburst phases we are for the first time able to reproduce E+A features in EROs as alternative to dusty star-forming galaxies. These post-starburst galaxies explain the observed number densities and masses and offer the potential to study the merger rate at high redshifts. **d)** DRGs can be either explained by post-starbursts or galaxies with moderate amounts of dust. Our grid explains both their high masses and SFRs, identifying them as progenitors of local ellipticals. **e)** LRGs are also excellently described by very massive post-starbursts with high metallicities and are the younger counterparts of the most massive ellipticals found in the local universe.

We conclude that our model grid explains in an excellent way many findings derived by spectroscopy in a unified and physically sound way. It therefore present an ideal template set to be used with photometric redshift codes and offers a unique insight into physical properties across galaxy types and over a wide range of redshifts .

4.1 Introduction

High-redshift galaxies have been classified into a number of different types: Lyman Break Galaxies (LBGs Guhathakurta et al., 1990) and Steidel & Hamilton (1992, 1993); Steidel et al. (2003), BzK Galaxies (Daddi et al., 2004), Extremely Red Objects (EROs Elston et al., 1988, 1989), Distant Red Galaxies (DRGs Franx et al., 2003; van Dokkum et al., 2003) and Luminous Red Galaxies (LRGs Eisenstein et al., 2001; Cannon et al., 2006) to just give their most common names. Many classifications contain some overlap in the sense that galaxies can be classified as more than one type simultaneously.

So far these different classes of high-redshift galaxies have been investigated using different approaches, not only in terms of observational techniques and wavelength ranges, but also in terms of models used in the analysis of their physical properties like present star formation rates (SFRs) and past star formation (SF) histories, total gaseous and stellar masses, metallicities, gas contents, etc. The use of different methods to study the individual classes of high-redshift galaxies makes it very difficult to establish evolutionary links among galaxies from different classes.

We here, for the first time, present an approach to consistently study this full range of high-redshift galaxies with *one* set of **GALEV** evolutionary synthesis models. This approach offers a much better avenue to investigate the existence of evolutionary links between galaxies of various subtypes and at a range of redshifts.

So far, our models are restricted in the sense that they do not yet include a consistent description of dust in absorption *and emission*. This precludes the interpretation of clearly dust-dominated spectra and galaxy types. We can, however, explain the properties of a considerable fraction of even the reddest galaxies *without* significant dust contributions.

This paper is organized as follows: First we will give a short summary of the model grid presented in the first paper (Kotulla, 2009a, hereafter Paper I) of this series. The following sections will in turn compare the colour evolution of our model grid to the empirical colour selection criteria of LBGs and their various subclasses, BzK, EROs, DRGs, and LRGs. We pay particular attention to the comparison of physical properties such as masses, star formation rates and metallicities. We conclude this paper with a summary and an outlook.

4.2 Chemically Consistent galev models

The foundation of the study presented here is an extensive set of galaxy models computed with our chemically consistent **GALEV** evolutionary synthesis models as, e.g. , presented in Bicker et al. (2004) and Kotulla et al. (2009). We will only give a brief summary of the models here and refer the reader to the detailed description in Paper I.

Our model grid is based on five different galaxy models E and Sa-Sd that are calibrated to reproduce all relevant properties (masses, colours, spectra, star formation rates (SFR), gas-phase metallicities, gas fractions and mass-to-light ratios) of real galaxies in the local universe (see Kotulla et al., 2009, for details on this calibration). However, this limited model grid does not reproduce the full range of observed galaxy colours. We therefore extend the grid with galaxy models that, in addition to their undisturbed SFH, encounter a strong starburst at some stage of their evolution. The final model grid hence contains in total 25 models: five undisturbed models (E, Sa, Sb, Sc, and Sd) and 20 models with bursts, all starting with Sb-type progenitors and encountering bursts at ages varying from $0.5 - 10$ Gyr in steps of 0.5 Gyr. Every burst consumes 75% of the gas available at the beginning of the burst, so that the total amount of new stars formed in the burst, the relative amount of pre-burst and burst stars, the SFR during the burst and the spectral and photometric evolution of the galaxy during the starburst and post-starburst

phases all depend on *when* the burst starts, i.e. the evolutionary age of the galaxy at the onset of the burst.

For the undisturbed galaxy models E, and Sa through Sd we include a chemically consistent treatment of the chemical evolution in our models, ie, we fully account for the increasing initial abundances of subsequent stellar generations. This approach, however, is not plausible for the models including bursts, since these are likely to be triggered by external interactions (e.g. mergers), and hence our assumptions of a closed-box not justified. We decided to use a fixed metallicity of half the solar value for these models as this metallicity is the dominating metallicity of massive and yet still gas-rich spirals (see, e.g. , Kotulla & Fritze, 2009, for details on the chemical evolution of spirals).

To compare this model set to observations we use a concordance cosmological model with $H_0 = 70\,\mathrm{km\,s^{-1}\,Mpc^{-1}}$, $\Omega_M = 0.30$, $\Omega_\Lambda = 0.70$ (Spergel et al., 2007; Komatsu et al., 2009). To map galaxy ages to redshifts we assume that all galaxies started forming stars at redshift $z_{form} = 8$. Small changes to this formation redshift as suggested by Noeske et al. (2007b) do not significantly affect our results or conclusions.

We account for the attenuation of flux shortwards of the Lyman-α line due to intergalactic neutral hydrogen by using the description by Madau (1995).

Our models naturally contain both cosmological and evolutionary corrections and are hence well suited to probe our current understanding of galaxy formation and evolution.

In the following we compare our models to empirically derived colour selection criteria for a variety of high-redshift galaxies. The main advantage of colour selection is the need for only one or two colours. This technique therefore allows to very efficiently (pre)select high redshift galaxies for spectroscopy with a minimum amount of telescope time (e.g. Steidel et al., 2003; Willmer et al., 2006). However, they only allow a rough redshift determination within wide ranges or only give lower limits, making them principally inferior to more advanced techniques such as photometric redshift estimates.

4.2.1 Words of caution

We stress that the galaxy types we attribute to high redshift galaxies are those that correspond to the SFH of these galaxies *prior* to the time of observation. Only if galaxies evolve without further disturbance in their SFHs, these will still be the galaxy types observed today. Merging and accretion events after the time of observation may change the galaxy type until redshift zero, but only if they involve gas and hence affect the SFH. If those events are violent enough to enhance SF or trigger a burst, the present-day galaxy type will be earlier that the one identified at high redshift. Only in the case of very steady and low-rate accretion of gas may an early-type galaxy at high redshift rebuild a gaseous and later possibly stellar disk and thus evolve into a later-type galaxy. Galaxy masses can only increase beyond those already present at high redshift. The relatively small mass range of present-day spirals limits the number of spiral galaxies that can result from such a secondary disk-building scenario out of early-type galaxies that are bright enough at high redshift to make it into the photometric sample. For more details, in particular on how these scenarios can be treated with **GALEV** models see Sect. 2.2 and 5.8 in Paper I.

4.3 Lyman Break Galaxies

One of the earliest efficient means to detect high-redshift galaxies in large numbers was the Lyman break technique introduced by Guhathakurta et al. (1990) and Steidel & Hamilton (1992, 1993). It is based on the fact that intergalactic neutral hydrogen clouds are very efficient in absorbing radiation at wavelengths shorter than the Lyman-α line, causing a sharp break in the spectrum. This causes the galaxy to have unusual colours that are very red in the blue and very blue in the red spectral region, if the Lyman break happens to lie between the two. We refer the reader to the review by Giavalisco (2002) for more details on LBGs.

4.3.1 Colour selection criteria

Steidel & Hamilton (1992) and Steidel et al. (2003) define four groups of LBG, according to two colour selection criteria in their special-purpose filter system. Both C and D-type LBGs fulfill the selection criteria

$$
\begin{aligned}
G - \mathscr{R} &\leq 1.2 \\
U_n - G &\geq G - \mathscr{R} + 1.5
\end{aligned}
\tag{4.12}
$$

The difference between both classes is that C-type LBGs are those still detected in U_n, while D-type LBGs are not. M and MD-type LBGs are selected by a slightly relaxed colour selection:

$$
\begin{aligned}
G - \mathscr{R} &\leq 1.2 \\
U_n - G &\geq G - \mathscr{R} + 1.0 \\
U_n - G &\leq G - \mathscr{R} + 1.5
\end{aligned}
\tag{4.13}
$$

Again M-type LBGs are those detected in U_n, while galaxies of the MD-type are not.

Using the same filter set, Erb et al. (2003), Steidel et al. (2004), and Adelberger et al. (2004) introduced further selection criteria targeting galaxies in the redshift desert at slightly lower redshifts. Their BM galaxies at redshifts $1.5 \lesssim z \lesssim 2.0$ fulfill the criteria

$$
\begin{aligned}
G - \mathscr{R} &\geq -0.2 \\
U_n - G &\geq G - \mathscr{R} - 0.1 \\
G - \mathscr{R} &\leq 0.2(U_n - G) + 0.4 \\
U_n - G &\leq G - \mathscr{R} + 0.2
\end{aligned}
\tag{4.14}
$$

while their BX galaxies with redshifts $2.0 \lesssim z \lesssim 2.5$ are selected by:

$$
\begin{aligned}
G - \mathscr{R} &\geq -0.2 \\
U_n - G &\geq G - \mathscr{R} + 0.2 \\
G - \mathscr{R} &\leq 0.2(U_n - G) + 0.4 \\
U_n - G &\leq G - \mathscr{R} + 1.0
\end{aligned}
\tag{4.15}
$$

In Fig. 4.1 we present a part of our model grid in the $(U_n - G)$–$(G - \mathscr{R})$ colour plane. We only show three undisturbed galaxy types representing E, Sa, and Sd, plus those burst models with bursts before $z = 3$, since all other models are still undisturbed before this redshift. The regions selecting C/D and M/MD galaxies are shown as shaded green and orange regions, respectively. The regions selecting the lower redshift BX and BM galaxies are also shown in grey (BX) and darker green (BM).

As can be seen from this figure, all our models fulfill the colour criteria identifying them as LBGs in the respective selected redshift range. Only one model with a very early burst starting at an age of 0.5 Gyr has colours near the edge of the selection region and does not fulfill the BX and BM criteria. The reason for this is that we assume a rapid exponential decline of star formation after the burst, reducing the strength of the UV continuum, which in turn leads to redder $G - \mathscr{R}$ colours.

4.3.2 Properties of LBGs

Shapley et al. (2001) studied rest-frame optical spectra of a large sample of LBGs and found a wide range in the observed stellar masses, ages and derived SFRs. Splitting their sample into "young" (age < 35 Myr) and "old" (age > 1 Gyr) LBGs, they found mean values of ($210\,\mathrm{M_\odot\,yr^{-1}}$,
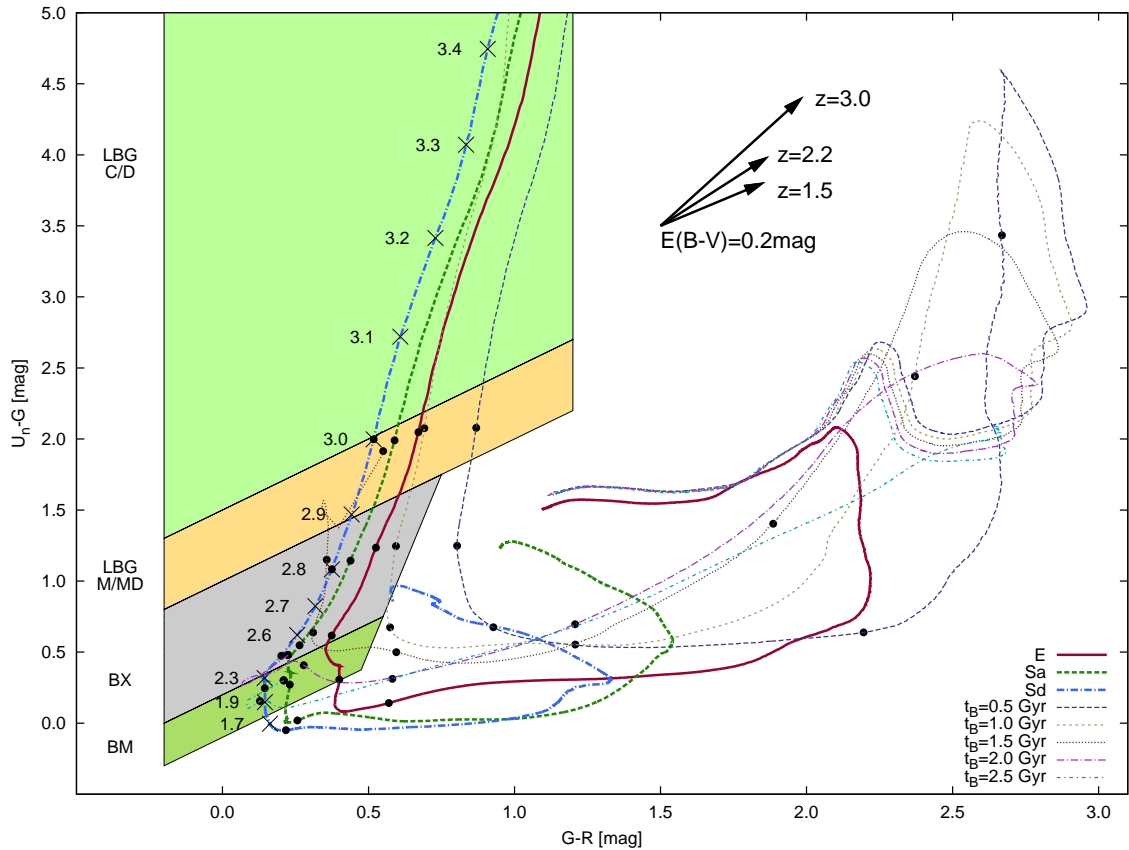
Figure 4.1: Evolution of several representative galaxies from our model grid in the $U_n - G, G - \mathscr{R}$ colour-colour plane. The colour selection regions as given in Steidel et al. (2003) are shown in green (C and D-type LBGs) and orange (M and MD-type).

$2.9 \times 10^9 M_\odot$) and ($25\,M_\odot\,yr^{-1}$, $4 \times 10^{10} M_\odot$) respectively for their SFRs and masses, or equivalently *specific SFRs*, i.e. the SFR per unit stellar mass, of $7 \times 10^{-8}\,yr^{-1}$ and $6.3 \times 10^{-10}\,yr^{-1}$. Both types of LBGs can be explained by our models.

The "young" population is well matched by our starburst models in an early phase of the burst. During this phase the young populations - despite their comparably low mass fraction relative to the older ones - completely outshine the underlying older population (see Fig. 13 in Paper I), explaining the [3] young ages. High star formation rates and the resulting amounts of dust naturally explain the higher extinction values found in this young LBG population as compared to the older one.

The old LBG population is well described by our undisturbed galaxy models. However, in order to reach the observed absolute SFRs (tens of $M_\odot\,yr^{-1}$) we require total, i.e. stellar + gaseous, masses of the order of $10^{11}\,M_\odot$, typical for present-day elliptical and early-type spiral galaxies. For those types our models predict metallicities (see, e.g. , Fig. 1 in Kotulla & Fritze (2009) and Fig. 10 in Paper I) of $0.5\,Z_\odot$ (Elliptical), $0.2\,Z_\odot$ (Sa) and $0.1\,Z_\odot$ (Sb), encompassing the full range of spectroscopic metallicities $(0.1 - 0.5) \times Z_\odot$ as observed for LBGs by Pettini et al. (2001).

In return, if this old LBG population observed at redshifts z = 1.5 − 2.5 is to evolve into the local population of Sa/Sb through E-type galaxies, it is not expected to accrete significant amounts of matter [4] until z = 0, i.e. these old LBGs at z = 1.5 − 2.5 seem already to have $\geq 50\%$ of their present-day mass. This a posteriori justifies to some extent our use (for simplicity) of closed-box models.

---

[3] apparent very
[4] too seriously
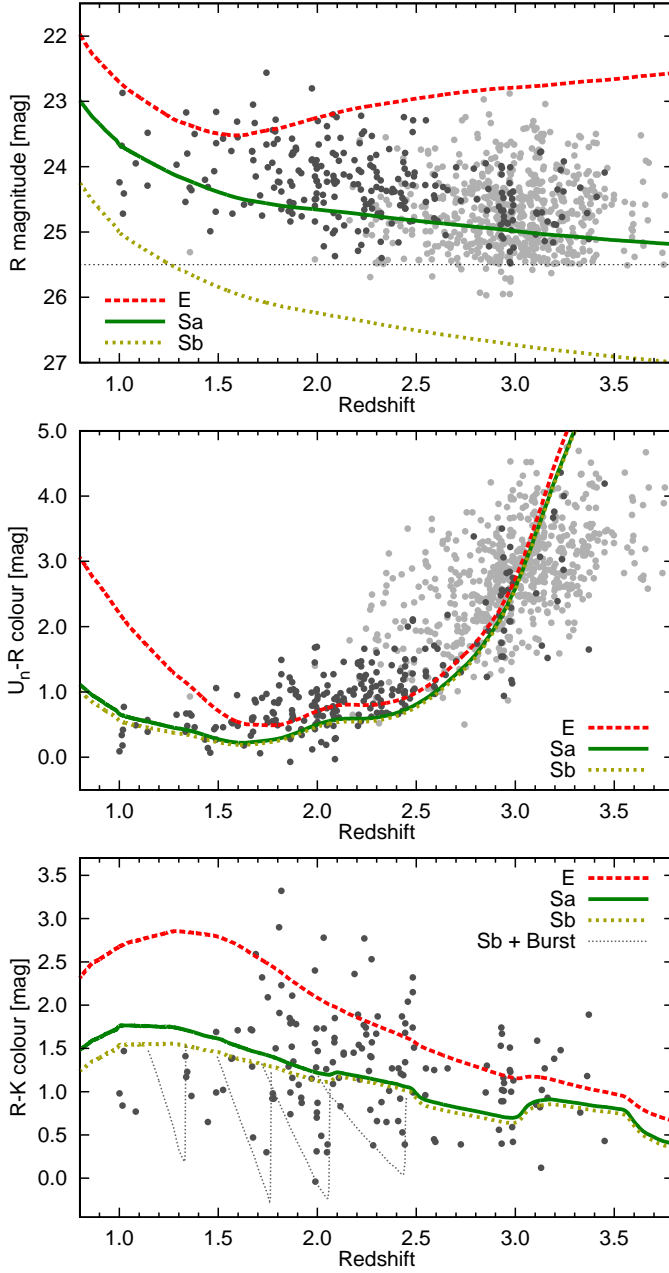
Figure 4.2:

Top panel: Redshift evolution of apparent R-band magnitudes for our E, Sa, and Sb models. Shown with black solid points are data from Reddy et al. (2006) for LBGs in the GOODS-North field, grey dots show LBGs from Steidel et al. (2003). The dotted line in the top panel corresponds to the selection limit of $\mathscr{R} < 25.5$.

Middle panel: Evolution of $U - \mathscr{R}$ colours. Data points as above.

Bottom panel: Evolution of $\mathscr{R} - K_s$ colours for E, Sa, Sb and several burst models with bursts occuring at galaxy ages of $t_B = 2.0, 2.5, 3.0$ and 4.0 Gyrs (according to redshifts $z_B = 2.45, 2.06, 1.77$, and 1.34). For the burst models we only show the evolution for the first 600 Myr after the onset of the burst. After this time SFRs and hence UV luminosities have decreased considerably.

The lower redshift BX and BM galaxies are also correctly predicted by our model grid, both in terms of colours (see Fig. 4.1) and physical parameters. Erb et al. (2003) derived mean dynamical masses of $M_{dyn} > 4 \times 10^{10} M_\odot$ and mean SFRs of $16 \, M_\odot \, yr^{-1}$ for their sample of 16 galaxies at $2.0 \leq z \leq 2.6$, yielding a mean sSFR $= 4 \times 10^{-10} \, yr^{-1}$. This is in good agreement with our model predictions for spirals (see Fig. 9 in Paper I). Typical stellar masses in our Sa-type models at these redshifts are $2.5 \times 10^{10} M_\odot$ with roughly the same mass still residing in the gas-phase. 40% of their sample showed evidence for ordered rotation indicative of gaseous spiral disks, in agreement with our assumptions.

In Fig. 4.2 we compare the magnitude and colour evolution of our E, Sa, and Sb galaxies to a large sample of LBGs compiled by Steidel et al. (2003) and Reddy et al. (2006). These three models are found to enclose the full range of $\mathscr{R}$-band magnitudes observed for LBGs in the redshift range $1 \leq z \leq 3.8$. Our Sa-type model yields the best overall match to the observed magnitudes, suggesting that LBGs are likely progenitors of local early-type spirals, confirming

our above results based on spectroscopic masses and metallicities. Further support for this scenario comes from excellent agreement of the observed colour evolution of LBGs over the redshift range $1.0 \leq z \leq 3.5$ with our models. The scatter of observed colours at the high-redshift end, $z \geq 3.0$, is most likely due to a combination of photometric scatter resulting from the faint U-band magnitudes (Steidel et al., 2003) and the stochasticity of the attenuation due to intergalactic hydrogen (Bershady et al., 1999; Tepper-García & Fritze, 2008).

4.4 BzK Galaxies

4.4.1 Colour selection

Daddi et al. (2004) proposed a photometric two-colour selection based on a combination of B, z, and K-band magnitudes, giving rise to their name "BzK"-galaxies. It targets both passive and star-forming galaxies in the redshift range $1.4 \leq z \leq 2.5$.

Star-forming BzK (sBzK) galaxies can be selected via their BzK value by

$$BzK = (z - K)_{AB} - (B - z)_{AB} > -0.2,$$ (4.16)

while passive BzK (pBzK) galaxies are also required to have red (z-K) colours:

$$BzK < -0.2 \quad \cap \quad (z - K)_{AB} > 2.5$$ (4.17)

In Fig. 4.3 we show the relevant part of our model grid in the redshift range $1.4 \leq z \leq 2.5$ overlaid with both BzK selection criteria. As expected the models of Sa and Sd-type galaxies are
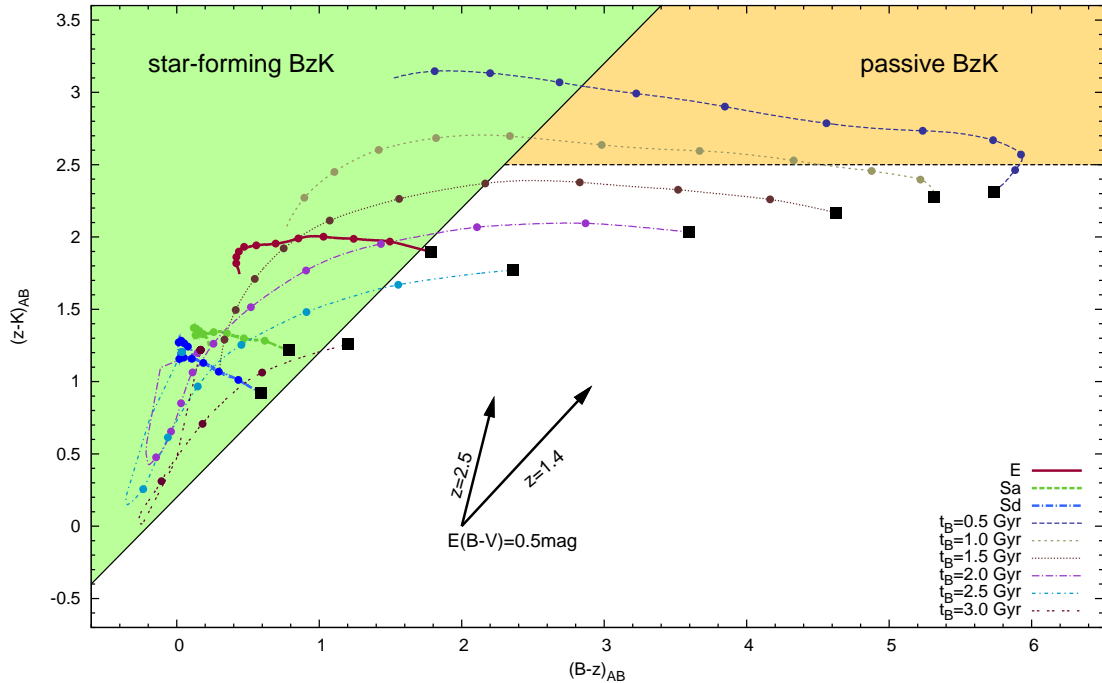
Figure 4.3: Color selection scheme for BzK galaxies overplotted with the part of our model grid that the BzK selection scheme aims at - galaxies with redshifts $1.4 \leq z \leq 2.5$. In the bottom middle of the plot we show reddening vectors for $E(B - V) = 0.5$ mag for both extreme redshifts $z = 1.4$ and $z = 2.5$. Large black squares mark the low-redshift end of the targeted redshift range at $z = 1.4$. Thin lines mark the colour evolution of several models of Sb-progenitors undergoing a starburst with bs = 0.75 at a galaxy age of t_B.
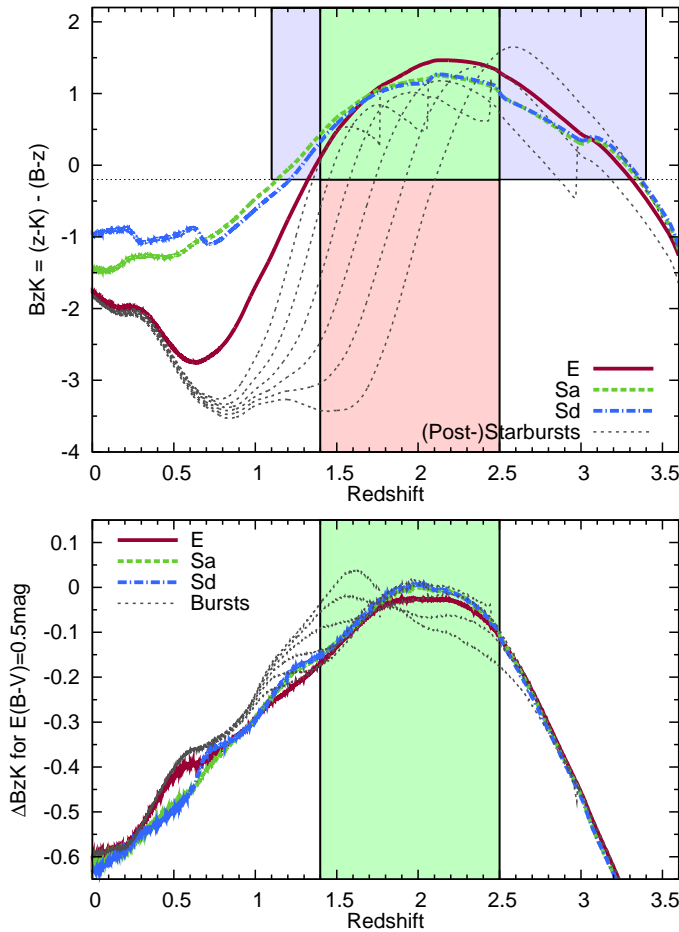
Figure 4.4:

Top panel: BzK criterion as function of redshift for our E, Sa, and Sd models. With thin dashed lines we also show tracks of models undergoing bursts with bursts starting at galaxy ages of (from right to left) $0.5 - 3.0$ Gyr in steps of 0.5 Gyr. The shaded regions mark the targeted redshift region where models fulfill the BzK selection criteria (green), models that are missed (red), and models contaminating the selection at higher and lower redshifts (blue).

Bottom panel: Change of BzK, ΔBzK, incured by an intrinsic reddening of $E(B - V) = 0.5$ mag.

correctly retrieved with the photometric selection of star-forming galaxies in this redshift range. Note that also the undisturbed E-type model fulfills the sBzK criterion, since at redshifts $z \gtrsim 1.4$ it still has a remaining SFR of $\approx 10\,\mathrm{M}_\odot\,\mathrm{yr}^{-1}$.

The region selected by the pBzK criterion is not reached by the undisturbed E-model, but only by post-starburst models with relative early bursts $t_\mathrm{Burst} \lesssim 1.5\,\mathrm{Gyr}$ or $z < 3$. This indicates that a starburst followed by a rapid termination of star formation is required to reach the red (B-z) colours.

In the top panel of Fig. 4.4 we plot the BzK values for a wide range of *dust-free* models of our grid. The green shaded region shows the targeted selection range of BzK > -0.2 and $1.4 \leq z \leq 2.5$ (light green region) and indeed this region overlaps with our model grid. However, there are several regions that only fulfill one of the criteria and hence are either missed by this colour selection or contaminate the clean redshift selection as outliers at lower and higher redshifts. As described above post-starburst models do not fulfill the criterion, but there is significant contamination from higher redshift galaxies at $2.5 \leq z \leq 3.2$ that also fulfill the BzK selection.

The bottom panel of Fig. 4.4 shows the changes ΔBzK incured by adding an intrinsic reddening of $E(B - V) = 0.5$ mag. Changes are small in the target redshift range $1.4 \leq z \leq 2.5$: $-0.1 \lesssim \Delta$BzK $\lesssim 0$. At lower redshift and in particular at higher redshift ΔBzK drops rapidly, causing galaxies to drop out of the BzK selection.
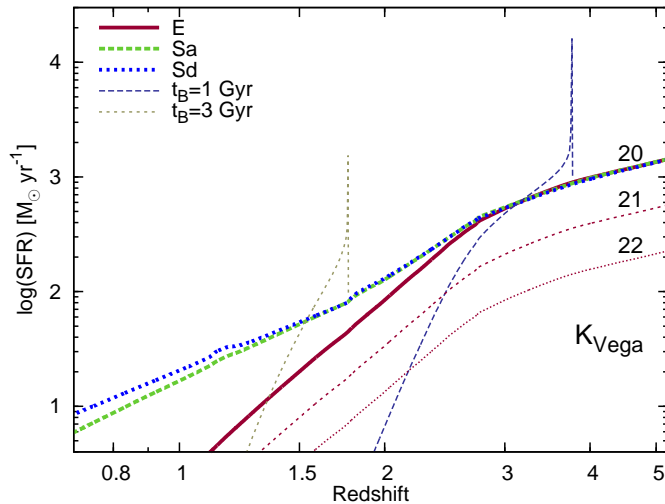
Figure 4.5: Star formation rates of several models from our grid as a function of redshift for *fixed K-band magnitude*, i.e. their masses generally changes with redshift. Most lines are for a K-band magnitude of $K_{Vega} = 20.0 \, mag$, but we also show the E-type model for K-band magnitudes of $K_{Vega} = 21.0 \, mag$ and $K_{Vega} = 22.0 \, mag$ (dotted lines).

4.4.2 Properties of BzK galaxies

Most recent studies of BzK-selected galaxies rely on photometric observations alone so that spectroscopic redshifts exist for only a small sample of galaxies. Daddi et al. (2004) found a median redshift $\langle z \rangle \approx 2.0$ (range $1.4 - 2.5$) from the K20 survey. Reddy et al. (2005) derived $\langle z \rangle = 2.01 \pm 0.33$ and $\langle z \rangle = 1.70 \pm 0.18$ for his sample of sBzKs and pBzKs respectively, and Hayashi et al. (2009) derived redshifts for 15 galaxies from Hα and found values ranging from 1.2 to 2.1 with $\langle z \rangle \approx 1.7$. These results indicate that the BzK selection, although principally selecting galaxies out to $z \lesssim 3$, mostly culls galaxies with $1.4 \leq z \lesssim 2.0$ with fewer candidates at $2.0 \leq z \leq 2.5$. The exact reason for this is not clear yet, but in part is certainly caused by technical difficulties to measure redshifts in the redshift range $2.0 \leq z \leq 2.5$ (see discussion in Hayashi et al., 2009).

Stellar masses and star formation rates as derived from SED fitting and UV luminosities are available for much larger samples, although with significantly differing (mass) completeness limits. Daddi et al. (2004) found stellar masses of $(0.6 - 5.0) \times 10^{11} \, M_\odot$ and a mean SFR of $210 \, M_\odot \, yr^{-1}$ for their sample of 30 galaxies with spectroscopic redshifts. Similar high masses of $\approx 10^{11} \, M_\odot$ and SFRs of a few $10^2 \, M_\odot \, yr^{-1}$ were also found be Daddi et al. (2005, 2008), de Mello et al. (2004), Reddy et al. (2005), and Kong et al. (2006).

In a deeper study (mass completeness down to $10^{10} \, M_\odot$ as compared to $\approx 10^{11} \, M_\odot$ in previous studies), Hayashi et al. (2009) found stellar masses of $(0.6 - 15) \times 10^{10} M_\odot$, but similarly high SFRs of $(50 - 700) \, M_\odot \, yr^{-1}$. The intrinsic reddening in all those cases is significant, with a median values in the range $E(B - V) = 0.2 - 0.5 \, mag$ but reaching up to $E(B - V) = 1.0 \, mag$ in the most extreme cases. All these values are correctly explained by our early type E and Sa models in the respective redshift range $z \approx 2$.

For these models spectroscopically derived metallicities from Hayashi et al. (2009) of $12 + \log(O/H) = 8.2 - 8.9$ confirm results from our models of $12 + \log(O/H) = 8.9$ (E-model) and $12 + \log(O/H) = 8.5$ (Sa). The lower value of $12 + \log(O/H) = 8.2$ (found for the lowest mass galaxy in their sample) is in excellent agreement with predictions of our lower-mass Sb-model.

To allow a more quantitative comparison of these properties we show the SFR of several galaxies from our grid as a function of redshift for a *fixed K-band magnitude* in Fig. 4.5. It is evident that at $z \gtrsim 3$ all models overlap due to their young ages and very active star formation activity. At $z \approx 2$, a model galaxy with $K_{Vega} = 20.0(21.0) \, mag$ has a SFR of $\approx 100(45) \, M_\odot \, yr^{-1}$, in excellent agreement with observational findings. It also confirms the lower star-formation rates found by Hayashi et al. (2009) in their deeper sample. The very sharp and narrow peaks shown in

this Figure are due to bursts in their very early phases, when the SFR reaches its peak, but the optical luminosity as traced by the observed K-band magnitude did not yet have the time to fully develop. These sharp peaks can also explain the finding of a very high SFR object with comparably little mass in Hayashi et al. (2009). Another possible explanation could be a significant underestimation of the stellar mass when a small amount of young stars outshines a much more massive host galaxy as described in Sect. 5.3 of Paper I.

(Kong et al., 2006, their Fig. 12, bottom panels) show a maximum SFR that increases roughly linear with increasing stellar mass, resulting in a roughly constant maximum sSFR of $sSFR_{max} = 5 \times Gyr^{-1}$. Similar values are also found as peak sSFRs for our starburst-models with bursts at $z \approx 2$. This is another piece of evidence that our model grid presented in Paper I gives an excellent description of BzKs over a wide range in redshift and allows to determine a wide range of physical parameters for these objects even without spectroscopy.

4.5 Extremely Red Objects

The advent of the first deep NIR observations revealed the existence of a new population of Extremely Red Objects (EROs; Elston et al., 1988, 1989) that are comparably bright in the NIR, mainly the K-band, but very faint in the optical. Typical colour selection criteria hence are $R - K > 5 - 6$ or $I - K > 4$.

Since their first detection evidence has accumulated that EROs are not one single population, but rather consist of several subpopulations. One possibility to explain their colours are extremely dusty starbursts (Cimatti et al., 1997; Dey et al., 1999; Smith et al., 2001; Smail et al., 2002; Brusa et al., 2002; Nagamine et al., 2005; Stockton et al., 2006) with extinctions reaching $E(B - V) = 0.5 - 1$ mag (Cimatti et al., 2002a; Bergström & Wiklind, 2004; Georgakakis et al., 2006). Other EROs feature evidence for an old underlying population with a continuum break, only little extinction and no ongoing star formation (Soifer et al., 1999; Glassman & Larkin, 2000; Daddi et al., 2000; Cimatti et al., 2002a; Miyazaki et al., 2003; Doherty et al., 2005).

In order to derive accurate photometric redshifts, the template set has to be able to reproduce these two populations. In Fig. 4.6 we present the $R - K$ (upper panel) and $I - K$ (bottom panel) colour evolution of our model grid.

4.5.1 Colour selection

As can be seen from Fig. 4.6 normal undisturbed *and dust-free* models do not reach the extremely red colours to be considered as ERO. However, by adding starbursts followed by an exponentially declining SFR we are able to reproduce the observed extremely red colours even in the absence of dust. The reddest $R - K$ colours are reached around $z \approx 2$, depending on when the burst started. The time delay between the bluest phase at the very onset of the starburst and the reddest colours during the ERO-phase, however, remains roughly constant at ≈ 2 Gyr (in the case of burst decline times of 250 Myr), independent of the time at which the burst starts.

The resulting redshift range in which galaxies undergo an ERO phase is in good agreement with spectroscopic redshifts derived for EROs by Moustakas et al. (2004) and Roche et al. (2006).

4.5.2 Properties of EROs

Fig. 4.6 also shows that whether or not a galaxy reaches ERO colours during its post-starburst evolution mainly depends on how early its burst took place. All starbursts earlier than z = 2.5 easily meet the $R - K > 5$ criterion, only those earlier than z < 3 the $I - K > 4$ threshold. Clearly the redder the colour of an ERO, the higher must have been the redshift when its starburst was
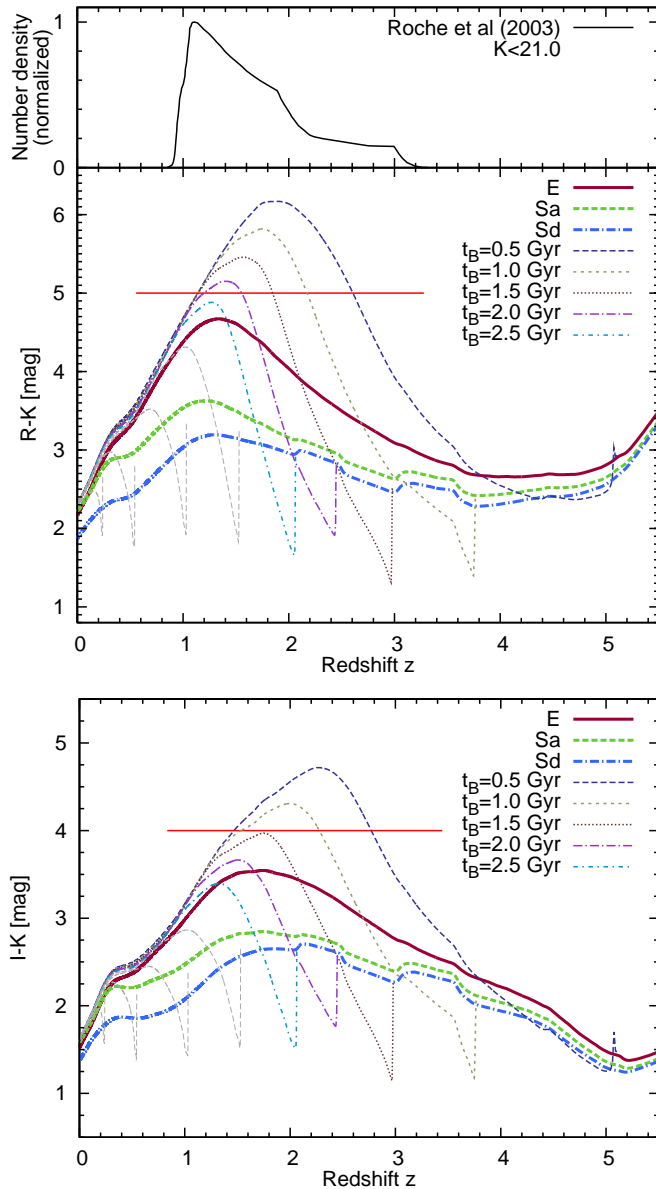
Figure 4.6: Colour evolution with redshift for a representative part of our model grid. Horizontal red lines mark the colour selection criteria for Extremely Red Objects (EROs): $R - K > 5$ (top panel) and $I - K > 4$ (bottom panel). The upper part of the top panel shows the model for the ERO number density as function of redshift from Roche et al. (2003), normalized to a peak-value of one.

triggered. A dust-free ERO with $R - K > 5.5$ or 6 for example must have had its starburst at $z > 3$ or $z > 4$. These (post-)starburst galaxies must have evolved *passive* since then, i.e. over a time span of 1 or 2 Gyr. This implies that the K20 EROs (Cimatti et al., 2002a), which are observed to be very massive at $z \approx 2$ where they are currently observed, must not have accreted any significant amounts of gas to fuel new SF between $z = 3 - 4$ and $z = 2$. At best, they could have increased their mass by dry mergers - if those existed already - during this timespan. This explains the old ages of several Gyrs found by Cimatti et al. (2002a).

The existence of a red post-starburst sequence, i.e. the fact that galaxies in their late post-starburst stages have almost identical colours independent of the beginning of their burst (see. Sect. 5.6 in Paper I) gives a physical explanation for the model of ERO number counts as a function of redshift and K-band magnitude derived on the basis of luminosity functions by Roche et al. (2002, 2003). This model, shown in the very top of Fig. 4.6, shows an increasing number density from $z \approx 3.5$ to a maximum at $z \approx 1.2$ and a sudden drop in the number density of $K < 21$ mag EROs at $z \lesssim 1$. With increasing age of the universe, i.e. decreasing redshift, galaxies are more likely to undergo a starburst that is then followed by an ERO post-starburst phase. The sharp
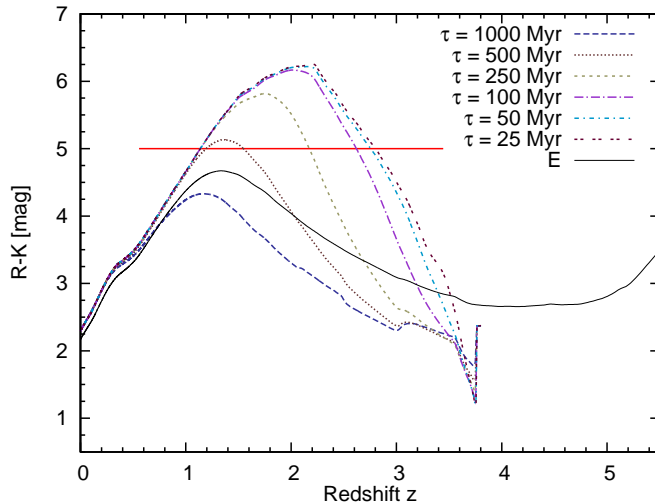
Figure 4.7: Colour evolution of one starburst model with t_{Burst} = 1.0 Gyr ($z_{Burst} \approx 3.8$) for a wide range of exponential decline times from 25 Myr to 1 Gyr. The colour evolution of the undisturbed E-type model is shown for comparison. The red horizontal line marks the ERO selection criterion.

drop at $z \approx 1$ almost perfectly coincides with our red post-starburst sequence dropping out of the ERO selection.

In Fig. 4.7 we present the colour evolution of one particular burst model with a burst occuring at a galaxy age of $t_B = 1$ Gyr, for which we vary the decline time of the burst over a wide range from 25 Myr to 1 Gyr. We find that only bursts with SFR decline times shorter than 500 Myr reach ERO colours.

Particularly noteworthy is the time delay between the onset of the burst and the time when the ERO reaches its reddest colours. For the model with decline time $\tau = 250$ Myr this time span is as long as 1.8 Gyr, while it only takes roughly 1 Gyr for $\tau \leq 100$ Myr. At this time after the burst the galaxy is still in an Hδ-strong phase and would spectroscopically be classified as an a+k or E+A galaxy, depending on nomenclature (Dressler et al. (1999); also see Falkenberg et al. (2009a,b) for more details on the modelling of post-starburst galaxies using **GALEV** models). Observational evidence for this scenario comes from Doherty et al. (2005) who found that $\approx 30\%$ of all EROs are found in this a+k phase. Using our grid of burst models we can therefore successfully explain not only the photometric, but also spectroscopic properties of this interesting galaxy population.

4.5.3 EROs as dusty starbursts

Another possible explanation to the extremely red colours is reddening due to significant amounts of dust within the galaxy. To explore this in greater detail we derived as a lower minimum the reddening that is required to reproduce the colour selection criterion $R - K = 5$ as a function of redshift and underlying galaxy type. The result is shown in Fig. 4.8. While as expected from previous plots post-starburst galaxies do not require any reddening, the required reddening for our elliptical and spiral models at redshifts $z \geq 0.8$ are significant, although not unreasonably high ($E(B - V) \gtrsim 0.1$ and $\gtrsim 0.3$ mag respectively). For our peak-starburst model, however, dust reddenings in excess of 0.5 mag are required to turn the intrinsic very blue colours into the observed red colours.

At low redshifts $z \lesssim 1$ the minimum dust reddening increases very rapidly with decreasing redshifts, reaching values of $E(B - V) > 0.6$ mag for an assumed redshift of $z = 0.3$. We can approximate this redshift dependence of the minimum dust reddening by a simple linear relation:

$$E(B - V)_{min}(z) \quad = \quad 1.00 - 1.62z \quad (0.25 > z) \tag{4.18}$$

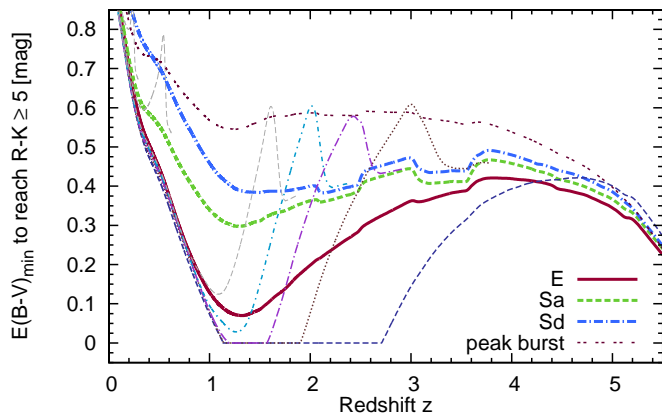$$= \quad 0.75 - 0.69z \quad (0.25 < z < 1.1) \tag{4.19}$$

Figure 4.8: Minimum amount of dust reddening required to produce colours that reach the $R - K > 5$ mag colour selection criterion. Several (post-)starburst are also shown but not included in the caption; for these the identification is identical with the one used in Fig. 4.6.
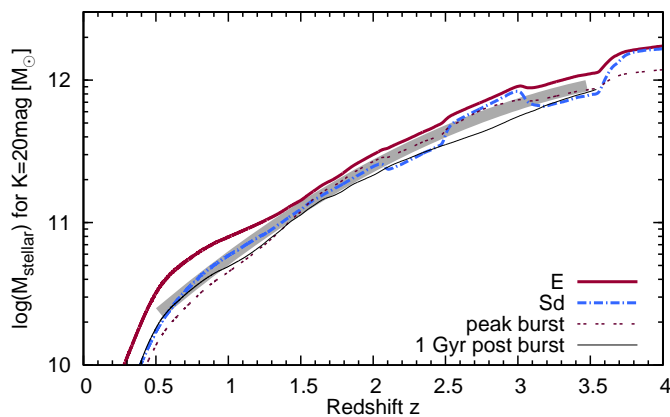

Figure 4.9: Minimum stellar mass that is required to reach an apparent magnitude of $K = 20$ mag. The grey thick line shows a 2nd-order polynomial fit to the models (see text for parameters).

Galaxies that require reddenings near this minimum value need to have the intrinsic red colours of an E or Sa-type model. These galaxies, however, are observed to contain only little gas and therefore only little dust. Local starbursts can harbour enough gas and dust to reach the high reddening factors $E(B - V) \geq 0.6$ at z < 1. We therefore conclude that the observation of ERO-like colours at low redshift is a strong indicator for a dusty and actively star-forming galaxy, while at higher redshift also passively evolving galaxies are likely ERO candidates.

In a next step we now compare the stellar masses that yield an observed K-band magnitude of $K = 20$ mag. The results for several galaxy types as a function of redshift are shown in Fig. 4.9. For all galaxies we require a $R - K$ colour of $R - K > 5$ by adding the amount of dust reddening shown in Fig. 4.8.

A surprising and very important result is that the stellar masses depends very little on galaxy type showing only a very low dispersion of 0.15 dex at redshift z = 1, increasing to 0.3 dex at redshift z = 0.5. This can be used to estimate accurate stellar masses for galaxies with known redshift, independent of the galaxy's star formation history ranging from passive (post-starburst) galaxies to ongoing starbursts. A second-order polynomial fit over the redshift range z = 0.5 − 3.5 provides a good approximation to the model curves:

$$\log\left(M_{stellar}^{ERO}[M_\odot]\right) = 17.89 + 0.97z - 0.11z - 0.4 \times K_{Vega} \qquad (4.20)$$

4.5.4 Discriminating between dusty and passive EROs

One advantage of evolutionary synthesis models such as **GALEV** is that they allow us to search for differences between models with similar observables as in the case of dusty starbursts (DSB)
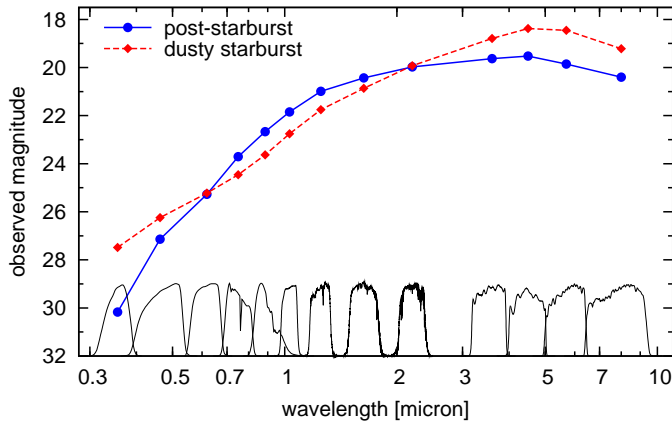
Figure 4.10: Comparison of a dusty starburst SED (red diamonds) and a post-starburst SED (blue circles) at redshift $z = 1.6$, both having identical colours of $r - K = 5.3$ mag and normalized to $K = 20$ mag. The SED is formed by magnitudes in the SDSS ugriz, UKIDSS YJHK and IRAC [3.6],[4.5],[5.7] and [8.0] filters that are shown for reference on the bottom of the plot.

and post-starbursts (PSB) with identical $R - K$ colours. The intrinsic output of **GALEV** are spectra from which we can then generate SEDs in any filter combination. One example is shown in Figure 4.10 where we compare the SEDs of the extreme ERO cases. Shown with blue circles is the full SED of a PSB galaxy with burst onset at a galaxy age of 1.0 Gyr and observed at redshift $z = 1.6$ in a commonly used filter combination of the five SDSS bands ugriz, the UKIDSS YJHK filters in the near-infrared and the four Spitzer-IRAC bands at 3.6 to 8.0μm. As a comparison we show the SED of a DSB at the same redshift, for which we added dust to yield identical colours as the PSB galaxy ($r - K = 5.3$ mag). Both magnitudes have been normalized to the same observed K-band magnitude of $K = 20$ mag to facilitate comparison. Despite their identical $r - K$ colours their overall SEDs look very different: The DSB has a steep overall slope and is very bright in the IRAC bands because dust does not significantly impact the rest-frame NIR observed in these bands. The PSB SED on the other hand is relatively faint in the MIR and has bluer colours than the DSB redwards of the H-band. It is also brighter than the DSB in the i- to H-band. In r- and K-band, both galaxies are, by construction, equally bright. At short wavelengths the PSB is much fainter ($\gtrsim 2$ mag in the u-band) than the DSB, although both galaxies are likely to be unobservable with most current observing facilities.

Although this was just one out of many possible examples it nonetheless demonstrates the capabilities of our **GALEV** models to help predict observable properties. This ultimately allows us to identify and discriminate between rare types of galaxies which otherwise is extremely difficult to do purely based on observations.

4.6 Distant Red Galaxies

4.6.1 Colour selection

In the recent past there has been some controversy in the nomenclature used in the literature. In the following we will adopt the currently most widespread terminology and use the term *Distant Red Galaxies* (DRGs) for galaxies fulfilling the criterion

$$(J - K)_{Vega} > 2.3 \tag{4.21}$$

Franx et al. (2003), van Dokkum et al. (2003, calling them Luminous Red Galaxies).

In the upper part of Fig. 4.11 we show the J-K colour evolution as a function of redshift for several models from our grid. In the ideal case that all galaxies are dust-free at all redshifts only models with early starbursts $t_B \leq 0.7$ Gyr followed by a rapid termination of SF afterwards reach the red $J - K$ colours needed to be considered DRGs.
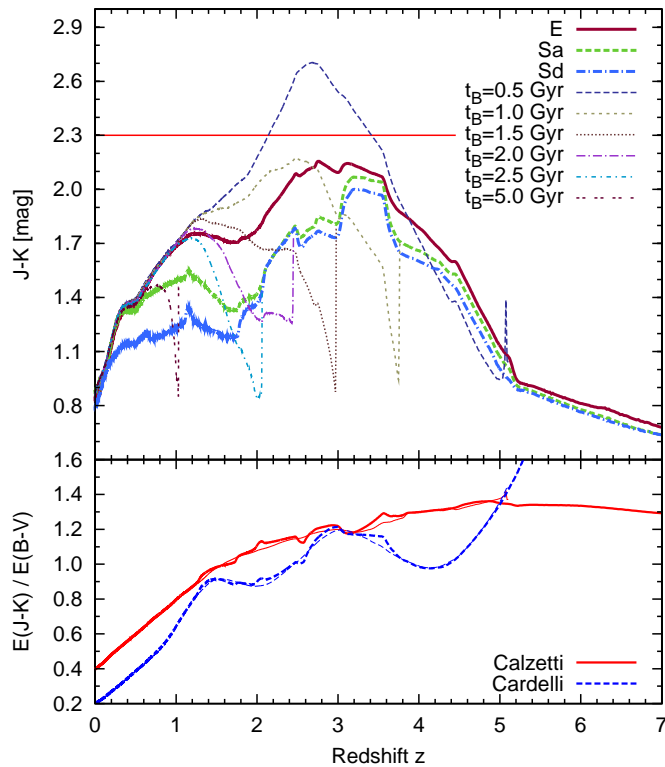
Figure 4.11: Upper part: $(J-K)_{Vega}$ colour evolution of a representative part of our model grid. The solid horizontal marks the selection criterion for Distant Red Galaxies of $J-K \geq 2.3$ mag. Lower part: Extinction ratio $E(J-K)/E(B-V)$ as function of redshift for two different choices of the extinction law.

In the lower part of Fig. 4.11 we also give the ratio of $E(J-K)/E(B-V)$. Over the relevant redshift range $1 \leq z \leq 4$ this ratio has values of $1.0 - 1.2$. Using this ratio we can make a wider range of models reach the required colour criteria of $(J-K) > 2.3$. For our E-type model in the range $2 \leq z \leq 4$ and models with later starbursts ($t_B \approx 1$ Gyr) we require an additional modest dust reddening of $E(J-K) \sim 0.2$ or $E(B-V) \sim 0.17$. Similar amounts of dust ($E(B-V) \sim 0.25$ mag) are needed to bring our spiral models without starburst into the colour range of DRG range for $3.0 \leq z \leq 3.5$. The values for the dust reddening required by our models to meet the colour selection criteria as well as the redshift range we predict for DRGs are in excellent agreement with spectroscopic redshifts presented for several DRGs in Franx et al. (2003, $z = 2.6 \pm 0.7$), van Dokkum et al. (2003, $z = 2.4 - 3.5$), and Quadri et al. (2007b, $z = 2 - 4$).

4.6.2 Physical parameters

Labbé et al. (2005) found that $\sim 3/13$ of their DRG sample are well described by old populations with mean ages of several Gyr and negligible ongoing SF, which we confirm with our post-starburst models. For the spectra of the remainder of their sample galaxies Labbé et al. (2005) obtained good fits with constant SFR models of age ~ 1.2 Gyr with moderate dust reddening $A_V \sim 1.7$ mag, equivalent to $E(B-V) = 0.5$ mag. Förster-Schreiber et al. (2004) and van Dokkum et al. (2004) derived extinctions, mean ages and SFR for a larger sample of ~ 30 DRGs at $z = 2.0 - 3.5$. They found SFR-weighted mean ages between 0.9 and 2.5 Gyr, SFRs of $70 \ldots 170 \, M_\odot \, yr^{-1}$, extinctions of $A_V \sim 1.2$ mag and stellar masses $M_* \sim (1.3 - 4.9) \times 10^{11} M_\odot$. All those results are in excellent agreement with our model predictions, e.g. of our E-type model ($A_V \gtrsim 0.5$ mag to reach the DRG criterion, $M_S(z = 3.5) = 2.6 \times 10^{11} M_\odot$, SFR($z = 3.5$) = $140 \, M_\odot \, yr^{-1}$). Similarly high SFR (few $\times 10^2 \, M_\odot \, yr^{-1}$) were also found by Reddy et al. (2005) and Papovich et al. (2006).

The metallicity of the E-type model at these redshifts ($z \sim 2 - 3$) has already reached values of 2/3 of solar, well within observational uncertainties of a factor 2 around the solar value.
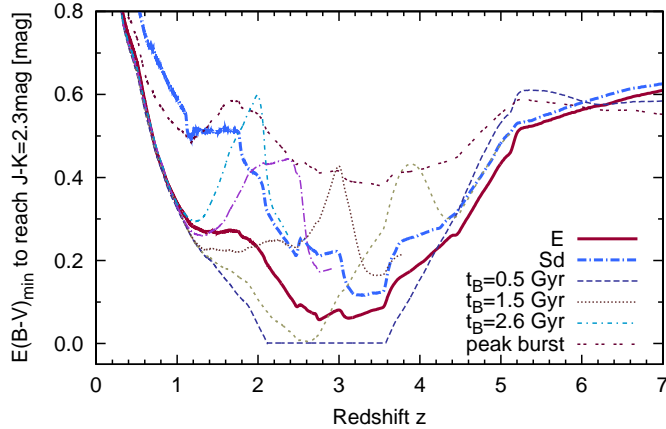
Figure 4.12: Minimum amount of required to reach the red $J - K = 2.3$ mag colour required by the DRG selection criterion.
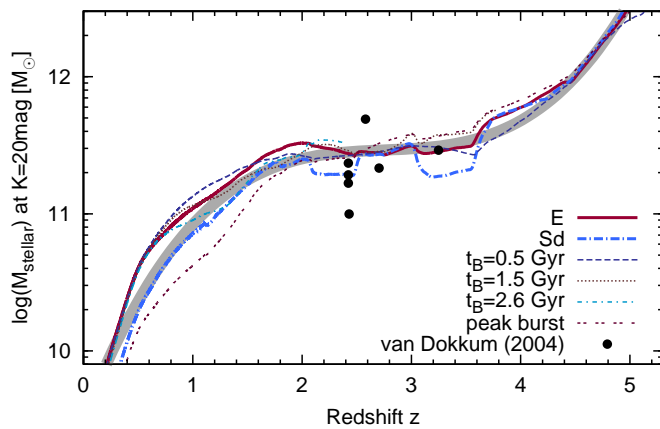

Figure 4.13: Stellar masses of galaxies with $k = 20$ mag and $J - K = 2.3$ mag for different models and, hence, star formation histories. The grey thick line shows a 3rd-order polynomial fit to the models (see text for parameters).

Shapley et al. (2004) studied DRGs and obtained good fits to their spectroscopic data with solar-metallicity models (solar metallicity was derived from optical emission lines available for their sample) with moderate amounts of dust ($E(B - V) = 0.1 - 0.2$) and ages of $1 - 2$ Gyr, in good agreement with the input values of our models.

We conclude that our current model grid is able to reproduce most if not all properties observed so far in the population of DRGs. Our models give a wealth of additional information about DRGs and, in particular, suggest evolutionary links to progenitor and successor galaxy populations. This is beyond the scope of the present paper and will be the topic of a following paper.

4.6.3 DRGs as Dusty Red Galaxies

In analogy to our discussion of EROs above, it is also possible to reproduce colours of DRGs by adding dust to star-forming galaxies. The amount of reddening required to give star forming galaxies colours of a DRG depends on both galaxy type and redshift and is shown in Fig. 4.12. Over the large redshift range z = 1 − 4.5 the amount of reddening is limited to $E(B − V) \lesssim 0.4$ mag for even the peak starburst model. At lower redshift z $\lesssim 0.6$ the required reddening again increases rapidly with decreasing redshift. However, ongoing SF activity in moderately dust-obscured, massive early-type spirals (e.g. Sa-type models) with SFHs in between our Sa and E-type models is a possible way to also explain DRGs at lower redshifts z ~ 1 as found observationally by Grazian et al. (2006) and Conselice et al. (2007).

In Fig. 4.13 we show for a range of models the stellar mass that is required to yield a K-band magnitude of $K = 20$ mag and DRG-like colours of $J − K = 2.3$mag. We find that this stellar

mass is roughly independent of galaxy type and hence of star formation history, showing only a small spread of $0.2 - 0.4$ dex. Even more remarkably, the curve is roughly flat for $z \approx 2 - 4$, allowing for a direct translation of observed K-band magnitudes into stellar masses. We fitted a third-order polynomial function to our models over the redshift range $z = 0.3 - 5.2$ to allow observers to directly get a stellar mass from their observations:

$$\log \left(M_{\text{stellar}}^{\text{DRG}} [M_\odot] \right) = 1.50 + 2.07z - 0.74z^2 + 0.089z^3 - 0.4 \times K_{\text{Vega}} \tag{4.22}$$

4.7 Luminous Red Galaxies

Luminous Red Galaxies are identified with less distant passively evolving galaxies commonly found in the Sloan Digital Sky Survey (SDSS) and in the 2dF Redshift Survey (e.g. Eisenstein et al., 2001; Cannon et al., 2006).

Fig. 4.14 shows observed $g - r$ colours of a large sample of LRGs from the 2dF-SDSS LRG and QSO survey (2SLAQ, Cannon et al., 2006). We overlay these data with the predicted colour evolution of our undisturbed E-type model as well as several of our burst models with bursts starting at galaxy ages of $1.0 - 6.5$ Gyr and fixed-to-solar metallicity. Note that unlike most models presented before we here chose to use solar metallicity instead of half solar metallicity since LRG are the most massive galaxies (Eisenstein et al., 2003; Loh & Strauss, 2006; Wake et al., 2006;
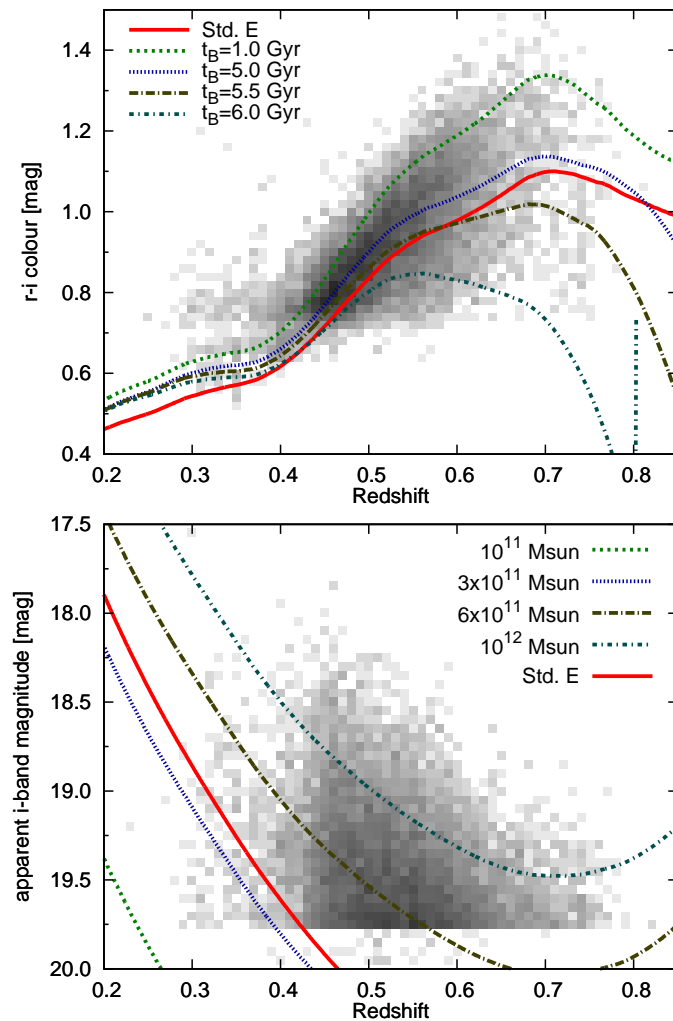
Figure 4.14: Top panel: Comparison of a large sample of observed LRG colours from 2SLAQ (Cannon et al., 2006) overlaid with the colour evolution of our undisturbed E-type model as well as several of our post-starburst models (using *solar* metallicity; models with half solar metallicity are bluer by ≈ 0.07 mag) with burst onset times varying from 1.0 Gyr to 6.5 Gyr. Bottom panel: Predicted apparent i-band magnitudes for a range of stellar masses.
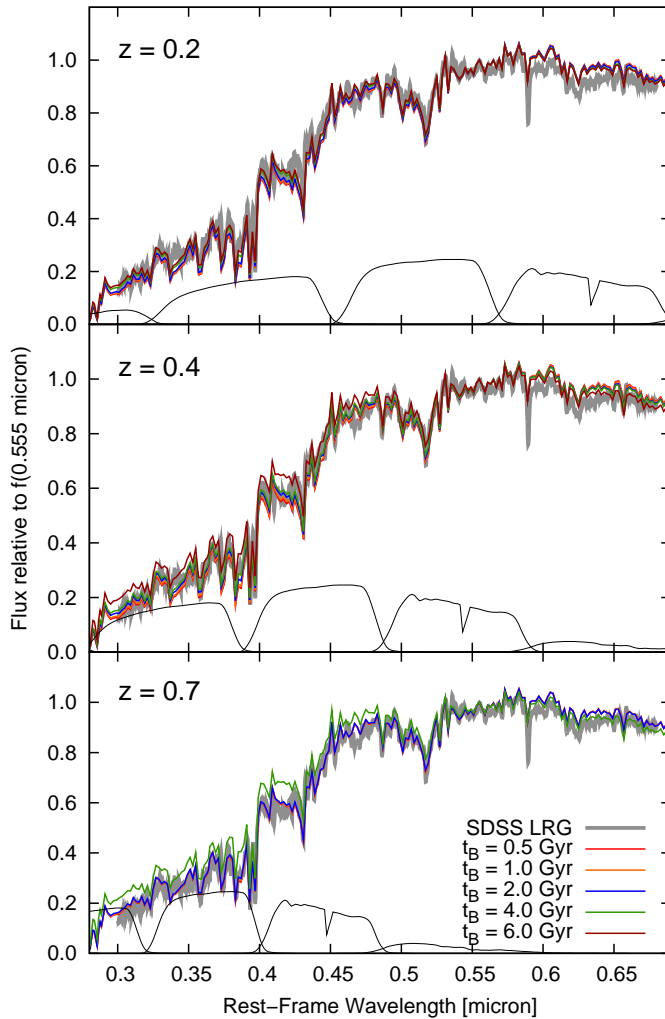
Figure 4.15: Spectra of post-starburst galaxies compared to the SDSS template spectrum for Luminous Red Galaxies (thick solid line). For reference we also show the SDSS ugriz-filters for each redshift.

Ross et al., 2008) and are found at relative low redshifts (e.g. . Cannon et al., 2006). Their high mass is likely to be associated with high metallicities as observed in mass-metallicity relations (Tremonti et al., 2004; Erb et al., 2006a), rendering solar metallicity a more likely assumption than the lower value of half solar.

Fig. 4.14 shows that with our model grid we are able to explain the full range of observed colours over the full redshift range $0.3 \leq z \leq 0.8$. In the lower panel of Fig. 4.14 we overplot observed apparent magnitudes with evolutionary tracks of different masses. It is evident that most LRGs have high stellar masses in the range of $(0.5 - 1.0) \times 10^{12} \, M_\odot$ with the brightest galaxies reaching masses of a few $\times 10^{12} \, M_\odot$, placing them at the bright end of the galaxy mass function. They are hence most likely the progenitors of giant ellipticals or cD galaxies in the local universe. This is also supported from their large correlation length found in numerous clustering studies (e.g. , Eisenstein et al., 2005; Ross et al., 2007; Wake et al., 2008).

In Fig. 4.15 we compare solar-metallicity post-starburst models with different burst onset times ranging from 0.5 Gyr to 6.0 Gyr at three different redshifts $z = 0.2$, $z = 0.4$ and $z = 0.7$ to the SDSS LRG template spectrum[5]. This clearly shows that our model grid is able to successfully explain the overall spectral shape of LRGs at all relevant redshifts.

At moderately high redshifts $z = 0.7$ (and hence beyond the redshift range of the original LRG selection by Eisenstein et al. (2001)) our models predict too high a flux shortwards of

---

[5]The SDSS template spectrum can be obtained from http://www.sdss.org/dr7/algorithms/spectemplates/index.html

5000. The reason for this is that the stellar population formed as a result of the starburst is still too young (the maximum galaxy age at $z = 0.7$ is 6.5 Gyr, assuming a formation redshift of $z_{form} = 8$). However, there is observational evidence for a change in the population of LRGs at these redshifts. In their average spectrum of LRGs at $z = 0.7 - 0.9$, Cool et al. (2008) found emission lines of [O II]3727Å, a strong indicator of SF activity, as well as an increased strength of Balmer absorption lines indicating an intermediate-age population. Both aspects can be naturally explained with our models if we assume a shorter exponential decline time as discussed in the context of EROs in Sect. 4.5. Further evidence for this scenario has been obtained by Eisenstein et al. (2003), Treu et al. (2005), Le Borgne et al. (2006), and Roseboom et al. (2006) who all found convincing evidence for ongoing and/or recent SF activity based on either the detection of [O II]emission lines or strong Balmer absorption lines and the k+a phenomenon, confirming our scenario of LRGs being the remnants of starbursts at higher redshifts.

4.8 Summary and outlook

In the first of these two papers, we generated a large grid of chemically consistent GALEV models of both undisturbed galaxies corresponding in their $z = 0$ properties to E and Sa through Sd as well as galaxies undergoing a strong starburst at some stage during their evolution. In this paper we use this grid to check empirically derived colour selection criteria and to compare model galaxies to observations in terms of physical parameters such as masses, star formation rates and metallicities. Galaxy classes under investigation are Lyman Break Galaxies (classical LBGs as well as BM/BX types), BzK galaxies, Extremely Red Objects, Distant Red Galaxies as well as Luminous Galaxies.

- **Lyman Break Galaxies:** All undisturbed galaxies of our grid fulfill both the classical definition of LBGs at redshifts $z \gtrsim 3$ as well as the lower-redshift BX ($z = 2.0 - 2.5$) and BM ($z = 1.5 - 2.0$) extensions. However, galaxies undergoing an early burst followed by SF truncation quickly become red and hence drop out of this colour selection. In addition to the rest-frame FUV colour selection our model grid correctly describes the rest-frame optical represented by $\mathcal{R} - K$ colours. Based on the shape (colours from U through K) and the normalization (apparent magnitudes as function of redshift) of their SEDs we conclude that LBGs are most likely progenitors of either local elliptical or early-type spiral galaxies, in agreement with observational evidence for massive rotating gas-disks found in some LBGs. For these types our model predictions of LBGs confirm to high accuracy the stellar masses, star formation rates and gas-phase metallicities derived from spectroscopic observations. This agreement provides a solid basis for the interpretation of the bulk of the LBG population *without* spectroscopy.

- **BzK Galaxies:** Our models predict that even galaxies outside the targeted redshift range of $1.4 \leq z \leq 2.5$ are potential BzK galaxies as long as they do not contain significant amounts of dust. Within this range all undisturbed models fulfill the BzK criterion. Our undisturbed E-type model is correctly identified as sBzK, while the pBzK criterion is only fulfilled by post-starburst galaxies. Stellar masses, star formation rates and metallicities as observed by several authors are well matched by our E- and Sa-type models with contributions by later spiral types at fainter magnitudes. Objects with low masses but high SFRs are well matched to our burst models. The maximum burst strength as found in Paper I furthermore explains the clear upper limit found for SFRs as a function of stellar mass.

- **Extremely Red Objects:** Galaxy models with early bursts reach colours in their post-starburst phases that are typically found in Extremely Red Objects without requiring any dust reddening in the redshift range $z \approx 1 \ldots 3$. If the decline time of the burst is sufficiently short ($\tau \lesssim 200$ Myr) the galaxy spectra are similar to E+A spectra characterized by strong Balmer absorption features, in excellent agreement with observations in $\approx 30\%$ of all ERO galaxies. This is the first time that these features are described by evolutionary

synthesis models and confirms the general applicability of our model grid. There is a correlation between maximum redness to increase with decreasing galaxy age at the onset of the burst, potentially allowing indirect insight into the merger rates at redshifts $z = 2 - 5$. Our derived colour evolution with redshift furthermore offers a physical explanation for the observed ERO number density evolution.

- **Distant Red Galaxies:** Depending on the amount of intrinsic dust reddening, our models can explain Distant Red Galaxies (DRG) with z $\approx 1.5\ldots 4$ by either dust-free post-starburst models with very early burst or by star-forming galaxies with small amounts of dust, in agreement with observations. DRG at lower redshifts require increasing amounts of dust to fulfill the DRG colour selection criterion and hence dusty starbursts are probably no DRG candidates. Based on a detailed comparison of model predictions with observed masses, metallicities and star formation rates we conclude that DRGs are most likely the progenitor of local ellipticals.

- **Luminous Red Galaxies:** Luminous Red Galaxies (LRGs) form a naturally extension of DRGs towards lower redshifts. Low-redshift LRGs (z $\lesssim 0.5$) are well described by our post-starburst models if the burst age is ≥ 2 Gyrs. Higher redshift post-starburst models in the redshift range z $\approx 0.7 - 1$ are intrinsically bluer than models at lower redshift, fitting well with observational evidence for recent star formation in LRGs at these redshifts. Our model grid correctly predicts the colour evolution of LRGs over the redshift range $0.3 - 0.8$. From their observed magnitudes we derive masses of $(0.5 - 1) \times 10^{12}$ M$_\odot$, in the range of the most massive galaxies observed locally and hence likely progenitors of giant ellipticals and cD galaxies, in agreement with results derived from their clustering properties.

Based on these encouraging results from this first comparison of our model grid with observed galaxies in these different classes we will next combine the grid of models presented here with our new photometric redshift code GAZELLE to study a large sample of galaxies from a number of deep fields on a galaxy by galaxy basis. This will give us not only accurate redshifts, but also a wealth of physical parameters for a large number of galaxies over a range of redshifts, granting us a deeper insight into galaxy formation and evolution.

Impact of sub-solar metallicities on photometric redshifts

Ralf Kotulla and Uta Fritze

Abstract:

With the advent of deep photometric surveys the use of photometric redshifts, obtained with a variety of techniques, has become more and more widespread. Giving access to galaxies with a wide range of luminosities out to high redshifts, these surveys include many faint galaxies with significantly sub-solar metallicities.

We use our chemically consistent galaxy evolutionary synthesis code GALEV to produce a large grid of template Spectral Energy Distributions (**SED**s) for galaxies of spectral types E and Sa through Sd – one accounting in a chemically consistent way for the increasing initial metallicities of successive stellar generations, the other one for exclusively solar metallicities – for comparison.

We use our new photometric redshift code GAZELLE based on the comparison of observed and model SEDs. Comparing the photometric redshifts obtained using solar-metallicity templates when working on a catalogue of artificially created chemically consistent SEDs, typical for low-metallicity local late-type galaxies and for intrinsically low-luminosity, and hence low-metallicity, galaxies in the high-redshift universe, we find a significant bias resulting from this metallicity mismatch. This bias consists in a systematic underestimate of the photometric redshift by typically $\Delta z \approx 0.1 \dots 0.2$ until $z \approx 1.2$, depending on galaxy type, of distant, faint and low-metallicity galaxies if analysed with solar-metallicity templates.

5.1 Introduction

Most of today's studies of large samples of high-redshift galaxies rely on photometric redshifts comparing observed spectral energy distributions (SEDs), i.e. magnitudes and colours in multiple filters, to a set of templates. For that reason the choice of the right set of template is crucial to determine accurate and unbiased photometric redshifts. The most widely used templates are either observed local templates, e.g. from Coleman et al. (1980), that do not including any evolutionary correction, or templates generated with evolutionary synthesis models which in most cases use fixed solar metallicities.

During the last years, evidence has accumulated that galaxies are not made out of stars of one metallicity, but show a wide range from very metal-poor to more metal-rich stars. This holds true not only for our Milky Way (Rocha-Pinto & Maciel, 1998b; Ak et al., 2007), but also for external galaxies like e.g. the LMC (Cole et al., 2000a) and giant ellipticals like NGC5128 (= Centaurus A, Harris et al., 1999; Harris & Harris, 2000).

Studying samples of local star forming galaxies Skillman et al. (1989) showed a trend of decreasing average metallicity of a galaxy with decreasing luminosity, used as an indicator of its mass, and spanning more than 12 magnitudes in luminosity. Larger samples, compiled e.g. from the SDSS (Tremonti et al., 2004; Kewley & Ellison, 2008) confirmed this mass-metallicity relation and extended it to even lower masses (Lee et al., 2006).

This is particularly important with respect to high redshift galaxies in the early universe, since those galaxies did not yet have the time to produce enough stars to enrich their ISM to high metallicities. Studies of Lyman Break Galaxies (Pettini et al., 2001), Damped Lyman-α Absorbers (Prochaska et al., 2003) and Gamma Ray Bursts (Prochaska et al., 2007) all show that galaxies get progressively more metal-poor if they are observed at high redshift. Furthermore dwarf galaxies, such as the LMC, that are metal-poor in the local universe, are observable out to considerable redshifts in deep imaging surveys. Note that Erb et al. (2006a) found a mass-metallicity relation for galaxies at redshifts of $z \approx 2$, confirming that the local trend was already established in the early universe.

For that reason evolutionary synthesis models that take the chemical enrichment of successive stellar generations into account are principally superior to more simplified models with fixed metallicity. In Bicker et al. (2004) we showed that with appropriate star formation histories (SFHs) our chemically consistent GALEV models agree well with a wealth of observed properties for local and high-redshift galaxies and showed how the presently observed stellar metallicity distributions in galaxies have evolved. In Bicker & Fritze (2005) we demonstrated the impact on non-solar metallicities on the determination of star formation rates (SFRs) from emission lines and UV-fluxes. Kodama et al. (1999) have shown that metallicities can have a significant impact on observed colours of high-redshift galaxies; the impact of metallicity on restframe colours was studied by other authors. However, the impact of those generally bluer colours on photometric redshifts has not been studied so far. In the present Letter we quantify the impact of neglecting those sub-solar metallicities on photometric redshifts.

5.2 Creation of template SEDs

5.2.1 Input models

To study the chemical enrichment history of the common spectral galaxy types E and Sa through Sd we used our chemically consistent galaxy evolution code GALEV. Assuming a closed-box model, GALEV allows us to compute the chemical enrichment of a galaxy's gas-reservoir from the yields of dying stars. We use isochrones from the Padova-group (Bertelli et al., 1994) with metallicities ranging from $[Fe/H] = -1.7$ to $[Fe/H] = +0.3$ and a Salpeter-IMF (Salpeter, 1955)

with mass-limits of $0.10\,M_\odot$ and $100\,M_\odot$. Note that a different choice of the IMF, e.g. Kroupa or Chabrier, does not affect the results obtained below. The spectral galaxy types are characterized by an exponentially declining SFR for the E-model, SFRs proportional to the available gas-mass for the Sa-Sc models (with factors of proportionality decreasing towards later types), and a constant SFR scenario for the Sd. These SFHs were shown to provide a good match to today's galaxy templates, e.g. from Kennicutt (1992) in Bicker et al. (2004). To derive the effects on photometric redshifts we also ran all those models again, this time fixing the metallicity to the solar value $[Fe/H] = 0.0$. Our GALEV models also include line and continuum emission from ionized gas, with line strength appropriate for the particular gaseous metallicity at each time. The importance of emission lines for accurate photometric redshifts has recently been shown by Ilbert et al. (2009).

To derive the SEDs for comparison with observations, we redshifted the spectra at all timesteps to the redshift corresponding to the age of each galaxy spectrum, adopting a concordance cosmology with $H_0 = 70\,km\,s^{-1}\,Mpc^{-1}$, $\Omega_m = 0.30$ and $\Omega_\Lambda = 0.70$. We assume that all galaxies started forming stars at $z = 8$. Variations of this formation redshift with spectral type, as e.g. suggested by Noeske et al. (2007b,a) for the latest spectral types has little effect on the present study since those show little evolution anyway. This means we consistently account for both evolutionary and cosmological corrections. Since some galaxies at high-redshifts are found to contain significant amounts of dust (e.g. Steidel et al., 1999), we convolve each spectrum with the dust attenuation curve of Calzetti et al. (2000). We chose a range of extinctions from $E(B-V) = 0.0\,mag$ to $E(B-V) = 0.5\,mag$ in steps of $\Delta E(B-V) = 0.05\,mag$. We include the effects of intergalactic absorption following Madau (1995) and then convolve each spectrum with a set of typical filters, here taken to be the SDSS ugriz and the standard 2MASS JHK filters. Galaxies were normalized as to show by z=0 the average observed Johnson B-band magnitudes for their respective types as given by Sandage et al. (1985a,b). We then added the bolometric distance modulus for each redshift. This results in a total of ≈ 3200 template SEDs with smaller redshift intervals at lower z and wider sampling at high redshifts for each of our ten models (5 types E, Sa-Sd, all chemically consistent and with metallicity fixed to solar for comparison).

5.2.2 Addition of noise

To simulate real observations, we added Gaussian noise observational errors to each magnitude. The amount of scatter added, Δm_i, depends on the magnitude m_i of the i-th filter:

$$\Delta m_i = a + b \times \exp(c \times m_i - d),$$

with $a = 0.03\,mag$ describing calibration or zeropoint uncertainties, $b = 3.75$ and $c = 0.75$ being constants defining the shape of the curve. d depends on the depth of the underlying observations, here chosen to correspond to 5σ limiting AB magnitudes of (26,27,27,27,26,25,25,24) mag for the (u,g,r,i,z,J,H,K) filters. This procedure was repeated $100\times$ for each input SED, resulting in an artificially created input catalog of $\approx 7 \times 10^5$ galaxies for each model. For the following analysis we then derived median values and 1σ-uncertainties in bins of $\Delta z = 0.05$.

5.2.3 Determining photometric redshifts

To derive the photometric redshifts we use our photometric redshift code GAZELLE described in more details in a companion paper (XXX missing reference XXX, 2035). In principle it uses a χ^2-algorithm to compare fluxes derived from the observed SEDs with a range of template SEDs. The resulting χ^2-values are then transformed into normalized probabilities. Masses are derived by scaling the model SEDs as a whole to match the observed SED on average. To determine 1σ-uncertainties for redshifts and all dependent parameters (masses, SFRs, metallicities, etc.) we derive the minimum and maximum values encountered while summing up normalized probabilities (from highest to lowest) until $68\,\%$ have been reached. We restrict our template set to

only undisturbed galaxies E, and Sa through Sd, since those are well calibrated against observed galaxy templates, and match observations in colours, spectra and metallicities (see Bicker et al., 2004; Kotulla et al., 2008b, for a detailed comparison).

In the following, we will focus on the redshift determination and the best-match χ^2-value.

5.3 Results

5.3.1 Evolution of metallicity with redshift

In Fig. 5.1 we present the metallicity evolution of the different spectral galaxy types E, Sa, and Sd with decreasing redshift. We show two different metallicity measures: The gas-phase or ISM metallicity and the luminosity-weighted stellar metallicity in a set of different rest-frame filters. The ISM metallicity is traditionally measured from emission lines, while stellar metallicities are derived from stellar absorption lines, as e.g. Lick indices (e.g. Trager et al., 1998; Schiavon et al., 2006), requiring spectra of much higher signal-to-noise ratio. Our models yield metallicities at $z = 0$ of $Z_E = Z_\odot$, $Z_{Sa} = 1.5\,Z_\odot$ and $Z_{Sd} = 0.25\,Z_\odot$, in good agreement with observed metallicities, e.g. from Zaritsky et al. (1994).

The most important point with respect to this paper, however, is that only the E and Sa models reach enrichment levels comparable to solar metallicity. Later spiral types, i.e. the Sb-Sd models only reach significantly sub-solar metallicities after a Hubble time, rendering the assumption of solar metallicity independent of redshift and galaxy type invalid. While solar metallicity is a moderately good approximation ($Z(t) > 0.5\,Z_\odot$) for early-type galaxies (E to Sa) back to fairly young ages or high redshifts, it becomes less and less valid for later galaxy types, in particular at earlier times or higher redshifts.

Low-metallicity stellar populations are brighter in the optical and UV (cf. Fig. 5.2), have bluer colours (since their stars are hotter) and produce more ionizing photons compared to their equal-mass solar metallicity counterparts. This leads to higher emission line fluxes and hence an over-estimation of SFRs by up to factors ≥ 2 (Bicker & Fritze, 2005) if solar-metallicity calibrations
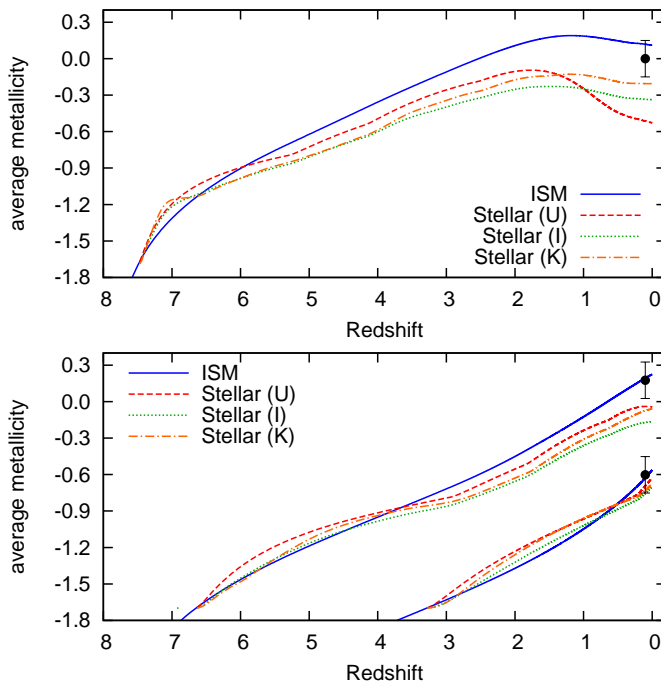
Figure 5.1: Chemical enrichment histories for galaxies of different spectral types E (top panel), Sa (lower panel, upper curves) and Sd (lower panel, lower curves). The blue solid lines marks the gas-phase or ISM-metallicity, while the dashed lines represent luminosity-weighted stellar metallicities in different bandpasses. Black points mark observed metallicities (Zaritsky et al., 1994) of local galaxies.
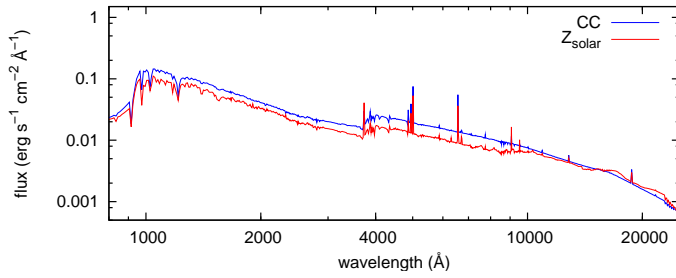
Figure 5.2: Spectrum of a 4 Gyr old constant star formation rate model (Sd) calculated in the chemically consistent way (upper blue curve) and the fixed solar metallicity only way (lower red curve), both having identical masses.

are used. At the same time, their higher overall luminosities lead to overestimations of galaxy masses by factors up to ≥ 5 and their bluer colors lead to an underestimation of their stellar population ages by factors up to ≥ 2, unless their sub-solar metallicities are properly taken into account.

5.3.2 Impact on photometric redshifts

We ran three different sets of photometric redshift determinations, comparing **(a)** the solar metallicity SED catalog to solar metallicity SED templates, **(b)** the chemically consistent (CC) SED catalog to CC SED templates, and **(c)** analysing the CC SED catalog using solar metallicity SED templates. The outcomes of runs a) and b) are shown by the green and blue lines and symbols in Figures 7.3 and 5.4; every datapoint represent the median-value in bins of $\Delta z = 0.05$ in redshift. As expected, we find very small χ^2-values for the best match and excellent correspondence between true and photometric redshifts. The third run analyzing the CC catalog with solar metallicity templates mimics the wide-spread analysis method for observation of low-metallicity galaxies in the early universe using close-to-solar metallicity SED templates. Those can either be locally observed galaxies that naturally have higher metallicities than their high-redshift counterparts, training sets of galaxies with available spectroscopic redshifts (and hence the brightest and with the mass-metallicity relation also most metal-rich galaxies at each redshift) or solar metallicity model templates. The result are shown as red symbols in both figures. As expected, the best-match χ^2/DOF-values (where degrees-of-freedom (DOF) means the number of filters) for run **(c)** are significantly larger at almost all redshifts. The trend towards smaller χ^2 values at higher redshifts can be understood as a consequence of photometric uncertainties increasing with decreasing brightness and finally a decreasing number of filters due to dropouts and magnitudes falling below the detection limit. This in turn allows more flexible matching by varying both shape, determined by galaxy type, redshift and extinction, and normalisation, i.e. galaxy mass, of the template SED.

Fig. 5.4 shows the offsets between true and retrieved photometric redshifts that result from the choice of templates not matching the observed metallicities. We also show the 1σ regions for each galaxy type as filled regions. It is obvious that even for the near-solar metallicity galaxy types E and Sa there are still significant offsets of $\Delta z = z_{\mathrm{phot}} - z_{\mathrm{spec}} \approx -0.1$ (equivalent to $\sigma_z = \Delta z/(1+z) \geq -0.05$) until $z \approx 1.2$. At higher redshifts $z = 1.5 \ldots 2.8$ we also find a bias but this is less prominent than at lower redshifts, in particular compared to the increased scatter at those redshifts. At even higher redshifts $z \gtrsim 3$ dropouts start to dominate the redshift determination. The reason for these biases is that although the metallicity is near solar for the early types E and Sa, the galaxy nevertheless contains a large fraction of lower metallicity stars (e.g. $\approx 2/3$ of the U-band flux of nearby elliptical galaxies is emitted by stars with $[\mathrm{Fe/H}] \leq -0.7$; Bicker et al. 2004). As a general trend, the retrieved photometric redshifts show a bias towards lower redshifts. This trend can be understood from the bluer SEDs of the CC-models, generated by the lower metallicity stars, that the photometric redshift code tries to compensate for by attributing lower redshifts to its $Z_\odot$ templates. This offset is, in particular at low redshifts $z \leq 1$, larger than the typical scatter of $\mathrm{\oe}_z \leq 0.03$ found for large samples of photometric redshifts (e.g. Mobasher et al., 2007).
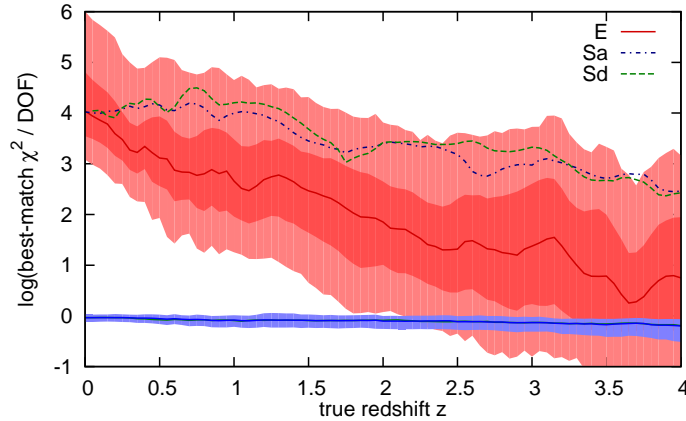
Figure 5.3: χ^2-value per degree of freedom (DOF) of best-matching galaxy-template combination as function of redshift for three different galaxy types E (solid, red line), Sa (blue dash-dotted line) and Sd (green dashed line). In all three cases we used solar-metallicity templates and chemically consistent input galaxies. Dark and light red shaded regions mark the 1σ and 3σ ranges for the E-type model. The blue shaded region marks the outcome of the matched template runs (solar vs. solar and CC vs. CC).

Furthermore, the amount of dust reddening also plays a role in the following sense: essentially dust-free models with $E(B-V) < 0.1\,\text{mag}$ have larger best-match χ^2 values and are more strongly biased towards too low redshifts than models with more dust, reaching a maximum for the Sd-type galaxy at $z \approx 0.4$ where $\Delta z = -0.2$ or equivalently $\sigma_z = 0.14$ (see dahed lines in Fig. 5.4). This point is particularly crucial at $z \gtrsim 1$ where we essentially observe the rest-frame UV. We here are biased towards UV-bright objects, i.e. those that are *not* hidden behind large amounts of dust. Photometric redshifts obtained by fitting solar-metallicity templates to those galaxies are therefore even more strongly biased towards too low redshifts than the median of all extinctions presented above.

Observational evidence for the bias described here can be found e.g. in Ilbert et al. (2006, Fig.3). There observed templates were used to derive photometric redshifts from a filter set similar to the one used here, and a underestimation until z $\approx$ 0.6 and in particular at $z_{\text{phot}} = 0.3, z_{\text{spec}} = 0.4$ was found.

5.4 Conclusions and summary

We used our chemically consistent galaxy evolutionary synthesis models GALEV to study the chemical enrichment histories of galaxies over a range of spectral types E and Sa through Sd. The E-type galaxy reaches enrichment levels of $Z > 0.5\,Z_\odot$ already at high redshifts $z \approx 4$ and remains almost from there on. Sa-type galaxies are significantly sub-solar at $z \gtrsim 1.5$, while later types such as Sd even after a Hubble time only reach levels of $1/4\,Z_\odot$.

This fact, in combination with observational evidence for a wide range in stellar metallicities of our and nearby galaxies and the decreasing stellar metallicities in galaxies at higher redshifts casts doubt on widespread methods of using only solar-metallicity templates to derive photometric redshifts from observed spectral energy distributions. We study the impact of the increasing importance of sub-solar metallicity populations in high-redshift galaxies on photometric redshift determinations using our photometric redshift code GAZELLE on several large synthetic galaxy catalogs and find a significant bias of $\Delta z \approx 0.1$ for galaxies at $z \leq 1.2$ towards systematically underestimated photometric redshifts as a consequence of their bluer SEDs.
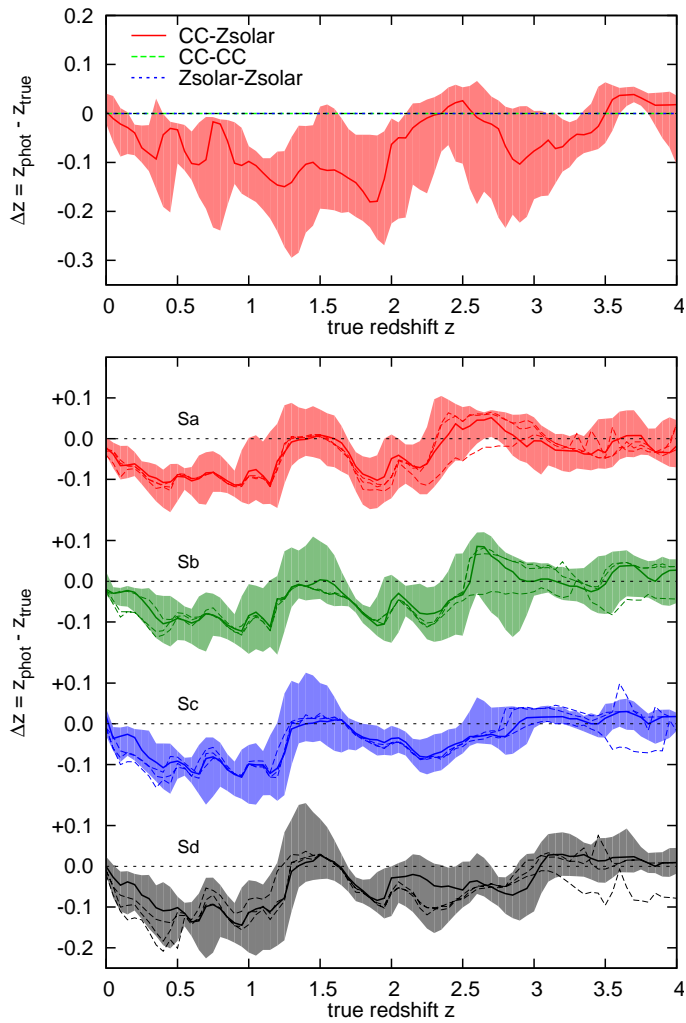
Figure 5.4: Redshift offset $\Delta z = z_{phot} - z_{true}$ for the elliptical (top panel) and spirals Sa, Sb, Sc, and Sd (lower panel). In the top panel, blue and green lines are for matching combinations, red symbols show the errors resulting from the use of solar metallicity templates for the analysis of lower metallicity galaxies. Each point represents the median value in a bin of width $\Delta z = 0.05$. The dashed lines in the lower panels show the bias for $E(B-V) \leq 0.1\,\mathrm{mag}$.

Galaxies to the redshift desert and beyond
The photometric redshift code GAZELLE and its application to a large number of deepfields

Ralf Kotulla

6.1 Introduction

Something about the history of photo-z

Different methods: Neural nets, training sets, template codes

Downside: No physical parameters or interpretation (because interpolation), no errors, no evolution in the templates

6.1.1 Why yet another photometric redshift code?

Despite the wealth of publicly available redshift codes such as HYPERZ (Bolzonella et al., 2000), BPZ (Benítez, 2000), ANNz (Collister & Lahav, 2004), ZEBRA (Feldmann et al., 2006), LePhare (Arnouts et al., 2002; Ilbert et al., 2006), EAZY (Brammer et al., 2008) to just name the more common ones we decided to create yet another one, which we called **GAZELLE** . The difference to the other codes are the used template set on the one side and an additional SED fitting functionality on the other hand.

The template set we use is based on **GALEV** models. They contain a full suite of emission lines that are calibrated to closely match observed line-ratios and hence allow for an accurate modelling of actively star forming galaxies, in particular of low-mass and hence low-metallicity systems. In addition to this line emission we also include continuum emission, that contribute significantly to the near-infrared luminosity of young stellar populations, but also affect the UV and blue spectral range in that they alter the strength of the Balmer break, and consequently impact on the stellar population ages inferred from the strength of this break.

Our template set furthermore contains the full spectral and chemical evolution of galaxies from the onset of star formation in the early universe until the present day. This naturally accounts for all observed stages of galaxy evolution, from the undisturbed evolution of isolated galaxies to starbursts and in particular the post-starburst phenomena in galaxies undergoing interactions with one or more nearby companions. On top of that, isolated galaxies are modeled chemically consistently, i.e. fully accounting for the increasing initial abundances of subsequently formed stellar populations.

To make best use of the wealth of information contained within these models, **GAZELLE** not only derives a photometric redshift for each galaxies, but rather physical properties such as masses, star formation rates, galaxy types, stellar population ages, etc. It therefore combines the functionality of a photo-z code with that of a fully eqipped SED fitting code in a self-consistent way, using identical templates and hence fully accounting for all involved and often mutually dependent uncertainties.

6.2 The photometric redshift code gazelle

To make best use of the wealth of information supplied by our **GALEV** models (Anders & Fritze, 2003; Bicker et al., 2004; Kotulla et al., 2009), we developed a new and innovative photometric redshift code that we named **GAZELLE** . Its working is described below.

6.2.1 The object photometry catalog: Required and optional information

As in most other photometric redshift codes the first processing step is to read the input catalog. This input catalog contains **a)** an arbitrary number of columns (the number can be specified via the configuration file) that allow to identify each individual galaxy, e.g. catalog numbers, coordinates, etc.; **b)** the galaxy photometry, either as measured fluxes or magnitudes. Each

photometric datapoint needs to be followed by its uncertainty, either expressed as flux error, magnitude error or signal-to-noise ratio.

After reading this input catalog, **GAZELLE** compares each input photometry against the detection limit of the respective filter. Detected magnitudes below the specified detection limit get flagged as suspicious, and non-detections in one or more filters for an otherwise detected object are also flagged depending on whether they lie outside the observed field-of-view (usually indicated by a magnitude of -99 mag) or unobserved because they are too faint (magnitudes of $+99$ mag). The reason for this flagging is detailed in Sect. 6.2.4. The format of this file hence is largely compatible with the requirements of the other codes to allow for easier inter-comparison of different codes.

6.2.2 The template set: Galaxy models including spectroscopic and chemical evolution

As mentioned earlier the major improvement of **GAZELLE** compared to all previous photometric redshift codes is that as comparison templates we use models that include the full spectroscopic and chemical evolution from the onset of star formation shortly after the Big Bang until the present day. For this reason it was inefficient to input the full spectra into **GAZELLE** and convolve them with the filter curves on-the-fly. Instead we decided to do this computational expensive process beforehand and use spectral energy distributions, apparent magnitudes in each of the specified filters that are generated by our **GALEV** models, as principle input into **GAZELLE** . These SEDs, one for each of the redshift range corresponding to the time-steps of our models, include both k- and e-corrections as well as the attenuation due to intergalactic neutral hydrogen clouds as shortly described above and in more detail in Kotulla et al. (2009). Supplementary input such as dust extinction for each filter as function of redshift (the SED-equivalent to extinction curves) as well as physical parameters (masses, star formation rates, metallicities, etc.) computed by **GALEV** are also read from their individual files and internally merged into a final catalog of SEDs and physical parameters.

6.2.3 The algorithm

The algorithm of **GAZELLE** is based upon a slightly modified χ^2 minimisation algorithm. For each (observed SED)-(model SED) combination we derive a χ^2 value by

$$\chi^2 = \sum_{i=1}^{\#\text{filters}} \left[w_i \frac{F^i_{\text{model}} - \alpha \times F^i_{\text{obs}}}{\sigma_i} \right]^2 , \tag{6.23}$$

where F^i_{model} and F^i_{obs} are the fluxes in the i-th filter from the model grid and the observations, respectively. σ_i, the uncertainty of this SED point is given by

$$\sigma_i = \sqrt{\sigma^2_{i,\text{obs}} + \sigma^2_{i,\text{model}}}, \tag{6.24}$$

where $\sigma_{i,\text{obs}}$ is the uncertainty of the observation, i.e. photometric errors. The additional term $\sigma_{i,\text{model}}$ represents uncertainties of the models to account for variations among galaxies of identical spectral types as well as uncertainties propagated from the modelling process, such as uncertainties in our knowledge of the Initial Mass Function, stellar evolution, incomplete stellar libraries, changes in metallicity due to gas infall or outflows, etc. (see Conroy et al., 2008, 2009, for more details on uncertainties of population synthesis models). We typically assume a model uncertainty of 0.1 mag independent of wavelength, although a wavelength-dependent parametrisation is supported by **GAZELLE** . The exact value for the model uncertainty is not crucial in the sense that it does not significantly affect the best-match solution; it does however influence the confidence ranges, with smaller model uncertainty ranges resulting in more

closely confined solutions. The inclusion of this additional error term was already successfully implemented by, e.g. , Anders et al. (2004a) and Brammer et al. (2008).

One crucial parameter in eq. 6.23 is the scaling parameter α. This parameter directly influences the resulting mass and all dependent parameters such as star formation rates of the galaxy by scaling all luminosities with the same factor to match the average observed luminosity. The α parameter is computed by

$$\alpha = \frac{\sum_i w_i F_{\text{model}}^i}{\sum_i w_i F_{\text{obs}}^i}, \tag{6.25}$$

where w_i is a weighting factor. Unlike most χ^2 algorithms we offer, in addition to the normal weighting with all $w_i = 1$ the possibility to use $w_i = \sigma_{i,obs}^2$ in anticipation of the upcoming χ^2 computation. Tests comparing both methods showed that this alternative method yields slightly better results, in particular in cases where different filters are observed to very different depths with consequently very different photometric uncertainties.

Another crucial step on the way to accurate redshifts is the determination of the intrinsic reddening, since this is able to dramatically change both the shape and the normalisation of the SED. To find the minimum χ^2 value for one particular (observed SED)-(model SED) combination as a function of reddening we implemented a golden section search to sparsely scan the allowed reddening range and confine the best solution to within a small range (typically $\Delta E(B-V) \leq 0.05$ mag) of the optimum. In a last step we fit a parabola to the points near the minimum to obtain the final, best-match value.

For a typical run, each model in the comparison grid contains ≈ 800 SEDs, covering the redshift range $z = 0 - 8$ in steps of 0.01. For each galaxy we scan the full grid, i.e. we compute χ^2 values for every SED of every model.

Once all χ^2 values for each possible (observed SED)-(model SED) combination has been computed we derive raw probabilities for each SED by

$$P_{\text{raw}} = \exp\left(\frac{-\chi^2}{2}\right), \tag{6.26}$$

and, in a next step normalise all raw probabilities P_{raw}^j to yield

$$P_{\text{norm}}^j = \frac{P_{\text{raw}}^j}{\sum P_{\text{raw}}^j \times \Delta z^j} \tag{6.27}$$

with P_{norm} fulfilling the condition

$$\sum P_{\text{norm}}(z) \times \Delta z(z) = 1. \tag{6.28}$$

$\Delta z(z)$ is the width of the redshift interval corresponding to this SED point. This is necessary as consequence of a potentially inhomogenous redshift sampling of our model. Optionally we offer the possibility to first normalise all χ^2 to yield $\chi_{\text{min}}^2 = 1$, in analogy with the approach presented in Le Borgne & Rocca-Volmerange (2002).

We now sort the resulting array of probabilities by increasing probabilities or equivalently decreasing χ^2 values. The model SED with the highest probability determines the best-match values for all parameters, i.e. for redshift, extinction, galaxy type, masses, star formation rate, etc. To derive confidence ranges we progress down this sorted list and integrate probabilities until 0.68 (in the case of 1σ uncertainties) have been reached. The confidence range is determined by the minimum and maximum values for each parameter reached within this interval. This implies that the extreme values covered by the confidence ranges do not necessarily result from the same point in the model grid. We also point out that we do not make any assumptions on the distribution of values around the best-match value. This leads to generally asymmetric confidence intervals that also do not need to be gaussian distributed.

6.2.4 Treatment of non-detections

The χ^2 algorithm described above is not able to work with non-detections that occur frequently for a number of reasons, either because

- **a)** the galaxy intrinsically does not emit flux in the observed wavelength range or all emitted flux is absorbed on the way towards us (e.g. shorewards of the Lyman break);
- **b)** the survey is not sufficiently deep to observe the faint flux from the galaxy; or
- **c)** the galaxy happens to lie outside the field-of-view covered by the observations in one or more of the filters (for instance in the case of a wide-field optical survey that was only partially followed up in the NIR).

Similar criteria also apply to the models, that can predict the galaxy to be undetected in one or more bands, for above reasons a) and/or b). Each of these cases contains information by itself and hence deserves proper inclusion.

In all above cases where either the model and/or the observed data are not detected in one or more bands, these filters are excluded from the computation of the mass scaling parameter α.

For the following χ^2 calculation we implemented the following behaviour:

- **Reason a) and/or b) for both model AND data:** In case that both observations and model agree on a non-detection (reason a) or b) apply to both e.g. for dropouts or non-detections due to too shallow data) this filter is taken as a perfect match and assigned $\chi_i^2 = 0$.
- **Reason a) and/or b) only apply to model OR data:** In the case of disagreement, e.g. the model predicts a magnitude brighter than the detection limit but the observations did not detect it, or vice versa, the model predicts too faint a magnitude but the object was detected, **GAZELLE** offers two possibilities: The χ_i^2 value for this filter can be assigned a fixed value to account for this mismatch or alternatively can be computed by the difference between magnitude limit and observed (or predicted) magnitude divided by the model uncertainty.
- **Reason c):** In the case the object was not detected because it does not fall into the observed area, this data point is excluded from the χ^2 calculation.

This process ensures best use of the available data.

6.2.5 Treatment of bandpasses beyond NIR

While non-detections are more relevant for the shortest wavelength filters there are also potential problems with bandpasses at long wavelengths. At rest-frame wavelength beyond K-band or $\lambda \approx 2.5\mu m$ the spectra of galaxies are increasingly affected by non-stellar emission, most prominently due to dust, that is currently not yet included in our chosen template set. We therefore exclude all filters from both the mass determination as well as the χ^2 computation for which the central wavelength, as derived form the filter curve, exceeds a certain maximum rest-frame wavelength (we chose a conservative value of $\lambda_{\max} = 3\mu$m as default value). Observations at longer wavelengths, for example from IRAC on board the Spitzer Space Telescope, are hence only used in the comparison with model SEDs above a certain redshift.

6.2.6 Implementation

The above algorithm is implemented in the software program **GAZELLE** . **GAZELLE** is programmed in C/C++ to allow easy modification and adaptations to more specific projects. However, most parameters that determine the behaviour of the algorithm (e.g. the maximum allowed wavelength, model uncertainties, etc.) can be configured via a parameter file so that **GAZELLE** is simple to use. For large datasets and/or large model grids **GAZELLE** can also be run in a MPI[6]-compliant multi-processor environment or even large CPU clusters to

---

[6]Message-Passing Interface, see http://www.mcs.anl.gov/research/projects/mpi/ or http://www.mpi-forum.org/ for further details

decrease the required wall-clock–time considerably. While **GAZELLE** is available on request from the author we also plan to implement a web-compatible version into the **GALEV** webpage (http://www.galev.org) to enable even easier access to the wider community.

6.2.7 Output of results

Once the algorithm described above has been applied to each SED of the model grid **GAZELLE** is able to derive a wealth of information about the object. The resulting output hence typically contains

- The best-match photometric redshift including its respective uncertainty ranges, typically including 68% of the total probability. Other and/or further confidence limits can also be configured.

- The galaxy model containing the best-match model SED. From this model we immediately can infer the most likely past star formation history and, in the case the galaxy contained a starburst or star formation truncation event, the age since this event.

- The mass scaling factor α. Since our undisturbed galaxy models are calibrated to match the properties, in particular masses and luminosities, of a typical $1L_\star$ galaxy of their respective spectral types in the local universe we can directly infer the mass relative to the characteristic mass of galaxies of this type.

- Physical parameters inferred from the above mass scaling factor α in combination with the galaxy type. These are both stellar and gaseous masses and hence total baryonic masses, star formation rates and stellar population ages. We furthermore can derive both integrated stellar and gas-phase metallicities as well as stellar population ages. Since we compute a complete probability density distribution we also obtain confidence ranges for each one of the above parameters, fully accounting for redshift, galaxy type, mass and dust reddening uncertainties.

- Optionally the full probability distribution function (PDF) for each object from the input catalog to enable follow-up studies. Another optional output is the best-match SED, including the effects of the mass scaling and dust extinction to allow for easy presentation and visualisation of the fit.

This enables us to not only derive the redshift of a galaxy, but also its star formation history, mass assembly history and chemical enrichment history.

6.2.8 GAZELLE as SED-fitting code

Based upon the above described functionality **GAZELLE** offers several other features more applicable to studies of galaxies with available spectroscopy and/or known distances. Among those features is the ability to also include spectral indices, e.g. in the Lick-system (Trager et al., 1998), in the comparison. The main difference between the treatment of observed magnitudes and spectral indices is that the latter do not scale with mass, and hence excluded from the calculation of α. The second feature is a generalisation of the above approach to enable fitting of spectra to a grid of **GALEV** models.

While the internal working, i.e. the χ^2 algorithm, is the same for all operation modes, the treatment of non-detections and the scaling of the input models with the factor α changes from case to case. A detailed description of each of these analysis modes will be given with the respective applications to data.
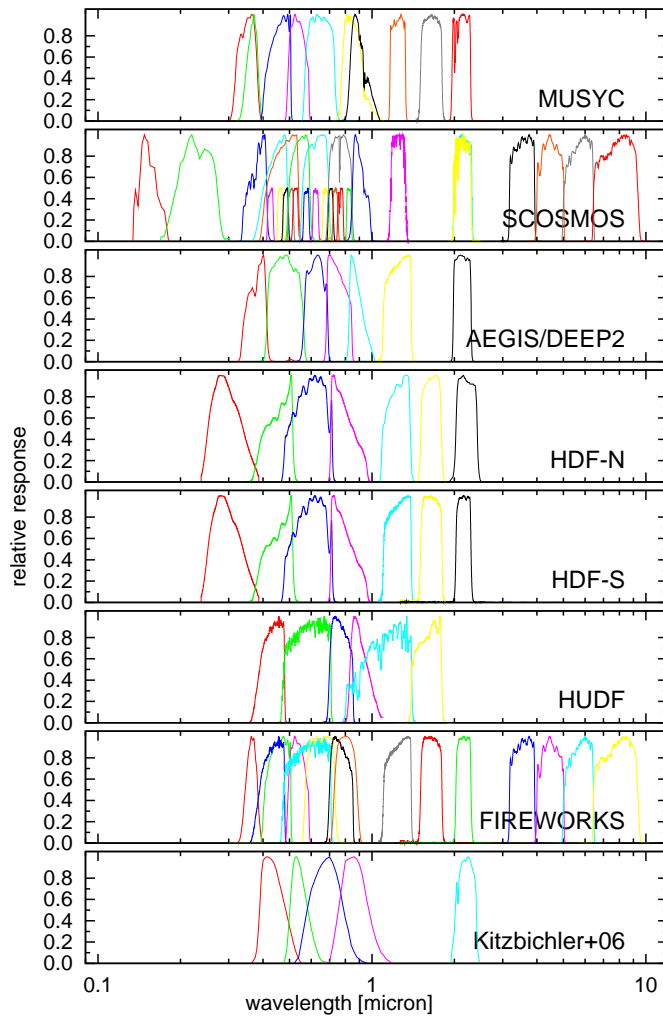
Figure 6.1: Response curves of the filters used in each of the survey.

6.3 The sample

To study the variation of the inferred mass functions on the deepfield at hand we compiled a large catalog from readily available public catalogs published by the teams of each respective survey. For each of the fields we used the filter functions for the according telescope and instrument to not include additional uncertainties due to colour transformations. Photometric redshifts as well as physical parameters were then derived individually for each field, so the accuracy of our photo-z compared to the true (spectroscopic) redshifts also varies from field to field as consequence of the varying filter coverage. In the following we detail the data we used for the presented analysis. A summary of field sizes, number of spectroscopic redshifts, filter sets and obtained accuracy can be found in Table **??**. For more details on data reduction, source selection, and alike we refer the interested reader to these papers.

In Fig. 6.1 we show the filter sets covered by each of the fields to give an overview of the covered wavelength basis and sampling of each of the SEDs.

6.3.1 COSMOS

The Cosmic Evolution Survey (COSMOS, Scoville et al. 2007b) covers a 2 sq.deg. equatorial field centred on $\alpha = 10^h 00^m 29^s$ and $\delta = +02°12'21''$, and features a very wide wavelength coverage

from X-rays (Brusa et al., 2007; Cappelluti et al., 2007; Finoguenov et al., 2007; Hasinger et al., 2007), UV (Zamojski et al., 2007), optical both ground-based in broad- and narrow-band filters (Taniguchi et al., 2007) as well as HST (Koekemoer et al., 2007; Scoville et al., 2007a), near-infrared (Capak et al., 2007), mid-infrared from Spitzer (Ilbert et al., 2009) to radio (Schinnerer et al., 2004, 2007; Bondi et al., 2008). As such, many spectroscopic redshifts have been obtained by various groups, e.g Lilly et al. (2007).

Our catalog is based on the latest (Release April 2009) i-band selected UV-optical-NIR catalog[7] including photometry in 16 broad- and 12 narrow-band filters. We restricted the catalog to sources that are also detected in the K-band to ensure the large wavelength coverage necessary to obtain reliable photo-z (our COSMOS catalog). We also matched the i+K-band selected catalog with the catalog of [3.6μm] detected sources (yielding our SCOSMOS catalog), so that we have two slightly different source catalogs for the COSMOS field.

6.3.2 FIREWORKS: GOODS-CDFS

The FIREWORKS-catalog[8] (Wuyts et al., 2008) contains K-band selected and aperture-matched photometry of the GOODS Chandra Deep Field South (CDFS, Giacconi et al. 2000) region and covers the wavelength range from U through 24μm with in total 18 filters. For reasons outlined in Sect. **??** we do not use the [5.8μm], [8.0μm] and [24μm] filters, though. The catalog furthermore contains spectroscopic redshifts for XXX sources (see Wuyts et al., 2008, and references therein), allowing for easy comparison of the obtained photo-z, making this catalog very convenient to use.

6.3.3 MUSYC: CW1255, SDSS1030, EHDFS and ECDFS

The Multiwavelength Survey of Yale-Chile (MUSYC[9]) covers a total area of $\approx$ 1sg.deg. spread out over four fields (Extended Hubble Deep Field South (EHDFS), Extended Chandra Deep Field South (ECDFS), plus an additional two fields centred on $\alpha = 10^h30^m27^s$, $\delta = 05°24'55''$ [SDSS1030] and $\alpha = 12^h55^m40^s$, $\delta = 01°07'00''$ [CW1255]). For this study we use the K-band selected deep and wide catalogs presented in Quadri et al. (2007a), Blanc et al. (2008), and Taylor et al. (in prep.). The deep versions differ from the wide versions by a K-band detection limit $\approx$ 1 mag deeper (22.8 vs. 21.7 mag) and the additional availability of J- and H-band photometry in addition to the UBVRIzK photometry common to all fields.

6.3.4 SXDF/UDS

The Subaru-XMM Deep Field (SXDF[10], Sekiguchi & et al. 2004) covers a 1.3 sq.deg. equatorial field centred on $\alpha = 02^h18^m00^s$, $\delta = -05°00'00''$ in four optical filters (BRiz) to great depth (Kashikawa et al., 2004). This field overlaps with the Ultra Deep Survey (UDS) of the UKIRT Infrared Deep Sky Survey (UKIDSS[11], Lawrence et al. 2007), adding deep near infrared data in the J- and K-bands (), and was also covered by the Spitzer Wide-Area Infrared Extragalactic (SWIRE[12], Lonsdale et al. 2003) survey, extending the wavelength range into the mid-infrared. For this study we use the public catalog presented in Williams et al. (2009).

---

[7]http://cosmos.astro.caltech.edu/
[8]http://www.strw.leidenuniv.nl/fireworks/
[9]http://www.astro.yale.edu/MUSYC/
[10]http://www.naoj.org/Science/SubaruProject/SDS/
[11]http://www.nottingham.ac.uk/astronomy/UDS
[12]http://swire.ipac.caltech.edu/swire

6.3.5 FIRES: MS1054

The Faint Infra-Red Extragalactic Survey (FIRES[13], Franx et al. 2000; Rudnick et al. 2001) covers the HDF-South and a field centred on the intermediate redshift galaxy cluster MS1054 with extremely deep NIR J-, H-, and K-band data. The catalog we use here is described in Förster-Schreiber et al. (2006) and contains the UBVRIJHK filters.

6.3.6 Hubble Deep Fields

The Hubble Deep Field (HDF) North covers the area of one WFPC2 footprint ($\approx$ 6 sq.arcmin) on the northern hemisphere, centred on $\alpha = 12^h36^m49^s$, $\delta = +62°12'58''$ (Williams et al., 1996). For the present study we use the catalog of Fernández-Soto et al. (1999), that supplements the optical HST data in UBVI with NIR-data in J, H, and K. The catalog also contains spectroscopic redshifts from 103 galaxies. The Hubble Ultra Deep Field (HUDF, Beckwith et al. 2003) was taken a few years later with the Advanced Camera for Surveys (ACS) onboard HST and observed an area of XXX arcmin of the southern sky in BVRI to even greater depth. In our study we use the catalog compiled by Coe et al. (2006), also containing J- and H-band data from HST-NICMOS.

6.3.7 AEGIS and DEEP-2

AEGIS, the All-wavelength Extended Groth Strip International Survey, covers an elongated patch of sky centred on $\alpha = 14^h17^m00^s$ and $\delta = 52°30'00''$ with multi-wavelength data spanning the range from X-ray, UV, optical, near- and mid-infrared to radio (Davis et al., 2007). It was also covered by the Deep Evolutionary Exploratory 2 Galaxy Redshift Survey (DEEP2 Willmer et al., 2006), supplying spectroscopic redshifts for a large sample of $R_{AB} \leq 24.1$ mag galaxies. The data we use in this study was compiled from two independent catalogs covering the Optical ugriz bands observed from CFHT (Davis et al., 2007) and the near-infrared J and K-bands from Palomar (Bundy et al., 2006). This compilation differs from the previous catalogs in that no PSF-matching between the different filters could be performed, and we will in the following discuss the implications of this. For the matching we started with the NIR catalog, and cross-correlated it with the optical catalog, using a matching radius of 2″. In the next step we cross-correlated the NIR+Optical catalog with the DEEP2 redshift survey (using data release 3), again using a matching radius of 2″. The final catalog hence contains only such galaxies that are detected in the NIR and the optical and where a spectroscopic redshifts is available from DEEP2.

6.4 The GALEV model set

For each of the aforementioned fields we used a homogenous set of model templates and, with exception of field-dependent detection limits, the same **GAZELLE** configuration between the fields to ensure that differences between the individual fields only reflect changes in the data and not in the configuration.

We use the following template set:

- 5 galaxy types representing the local spectral types E and Sa through Sd, using our chemically consistent (c.c.) models that include a self-consistent treatment of the chemical evolution and fully account for the increasing abundances of subsequently formed stellar populations. These c.c. models are closely calibrated to reproduce a wide range of observables in the local universe as described in Kotulla et al. (2009) and Kotulla & Fritze (2009). However, we can not a priori know whether the relation between galaxy spectral

---

[13]http://www.strw.leidenuniv.nl/ fires/

type and stellar mass holds out to arbitrary high redshifts. This could mean that galaxies at higher redshifts are more or less massive than predicted by our models, leading to different metallicities as a consequence of the mass-metallicity relation. To account for this uncertainty we also add, for each type, models with the same SFH, but with metallicities fixed to $(0.2, 0.5, 1.0) \times Z_\odot$.

- A range of starburst and post-starburst models with 16 different burst ages ranging from 0 Gyr (i.e. at the peak of star formation activity) to 10 Gyrs, (i.e. old and red galaxies as typically found for ellipticals in the local universe). This sequence naturally includes strong post-starburst at ages of $0.5 - 1.0$ Gyrs when their spectra show strong Balmer absorption lines typical for k+a type galaxies in the low-redshift universe (Dressler et al., 1999; XXX missing reference XXX, 2035; Falkenberg et al., 2009a,b), but that are increasingly found in high-redshift ellipticals (XXX missing reference XXX, 2035). Again we allow 3 metallicities of $(0.2, 0.5, 1.0) \times Z_\odot$ for each of these models. Using our c.c. approach for these models is not appropriate, as these starbursts are likely triggered by mergers, hence rendering our assumption of closed-box evolution invalid. However, we are currently working on implementing a multi-zone approach into **GALEV** , that could lift this limitation in the near future.

- A sample of stellar spectra from the Lejeune et al. (1997, 1998) library, covering the full range of effective temperatures from $2000 - 50000$ K. Adding these templates aims at finding remaining stellar contaminants that were not flagged as such based on morphological criteria.

For all galaxies we assume star formation to begin at $z = 8$ and then track the full evolution from there formation to the present day. We hence naturally include evolutionary corrections, accounting for the younger ages towards higher redshifts and increasing look-back times. This naturally ensures that all galaxies are younger than the age of the universe at each redshift. It also means that the number of available templates changes with redshifts, as, for instance, older post-burst galaxy templates are restricted to lower redshifts than models of ongoing bursts or undisturbed galaxies.

Our assumption of a fixed, universal formation redshift for galaxies of all types and across the mass-spectrum is supported by a wealth of evidence found in both the local and higher redshift universe, ranging from the existence of stars and star clusters as old as the universe in our own Galaxy (Harris, 1996; Mackey & Gilmore, 2003) and in nearby giant- (Kotulla et al., 2008a; Woodley et al., 2010) and dwarf-galaxies Grebel (1997). Based on integrated light we have evidence for already old stellar population in high-redshift galaxies (e.g. Shapley et al., 2001; Cimatti et al., 2002a; Förster-Schreiber et al., 2004). Furthermore the detection and spectroscopic confirmation of galaxies at redshifts $z \gtrsim 7$ (Iye et al., 2006) furthermore point towards the same redshift range, as do determination on the end of the epoch of reionization via the Gunn-Peterson effect (Gunn & Peterson, 1965) derived from high-redshift quasar spectra (Fan et al., 2006). Small variations of the exact value of z_{form} between $z = 6 - 10$ have negligible impact on our results and the conclusions drawn from them, as the difference in galaxy ages and hence evolutionary states imposed by these changes are small.

All models (spectra, apparent magnitudes, k- and e-corrections for all filters of the presented fields, stellar masses, SFRs, etc as function of time and/or redshift) are freely available from our website `http://www.galev.org`. Additional models for different assumptions and/or in different filters can also be computed via this web-site.

6.4.1 Comparison of predicted colour evolution with observations

The most important factor to derive accurate photo-z from templates is to ensure the models accurately trace the evolution of the observable SED with redshift. GAZELLE in this respect differs from all other photo-z codes currently available (see Hildebrandt et al., 2010, for an
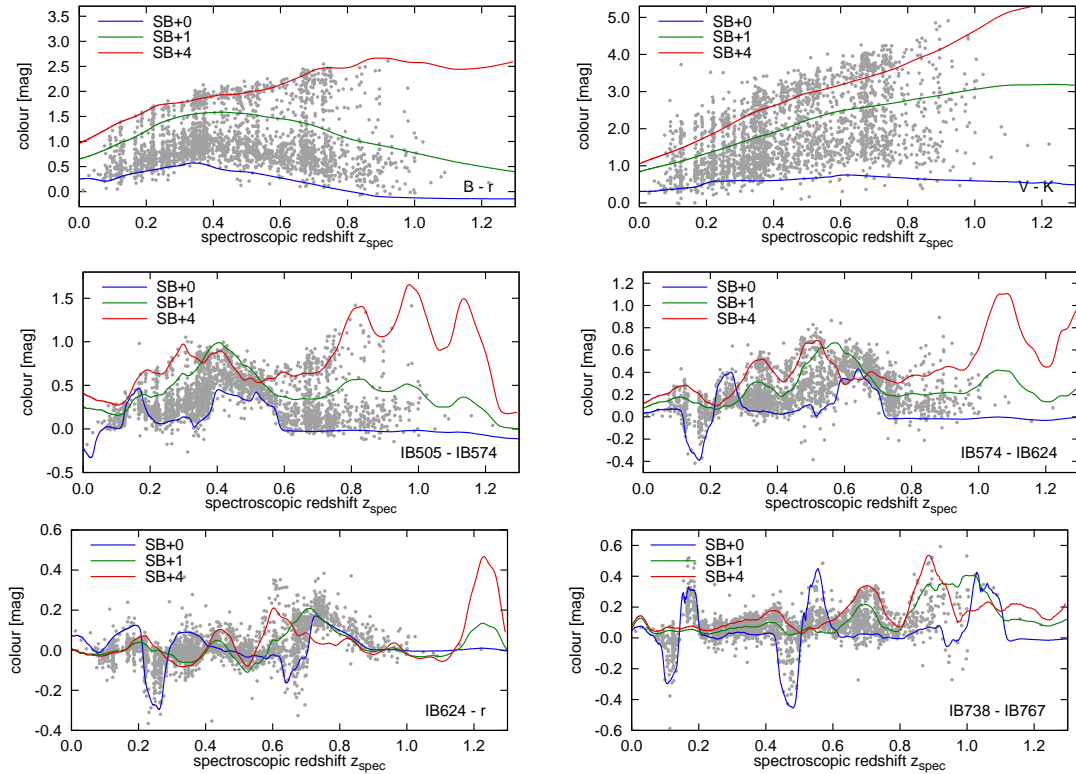
Figure 6.2: Comparison of the colour evolution with (spectroscopic) redshift as observed in COSMOS for a range of filter combinations: Top row: $B - r$ (left), $V - K$ (right); middle row: IB505 $-$ IB574, IB574 $-$ IB624; bottom row: I624 $-$ r, IB738 $-$ IB767. For comparison we show three of the models in our grid, a starburst at peak SFR and two post-starburst models 1 Gyr and 4 Gyrs after the SFR peak, each using a metallicity of 0.5 $Z_\odot$.

overview and short description of most other codes) in that it does not limit the template set to a few templates representing galaxies at different ages and then use the redshift as free parameter, but it rather assumes a fixed relation between galaxy age and redshift. Doing so eliminates one essential free parameter, and in turn imposes stringent requirements on the underlying star formation history, but at the same time makes the derived SFH more meaningful. Several codes (e.g. EAZY, Brammer et al. 2008) interpolate between templates to improve the quality of their photo-z fits, and while these interpolation factors can basically be used to derive SFHs, smooth SFHs are likely better representations of the true SFH than such consisting of only a few individual bursts.

In Fig. 6.2 we show observed colours of galaxies in the COSMOS field in a range of filter combinations, using both broad- and intermediate-band filters. We overplot a small selection of the models we use to derive photometric redshifts. All shown models are computed with fixed metallicity of 0.5 $Z_\odot$ and, as mentioned above, assume a formation redshift of $z_f = 8$.

Fig. 6.2 clearly shows that our models offer a best-possible match to the observations without requiring any additional free parameters or a-posteriori calibration (except the zero-point matching described above). We particularly note the close match to the bumps and wiggles that are caused by emission lines in the star-forming templates. Without emission lines many of the features that closely determine the photo-z accuracy, such as the P-Cygni like evolution of the starburst template in the bottom row panels, can not be explained. This was also found by Ilbert et al. (2009), who also found a significant improvement in photo-z accuracy after inclusion of emission lines into their templates.
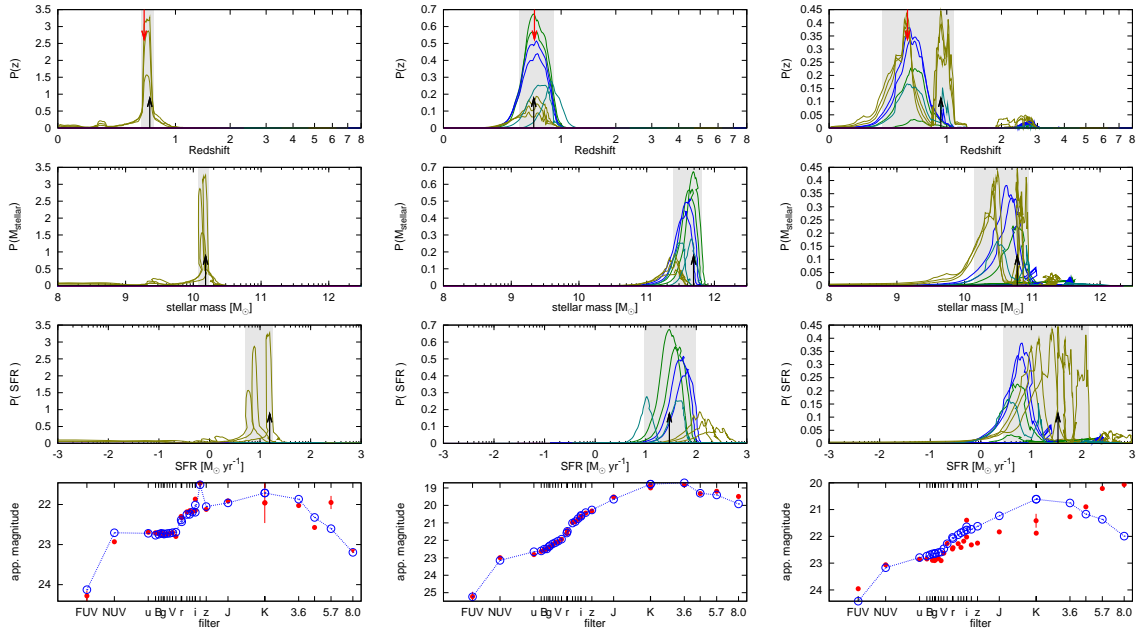
Figure 6.3: Examples for typical probability distribution functions for three galaxies in the COSMOS field. The top three panels show the probability distribution as function of redshift (top), stellar mass (second row) and star formation rate (third row); the bottom panel shows the observed (filled red circles) and corresponding best-fit SEDs (blue open circles, connected by lines). Black upward arrows mark the best-fit parameters (redshift, stellar mass and SFR), the downwards pointing red arrow in the top panel marks the spectroscopic redshift. The 1-σ confidence ranges are marked as gray-shaded regions.

The three galaxies are (ID [from zCOSMOS DR2 catalog], RA [deg], DEC [deg]): left: (811415, 150.242065, 1.826618); middle: (807424, 149.718628, 1.638003); right: (810153, 150.517227, 1.876145).

6.4.2 Advantages of this model coupling

The intended close coupling between GALEV evolutionary synthesis models on the one hand and GAZELLE as photo-z code on the other hand furthermore allows us to extract more information out of each SED than "only" a redshift. We already showed that in order to match the overall normalisation of the SED we need to apply a scaling parameter α (see eq. **??**). This factor not only scales the galaxy's stellar mass as source of the emitted light, but by linking to the galaxies SFH also affects the current SFR, and other mass-dependent parameters. Furthermore from our knowledge of the SFH we can get a handle on mass- and light-weighted stellar ages. Mass-weighted ages in this context are derived by weighting the age of each stellar population with its mass, while light-weighted ages are obtained by weighting each age with its luminosity. As stellar population of different ages dominate different parts of the emitted spectrum (e.g. young stars dominating the emission in the UV and Blue, while NIR is dominated by older, evolved giant stars), these light-weighted ages generally depend on the filter at hand, with longer wavelength bands generally yielding older ages than bluer bands. Furthermore if we assume that galaxies evolve as closed-boxes as done in this study[14], or alternatively assume some some prescription for gas infall and outflows, we can also infer the currently available gas-mass and gaseous metallicity. Although this approach introduces spurious relations merely reflecting the initial assumptions (e.g. a one-to-one relation between gas-mass and SFR in the case of our Sa-Sc templates) that have to be carefully considered during the analysis, it still allows to derive a wealth of physical information from the data at hand in a self-consistent manner.

Fig. 6.3 exemplifies this approach. Using the probability distribution derived from the SED fitting, we assign identical probabilities of each (observed SED)-(model SED) combination to each

---

[14]Note, however, that as consequence of the fraction-of-visible-mass parameter (see Kotulla et al., 2009, for details) the chemical evolution, but not the gas fraction, of our models is essentially equivalent to the model of Erb (2008) that assumes gas infall and outflows to be proportional to the star formation rate.

of the physical parameters of this model point, in this case the stellar mass and SFR. Confidence ranges for these paramters are then derived simultaneously with the photo-z confidence ranges by integrating probabilities from highest to lowest probability and deriving the extreme values reached within the 68% range.

This self-consistent and more realistic approach therefore also accounts for the uncertainties in the photo-z determination. This leads to generally larger uncertainties for each parameter as compared to the more common, sequential approach of first obtaining a (photometric) redshift, and then deriving masses and SFRs via SED fits *at fixed redshift* that ignores redshift uncertainties as major source of uncertainty for all other parameters.

Fig. 6.3 also demonstrates three out of four possibilities of principal shapes of probability distribution functions (PDFs), two of which lead to an correct photo-z estimate. In each of the panels, line-colours indicate the galaxy template, with red lines representing our E-type model, green lines early-type spirals Sa and Sb, dark blue lines late-type spirals Sc and Sd, brown lines early burst-models with burst ages $\leq$ 500Myr, turqoise intermediate-age bursts with $500 <$ burst age < 1500 Myrs, and finally violett lines post-starburst models with burst ages > 1.5 Gyrs. In each sub-panel the upward facing arrows indicate the best-match value; the red, downward facing arrow in the top $P(z)$ panels marks the spectroscopic redshift. We furthermore indicate the 1σ confidence intervals with the grey-shaded regions. The bottom sub-panels give the observed photometry data and their errors with red points; the best-match model SED is given by blue open circles. Note that the lines connecting the model SED points are only meant to guide the eye.

The first case, shown in the left panel, illustrates the ideal case of having only a single template that can reproduce the observed SED. In essentially all cases this is caused by one or more strong features in the SED, either a strong break (as in the case of dropouts) or, as for this galaxy, strong emission lines that dominates the flux in at least one filter. These features can only be reproduced over a very narrow redshift range (typically $\Delta x \approx \Delta\lambda/\lambda$ of the filter that covers the feature) and hence lead to very peaked PDFs. We remark that the SFR PDF splits up into three components that coincide in their redshift- and stellar mass PDFs. These represent three young bursts at different stages or burst ages, that despite their different physical parameters show indistinguishable observables in form of their SEDs.

The second case shown in the middle column of Fig. 6.3 is a more typical case where no sharp features are detected and the photo-z determination is dominated by a fit to the continuum. This also allows for dust extinction as additional degree of freedom to come into play. Dust reddening affects the spectral slope globally, but does not affect the shape and/or position of spectral lines or breaks, so we naturally expect and indeed observe a much wider PDF in these cases. The stellar mass PDF is not symmetric around the best-match value, but rather skewed due to the width of the photo-z distribution.

The third, right column in Fig. **??** is characteristic for a case where the PDF has more than one peak. Reasons for this can be found in degeneracies due to large photometric errors and/or insufficient sampling of the SED, e.g. too few filters not allowing to discriminate effects of stellar population age and dust reddening or confusing the Balmer and Lyman breaks due to lacking/too shallow UV coverage. In most of these cases the PDF still shows a local but no global probability maximum at the correct redshift. If both peaks are close in redshift space this effect is likely to average out for larger samples, as the scattering of best-match values from the correct into the wrong peak is proportional to their relative amplitudes. For larger distances (e.g. as in the case of confused Balmer and Lyman-breaks) the effects are more severe, because nearby, low-mass and galaxies that get interpreted as high-redshift galaxies are more numerous than massive galaxies at high-redshift. However, in most of these cases the resulting photo-zs are assigned very large uncertainties to represent this degeneracy and can be excluded from any subsequent analysis.

The fourth case not shown here are "catastrophic failures", where the spectroscopic redshift does not correspond to even local maxima and lies outside the confidence ranges. This can be

the case, e.g, for strong AGNs or typically late-type stars that are not represented by the template grid. In particular the latter can potentially be excluded if high-resolution imaging, e.g. from HST or using adaptive optics, are available, e.g. using the Stellarity parameter from SExtractor (Bertin & Arnouts, 1996) or by comparing the FWHM to the FWHM of bona-fide points sources. However, doing so from ground-based observations alone with typical seeing of $\lesssim 1$ arcsec is less straightforward, explaining the significant fraction of objects falling into this category.

Another source of discordant photo-zs are wrong spectroscopic redshifts. Fernández-Soto et al. (2001) compared spectroscopic and photometric redshifts for a sample of 140 galaxies in the HDF-N. They find for 5 out of 9 discordant redshifts the spectroscopic redshift is at fault, while only in 1/9 the photo-z is incorrect. This fraction is particularly troublesome for training-set based photo-z techniques such as ANNz (Collister & Lahav, 2004).XXX

6.5 Performance evaluation

To test the accuracy and reliability of our code we applied **GAZELLE** to a range of different surveys with available spectroscopic redshifts. The fields under investigation are the original Hubble Deep Fields North (HDF-N, Fernández-Soto et al., 1999) and South (HDF-S, Labbé et al., 2003), the Hubble Ultra Deep Field (HUDF, Coe et al., 2006), Chandra Deep Field South (CDF-S, using the FIREWORKS catalog by Wuyts et al., 2008) and the AEGIS (All-wavelength Extended Groth Strip International Survey, data from Bundy et al., 2006; Davis et al., 2007). The wavelength coverage of each of these fields is summarised in Table 6.1.

For each of these fields we first ran a calibration run, in which the redshift of all templates is fixed to the spectroscopic redshift of each object. This allows to derive empirical zero-point offsets that need to be applied to the data to minimise systematic offsets between the photometric and spectroscopic redshifts. Possible reasons for these zero-point shifts are imperfect calibration of the data with respect to the quoted magnitude system (as is the case, e.g. , for the SDSS u- and z-filters, (Doi et al., 2010)). On the modeling side small changes to the filter response curves as consequence of different airmasses or insufficient knowledge of the response of telescope mirrors and/or detector as function of both time and wavelength can also lead to minor offsets. However, the required offsets are typically small ($\lesssim 0.05$ mag) and well within the assumed uncertainties of our models of 0.1 mag.

The resulting one-to-one comparison is shown in the left panel of Fig. 6.4 and also summarised in Table 6.1. We generally find a very good agreement between the spectroscopic and our derived photometric redshifts. Two notable cases are SCOSMOS and AEGIS/DEEP-2. SCOSMOS shows by far the best performance, which we attribute not only to the large number of filters that finely sample the SED in much the same way as a low-resolution spectra does, but also to its

Survey / Field	wavelength coverage	filters	$N(z_{\text{spec}})$	$\left\langle \frac{\Delta z}{1+z_{\text{spec}}} \right\rangle$	œ$_z$	# outliers[1]
HUDF	B - J	6	86	-0.013	0.108	30
HDF-N	U - K	7	103	-0.027	0.056	17
HDF-S	U - K	7	49	-0.021	0.059	7
AEGIS/DEEP	u - K	7	5026	-0.037	0.067	1285
FIREWORKS	U - [8.0]	16	582	-0.057	0.062	117
SCOSMOS	FUV - [8.0]	16+12	2375	-0.003	0.017	148
combined	-	-	8221	-0.018	0.052	1604
Kitzbichler+06	B-K	5	112k	-0.013	0.054	14345

[1] defined as having $\Delta z \equiv |z_{\text{spec}} - z_{\text{phot}}| > 0.1 \times (1 + z)$

Table 6.1: Surveys in comparison
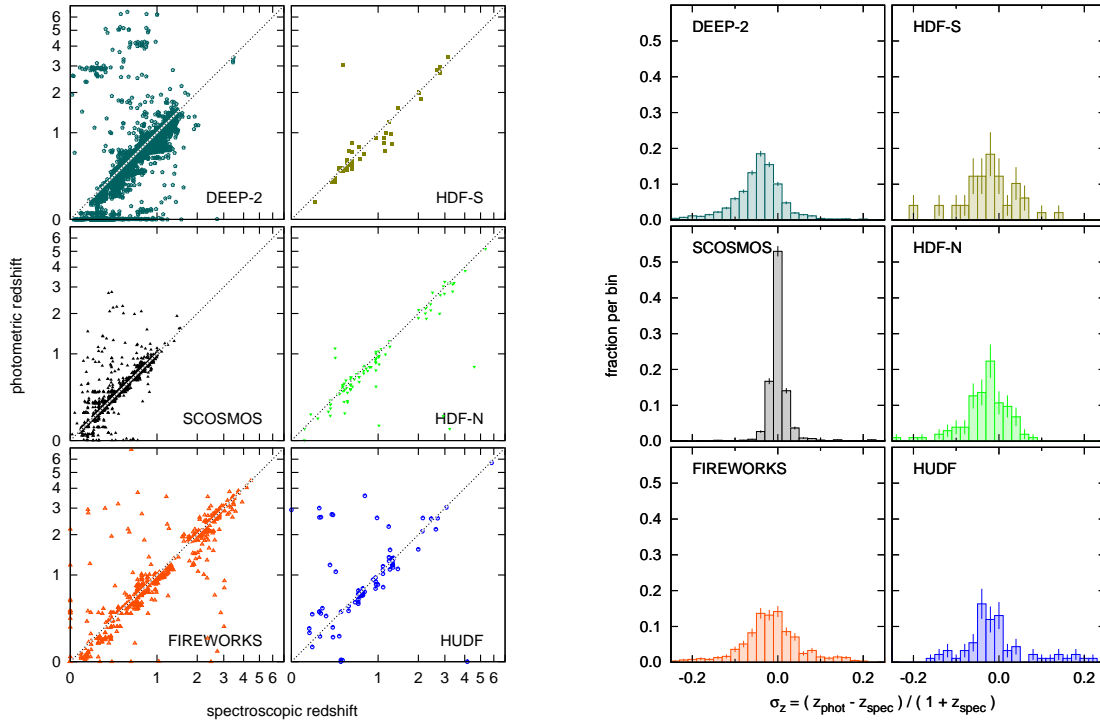
Figure 6.4: Comparison of spectroscopic and photometric redshifts. Direct comparison of z_{phot} and z_{spec} for the surveys listed in Table **??**. The mean deviation $\langle z_{spec} - z_{phot} \rangle = -0.03XXX$, the scatter is XXX. **Right panel:** Histogram of the deviation

large wavelength coverage from FUV (0.15μm) to Mid-Infrared at 8.0μm (note, however, that in particular the [5.8μm] and [8.0μm] bands are mostly excluded from the fitting due to the low redshifts of the spectroscopic sample). This greatly helps to constraint dust extinctions, alleviating degeneracies of dust extinction, stellar population age and redshift. On the other end of the spectrum is our AEGIS/DEEP-2 sample, showing a relatively large number of objects with large derivations from the ideal case. We attribute this to the way the photometry sample was assembled, as described earlier in Sect. 6.3.7.

The right panel of Fig. 6.4 shows the distribution of photometric redshift offsets $\sigma_z = (z_{phot} - z_{spec})/(z_{spec} + 1)$ for all six fields. All fields show a minor bias of $\sigma_{z,median} \approx -0.02$ towards slightly underestimated photo-z as compared to the true spectroscopic redshift. This bias however does not significantly impact on the derived physical parameters, in particular at $z > 0.5$; small deviations in redshift do not change the overall evolutionary state of the galaxy, and the resulting error in the distance modulus ($\delta(m - M)/\delta z \leq XXX$) which affects masses and mass-dependent parameters is small compared to the uncertainties from different model types, i.e. star formation histories (also see Fig. 6.3). The dispersion of $\sigma_z \approx 0.05$ is comparable to other state-of-the-art photo-z codes on the same and/or similar datasets (Hildebrandt et al., 2010).

6.5.1 Distribution of photometric redshift errors

One important factor during the derivation of photo-z is to determine how robust that redshift estimate is, or what its confidence ranges are. As mentioned earlier (Sect. 6.2.3) GAZELLE derives confidence ranges directly from the probability distribution, accounting for potential multiple probability maxima.

In Fig. 6.5 we show the cumulative error distribution derived from all galaxies with available spectroscopic redshifts. When compared to the theoretical expectations we find that for most fields the curves lie left of the gaussian distribution (shown as thicker grey line), meaning that for
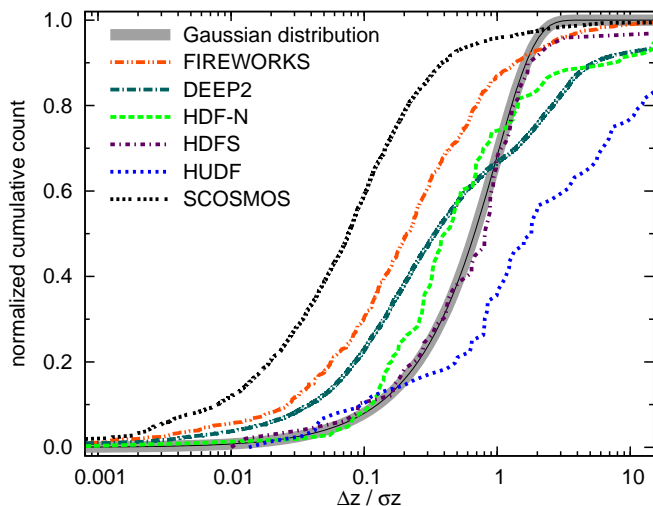
Figure 6.5: Cumulative distribution of $|\Delta z|\sigma_z = |z_{spec} - z_{phot}|\sigma_z$ for all galaxies in our sample with available spectroscopic redshift. For comparison we show the expected distribution in case of gaussian errors.

these we generally overestimate the uncertainties and photo-z are more accurate than could be expected from the error bars. This is most likely due to PDFs with multiple peaks, in particular in cases where distinguishing between the Balmer- and Lyman-break is difficult based on the available photometry. Another contributor are degeneracies intrinsic to the template set and parameter space; for instance, galaxy age, redshift and dust reddening to first order have similar impacts on the observed SEDs. Only in the case of the HUDF are errors underestimated, feigning overly accurate results. However, this field also has the lowest number of spectroscopic redshifts and is selected differently from all the other fields, and so our result for this particular field has lower statistical significance.

We also note that at large deviations our estimated errors drop below the gaussian distribution. This originates from the fraction of "catastrophic failures" or outliers from the photo-z vs. spec-z identity. For these cases the quoted error bars are often significantly underestimated.

6.5.2 Systematic uncertainties in stellar mass and star formation rate due to simplified SFHs

As **GAZELLE** simultaneously serves as SED fitting code to derive physical parameters, we need to make sure that our assumption of smoothly varying star formation histories is capable to deal with the often complex star formation histories observed in detailed studies of individual galaxies. For this purpose we chose a large sample of galaxies from semi-analytical models. These galaxies have more realistic SFHs derived from the Millennium simulation (Springel et al., 2005), but, owing to their model nature, well known parameters, making them advantageous over real galaxies for this comparison. We use a sample of galaxies from the De Lucia & Blaizot (2007) and Bower et al. (2006) models. For all cases we correct the stellar masses and star formation rates for differences in the IMFs, following the prescription in the respective papers. In all cases we use the simulated photometry and apply the photo-z and SED fitting using identical parameters as in the real analysis of the deepfields.

The comparison with the models from De Lucia & Blaizot (2007) are shown in Fig. 6.6. The redshift for the four runs, i.e. $z = (0.36, 0.76, 1.50, 3.06)$, have been chosen to as closely as possible match the central redshifts for the redshift bins of the subsequent analysis, to not introduce uncertainties. We chose the photometry in the SDSS ugriz and 2MASS JHK filters, as these filters more closely represent current observations as compared to the Buser BV and Johnson RIK filters.

We find that, for galaxies more massive than $10^9 M_\odot$, stellar masses can be reproduced with a typical 1σ scatter of 0.07 dex; 99.9 per cent of all galaxies have stellar masses within $0.17 \ldots 0.24$
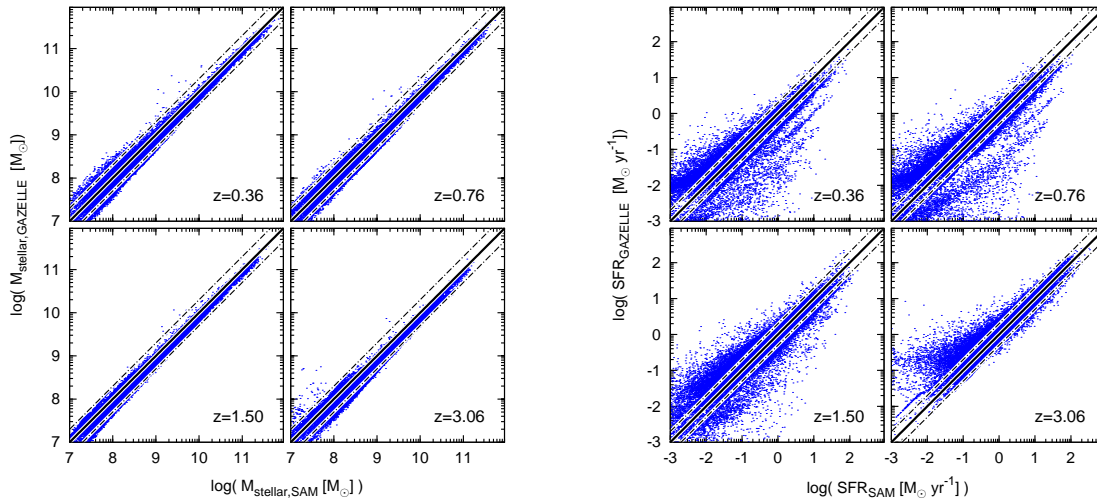
Figure 6.6: Comparison of stellar masses (left panels) and star formation rates (right panels) taken from a semi-analytical galaxy formation model (De Lucia & Blaizot, 2007) based on the Millennium simulation with the parameters obtained by fitting the synthetic rest-frame SEDs to a set of GALEV models using GAZELLE. All data were corrected to use the same cosmology and a Salpeter IMF. Data points are shown with blue dots, perfect one-to-one agreement is shown by the solid line, and dashed lines mark 0.3 dex offsets to either side.
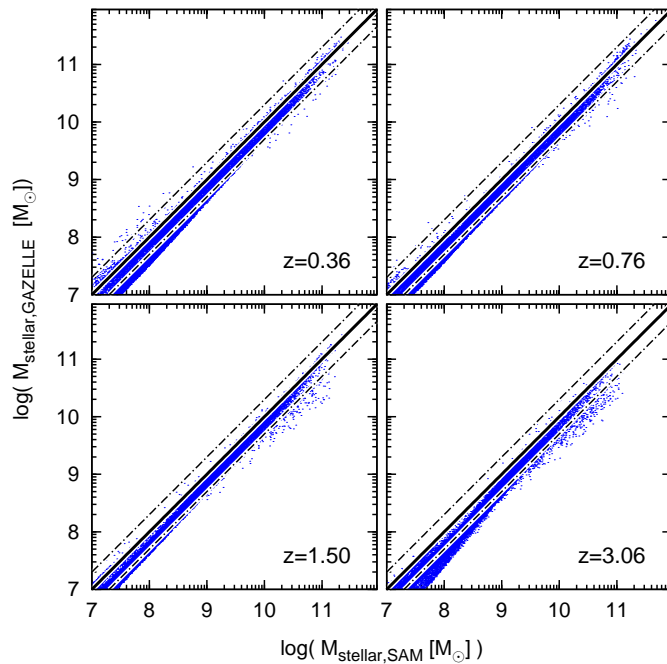
Figure 6.7: Comparison of stellar masses taken from the semi-analytical galaxy formation model of Bower et al. (2006) with the parameters obtained by fitting the synthetic rest-frame SEDs to a set of GALEV models using GAZELLE. Other details as in XXX Fig. 6.6.

dex (with lower values towards higher redshifts) of the true model mass. Star formation rates for the $M_{stellar} > 10^9 M_\odot$ selected sample are typically good to 0.5 dex (1σ) but show logarithmic large scatters, mostly due to very low SFR that have very little effect on the SED. Restricting the sample to galaxies with SFR ≥ 1 $M_\odot$ yr^{-1} significantly improves this situation, with scatter being reduced to 0.18 dex (1σ), and > 0.999 of all galaxies agreeing to better then 0.5 dex.

The results using the models of Bower et al. (2006) and our fits to the UBRIJHK photometry are shown in Fig. 6.7. These models do not give star formation rates, so we have to restrict the comparison to stellar masses. The scatter here amounts to $0.08 \ldots 0.12$ dex. In all cases essentially all galaxies have photometric stellar masses within 0.25 dex of the true value.

While these results are already more than encouraging, so far we could only fit rest-frame pho-
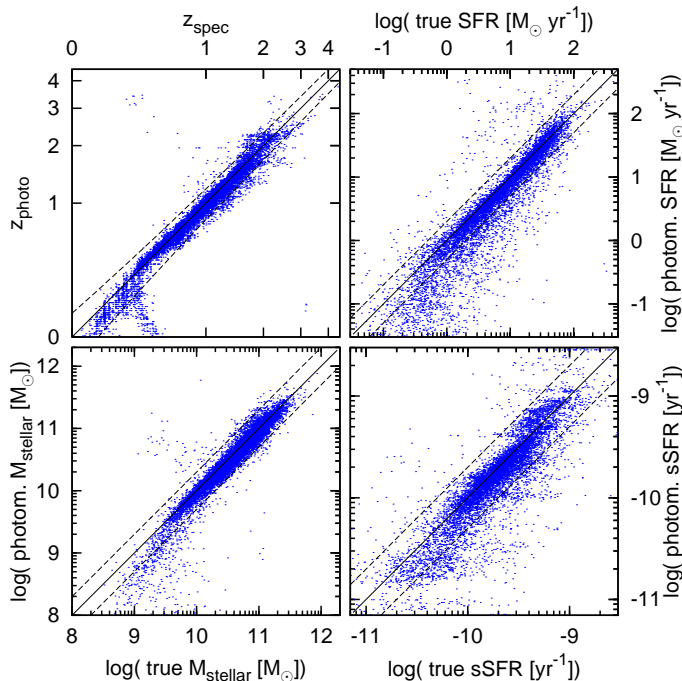
Figure 6.8: Comparison of values obtained from the obtained photometric redshifts with the true values as given by the semi-analytical models for a 2 sq.deg. light-cone from Kitzbichler & White (2007). Top left: true and photometric redshifts; bottom left: stellar masses; top right: star formation rates; bottom right: specific star formation rates (= SFR/$M_{stellar}$). The solid black line shows the identity between true and photometric values; dotted lines mark confidence ranges of $\pm 0.1(1 + z_{spec})$ and 0.3 dex ($M_{stellar}$, SFR, and sSFR).

tometry for which we had to restrict the redshift range to match the models. This prevented us from determining the true accuracy with redshift as additional free parameter. To overcome this we also applied **GAZELLE** to synthetic light-cones from Kitzbichler & White (2007). These light-cones are also based on the Millennium simulation, but account for redshift by using appropriately shifted BVRIK filters. The results derived from these relatively sparse SEDs are shown in Fig. 6.8.

We generally find very good agreement of the true values and those derived from the galaxy SEDs.

6.6 Results

6.6.1 Redshift distribution

The first step in our comparison of the individual fields is the distribution of the derived photometric redshifts. To make the samples comparable for all subsequent analyses, we select a K-band bright sample of $m_K < 22$ mag galaxies. This brightness is reached in all samples except the HUDF that only extends to the H-band. Furthermore the HUDF catalog combines galaxies in any of the BViz frames (Coe et al., 2006) and hence should be considered carefully. Also note that the COSMOS field is actually based on a combined i-band and K-band selection. However, the i-band selection reaches significantly deeper than the K-band (26.1 vs 23.8 mag at 10σ, Capak et al. (2008, in preparation), also see Ilbert et al. 2009), which in turn is nearly 2 mag deeper than our conservative limit and hence will not likely affect the following results except in the case of extremely red ($i - K > 4$) object.

Fig. 6.9 shows the resulting redshift distribution for all fields, normalised by the area of each field (top panel) and the total number of galaxies of each respective field (bottom panel).

As can be seen from this figure, the photo-z distributions of most fields roughly agree in that they show a rise at low redshifts to a maximum at $z \approx 0.5$, and a sharp decline towards higher redshifts. This agrees well with results from other groups for the same fields (Grazian et al.,
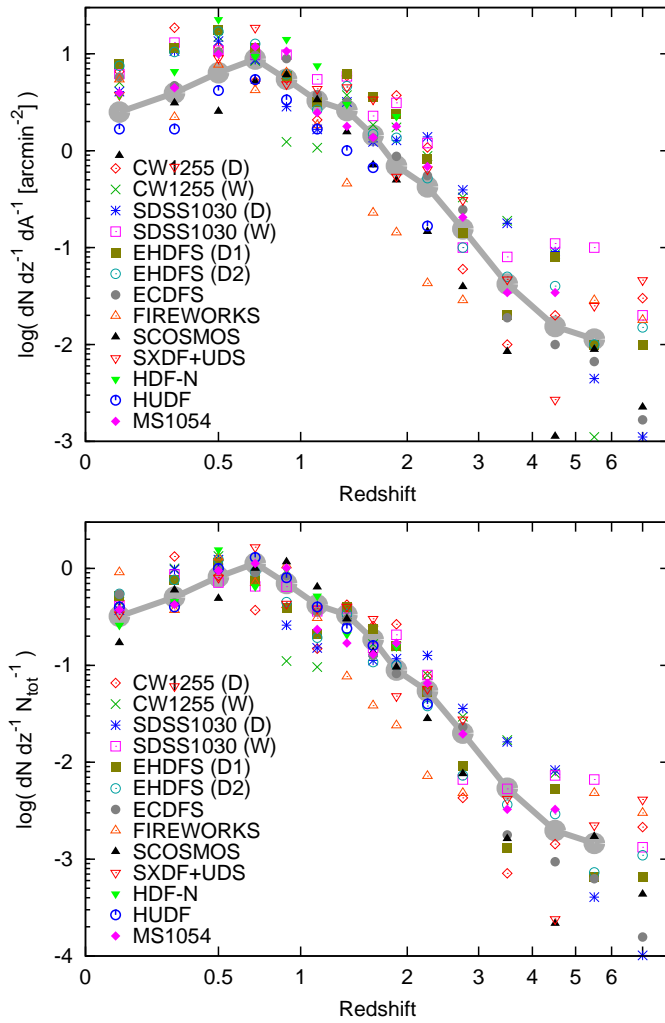
Figure 6.9: Projected density of galaxies per unit redshift, normalised by the area of each field in arcmin^2 (top panel) and by total number of galaxies in each field (bottom panel) as a function of redshift. The thick grey line marks the average of all fields (using the wide fields where both wide and deep are available);

2006; XXX missing reference XXX, 2035), re-emphasising that both the code and our underlying model grid compare well with other solutions currently available, but with the added benefit of physical parameters from the intimate coupling to our models. A striking feature of both number- and area-normalised plots is the large scatter between the fields. Despite our restriction to a homogeneous, $m_K < 22$ mag selected sample we still find differences of a factor of three near the peak of the distribution at $z \approx 0.5 - 0.8$. This discrepancy between the individual grows larger still with increasing redshift, but with reduced statistical significance due to the smaller number of detected galaxies at these redshifts. Possible reasons for this effect are **1)** differences in the selection of the sample; **2)** different reduction steps from the data data to the actual catalogs, including calibration uncertainties; **3)** photometric redshift errors that scatter galaxies between the individual redshift bins; **4)** real physical differences in the high-redshift galaxy populations at higher redshifts;

The first suspect was largely ruled out by our restriction to a well defined sample as outlined above. In particular the chosen magnitude limit is significantly brighter than the quoted incompleteness limits of the individual fields (see, e.g. , Quadri et al. 2007a for the MUSYC fields). Furthermore the reduction steps that lead to these catalogs largely, i.e. not considering certain steps necessary to account for the different instrument characteristics (XXX missing reference XXX, 2035), follow widely-accepted standard reduction procedures, so that also the second point seems unlikely to cause the large observed discrepancies.

The third point of photometric redshift uncertainties shuffling galaxies among the bins can be
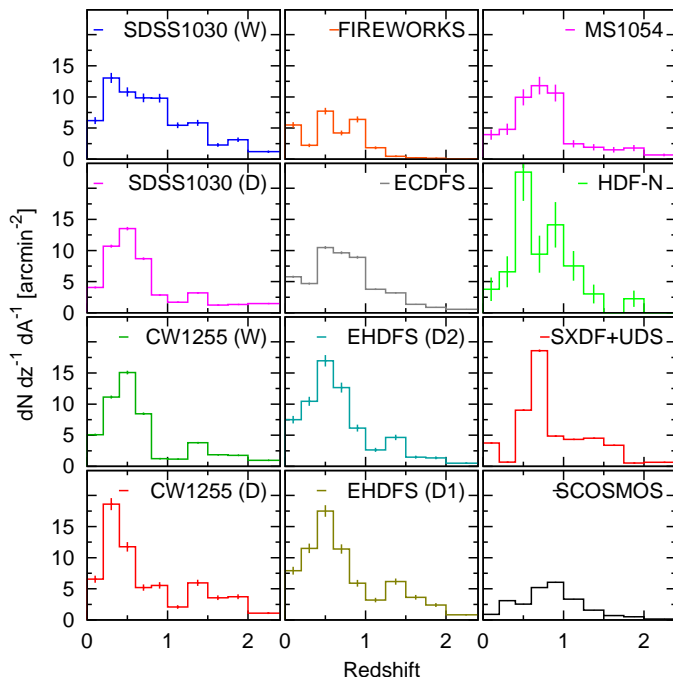
Figure 6.10: Redshift distribution for each individual sample, normalised by the are of each field. Poisson errors have been plotted for each individual field, but are too small in the case of SCOSMOS, ECDFS and SXDF+UDS to be recognisable.

addressed by comparing two nearly identical fields. For this purpose we chose the MUSYC CW1255, SDSS1030, and EHDFS fields, as they were both published by Quadri et al. (2007a), are based on data from the same instrument, and have photometry of equal quality in identical filters, and hence should be affected by photo-z scatter in very much the same way. However, even among these fields we still find significant $(3-5\sigma)$ differences at redshifts $z = 0.8\ldots2.5$. At higher redshifts $z \leq 2.5$ the redshift distributions from the wide catalogs agree very well, while the deep catalogs still show some differences, but due to the small number of galaxies the statistical significance of this finding is questionable.

We will discuss the evidence for the fourth point below in the light of mass functions derived from the data for each of the fields.

Another interesting feature in several fields (CW1255 D/W, SDSS1030 W) is a deviation at $z \approx 1.5\ldots2$ in the decrease rate towards higher redshifts. This can be more clearly seen in Fig. 6.10 where we show the area-normalised redshift distribution of each individual field.

To test whether this is indeed a real feature or an artefact of our photo-z determination we created a large mock-catalog of simulated observations for each of our input templates. For each we started from our model SED, added dust extinction with $E(B - V) = 0 - 0.4$ mag drawn from a flat distribution, varied the mass function to represent a Schechter-function with faint-end slope $\alpha = -1.0$ and a typical mass of $3 \times 10^{11} M_\odot$. Finally we added photometric noise, drawn from a gaussian distribution with zero mean and a standard deviation that depends on the filter and the apparent magnitude (see Kotulla & Fritze, 2009, for a more detailed description). We used the same filter set and detection limits as in the MUSYC-ECDFS field. These catalogs were then used as input catalog for GAZELLE and we determined photometric redshifts and physical parameters with parameters identical to what we used for the real data. The very last step then culled only these galaxies that fulfil the $m_K < 22$ mag criterion to make the simulation comparable to above findings. In Fig. **??** we show the comparison between true, input redshift distribution and the retrieved, photo-z distribution.
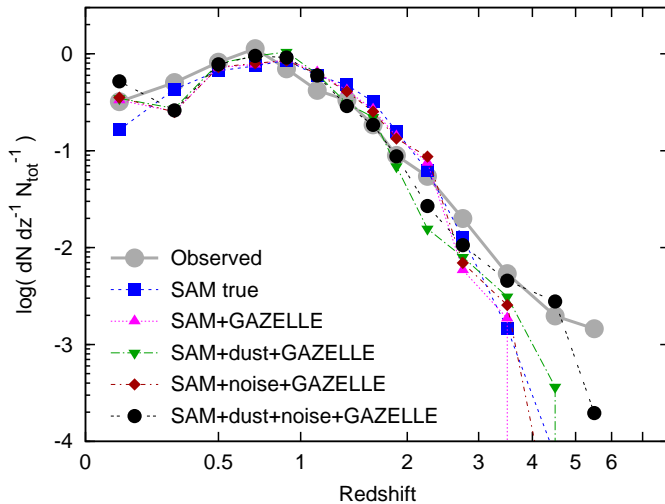
Figure 6.11: Comparison between the observed (thick grey line) projected density of galaxies per unit redshift, normalised by total number with the results from the artificial light-cones from Kitzbichler & White (2007) that are based on the Millennium simulation. The different lines represent results from different simulations also accounting for dust-extinction of photometric noise.

6.6.2 Comparison with simulated light cones

Now that we have obtained all these redshift distributions the next step is to compare them with predictions from cosmological simulations. For that purpose we use the artificial light-cones from Kitzbichler & White (2007) that are based on the Millennium simulation. Each of these light-cones covers a simulated region of 2 sq.deg., hence are well matched to the area covered by our combined sample. To make the comparison as realistic as possible, we use the simulated photometry from these light-cones and process them in the same way as we did with the real observations. We furthermore added different levels of sophistication to check how well we are able to reproduce the underlying distribution. In a first step we use the dust-free photometry, while disabling dust extinction as free parameter in the analysis. The second step was using the photometry including intrinsic dust reddening, and also allowing for reddening in the analysis. Both these steps directly operated on the ideal photometry, and hence not accounting for photometric scatter as major source of uncertainty. We remedy this in a second set of simulations where we add photometric scatter to each of the SED points. The amount of scatter was drawn from a gaussian distribution with zero mean and standard deviation Δm, which depends on the apparent magnitude and the filter:

$$\Delta m(m) = 0.03 + 3.75 \times \exp\left(0.75 \times (m - m_{\text{limit}})\right). \tag{6.29}$$

m_{limit} was chosen such to reproduce 5σ detections ($\Delta m = 0.2$ mag) for an (B, V, R, I, K) magnitude of $(26.5, 26.5, 26, 24.5, 22.5)$ mag.

The results for these different runs are shown in Fig. 6.11. Overall we find a good agreement between the underlying, true redshift distribution and the composite distribution compiled from our sample. Only towards higher redshifts do both distributions start to separate, with more observed galaxies at high redshift than expected from the simulations. However, this disagreement is solved when we account for all involved observational effects, in particular dust extinction and photometric noise. Dusty galaxies are fainter than their less dusty counterparts, leading to larger photometric uncertainties and hence to a greater chance of being associated with an incorrect redshift, leading to comparably low-redshift galaxies being scattered up to higher redshift.

We therefore conclude that our derived redshift distribution agrees with what we find for the simulated light-cones. The next step to ensure is that we also reproduce the mix of galaxy types, and the distribution of stellar masses, star formation rates, dust extinctions etc, and while we will address stellar mass functions below we leave a discussion of the other mentioned factors for an upcoming paper.
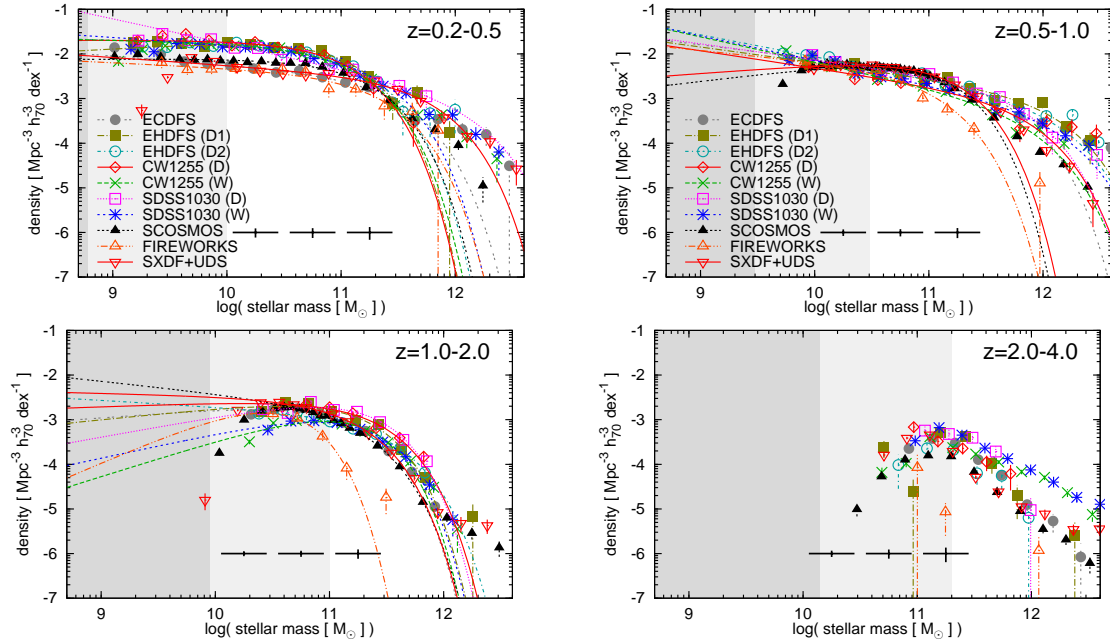
Figure 6.12: Mass functions for each of the fields in four different redshift bins $(0.2, 0.5)$, $(0.5, 1.0)$, $(1.0, 2.0)$, and $(2.0, 4.0)$. Points represent the actual data, while lines represent the best-fit Schechter functions. The grey-shaded regions mark the regions where incompleteness affects a) passive and predominantly old galaxies at the upper end of the redshift bin (light grey) and b) actively star-forming galaxies at the lower end of the redshift range (darker grey), both assuming no dust extinctions. Symbols in the lower panels are identical with those in the upper panels. Small black error bars near the top of each panel indicate the additional uncertainty for each datapoint as result of cosmic variance, assuming a rectangular field size of 10×10 arcmin, and using the recipe of Moster et al. (2010).

6.6.3 Stellar mass functions

In a next step we compare the galactic stellar mass functions for each of the fields to search for mass-dependent differences between the individual fields. This is done in four redshift intervals $(0.2, 0.5)$, $(0.5, 1.0)$, $(1.0, 2.0)$, and $(2.0, 4.0)$, each covering a timespan of ≈ 2 Gyrs in our chosen cosmology, and avoiding both the redshift extremes at very low and very high redshifts were even small redshift uncertainties have significant effect, or source densities are low, respectively.

Stellar masses for each of the galaxies is taken to be the best-match value. To account for incompleteness at low stellar masses we used the V/V_{max} technique (Schmidt, 1968) and computed, for each galaxy, its space density in the volume over which the galaxy fulfils the detection- and selection criteria for our sample. To derive this maximum volume we derived the maximum redshift out to which the best-match galaxy model would be observable. This ensures that we fully and consistently account not only for the changing luminosity distance, but also for k- and e-correction, i.e. changes to the observed magnitude due to a shift in filter position relative to the rest-frame spectrum and due to the younger galaxy age towards higher redshifts. We then fitted each mass function with a Schechter profile (Schechter, 1976). The results are shown in Fig. 6.12.

For each field we show the derived mass-function as data points with error bars (assuming Poisson noise) and our fitted Schechter profile as line. The two different gray-scale regions indicate two extreme mass completeness limits for an old, passively evolving galaxy at the upper end of the redshift range in light grey and a starbursting galaxy at the lower end of the redshift range in darker grey. For both models we do not assume any dust extinction; for the old galaxy with little to no ongoing SF we do not expect significant amounts of dust, in agreement with spectroscopic observations (Kriek et al., 2006, 2009). For the starburst on the other hand the case without dust represent the extremely blue case, as in a more general case the addition of dust would shift the mass completeness limit to higher masses.

Comparing the mass-functions we generally find good agreement between the individual fields for masses $M \lesssim 5 \times 10^{11} M_\odot$. At low redshift ($z = 0.2 - 0.5$) we find a small offset between the SCOSMOS, ECDFS and SXDF fields as compared to the remaining fields. The reason for this is that these fields were particularly chosen to be devoid of bright and hence mostly nearby sources, leading to a lower source density in our lowest redshift bin. All higher redshift bins, in which galaxies are generally faint and would not interfere with this field selection criterion, do not show the same offset, hence strengthening this interpretation.

Massive galaxies: Cluster formation at work

The population of the highest-mass galaxies with $M_{\mathrm{stellar}} \geq 3 \times 10^{11} M_\odot$ gets more prominent from $z = 0.2 - 0.5$ to $z = 0.5 - 1.0$, while quickly decreasing towards higher redshifts $z > 1.0$. A closer look at the galaxy types these galaxies were fitted with reveals, that, for instance in the case of the 641 galaxies of the ECDFS field that fall into that category, 70/641 (11%) are best described by our Sa-Sd templates, only 8/641 (1.2%) with starbursts and young post-starbursts less than 1 Gyr after the peak of the burst. All remaining galaxies or $> 87\%$ of this high-mass population are assigned either our Elliptical models or post-starburst templates, and this fraction rises to 100% at even higher masses of $M_{\mathrm{stellar}} > 10^{12} M_\odot$. As most of these galaxies in the local universe are found in dense environments such as galaxy clusters, we take this as strong evidence that with these galaxies we observe the formation of the galaxy cluster population. This agrees with spectroscopic findings by Andreon (2006) and De Lucia et al. (2009) finding well established red-sequences in several high-redshift clusters at $z = 0.4 - 0.8$. In our next higher redshift bin $z = 1.0 - 2.0$ this population has decreased in number by nearly two orders of magnitude, in fair agreement with spectroscopic results from Arnouts et al. (2007) who also find a major build-up of the quiescent galaxy population from $z = 2$ to $z = 1.2$. Also the galaxy population mix has changed, with the number of galaxies best fit by our spiral or starburst models increasing to 61/524 (12%), and ongoing starburst to 47/524 (9%). Furthermore, if we also consider our E-type model at redshifts $z > 1$ as star-forming (the specific SFR at $z = 1$ is $10^{-11} \mathrm{yr}^{-1}$, resulting in a SFR$> 3 M_\odot$ at these masses and increasing to SFR$\gtrsim 30 M_\odot \mathrm{yr}^{-1}$ at $z = 2$) this would add another 176/524 (34%) galaxies to this category. Passive post-starburst galaxies account for 233/524 galaxies (44%) at $M_{\mathrm{stellar}} > 3 \times 10^{11} M_\odot$ and for 15/29 (51%) of the most massive ($M_{\mathrm{stellar}} > 10^{12} M_\odot$) galaxies. Comparing the two redshift intervals we find a significant increase in the fraction of star-forming, yet massive galaxies from 13% at $z = 0.5 - 1.0$ to 21% and possibly up to 55% at $z = 1.0 - 2.0$. XXX Downsizing XXX.

A closer look at the distribution of galaxy types reveals, that the number of the oldest galaxies as determined by the post-starburst ages increases towards lower redshifts, while the number of galaxies with intermediate post-starburst ages remains roughly constant. This supports the scenario, that massive and passive galaxies predominantly grow by dry-mergers, as wet mergers, i.e. the merging or accretion of gas-rich galaxies would likely trigger a starburst that in turn would decrease the stellar population age, in agreement with conclusions by Bell et al. (2004) and Faber et al. (2007).

Extending this analysis to lower redshifts and trying to match them to observations of galaxies in the local universe is problematic due to the small survey volume as result of the small angular extents of most of the fields presented here. A second important factor are selection effects inherent to the individual fields, i.e. to contain no bright source at either UV/optical, X-ray and radio-wavelengths. For instance, fields containing a galaxy cluster at low- and intermediate redshift would likely be excluded for a number of reasons, e.g. due to the brightness of the most massive galaxies inside the cluster, the diffuse X-ray emission from the ICM of the cluster or potentially the radio-emission of a radio galaxy as member of the cluster. Extension to higher redshifts is not less problematic, not only due to the faintness of the galaxies at these redshifts, but also due to the limited rest-frame wavelength coverage for these galaxies. A passive galaxy with negligible UV emission shortwards of the 4000Å-break at redshift $z = 2$ for instance would, without mid-infrared photometry as in most surveys , only be detected in the H- and K-bands,
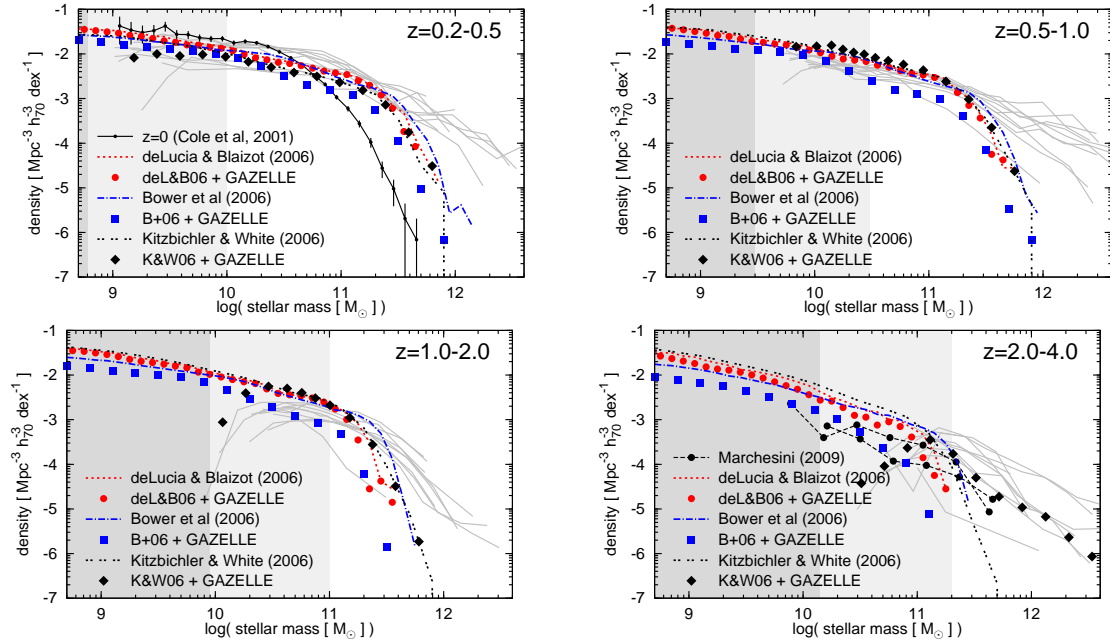
Figure 6.13: Mass functions for each of the fields in four different redshift ...

hence yielding insufficient photometry do obtain a photometric redshift, let alone a galaxy type or physical parameters. Furthermore, beyond redshift $z = 3$ we do not expect to find ANY passive galaxies since the age of the universe at that redshift is still to small to harbour "old" (age $> 1 - 2$ Gyr; see, e.g. , Newberry et al., 1990; Barger et al., 1996; Poggianti et al., 1999; Falkenberg et al., 2009a,b) galaxies.

Cosmic variance

Larger scatter at higher masses: field/cluster variations?

$z > 1$ outliers at high masses are photo-scattered lower-mass low-z galaxies

6.6.4 Comparison to semi-analytical galaxy formation models

In this section we want to compare our results, in particular our mass functions, with predictions of semi-analytical galaxy formation models. As most of our data is based on photometric redshifts and as most of our galaxies are too faint to be followed up by spectroscopy, this comparison will allow us to get a handle on systematic effects that otherwise would remain hidden. As comparison set we use the simulated photometry from De Lucia & Blaizot (2007) and Bower et al. (2006). These are the same models as presented in the comparison of true and inferred stellar parameters in Sect. 6.5.2. We supplement these with the artificial light-cones from Kitzbichler & White (2007), including both intrinsic dust extinction and our added simulated photometric noise.

For each of the catalogs we used the photometry, ran it through GAZELLE and then constructed mass function from the results, in an identical manner as done on the actual data. The results are presented in Fig. 6.13. For reference we also show the observed mass functions from Fig. 6.12 as grey lines.

As can be seen from the Fig. our mass functions derived from the observed data agrees very nicely with the mass function derived from the semi-analytical photometry as long as we restrict such comparison to the low-mass part with $M < M_\star$.

6.6.5 A combined MF across all fields

Somehow ???? combine all fields into one MF that covers all galaxies in all fields, then derive MF, fit parameters and hope the resulting values agree with the average of the individual.

with present and explain, show how well models at given redshifts are recovered, what range of uncertainties is.

6.7 Discussion

GALEV models are for M_B^* galaxies of every type. Use observed L-Z relations for SFing and passive galaxies to estimate effects for super/sub-luminous galaxies: how much higher/lower is their metallicity ? L-Z relation available for local galaxies and for z=1 (Tremonti+)

Estimate from models changes expected for L-Z and TF (and FJ) relations: luminosity changes/ metallicity changes, compare to models with $Z_\odot$ only.

Extrapolate to $z = 2.5$????

6.8 Conclusions

Chapter **7**

Young Globular Clusters in an old S0:
Clues to the Formation History of NGC 4570

R. Kotulla, U. Fritze and P. Anders
MNRAS xxx

Abstract:

We here present our first attempt to use Globular Clusters as tracers of their parent galaxy's formation history. Globular Cluster Systems of most early-type galaxies feature two peaks in their optical colour distributions. Blue-peak Globular Clusters are generally believed to be old and metal-poor. The ages, metallicities, and the origin of the red-peak Globular Clusters are being debated. We here present our analysis of the ages and metallicities of the red peak Globular Clusters in the Virgo S0 NGC 4570 using deep K_s-band photometry from NTT/SOFI (ESO program ID 079.B-0511) for the red-peak Globular Clusters in combination with HST-ACS archival data to break the age-metallicity degeneracy.

We analyze the combined g, z, and K_s spectral energy distribution by comparison with a large grid of GALEV evolutionary synthesis models for star clusters with different ages and metallicities. This analysis reveals a substantial population of intermediate-age (1–3 Gyr) and metal-rich ($\approx$ solar metallicity) Globular Clusters. We discuss their age and metallicity distributions together with information on the parent galaxy from the literature to gain insight into the formation history of this galaxy.

Our results prove the power of this approach to reveal the (violent) star formation and chemical enrichment histories of galaxies on the basis of combined optical and near-infrared photometry.

7.1 Introduction

Globular Cluster (GC) systems are now recognized as powerful tracers of their parent galaxy's formation history (West et al., 2004; Fritze, 2004; Brodie & Strader, 2006). From their age and metallicity distributions one can reconstruct the parent galaxy's (violent) star formation and chemical enrichment histories all the way from the very onset of star formation in the Early Universe to the present.

Most early-type galaxies show bimodal color distributions for their GC systems (e.g. Gebhardt & Kissler-Patig, 1999; Kundu & Whitmore, 2001a,b; Peng et al., 2006): A universal blue peak and a red peak for which the color and height relative to the blue peak vary from galaxy to galaxy. The blue peak GCs are generally agreed to be old and metal-poor, the properties and origin of the red peak GCs is still unclear. Scenarios for the formation of the red peak GCs range from *in situ* formation of a secondary more metal-rich population of GCs within their parent galaxy shortly after the first one (Forbes et al., 1997) to major gas-rich mergers (e.g. Ashman & Zepf, 1992) and hierarchical accretion events involving enough gas to trigger the formation of new GC populations (e.g. Beasley et al., 2002). The age distributions of the secondary GCs predicted by these different scenarios are different: almost as old as the old and metal-poor blue peak GCs but more metal-rich than those in the first case, of some intermediate age reflecting the time of the gas-rich merger in the second case, and broad or multi-peaked for a series of hierarchical accretion events involving gas in the third case. The metallicities of the secondary, and eventually any further generations of GCs should reflect the ISM abundances in the merging or accreted objects at the time of merging or accretion. They could, at most, be somewhat higher for those GCs that formed late enough in a burst to already incorporate some enrichment during the burst itself. Hierarchical accretion without gas and the formation of new generations of GCs cannot explain the red-peak GCs since dwarf galaxies known so far contain old and metal-poor, hence blue GCs.

To determine the ages and metallicities of the red-peak GCs in one of those early-type galaxies with clear bimodality in its optical GC colour distribution is the aim of our present investigation and should help constrain the formation scenario for the red-peak GCs in this particular galaxy.

7.1.1 Our approach to lift the age-metallicity degeneracy

Optical data alone do **not** allow to disentangle ages and metallicities: Colour-to-metallicity transformations have to assume an age, while colour-to-age transformations are only valid for one metallicity. The degeneracy, however, can be broken by including near-infrared data that are more sensitive to metallicity rather than to age.

Anders et al. (2004a) used extensive artificial star cluster tests and showed that observations in three passbands for GCs in dust-free E/S0s (or four passbands for young star clusters in dusty environments), spanning as wide as possible a wavelength-basis (U through K) and including at least one NIR-band (e.g. H or K) with photometric accuracies ≤ 0.05 mag in the optical and ≤ 0.1 mag in the NIR allow to disentangle ages and metallicities and to determine **individual GC metallicities to** $< \pm 0.2$ **dex, and ages to** $< \pm 0.3$ **dex**. I.e., these data allow to distinguish $\leq 7\,$Gyr old GCs from those $\geq 13\,$Gyr old.

Similar studies also using NIR-data to determine ages and metallicities of globular clusters have only been done for a few galaxies until now (Puzia et al., 2002; Kissler-Patig et al., 2002; Hempel et al., 2003; Larsen et al., 2005; Hempel et al., 2007). More than half of these galaxies were found to host a population of GCs that is younger and/or more metal-rich than the ubiquitous old and metal-poor GC population.

Some of these previous studies discussed average properties of the blue and red peak GCs by investigating the mean colours of blue and red GC. We here derive ages, metallicities, and

masses for every individual cluster with (g, z, K) photometry. This also enables us to study whether there is more than one generation of GCs in the red peak, to look for correlations of these parameters, and investigate their spatial distributions.

We have chosen the Virgo cluster S0 galaxy NGC4570 (= VCC1692) for our pilot study because it has archival $g-$ and $z-$band data from the ACS Virgo Cluster Project (Peng et al., 2006) that show two very clear peaks in the optical $g - z$ colour distribution of its GC system. The red peak is about two thirds the height of the blue one, both have very similar widths. In particular, the optical colour distribution shows no evidence for substructure within the red peak or for a third peak. The mean $g - z$ colours of the blue and red peaks are 0.88 ± 0.01 and 1.38 ± 0.03, respectively, with a fraction of 39 % of all the 122 GCs detected belonging to the red peak. NGC4570 has $B_T = 11.82$ mag (Côté et al., 2006), which at a kinematic distance modulus of $BDM = 31.16$ (Mei et al., 2007) gives it an absolute $M_B = -19.3$ mag, i.e. it is an average luminosity S0.

van den Bosch et al. (1998) and van den Bosch & Emsellem (1998) detected a nuclear stellar disk with a radial extent of ≈ 7 arcsec. From both spectroscopy based on Hβ and [MgFe] line indices as well as photometry in U, V and I they estimate an age of the stellar population inside that structure of ≤ 2 Gyr and a metallicity close to solar.

From the same ACS Virgo Cluster survey that reported the GC colours Ferrarese et al. (2006) show that NGC 4570 shows a nested-disk structure composed of two morphologically distinct inner and out disks. Detailed isophotal analysis reveals a blue stellar ring with radius 150 pc, but less than 7 pc wide, around the nucleus. This ring leaves a clear imprint on the major axis $g-$band surface brightness profile (cf. Fig. 104 of Ferrarese et al., 2006). The structure of this inner region was discussed by van den Bosch & Emsellem (1998) in the context of secular bar evolution.

7.2 Models

We used our GALEV evolutionary synthesis models for star clusters (Schulz et al., 2002; Anders & Fritze, 2003) to compute a large grid of models for five different metallicities $-1.7 \leq$ [Fe/H] $\leq +0.4$ and ages between 4 Myr and 16 Gyr in time-steps of 4 Myr. Our models are based on Padova isochrones and a Salpeter (1955) initial mass function (IMF) with a lower-mass limit of $M_{low} = 0.10\,M_\odot$ and upper mass limits between $M_{up} \approx 50 - 70\,M_\odot$ depending on metallicity.

Since early-type galaxies in general, and NGC 4570 in particular, do not contain significant amounts of dust we did not include internal extinction into our grid but assume $E(B - V) = 0$ throughout. We therefore only need three filters (HST F475W, F850LP and SOFI K_s) to determine all relevant parameters (age, metallicity, and mass) for each cluster.

Note that we do not depend on color transformations from the HST to Standard Johnson filters. For optimal accuracies, our models first compute spectra as a function of time, that later are convolved with the corresponding filter curves, in this case for the HST F475W and F850LP filters and the SOFI K_S filter, to yield the final magnitudes.

Figure 7.1 shows examples of Spectral Energy Distributions (SEDs) for star cluster models at two different ages of 1 and 13 Gyr, and all five metallicities for each of them. The SEDs shown have been scaled to match the g-band magnitude of a solar metallicity star clusters with initial mass $10^6\,M_\odot$. Fluxes in all filter bands of course scale with cluster mass. At both ages the lines representing the different metallicities split up towards both longer and shorter wavelengths. We exploit this to separate the effects of age and metallicity.
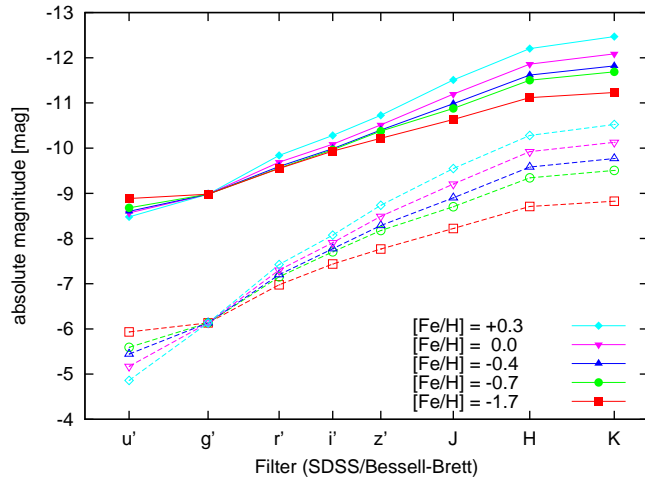
Figure 7.1: Spectral energy distributions (SEDs) for star cluster models at two different ages of 1 Gyr at brighter and 13 Gyr at fainter absolute magnitudes, respectively, and 5 different metallicities ranging from $1/50\,Z_\odot$ to $2.5\,Z_\odot$ in each case. All SEDs have been scaled to match the g-band magnitude of the solar metallicity model with initial mass $10^6\,M_\odot$.

7.2.1 AnalySED

To obtain accurate ages, metallicities and masses for the detected clusters we used the SED analysis tool AnalySED developed by Anders et al. (2004a). This program compares the observed SED of a star cluster with a large grid of model SEDs and finds the best-fitting match to the observations. In this process ages and metallicities for each cluster are derived from the observed spectral energy distributions. Once those parameters are found the observed brightnesses are translated into masses.

Since we keep the full χ^2 distribution and not only the best fitting solution we are able to determine the 1σ uncertainties for all our derived parameters by summing up the normalized probabilities sorted from the highest to the lowest values until an integrated probability of 0.68 is reached. The uncertainty ranges for the different parameters are then given by their extreme values reached within this 1σ probability range (cf. Anders et al. (2004a) for details of the method and e.g. Anders et al. (2004b) for an earlier application).

7.3 Observations and data reduction

7.3.1 Near-infrared data

We observed NGC 4570 in two subsequent nights (2nd to 4th March 2007) using the ESO-NTT equipped with the SOFI near-infrared imager. This instrument consists of a Hawaii HgCdTe 1K×1K chip and 0.288″ pixels yielding a field-of-view of $\approx 5 \times 5$ arcmin. To avoid non-linearities of the detector we chose an detector integration time (DIT) of 6 seconds. 12 of these exposures were internally averaged by the readout electronics, resulting in an exposure time per frame of 72 seconds. Since NGC 4570 has an extent of only $4' \times 1.1'$, we could use one half of the chip for the object while obtaining a simultaneous sky-exposure in the other half of the chip, swapping sides after each exposure and applying small shifts to avoid contamination by bad pixels.

Reduction

Data reduction largely followed the procedures outlined in the SOFI instrument handbook. The individual frames were corrected for the inter-row cross-talk and then corrected with a flat-field to remove pixel-to-pixel sensitivity variations. These flat-fields consisted of three different components: dome-flats corrected for their characteristic on-off pattern using the recipe provided on

the NTT-SOFI web-site; illumination correction surface obtained from repeated observations of a standard star at different positions of the detector to remove the illumination gradient introduced by the dome flats; a "super-flat" created from the sky frames of both nights to remove remaining inhomogeneities and cosmetics from dust on the filter. Since the observations were carried out under non-photometric conditions we used the data from the instruments web-page[15] to obtain the illumination correction.

After flat-fielding all the frames we estimated the background in all frames by iteratively clipping values larger then 3σ above the mean of the full frame. We then used six sky-frames that were obtained closest in time, scaled each of them individually to the sky-value of the object frame and subtracted their average from the object frame. We varied the number of frames to average, but found that six is the best compromise between signal-to-noise and artifacts introduced by the pupil-rotation of the alt-az mounted telescope.

All the sky-subtracted frames were aligned by matching coordinates of several background galaxies in each frame to coordinates in a reference frame; we used galaxies instead of stars because due to the high galactic longitude there were too few stars to allow for proper matching. In a final step we stacked all but those frames with a sky-value deviating more than 2σ from the average.

Combining all those exposures from both nights results a total exposure time for our K-band image of $t_{exp} \approx 25$ ks ≈ 9.5 hours.

Photometric calibration

We could not base our photometric calibration on standard stars, because during both nights observations were hampered by a varying degree of cloudiness. We therefore compared brightness profiles of the host galaxies with calibrated data from the 2MASS survey (see Skrutskie et al. (2006) for a review) and own observations obtained later with the SIRIUS instrument at the InfraRed Survey Facility at the South African Astronomical Observatory. Both results showed excellent agreement within the error ranges of $\Delta m_K \approx 0.03$ mag, that can easily be explained by minor differences in the filter transmission curves. However, we account for this uncertainty by adding the calibration error in quadrature to the photometric errors. Calibration of exposures from both 2MASS and SIRIUS finally relied on standard stars from the Persson et al. (1998) catalog, so our K-band magnitudes are in the VEGA magnitude system.

This allows us to detect point sources down to $m_{Ks} \approx 21$ mag at the 10σ-level, making the depth of our observations comparable to deep surveys obtained with the same configuration, e.g. the K20 survey (Cimatti et al., 2002b).

7.3.2 HST data

The HST data consisted of two datasets taken with the Advanced Camera for Survey (ACS) on-board the Hubble space telescope as part of the ACS Virgo cluster survey (Côté et al., 2004). For both datasets with filters F475W ($\approx$ SDSS g) and F850LP ($\approx$ SDSS z) we relied on the On-the-fly reduction performed automatically upon retrieval from the MAST Archive[16] and using the best reference files. We then performed an additional alignment step to ensure a match of coordinates in both frames as good as possible.

Calibration of the HST data was done using the appropriate header entries from the fits-files. For details on this process see the HST Data Handbook (Pavlovsky et al., 2005). To avoid any unnecessary conversion between different magnitude systems, we performed photometry in both HST filters using ST magnitudes.

---

[15]http://www.ls.eso.org/lasilla/sciops/ntt/sofi/
[16]http://archive.stsci.edu/

7.3.3 Cluster selection

Globular Cluster candidates were selected from the HST images using SExtractor (Bertin & Arnouts, 1996). A valid detection is characterized by at least 4 adjacent pixels with intensities of 3σ above the local background, resulting in two catalogs with > 1000 objects each. We then cross-correlated these catalogs to remove remaining spurious detections as e.g. remaining cosmics.

For the ≈ 330 remaining candidates we derived intrinsic source sizes using the ISHAPE-package from BAOLAB (Larsen, 1999). This algorithm in our case convolves a King profile with a fixed concentration parameter $c = \frac{r_t}{r_c} = 30$ (or equivalently $\log(\frac{r_t}{r_c}) \approx 1.5$) but variable radii with the instrumental point spread function (PSF) created by TinyTim (Krist, 2004) and determines the best fitting radius via χ^2-minimization. We rejected all objects appearing stellar-like (intrinsic radius $r_i < 0.2$ px ≈ 0.8 pc at a distance $D \approx 17$ Mpc (Tonry et al., 2001), 17 objects) or too extended ($r_i > 5$ px ≈ 20 pc, 37 objects) to be a globular cluster.

7.3.4 Photometry

For the remaining ≈ 280 GC candidates we obtained aperture photometry using commands from the ESO-MIDAS package. For the HST images we used an aperture radius of 15 pixels and a sky annulus from 17 to 20 pixels. To compensate for the low-intensity extended wings of the ACS PSF we applied an aperture correction of 0.067 (0.082) mag to the F475W (F850LP) magnitudes according to the tabulated Enclosed Energy values of 0.940 (0.927) determined by Sirianni et al. (2005). Although these factors still depend both on the position of the GC on the detector and intrinsic colour of the GC, the implied uncertainties are much smaller than the photometric uncertainties and can therefore be neglected.

To derive photometry for the ground-based K_s-imaging we transformed the coordinates from the combined HST catalog into physical coordinates in the K-image and then used these coordinates as center positions for the photometry. Using SExtractor to also obtain a K-band detection catalog yielded less reliable results and missed many of the sources found with the superior resolution of the HST. We used an aperture of $2''$ and an aperture correction derived from stellar photometry within the field-of-view of (0.2 ± 0.03) mag. For 117 candidates we could not derive a K-band magnitude, mostly because they were not included within or too near to the edge of the K-band field-of-view, and in some cases because they were out-shined by the bright galaxy background.

To remove last outliers we introduced a colour selection criterion of $(g_{ST} - z_{ST}) \leq 1.0$ and $(z_{ST} - K_{s,Vega}) \leq 4.5$, covering the color range of our models. We further removed all candidates with magnitude errors ≥ 0.1 mag in g and z and ≥ 0.3 mag in K_s (see Fig. 7.2 for the distributions of magnitude uncertainties as a function of luminosity in all three bands). This leaves us a final sample of 63 *bona fide* GCs.

7.4 Results

For three selected clusters we present the detailed χ^2 distributions in Fig. 7.3. This Fig. demonstrates that the reason for the uncertainties in the derived parameters are mostly relatively to isolated secondary peaks in the probability distribution. The cluster in the upper panel has a well-defined best-fit age of $1.12^{+0.90}_{-0.33}$ Gyr, a metallicity of $[Fe/H] = -0.3^{+0.3}_{-0.4}$ and a derived mass of $(2.64^{+1.59}_{-0.25}) \times 10^5$ M$_\odot$. Its χ^2 value for the best solution with $[Fe/H] = -0.4$ is a factor of 10 better than that for the somewhat lower metallicity $[Fe/H] = -0.7$ paired with slightly higher age. The cluster in the middle panel has an age of $16.0^{+0.00}_{-10.9}$ Gyr, a metallicity of $[Fe/H] = -1.7$ and a derived mass of $(4.81^{+0.00}_{-2.87}) \times 10^5$ M$_\odot$. It is clearly seen that the old age low metallicity
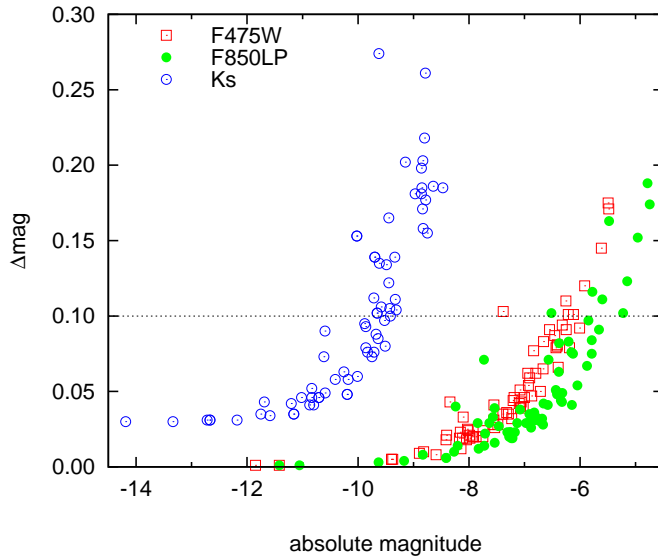
Figure 7.2: Photometric errors as function of absolute magnitudes for the HST filters F475W and F850LP and the NTT filter K_s.

solution has a χ^2-value about two orders of magnitude better than that for any other metallicity. Also the intermediate age solution for the same metallicity has a significantly higher χ^2. The cluster in the lower panel has an age of $5.62^{+10.4}_{-4.39}$ Gyr, a metallicity of $[\text{Fe/H}] = -1.7$ and a derived mass of $(9.96^{+13.6}_{-7.33}) \times 10^5$ M$_\odot$. Note the large age uncertainty for this cluster, that directly influences the derived mass of the cluster. Again, however, only the lowest metallicity gives an acceptable fit. Note that since our grid of models does not sample the covered metallicity range finely enough. Therefore only the lowest metallicity model results in a good fit hence we do not give errors on metallicity for those two clusters.

These three GCs represent typical cases for a very good fit with a fairly well constrained age, a securely old (> 5 Gyr) but less well constrained age, and a poorly constrained age, respectively.

7.4.1 Ages

Figure 7.4 shows the age distribution of all the GCs from our final sample. At old ages (age $> 10^{10}$ yr) we see the analogues to our old Milky Way GCs formed during an early phase of galaxy formation.

We also find a significant population of younger GCs with ages of $1 - 3$ Gyr that must have formed during some violent star formation event. Possible candidates for such events are massive bursts of star and star cluster formation that come along with a merger of two gas-rich spirals or the accretion of a gas-rich companion.

While the light grey histogram in Fig. 7.4 shows the age distribution of all our GCs, the dark histogram shows metal-poor GCs only. The old peak contains GCs with $[\text{Fe/H}] = -1.7$ close to the metallicity of the halo GCs in our Milky Way, but also more metal-rich GCs while the intermediate-age peak is predominantly made up by GCs with metallicities higher than $[\text{Fe/H}] = -1.7$.

A detailed look at the 8 GCs in the log(age) bins 8.65-8.9 and 9.15-9.4 shows that within their error bars they might as well be part of the 8.9-9.15 Gyr peak. The GCs in the age bins 9.4-9.9, on the other hand, could, within their 1σ uncertainties as well be part of the truely old, i.e. $10 - 13$ Gyr population.
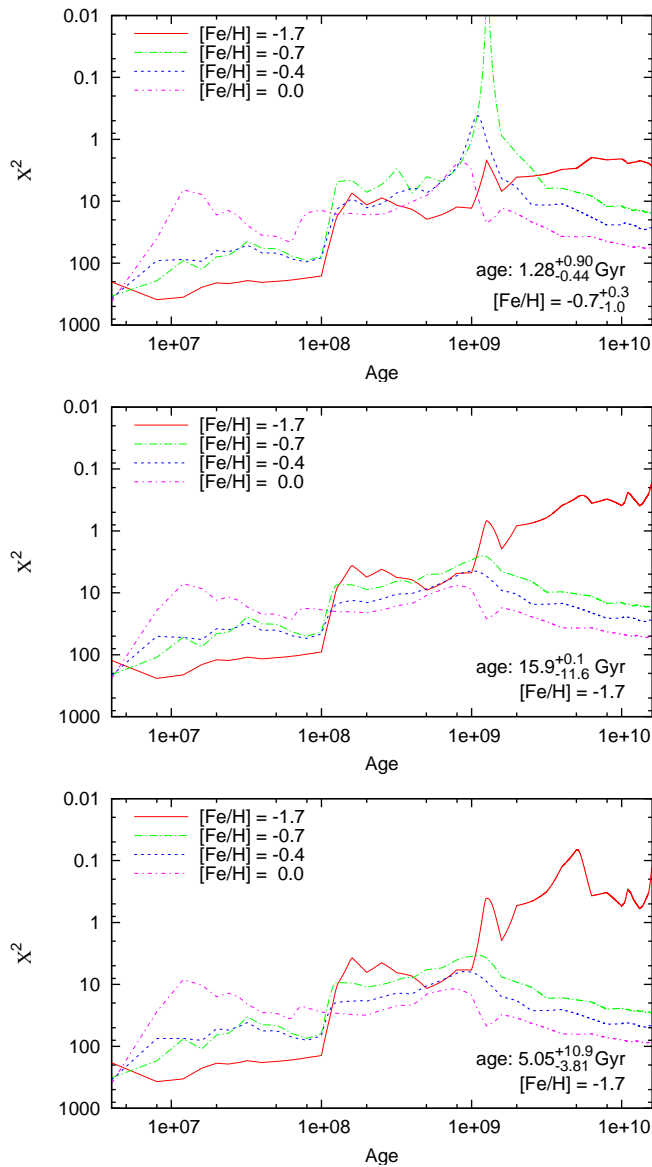
Figure 7.3: χ^2 values as function of metallicity and age for 3 different clusters.
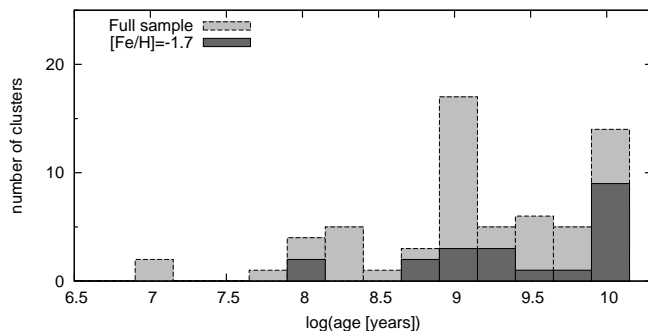
Figure 7.4: Age distribution of our detected globular clusters.
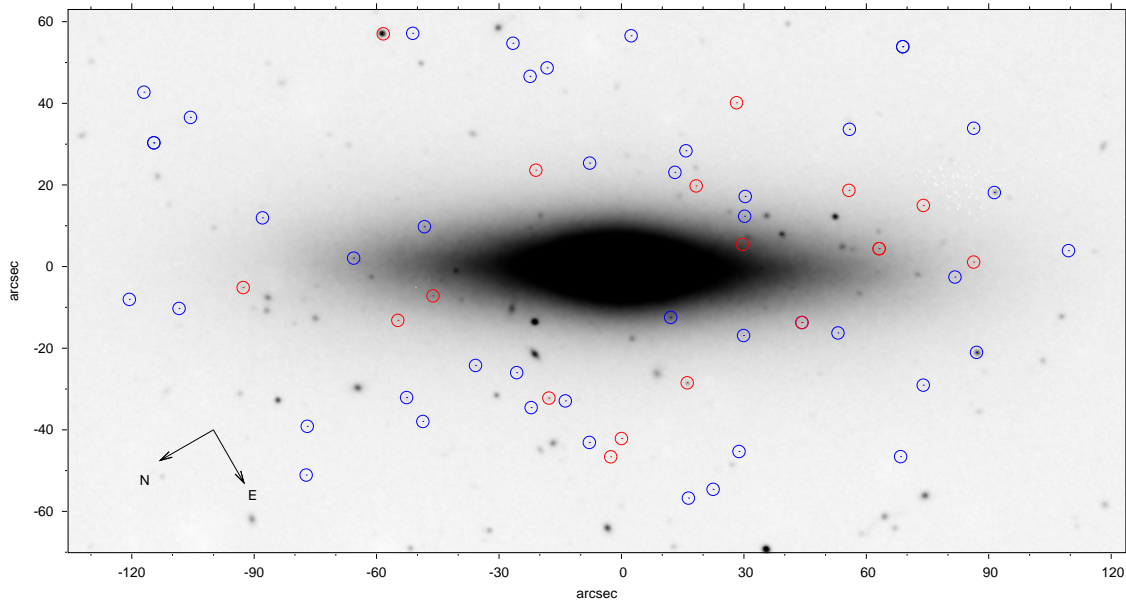
Figure 7.5: Spatial distribution of our Globular Cluster sample, overlayed over our K-band image obtained with NTT/SOFI. Blue circles mark GCs with best-fit ages < 3 Gyr, while red circles mark GCs older than 3 Gyr. Most of the bright sources are either stars or (in most cases) background galaxies, that are resolved on the HST images.

Old and metal-rich GCs

4 out of the 10 old clusters have SEDs best described by solar metallicity. This, however, does not seem very plausible, since it would require an incredibly fast global chemical enrichment to solar metallicity within a timescale of only about a Gyr. On nearer inspection, one of these four GCs has a large age uncertainty ranging down to 1.25 Gyrs, so it might well belong to our newly detected intermediate age population. The three remaining GCs are located within the extent of the host galaxy, so that their photometry might still be contaminated by light from the surrounding galaxy. This is also supported by the poor quality of their SED-fit with remarkably low unnormalized integrated probabilities $\lesssim 10^{-10}$.

7.4.2 Spatial distribution

There is no obvious difference in the spatial distributions of the old and younger GCs, as seen in Fig. 7.5. GC numbers, however, are too small for meaningful statistical tests.

We note that the bulk of the GCs we detect belong to the red peak of the optical GC colour distribution. Only the very brightest GCs from the blue optical peak are detected in K_s and, hence, part of our sample.

7.4.3 Metallicities

The metallicity distribution (Fig. 7.6) is dominated by a large population of 27 out of 63 clusters with solar metallicity, only 21 clusters have very low metallicities of $[\mathrm{Fe/H}] = -1.7$ in the range of Galactic old GCs.

The fact that we find only relatively few old and metal-poor GCs can be explained as a selection effect: Since we only include clusters that were also detected and also have good photometry in
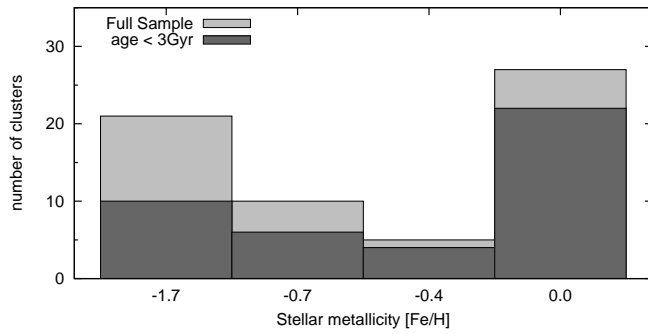
Figure 7.6: Metallicity distribution of our GCs. Light grey histogram: all GCs, dark: GC with ages younger than 5 Gyr.
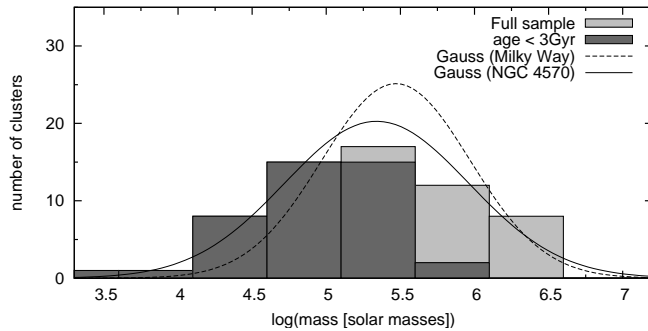
Figure 7.7: Mass distribution of the GCs in NGC 4570. The light grey histogram is for all GCs from our sample, the dark one for the subsample of GCs younger than 3 Gyr. The solid line is a Gaussian fit to our unbinned GC mass distribution with a median of $\log(\langle M_{GC}[M_\odot]\rangle) = 5.3$ and $\sigma(M_{GC}) = 0.6$ dex, normalized to the number of GCs in our sample. The dotted line gives the Gaussian for the Milky Way GCs with $\log(\langle M_{GC}[M_\odot]\rangle_{MW}) = 5.47$ and $\sigma_{MW}(M_{GC}) = 0.50$ dex, normalized to the number of GCs in our sample.

K_s we prefer intrinsically red objects. Old Milky Way-type globulars, however, have blue colors due to their low metallicity and are hence not included in our sample. Indeed, the bulk of all our GCs, and of the metal-rich ones in particular, are younger than 3 Gyr, again a selection effect, since 3 Gyr old GCs are brighter than 13 Gyr old ones by 1.1 to 1.3 mag, depending on metallicity and filter.

7.4.4 Masses

Fig. 7.7 shows the mass distribution of our GCs, again for the full sample in light grey and for the subsample of GCs with ages < 3 Gyr in dark grey. The mass distribution of the full GC sample clearly looks like a Gaussian with a turn-over mass around $\log(\langle M_{GC}[M_\odot]\rangle) = 5.3$ and $\sigma(M_{GC}) = 0.6$ dex, very similar to the turn-over of the GC mass function in the Milky Way which occurs at $\log(\langle M_{GC}[M_\odot]\rangle_{MW}) = 5.47$ with $\sigma_{MW}(M_{GC}) = 0.50$ dex (Ashman et al., 1995). The fact that the mass distribution of the young GCs does not extend to the same high masses as that for the old ones cannot be a selection effect, since more massive clusters of young age would be easily detectable if they were there. It seems that the secondary event that formed the ∼ 2 Gyr old GCs in NGC 4570 did not form the GCs with the same mass function as the old GC population. Careful modeling of cluster destruction effects were required to really prove this conjecture. Dynamical friction, which is most important for massive clusters, might have preferentially destroyed those, in particular if the secondary GC population were more centrally concentrated than the primary one, as previously found in many, but not all, bimodal GC systems. In addition to that we might have missed massive GCs in front of the bright galaxy background if they either were initially closer to the centre (mass segregation) or driven towards the centre by dynamical friction faster than the lower mass ones.
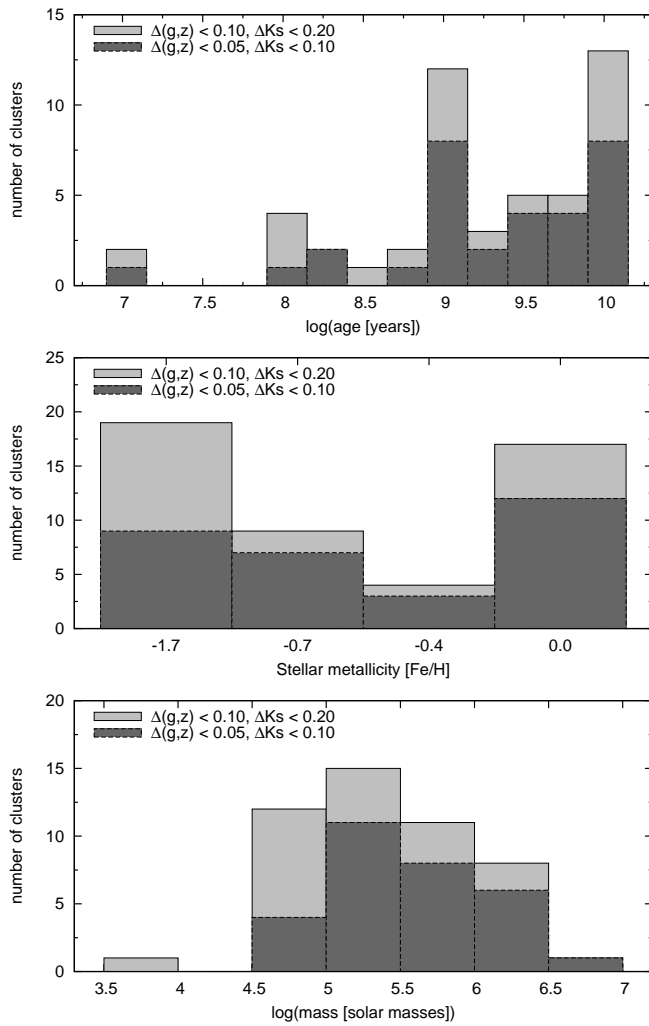
Figure 7.8: Age, metallicity, and mass distributions for the subsample of GCs with high (light grey) and very high (dark grey) photometric accuracies.

7.4.5 The subsample of GCs with high photometric accuracy

In Fig. 7.8 we present our results for the age, metallicity, and mass distributions of the subset of GCs from our sample with the best photometric accuracies: $\Delta g, \Delta z < 0.10$, $\Delta K_s < 0.20$ mag and $\Delta g, \Delta z < 0.05$, $\Delta K_s < 0.10$ mag, respectively. This Fig. shows that our results are unaffected by the slightly higher uncertainties in our full sample. The age, metallicity, and mass distributions are robust. High photometric accuracies are only achieved for the brightest clusters. Hence it is no surprise that the high accuracy subsample lacks some of the low mass GCs.

7.4.6 Alternative solutions

Ages for fixed metallicities $[\mathrm{Fe/H}] = -1.7$ **or** $[\mathrm{Fe/H}] = 0.0$

In this subsection we explore to what extent our results change if we artificially restrict the allowed parameter range. Our aim is to see whether our basic finding of $\sim 1 - 3\,\mathrm{Gyr}$ old/young GCs in NGC 4570 is affected by these assumptions.

If we limit the available parameter range to a metallicity $[\mathrm{Fe/H}] = -1.7$ (see. upper panel of Fig 7.9 for comparison) many clusters are better described by older ages. These are needed to counter-balance the bluer colours of the lower metallicity models. The older ages, in turn, also result in slightly higher masses. However, the principle structure of the age distribution
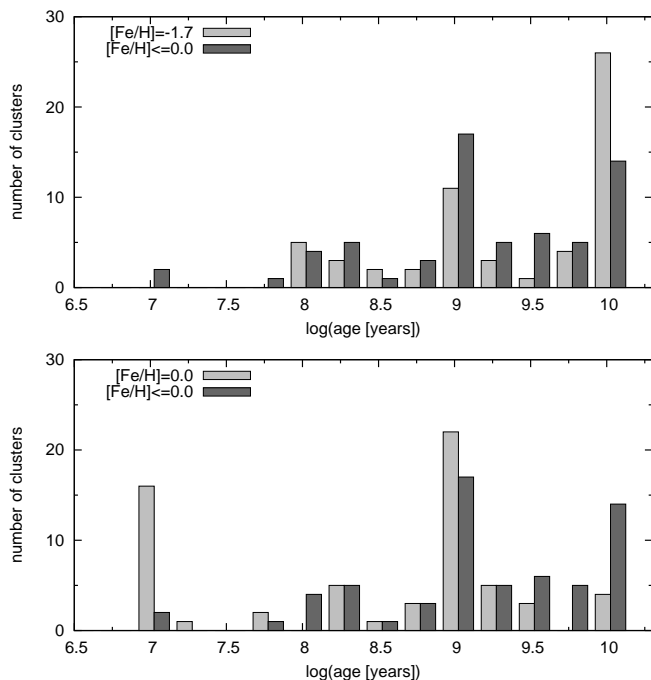
Figure 7.9: Age distributions of our GC sample under the assumption of a fixed low metallicity [Fe/H] = −1.7 (upper panel) and [Fe/H] = 0.0 (lower panel). Bin sizes are the same as in Fig 7.4, only the two histograms for free and restricted metallicities are plotted next to each other to better reveal the differences.

and, in particular, the peak at intermediate ages of 1–3 Gyr remain. This "worst-case" scenario emphasizes the robustness of our cluster age determination.

We also determined ages for a metallicity fixed to the solar value and again found little difference compared to the original results (see lower panel of Fig. 7.9). Although clusters on average get slightly younger in this case, the peak of the distribution around 1–3 Gyr still remains, only the tail towards younger ages become slightly more pronounced.

We conclude, that our finding of a substantial population of intermediate-age GCs with ages of order 1 − 3 Gyr and approximately solar metallicities in NGC 4570 is very robust, even under extreme test changes in metallicity.

7.5 Discussion

7.5.1 Formation scenarios for red-peak GCs

Our detection of a substantial population of 1 − 3 Gyr old GCs is most naturally explained in terms of a merger or accretion event which involved significant amounts of gas and triggered a strong starburst in which, together with some hitherto undetected population of field stars, the presently observed GC formed. The star clusters we find have all the properties of GCs, they are compact with half-light radii of order 3–7 pc and have masses in the range of typical GC masses. Those clusters that we observe with ages of 1 − 3 Gyr certainly are only a small fraction of all the star clusters formed in such an event. They have already survived the most dangerous phase in their lives, the infant mortality and dynamical restructuring phase after the first SNe have expelled the gas left-over from their formation. They probably have also survived the violent relaxation phase that restructured the merging/accreted galaxies into the presently observed S0. The sheer number of young GCs requires substantial gas masses involved and their high metallicities indicate that it could not have been a minor accretion event involving e.g. an SMC type galaxy swallowed by some major gas-free/poor E/S0/Sa type galaxy. Solar

metallicities in the ISM out of which the new GCs were formed require at least one Sbc- or Sb-type progenitor. Sa-type galaxies have higher metallicities, but lack the required amounts of gas to fuel the starburst.

It is intriguing that the age we find for the young GCs agrees very well with the stellar population age of ≤ 2 Gyr estimated by van den Bosch & Emsellem (1998) for the nuclear stellar disk in the host galaxy (van den Bosch et al., 1998; van den Bosch & Emsellem, 1998; Scorza & van den Bosch, 1998). Our detection of a substantial population of GCs does not, however, support the internal bar instability scenario they favor for the formation of this nuclear stellar disk. Nuclear stellar disks are in fact seen in dynamical simulations of galaxy mergers/accretion events (cf. Bournaud et al., 2004; Springel & Hernquist, 2005), as well as in real merger remnants, e.g. in Arp 214 and Arp 224 (Jog & Chitre, 2002). The fact that NGC 4570 does not feature any obvious tidal tails can be understood as a consequence of its location in a high galaxy density region of the Virgo cluster, where tidal tails are shred down as soon as they start to develop.

We hence suggest that the young GCs we detected and the nuclear stellar disk in NGC 4570 have been formed by the same merger/accretion event.

7.6 Future prospects

HST NIC3 data would be very valuable in order to detect young GC closer to the centre of NGC 4570 and see whether the young GC system is more centrally concentrated than the old one or not. Of equal value would be an extension of the SED to shorter wavelengths. As can also be seen from Figure 7.1 for both old and young clusters the U-band is both sensitive to ages and metallicity and can help discriminate between both. However, imaging in further intermediate band-passes would only be necessary for other galaxies containing dust (for further details see Anders et al., 2004a). Spectroscopy, albeit challenging, would allow to confirm and eventually further constrain the photometric ages, metallicities and masses for these young GCs, while abundance ratios, e.g. of $[\alpha/Fe]$ could give further clues to the progenitor galaxies and to the star cluster formation scenario.

A natural next step seem to combine our results from this GC analysis with a detailed analysis of the stellar population across the main body of the galaxy to evaluate the contribution (and location) of field stars from the age range of the young GCs. This could either be done on the basis of multi-band imaging in a pixel-by-pixel analysis of the kind we did for the Tadpole and Mice galaxies (de Grijs et al., 2003b) or analyzing the integrated spectrum with starburst models as we have done for the ~ 1 Gyr old merger remnant NGC 7252 (cf. Fritze & Gerhard, 1994a,b).

7.7 Summary

On the basis of deep NTT-SOFI K_s- band imaging in conjunction with archival HST ACS deep optical imaging we identified a substantial population of star clusters with ages in the range 1 – 3 Gyr and metallicities around solar in the Virgo S0 galaxy NGC 4570. All these clusters are compact with half-light radii in the range 3–7 pc and have masses of order 10^5 M$_\odot$. They have successfully survived their infant mortality phase and, hence, merit to be called young GCs. The clusters we detect in K_s make up an important fraction of the red peak of the bimodal GC optical colour distribution reported by Peng et al. (2006) from the ACS Virgo Cluster Survey.

We performed a number of test that showed our results to be robust.

The ages we find for the young GCs agree well with stellar population ages previously determined for the nuclear stellar disk in NGC 4570. We suggest that both the nuclear stellar disk and the young GC population have been formed in the same merger/accretion event. The presently observed GCs certainly are only a small part of the originally formed star cluster population,

since only a small fraction of clusters usually survives until ages of ≥ 1 Gyr. The sheer number of young GCs suggests that the merger/accretion event must have involved substantial gas masses, the high metallicity of the new GCs suggests that the gas involved in this event must have been enriched at least to a level observed in present-day Sbc galaxies.

Our analysis has shown that GC populations are valuable tracers of their parent galaxy's star formation, chemical enrichment, and mass assembly histories.

Clearly further analyses, in particular of the stellar population across the main body of NGC 4570, are required before we fully understand the details of the scenario that gave rise to the present-day Virgo S0 NGC 4570 with its nuclear stellar disk and young GCs.

Rescuing the Initial Mass Function for Arp 78

Ralf Kotulla, Uta Fritze & John S. Gallagher III

Abstract:

We present deep R, and narrow-band Hα images of Arp 78 obtained with the WIYN 3.5-m telescope on Kitt Peak. GALEX observations had shown a very extended UV structure for this system, reaching beyond the optical radius of Arp 78 and also beyond its previously known H$\alpha-$radius. Our new Hα data now show agreement not only with the spatial extent of the near- and far-UV maps, but also in terms of structural details. Star formation rates derived from L(Hα) and L(FUV) are in agreement, showing that in this case the upper stellar IMF in the UV-bright outer arm is relatively normal. The star forming sites in the outer arms are younger than $\sim 15\,$Myr and massive enough to properly sample the IMF up to high masses.

8.1 Introduction

A major surprise from early data taken with the GALEX ultraviolet explorer satellite was the detection of extended near- and far-UV (NUV, FUV) emission in the extreme outer environment of star-forming galaxies like M83 and NGC 4625 (Thilker et al., 2005; Gil de Paz et al., 2005). Other examples include both apparently undisturbed spirals where the UV emission reveals the inside-out growth of the stellar disk and galaxies that are surrounded by filaments and substructure indicative of tidal encounters with active star formation (SF) going on within these filaments.

An analysis 189 disk galaxies (types S0-Sm) within 40 Mpc from the GALEX Atlas of Nearby Galaxies (Gil de Paz et al., 2007; Thilker et al., 2007) establishes that extended UV (XUV) galaxies are surprisingly common, showing up in $> 30\%$ of this sample. Two classes of XUV galaxies are defined from this sample. Arp 78 (NGC 772), that we study here, belongs to the XUV-type 1 class of objects, that make up $\geq 20\%$ of the 40 Mpc sample and of which over 75% show optical or H ɪ morphological evidence for recent interactions or external perturbations. A prototype of this class is M83.

These galaxies have structured, UV-bright, optically faint emission features beyond their optical radii and in regions beyond the traditional SF threshold. The latter is defined as the surface brightness contour corresponding to $\Sigma_{\mathrm{SFR}} = 3 \times 10^{-4}\,\mathrm{M_\odot\,yr^{-1}kpc^{-2}}$, evaluated at 1 kpc resolution. With Kennicutt (1998)'s star formation rate (SFR) calibration, this threshold corresponds to $\mu_{\mathrm{FUV}} = 27.25$ ABmag/arcsec^2 or $\mu_{\mathrm{NUV}} = 27.35$ ABmag/arcsec^2. These UV surface brightness thresholds correspond to an H ɪ column density threshold for actively star-forming zones, as predicted by (Schaye, 2004, see also Thilker et al., 2007), as well as to the Hα "edge" in galaxies from the sample of Martin & Kennicutt (2001), as demonstrated by Boissier et al. (2007).

A great deal of discussion has focused on objects where UV emission was detected at larger radii than Hα emission from H ɪɪ regions, as was the case for Arp 78. A variety of possible explanations for this discrepancy have been put forward, e.g. a top-light IMF as a consequence of a low level of SF with the resulting low star cluster masses precluding the formation of ionising stars while still forming enough stars below the ionisation limit to account for the FUV flux (Weidner & Kroupa, 2006; Boissier et al., 2007). Wholesale truncations of the IMF at the upper end also have been suggested to simply cut off sources of photoionisation. This situation could be attributed to the low gas column densities in the outskirts of galaxies. Under these conditions fragmentation of a molecular cloud happens too quickly for it to grow to a point where it can readily produce stars massive enough to ionise the surrounding gas (Krumholz & McKee, 2008).

Alternatively, age effects have been discussed, in the sense that presumably episodic SF events ceased in the outskirts of some galaxies long enough in the past for H ɪɪ regions to have faded below detection, but recently enough for the stellar UV flux to still be measurable (Zaritsky & Christlein, 2007). Leakage of ionising photons in the very low density environment of these outer regions provides yet another possible explanation, as this would act to decrease the observability of photoionised regions (Oey & Kennicutt, 1997).

In some undisturbed face-on spirals, Ferguson et al. (1998b) were the first to show that very deep Hα exposures revealed small and low-luminosity H ɪɪ regions beyond – and sometimes *far* beyond – the optical radius, giving evidence for low-level SF activity going on beyond the optical radius and interpreted as a signature of the inside-out growth of stellar disks. Another factor then is the question of detectability of H ɪɪ regions versus the UV light of stars.

Here we present deep narrow band Hα imaging of Arp 78, including its outer regions, to check whether we can find Hα flux from H ɪɪ counterparts to the XUV flux detected by GALEX. Our approach involves comparing SFRs derived from L(Hα) with those based on L(FUV) assuming a normal relationship between these two measures of massive stellar populations. In this way we can check whether or not the outer regions of Arp 78 have normal young stellar populations.

8.2 Arp 78 – NGC 772

Arp 78 is a luminous ($M_B = -21.6$) galaxy with pronounced spiral structure at an adopted distance of 34Mpc ($v_r = 2472\,\mathrm{km\,s^{-1}}$). It is experiencing multiple interactions involving its spectroscopically confirmed low-luminosity ($M_B = -18.2$) elliptical satellite, NGC 770, at a projected distance of ~ 30 kpc, plus two more companions ($M_B = -15.5$ and -16.2, respectively) within projected distances ~ 400 kpc (Zaritsky et al., 1997).

The outer regions of Arp 78 feature an obviously disturbed, one-sided spiral arm-like morphology that appears to be a tidally driven structure. The XUV emission in Arp 78 is clearly associated with this region, as seen in Fig. 8.1. Whether or not the stellar population age in the filaments agrees with the nuclear starburst age of ~ 2 Gyr as determined by Ganda et al. (2007) and possibly even with the stellar population age of 3 ± 0.5 Gyr given by Geha et al. (2005) for the counter-rotating disk in the companion NGC 770, are subjects of our ongoing more extensive multi-band analysis.

8.3 Observations and Data reduction

Our optical observations were obtained using the WIYN 3.5 m telescope at Kitt Peak equipped with the MiniMosaic camera. MiniMo consists of two 2K×4K CCD chips with a spatial sampling of 0.14 arcsec per pixel resulting in a field-of-view of 9.5 × 9.5 arcmin. The seeing in the R-band was $\approx 1.0''$ and $\approx 1.2''$ in Hα.

Data reduction consisted of overscan- and bias-subtraction, flat-fielding and cosmic ray removal. We took special care to correct for slight gain variations between the two CCDs to yield a flat background across the full FoV by multiplying them individually with correction factors ≈ 1 until sky-noise and background level were identical in all readout zones. The resulting frames were then aligned by matching the positions of several stars in each frame and stacked; bad-pixel-masks were used to remove bad pixels and the small gap between the detectors.

Obtaining a proper continuum subtraction requires that we match the point spread function (PSF) in the R and Hα filters. We accomplished this by iteratively smoothing the R-band image with a Gaussian of varying widths in the x- and y-directions until the PSFs in both filters matched and residuals were acceptable. To remove the continuum contribution from the Hα image, we measured the intensity of several stars in both the R-band and Hα frame, scaled the R-band so that the stars have on average the same count rates in both R and Hα and subtracted this frame from the Hα narrow-band exposure. The resulting scaling factor is in good agreement with that derived from the widths of the filter transmission curves, but allows for a more accurate continuum subtraction. Although the WIYN W16 narrow band filter also includes the [NII] emission lines, we refer to the continuum subtracted data as Hα images since this is the dominant source of emission line flux.

The GALEX images have been obtained from the GALEX science archive at the Space Telescope Science Institute. To minimise offsets introduced by slightly differing coordinate systems we aligned the FUV and NUV frames relative to the optical data by matching the positions of several stars. The full width at half maximum of the FUV PSF is $4.2''$ sampled with $1.5''$ pixels (Morrissey et al., 2007).

8.4 Results and Implications for IMF

Figure 8.1 shows the FUV image of Arp 78 as gray-scale with WIYN narrow band Hα-brightness contours overplotted. To suppress noise from the image we used adaptive and median-filtering
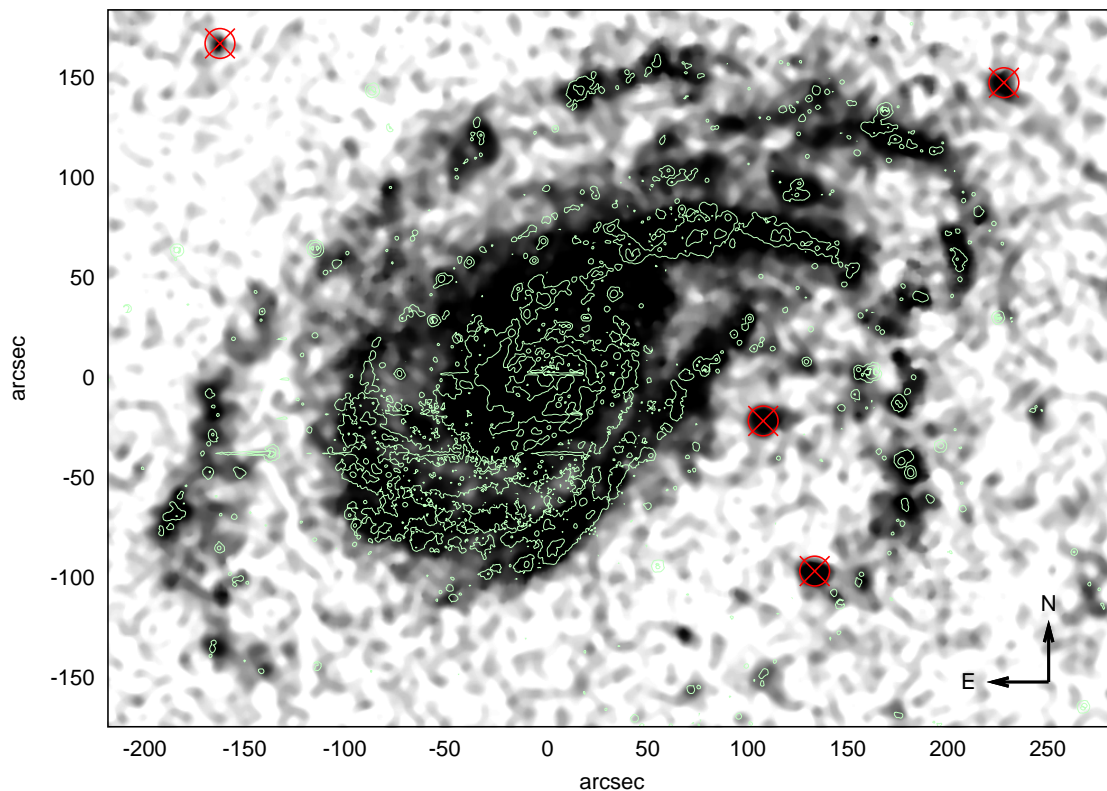
Figure 8.1: The far-UV image of Arp 78 shown as gray-scales is overplotted with contour lines for the Hα emission. The four circles mark positions of three background galaxies and a point source (probably an AGN or a hot star) that show up in the FUV, but not in our Hα images.

of the FUV image. The Hα contours, however, have been constructed from the original contin-uum subtracted Hα frame to make sure this filtering does not induce artifacts into our results.

This Figure clearly shows a nearly perfect match between the FUV and H ɪɪregions, as is expected if both the UV-flux and Hα flux are emitted by the young stars in the same regions where the IMF extends up to high stellar masses. The close coincidence between FUV- and Hα emitting regions both in the inner disk and in the outer tidal features is *inconsistent* with a scenario where a low level of star formation in the XUV-disk leads to a low upper stellar mass cutoff of the IMF. It also excludes timing models where the FUV-emitting star clusters are systematically too old to produce significant Hα emission through photoionisation, i.e. older than $\approx 7\,\text{Myr}$.

Several small isolated regions seen in the UV GALEX images but lacking Hα emission can be identified as background galaxies in our WIYN optical images; they are marked by encircled crosses in Figure 1. The bright FUV source in the lower right part of the frame is the centre of the companion galaxy NGC 770. There are a few horizontal structures visible in the Hα contour map: these originate in chip defects or saturated stars that could not perfectly be corrected for in the data reduction process.

8.4.1 Comparing SFRs from FUV/NUV and Hα

The existence of H ɪɪregions could be consistent with models where the upper IMF is biased in outer regions of galaxies, e.g. the Weidner & Kroupa (2006) models. To test for this possibility we compare the SFRs obtained from the FUV and Hα luminosities using the empirical calibrations of Kennicutt (1998). Although those were obtained – and hence are strictly accurate only – for close-to-solar metallicity, they provide a reasonable first estimate for the outer regions of Arp 78.
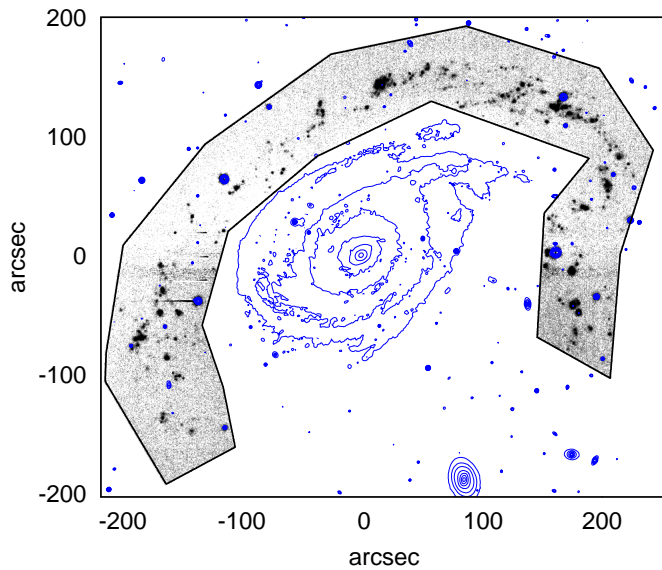
Figure 8.2: Regions used to compute the SFR are shown in gray-scale with contour lines of the R-band image overplotted.

While central spectroscopy has revealed solar to slightly super-solar abundances (Ganda et al., 2007), we expect the outer regions to have subsolar – albeit probably not dramatically subsolar – abundances. If IMF biasing exists in the XUV regions, then we expect the SFR derived from the Hα luminosity to be significantly lower than that based on FUV data.

To obtain the fluxes in the outer tidal filaments, we masked the outer ring-like structure (cf. Fig. 8.2) and obtained integrated count rates for this region from which we derive fluxes. Using the Galactic extinction law from Valencic et al. (2004), we derive a value of $A_{FUV} = 0.63$ mag at 1540 Å from the Galactic extinction $E(B - V) = 0.073$ mag towards Arp 78 (Schlegel et al., 1998). At the distance of 34 Mpc towards Arp 78, this yields a FUV-luminosity of 2.5×10^{39} erg s^{-1} cm^{-2} $^{-1}$. Based on uncertainties in the background determination and sky- and readout noise we estimate that this luminosity is accurate to $\approx \pm 15\%$. From this FUV luminosity we estimate a SFR of $SFR_{FUV} = (0.3 \pm 0.05)$ M$_\odot$ yr^{-1} using the calibration from Kennicutt (1998).

To derive the Hα flux we use the calibration data from the R-band to convert the measured count rate into physical units. Using an effective filter width of 72 Å for the WIYN-W16 filter yields $L(H\alpha) = 10^{41}$ erg s^{-1} for the regions marked in Fig. 8.2, corresponding to a SFR in the tidal debris region of $SFR_{H\alpha} = 0.7$ M$_\odot$ yr^{-1}, also based on the Kennicutt (1998) calibration. In deriving this SFR we reduced the observed flux in the W16 filter by 20% to account for [NII] emission in the bandpass. The SFR from Hα is a factor ≈ 2 higher than the SFR we derive from the FUV luminosity. From the noise in the continuum-subtracted Hα image and uncertainties in the flux calibration we estimate an error for the Hα-derived SFR of $\pm 30\%$ or $\Delta SFR = \pm 0.2$ M$_\odot$ yr^{-1}. These results reveal a comparatively normal Hα-to-FUV flux ratio, supporting the presence of a normal high mass stellar IMF in this case.

The factor ≈ 2 in the ratio $SFR_{H\alpha}/SFR_{FUV}$ can be caused by two effects: First, we only corrected for Galactic foreground extinction and not for internal extinction in Arp 78 in our derivation of the FUV luminosity. Even small amounts of dust inside the FUV-emitting regions will easily absorb some FUV radiation, so that the intrinsic, dust-corrected luminosity – and with that the true FUV-based SFR – is certainly somewhat higher. Second, as mentioned above, the calibration for the SFR derived from Hα is only valid for solar metallicity galaxies, while the outskirts of Arp 78 are likely to have somewhat sub-solar metallicities. Investigating the metallicity dependence of SFR indicators with our GALEV models, we found that SFRs in low metallicity regions are over-estimated by factors up to 2 if derived from $L(H\alpha)$ and by up to 50% if calculated from $L(FUV)$ using empirical calibrations obtained for close-to-solar metallicity environments (cf. Bicker &

Fritze, 2005). Accounting for the probably subsolar metallicities in the outer regions of Arp 78 thus acts to bring our SFR estimates from FUV and Hα into closer agreement.

After allowing for these two effects, we consider the SFR derived from Hα and from the FUV luminosity to be in acceptable concordance, and estimate it to be SFR(outer) $\approx (0.5 \pm 0.2) \, \mathrm{M_\odot \, yr^{-1}}$ across the extended tidal structures in Arp 78 outlined in Fig. 2. This agreement further reinforces our conclusion that the average upper mass stellar IMF in this region is normal.

8.4.2 Extended UV Emission and the IMF in Arp 78

The UV-bright outer arm of Arp 78 contains several H ɪɪregions with L(Hα) $\geq 10^{38}$ erg s^{-1}. Photoionisation requires some component of the region to have an age of $\leq 7 - 9$ Myr and for a normal mass function the inferred young stellar masses in these regions are $> 10^4 \, \mathrm{M_\odot}$. Hence, these young clusters are sufficiently massive to properly sample the IMF up to high masses (Weidner & Kroupa, 2006; Boissier et al., 2007).

Why then is the XUV outer arm structure so obvious in Arp 78 while the optical counterpart is faint? This appears to be an effect similar to what is observed in the context of Tidal Dwarf Galaxies, where the mass and the NIR light can be dominated by stars inherited from the spiral disk while the short-wavelength light is due to stars formed in a major outer SF event triggered by the ongoing interactions in this system.

8.5 Summary

Deep narrow-band Hα imaging from the WIYN 3.5-m telescope on Kitt Peak allowed us to detect Hα emission in good coincidence with the extended GALEX FUV structure all across the inner part and, in particular, across the XUV extended outer structures of Arp 78, that very probably are of tidal origin. We calculated the SFR across these outer structures and found a value of $0.5 \pm 0.2 \, \mathrm{M_\odot \, yr^{-1}}$ from both the FUV and Hα luminosities. The agreement between these two measures points to a normal upper stellar upper IMF in this system. We also find the star forming regions in this system to be younger than ~ 15 Myr and sufficiently massive to properly sample the IMF up to high masses.

The XUV-strong and optically faint outer structures of Arp 78 are consistent with ongoing SF superimposed on an older stellar population torn out from the spiral disk by tidal forces. A detailed investigation of stellar population ages and metallicities across this galaxy will be the subject of a forthcoming paper.

Chapter 9

Summary and outlook

9.1 Outlook and future work

tbc

Appendix A

How GALEV works – a picture story

Ralf Kotulla, Uta Fritze, Peter Weilbacher, and Peter Anders
submitted as appendix to MNRAS XXX

In the following we will present the workings of **GALEV** in a more vivid way by guiding the reader through a series of steps. We give examples for the input physics **GALEV** uses and show how this is used throughout the process of modelling a galaxy.

A.1 General steps

In the first step we present how one gets from isochrones, a stellar IMF, spectral library, and atomic physics to an integrated isochrone spectrum. For this example we choose to work with isochrones from the Padova group, a Salpeter-IMF from $0.1M_\odot$ to $100M_\odot$ and stellar spectra from the Lejeune library, all using solar metallicity.

A.1.1 Step 1: Choose set of isochrones

Fig. A.1 shows solar-metallicity isochrones for three different ages of 4 Myr, 100 Myr and 1 Gyr as a colour-magnitude diagram. For very young ages the main sequence reaches up to high masses and hence very high luminosities ≈ -10 mag. For the later stages the red giant branch (RGB) at $(B-V) \approx 1 \ldots 1.4$ is clearly visible and also the asymptotic giant branch (AGB). Note that stars on the AGB can reach extremely red colours of $(B-V) \approx 4$ mag and at the same time get very bright in the NIR ($M_K \sim -10$ mag) during the thermal pulsation (TP) phase.

A.1.2 Step 2: Select Initial Mass Function

In a second step we have to choose a parameterisation for the number of stars as function of their mass. Fig. A.2 shows two common IMFs, the Salpeter and Kroupa IMFs. For masses $\geq 1M_\odot$ both predict roughly comparable number of stars, but they differ in the low mass regime $\leq 1M_\odot$. This will not only affect mass-to-light ratios, but also have an impact on the resulting spectra and in particular the chemical enrichment, since fewer low-mass stars also means that less mass gets locked up in long-lived stars.
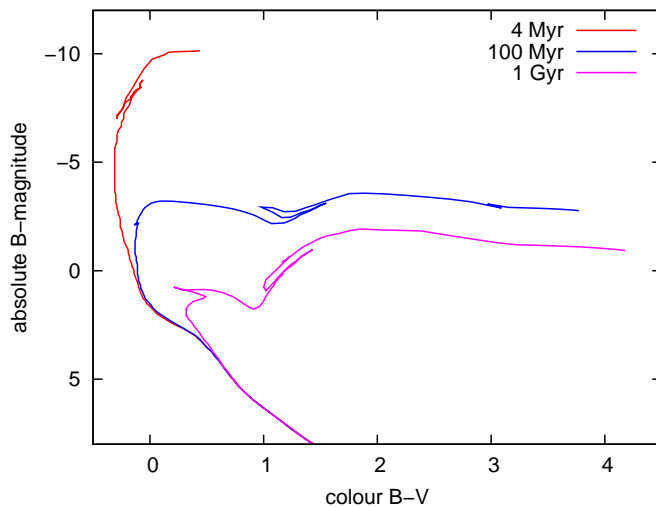
Figure A.1: Solar metallicity isochrones from the Padova group for three different ages of 4 Myr, 100 Myr and 1 Gyr
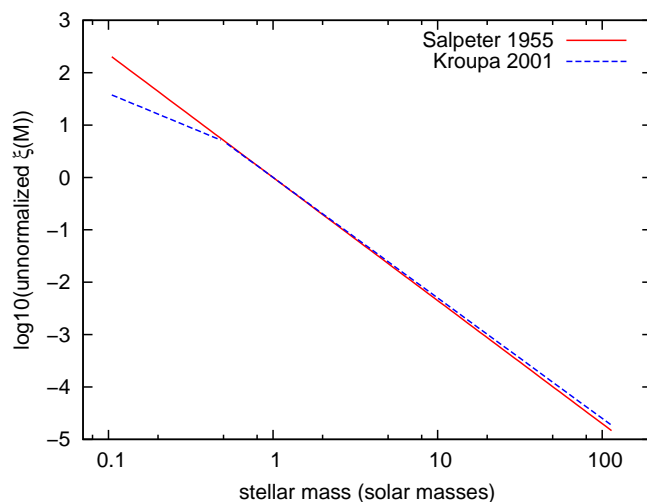
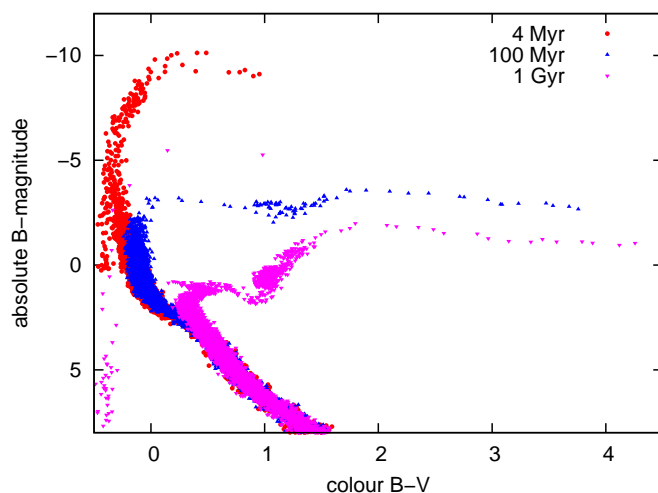**Figure A.2:** Two examples of initial mass functions, here from Kroupa (2001) and Salpeter (1955)

Figure A.3: Synthetic colour magnitude diagram where each point from the isochrone is assigned a numbers of stars based on the IMF. We added some scatter around each point to produce a smoother appearance.

A.1.3 Step 3: Populate isochrones with stars

With both isochrones and IMF at hand we can now populate the isochrones with stars taken from an IMF. For each mass point on the isochrone the IMF tells us how many stars were being formed with this mass. The results are shown in Fig. A.3, where we also added some scatter around the individual points to give the artificial colour-magnitude diagram a smoother and more realistic appearance. We also added at least one star to each point to bring out all phases of stellar evolution. However, in reality, this might not be the case, since some phases, e.g for very young and extremely hot white dwarfs last for a very short timescale only.

A.1.4 Step 4: Assign a spectrum to each star

Next we assign a spectrum to each star in the colour-magnitude diagram. The parameters required for this are either directly given in the isochrones (e.g. the effective temperature T_{eff}) or can be derived from other parameters (e.g. the surface gravity $\log g$ can be calculated from the stellar mass, its bolometric luminosity and effective temperature). In Fig. A.4 we show four sample spectra for stars with identical $\log g = 4.0$, but temperatures ranging from 20000 K down to 2000 K. Hot stars have a smooth slope and are bright in the UV. Stars with $T_{eff} \approx 10000$ K
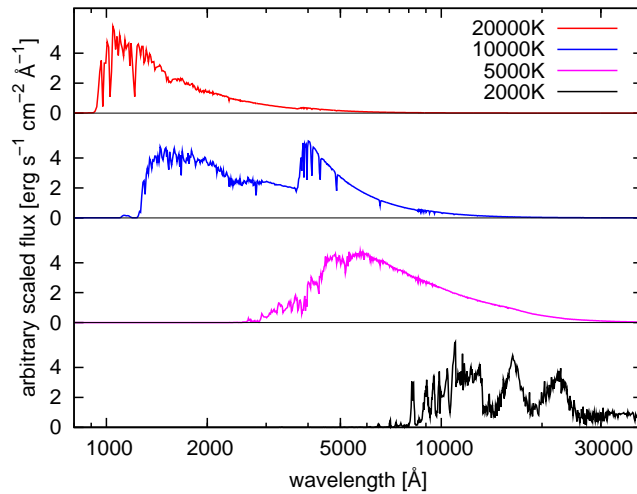
Figure A.4: Sample spectra from the Lejeune stellar library for stars with $\log g = 4.0$ and $T_{eff} = (20000, 10000, 5000, 2000)$K.
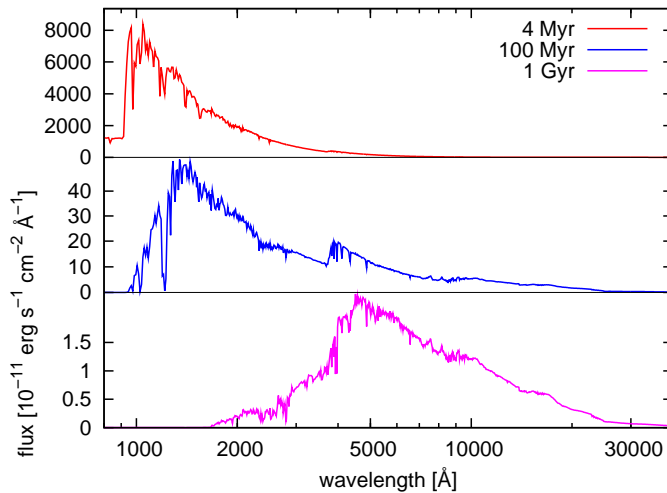

Figure A.5: Integrated starlight for the three isochrones shown in Fig. A.1.

have prominent Balmer absorption lines characteristic for spectral type A stars. Cool stars are dominated by broad molecular absorption bands and only emit at long wavelengths. Not all stellar parameters are directly covered by the library, all other values have to be interpolated between neighbouring points in the library. Is is therefore crucial for the stellar library to cover the full parameter range.

A.1.5 Step 5: Integrate spectra of all stars

To create stellar isochrone spectra we now integrate the light of all stars. Special care has to be taken to account for the different luminosities of stars at their respective stages of evolution. In Fig. A.5 we show spectra for the same ages discussed above, 4 Myr, 100 Myr, and 1 Gyr. The youngest spectrum is almost completely dominated by the hottest and brightest high-mass stars that also dominate part of the 100 Myr spectrum. For this spectrum the highest-mass stars have already exploded as supernovae and with them the flux in the FUV already has decreased considerably. In the optical the 4000 break starts to appear, becoming stronger with time. After 1 Gyr there is little UV flux remaining, the spectrum is now dominated by stars with lower masses $\approx 2 M_\odot$.
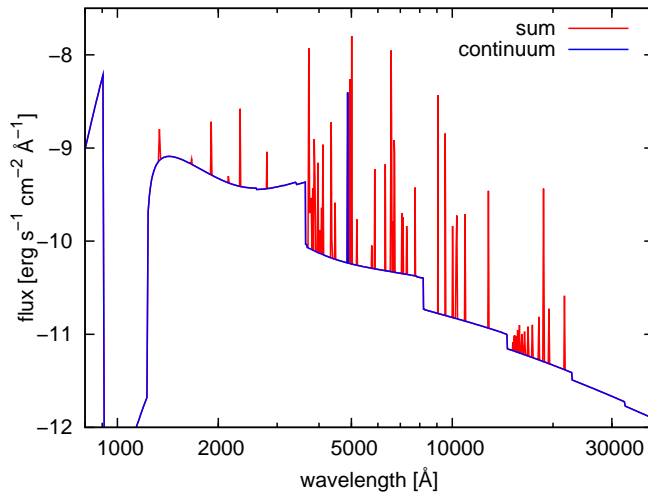
Figure A.6: Gaseous emission spectrum for solar metallicity. Shown in blue is the continuum emission, and continuum and line emission in red.

A.1.6 Step 6: Compute gaseous line and continuum emission

Until now we have only dealt with stellar light. However, as mentioned earlier, at young ages isochrones contain large contributions from high mass stars. These emit a large fraction of their light in the UV and also produce significant numbers of photons energetic enough to ionise hydrogen. The energy injected into the surrounding interstellar medium produces both emission lines and also continuum emission. The detailed mechanisms of this are discussed in Sect. 2.3.3 and shown in Fig. A.6. Note that while the strength of the heavy element emission lines depends on the metallicity of the gas, the strength of the continuum emission and hydrogen emission lines purely depends on the ionising photon flux.

A.1.7 Step 7: Add gas emission to stellar spectrum

For each isochrone we now compute the gaseous emission spectrum based on the metallicity and ionising photon flux derived from isochrones and IMF. Since the latter heavily depends on the age of the isochrone so does the strength of the gaseous emission. In Fig. A.7 we show the same spectra as in Fig. A.5, but now with gaseous emission included. For the first spectrum at an age of 4 Myr the emission lines clearly stand out in the optical. However, for the later stages there are no changes compared to the purely stellar spectra, since only stars with masses $\gtrsim 20 M_\odot$ and hence very short lifetimes $\lesssim 10$ Myr produce the majority of the ionising flux.

In **GALEV** those previous steps are repeated for all metallicities and ages available from the isochrone set, yielding a full set of isochrone spectra including both stellar and gaseous emission.

A.2 Additional steps for star clusters

Continuing from the library of isochrone spectra **GALEV** can now compute the finer grid required for the study of star clusters.

A.2.1 Step 8: Interpolate between ages given by the isochrones

The time resolution offered by the isochrones in general only spans a relatively coarse grid with logarithmic age spacing. However, it is advantageous to create a grid with smaller and linear
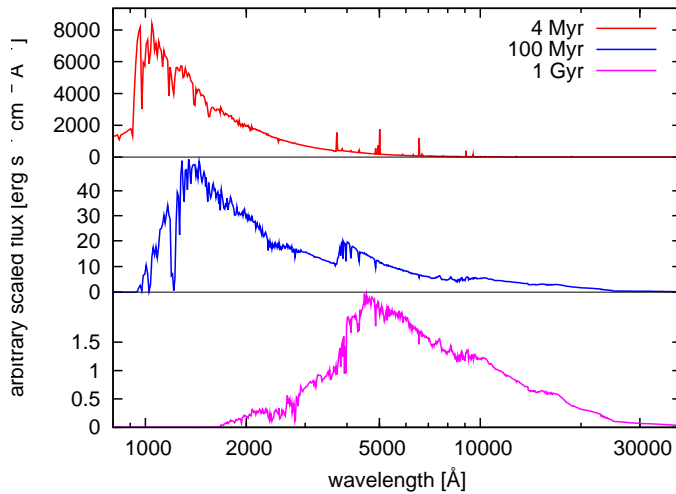
Figure A.7: Integrated isochrone spectra for the same isochrones shown in Fig. A.1 and Fig. A.5, including both stellar and gaseous emission.
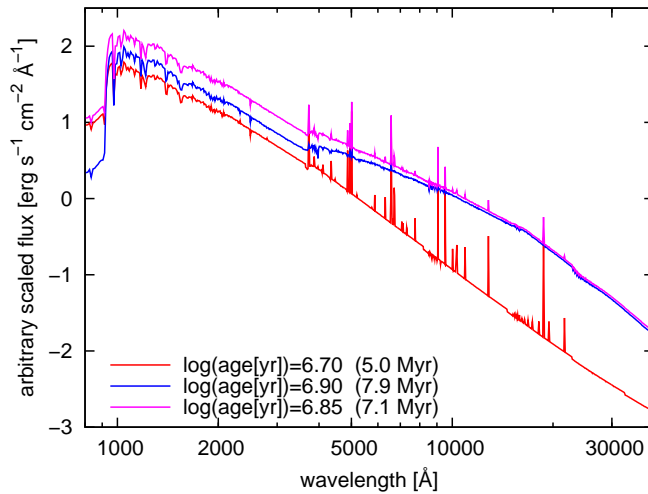

Figure A.8: Example for contributing isochrone spectra during interpolation in age.

age steps. This can be done by interpolating additional ages to fill the gaps in the isochrone grid. Since spectra vary roughly linearly with logarithmic time, i.e. changes are larger at small ages and small at large ages we use this as basis for our algorithm. In Fig. A.8 we show two isochrone spectra for ages of $\log(t) = 6.7$ and $\log(t) = 6.9$ and the resulting spectrum for $\log(t) = 6.85$. The resulting spectrum was computed by $\text{Spec}(\log(t) = 6.85) = 0.25 \times (\text{Spec}(\log(t) = 6.7) + 3 \times \text{Spec}(\log(t) = 6.9)$.

To obtain a full grid to be used e.g. for age-dating star clusters one has to repeat this procedure for each required time step and each metallicity. The steps involved with applying dust extinction and computation of magnitudes from spectra is explained in Steps 11 and 14 below.

A.3 Additional steps for galaxies

Galaxies are completely different from star clusters since they contain multiple stellar populations, generally covering a range of ages and metallicities. We explain the basic steps dealing with multiple populations based on a toy-model of a galaxy made from only two populations with different ages and metallicities. The subsequent explanations use the model of an undisturbed elliptical galaxy.
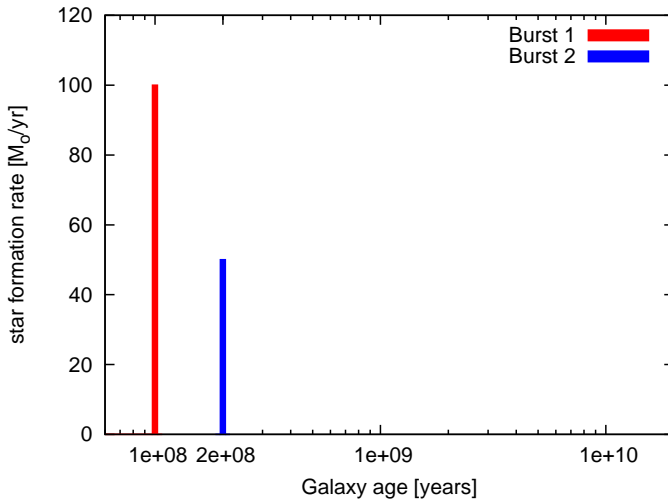
Figure A.9: For our toy-model we construct a very primitive star formation history of 2 bursts, with SFRs of $100\,M_\odot\,yr^1$ and $50\,M_\odot\,yr^1$, each lasting 10^6 years.

A.3.1 Step 8: Compute initial abundances for next generation

To derive the chemical evolution of galaxies we have to know four things: 1) The total mass of the galaxy, including both the mass of stars and gas. 2) The star formation history (SFH), i.e. how many stars are formed at each particular time. 3) The life times of the stars formed. This in combination with the SFH yields some form of star death record. And we have to know 4) the end products of each star, i.e. the mass of its remnant, and the mass of gas and heavy elements returned to the surrounding ISM. For each time we then have to keep track of the masses of stars, gas and metals in the gas. All those quantities are changed by star formation and the return of gas and heavy elements from dying stars. The ratio of metals to gas is the crucial factor since it determines both the spectra and lifetimes of the newly formed stars.

A.3.2 Step 9: Interpolate between ages AND metallicities

For all galaxies with an extended SFH we will have stellar populations not agreeing with the coarse grid given by the isochrones. We therefore have to interpolate between isochrone spectra of different ages and also different metallicities. The details of this process are described in the context of star clusters above and are also shown in Fig. A.8.

A.3.3 Step 10: Add up spectra weighted with SFH

To ease the understanding how **GALEV** assembles a galaxy spectrum from the individual spectra of each of its constituent populations, we first consider a toy model of a galaxy made from only two populations. Both populations are described by intervals of 1 Myr duration each, occuring at an age of 100 and 200 Myr and forming stars at a rate of $100\,M_\odot\,yr^{-1}$ and $50\,M_\odot\,yr^{-1}$, respectively (see Fig. A.9). Both intervals are short compared to the age of the youngest isochrone so that they each can be described as a population of one age. We further assume that the earlier population (Burst 1) is formed with a metallicity of $[\mathrm{Fe/H}] = -1.7$ or $1/50Z_\odot$, and the second (Burst 2) with a metallicity of $[\mathrm{Fe/H}] = -0.7$ or $1/5Z_\odot$.

We will now show how to derive the spectrum of our toy-galaxy at two ages of 300 Myr and 1 Gyr. For each timestep t one needs to derive the ages τ and metallicities of all populations formed prior to this time. Those are then weighted by the SFR at their respective formation time $\mathrm{SFR}(t - \emptyset)$ multiplied with the length of a time step. Those are then added up to yield the galaxy spectrum. For our toy galaxy at an age of 300 Myr we know that Burst 1 has metallicity
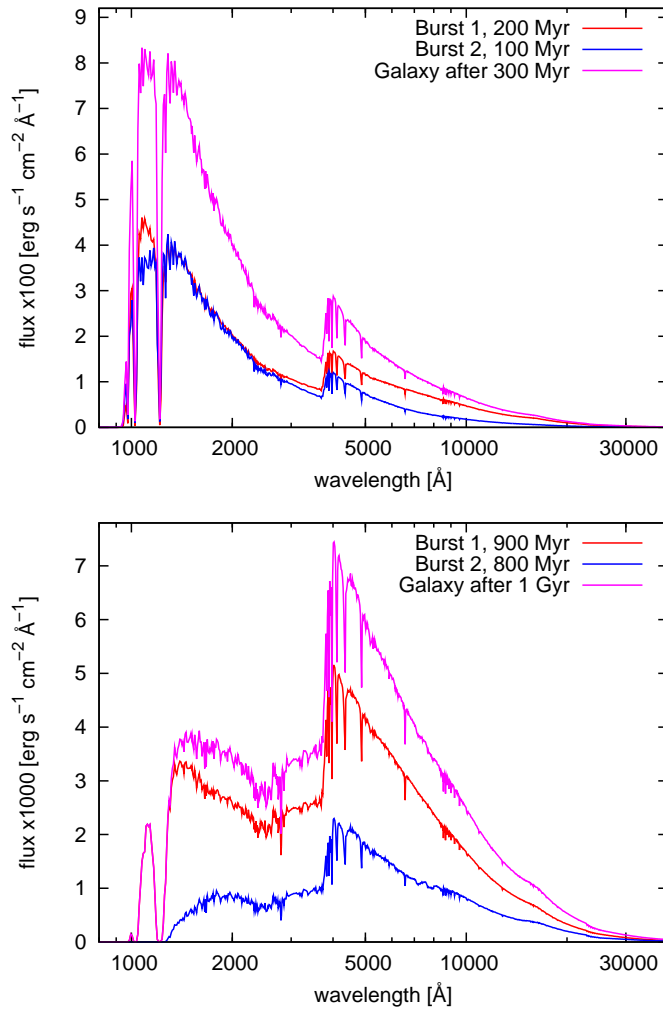
Figure A.10: Interpolated isochrone spectra for each burst and the resulting galaxy spectrum, for galaxy ages of 300 Myr (top panel) and 1 Gyr (bottom panel).

$[Fe/H] = -1.7$ and an age of 200 Myr. Burst 2 has metallicity $[Fe/H] = -0.7$ and an age of 100 Myr. The resulting spectrum thus can be constructed by added up those two isochrone spectra. The resulting spectrum is shown in the upper panel of Fig. A.10.

The spectra for all other times are created in a similar way. Metallicities for each population stay the same, while ages increase with time. The resulting spectrum of our toy-model galaxy at an age of 1 Gyr is shown in the bottom panel of Fig. A.10

In the following we will leave our toy-model galaxy and instead show the remaining steps that are necessary to derive magnitudes for an elliptical galaxy with a small amount of dust at redshift $z = 3$.

A.3.4 Step 11: Apply evolutionary correction

Since we want to model the galaxy at a cosmologically significant redshift of $z = 3$ we have to take evolutionary corrections into account, i.e. we observe the galaxy at an earlier evolutionary state. We therefore have to know the age of the galaxy at this redshift. In Fig. A.11 we show the redshift-galaxy age relation for a small range of cosmological parameters. It is obvious that the density parameters Ω_M and Ω_Λ influence the solution, but also the formation redshift z_{form}, the redshift at which the galaxy started forming stars. The impact of those evolutionary corrections can be seen in Fig. A.14. The first row shows the galaxy at redshift z=0 with an age of ≈ 13 Gyr.
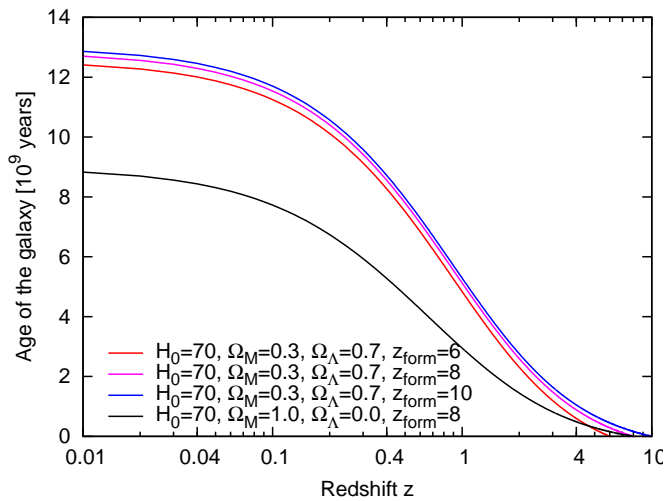
Figure A.11: Relation between galaxy age and redshift for different cosmological parameters and in particular varying formation redshifts.
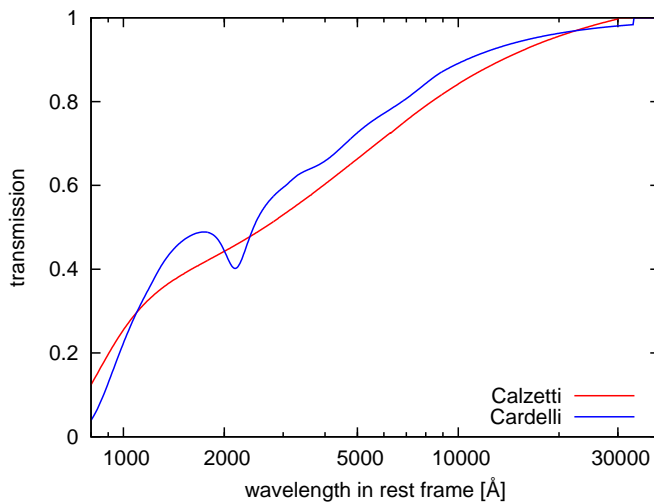

Figure A.12: Extinction curves from Calzetti and Cardelli. Both show very little transmission at short wavelengths indicating that most of the light gets absorbed.

The second row shows the galaxy at its evolutionary state at $z = 3$; the galaxy at redshift 3 started forming stars only $\approx 1.5\,\mathrm{Gyr}$ earlier.

A.3.5 Step 12: Apply extinction

In a next step we apply the attenuation due to interstellar dust. For our example we choose the Calzetti et al. (1994) extinction law (see Fig. A.12 and choose an intermediate degree of extinction, E(B-V)=0.2. For comparison we also show the dust attenuation curve of Cardelli et al. (1989). Both extinction curves have in common that the transmission, i.e. the fraction of light that remains unabsorbed, drops towards shorter wavelengths, leading to a reddening of the galaxy light. The results on the spectrum can be seen from the difference between the second and third row in Fig. A.14

A.3.6 Step 13: Redshift spectrum

The spectrum now has to redshifted by a factor (1+z). Note that also the flux has to reduced by the same factor (1+z) to properly account for the cosmic expansion.
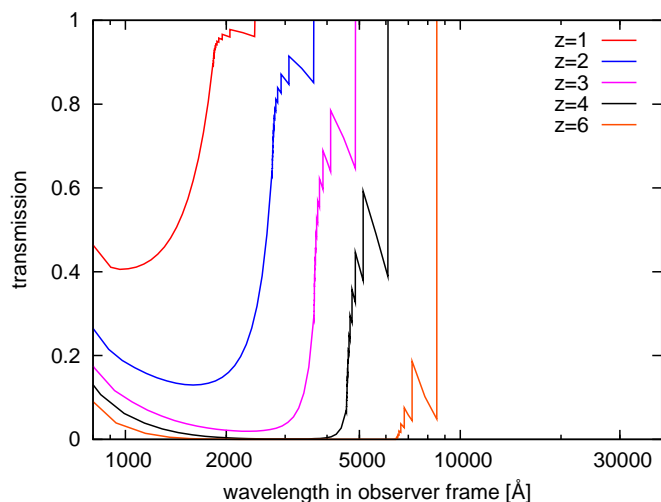
Figure A.13: Transmission of the intergalactic medium as function of observed frame wavelength for sources at different redshifts.

A.3.7 Step 14: Apply intergalactic attenuation curve

Due to the high redshift at which we observe our galaxy we have to correct for intergalactic absorption due to intervening neutral hydrogen clouds. These absorb light shortwards of the Lyman-α line (1216 Å) and hence reduce the flux in this region. Fig. A.13 shows the transmission of the IGM as function of observed frame wavelength for sources at different redshifts $z = 1 \ldots 6$. For a galaxy at redshift 3 this means that $\approx 30\%$ of the light between the Lyman-break (912 Å) and the Lyman-α line is absorbed, while shortwards of the Lyman-break essential all flux is absorbed (hence the name Lyman-break). Fig. A.14 shows in the two bottom rows the spectrum with (5th row) and without (4th row) this attenuation.

All the previously mentioned effects are summarised in Fig. A.14. The first row shows the spectrum of the galaxy at redshift $z = 0$ at an age of 13 Gyr. The second row still is at $z = 0$, but at an evolutionary state already corresponding to $z = 3$. The following panel shows the spectrum with a reddening of $E(B - V) = 0.2$ mag; Here most of the far-UV flux is already absorbed by dust. The fourth row shows the spectrum redshifted to $z = 3$ and the last row also takes intergalactic attenuation into account.

A.3.8 Step 15: Convolve with filter response curve to compute magnitudes

We can now convolve the final spectrum with filter response curves. Therefore each point in the spectrum is weighted with the relative filter response at the corresponding wavelengths and then integrated over all wavelengths. To convert the resulting fluxes into observable magnitudes we have to apply zero-points according to the requested magnitude system, e.g. Vega or AB. In Fig. A.15 we show a wide selection of currently available filters from different space and ground-based telescopes.

A.3.9 Step 16: Add distance modulus

In a very last step we can convert the absolute magnitudes obtained with the filters into apparent magnitudes. This is done by simply adding the bolometric distance modulus for the particular redshift. In Fig. A.16 we show the evolution of the distance modulus with redshift for a small selection of possible cosmological parameter sets. For the previously studied galaxy at redshift $z = 3$ we have to add a distance modulus of 47 mag.
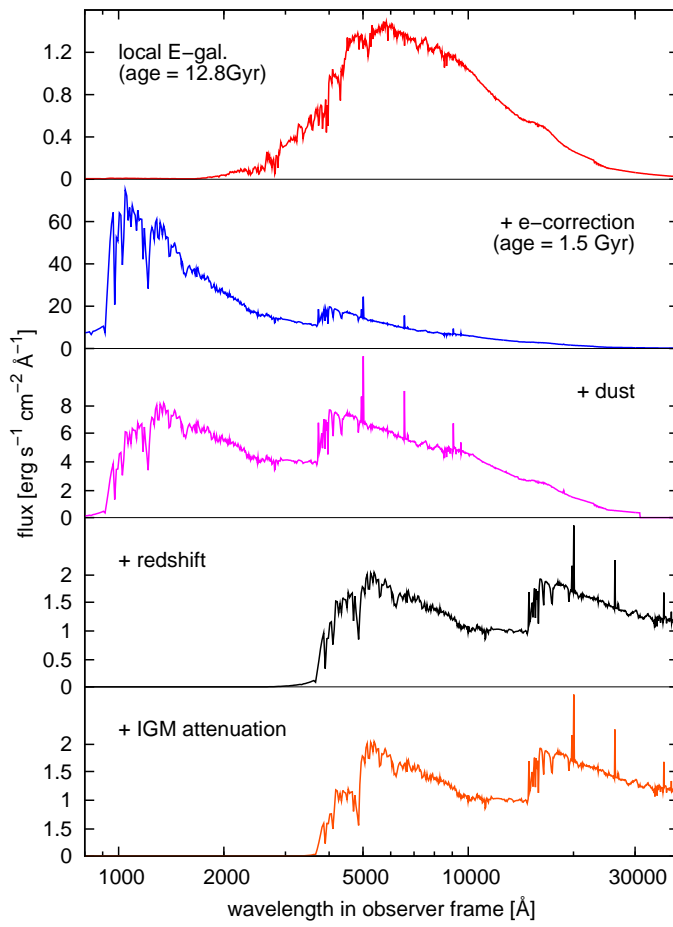
Figure A.14: Galaxy spectrum of an elliptical galaxy at different stages of the modelling process. Each following spectrum includes all effects shown above.
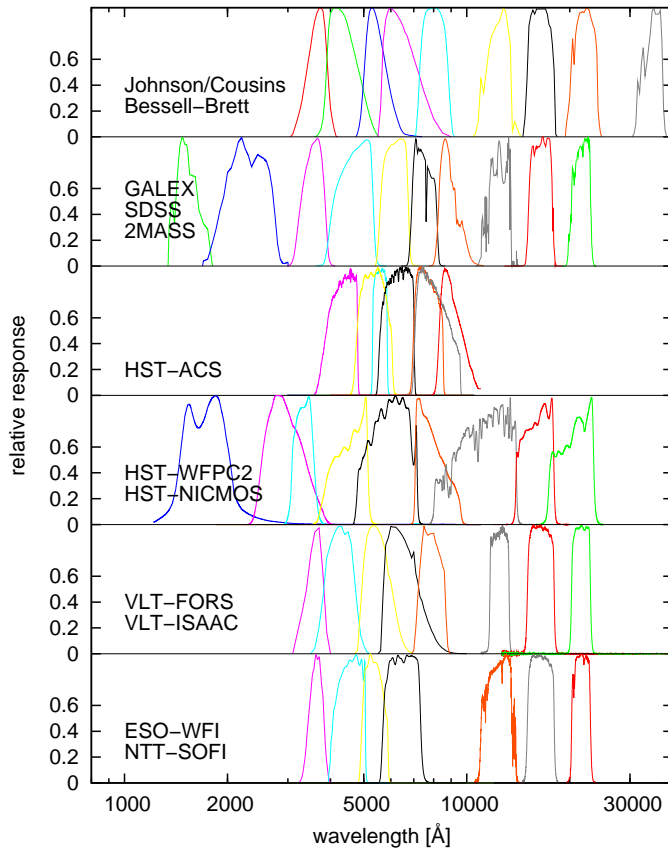
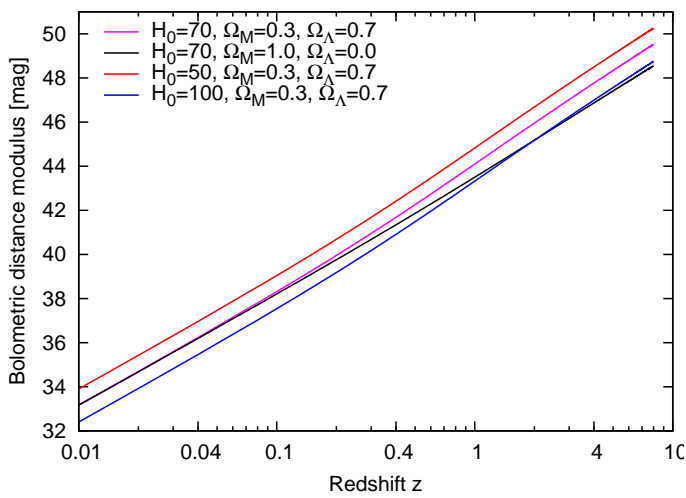**Figure A.15:** Selection of the filters currently offered by **GALEV** , ranging from the far-UV to near-infrared.

Figure A.16: Bolometric distance modulus as function of redshift for a range of cosmological parameter sets.

Appendix **B**
Further publications

B.1 Publication list

B.2 Conferences

B.3 Abstracts of co-authored papers

B.3.1 The role of E+A and post-starburst galaxies
I. Models and model results

Authors: M. A. Falkenberg, **R. Kotulla**, and U. Fritze

published in Monthly Notices of the Royal Astronomical Society 397, 1940–1953 (2009)

Different compositions of galaxy types in the field in comparison to galaxy clusters as described by the morphology-density relation in the local universe is interpreted as a result of transformation processes from late- to early-type galaxies. This interpretation is supported by the Butcher-Oemler effect. We investigate E+A galaxies as an intermediate state between late-type galaxies in low density environments and early-type galaxies in high density environment to constrain the possible transformation processes.

For this purpose we model a grid of post-starburst galaxies by inducing a burst and/ or a halting of star formation on the normal evolution of spiral galaxies with our galaxy evolution code GALEV. From our models we find that the common E+A criteria exclude a significant number of post-starburst galaxies and propose that comparing their spectral energy distributions leads to a more sufficient method to investigate post-starburst galaxies. We predict that a higher number of E+A galaxies in the early universe can not be ascribed solely to a higher number of starburst, but is a result of a lower metallicity and a higher burst strength due to more gas content of the galaxies in the early universe. We find that even galaxies with a normal evolution without a starburst have a Hδ-strong phase at early galaxy ages.

B.3.2 The role of E+A and post-starburst galaxies
II. Spectral energy distributions and comparison with observations

Authors: M. A. Falkenberg, **R. Kotulla**, and U. Fritze

published in Monthly Notices of the Royal Astronomical Society 397, 1954–1965 (2009)

In a previous paper (Falkenberg, Kotulla, & Fritze, 2009a, see Sect. B.3.1 for an abstract) we have shown that the classical definition of E+A galaxies excludes a significant number of post-starburst galaxies. We suggested that analysing broad-band spectral energy distributions (SEDs) is a more comprehensive method to select and distinguish post-starburst galaxies than the classical definition of measuring equivalent widths of the Hδ and [O $\textsc{ii}$] lines.

In this paper we will carefully investigate this new method and evaluate it by comparing our model grid of post-starburst galaxies to observed E+A galaxies from the MORPHS catalog.

In a first part we investigate the UV/U-optical-NIR SEDs of a large variety in terms of progenitor galaxies, burst strengths and timescales of post-starburst models and compare them to undisturbed spiral, S0 and E galaxies as well as to galaxies in their starburst phase. In a second part we compare our post-starburst models with the observed E+A galaxies in terms of Lick indices, luminosities and colours. We then use the new method of comparing the model SEDs with SEDs of the observed E+A galaxies.

We find that the post-starburst models can be distinguished from undisturbed spiral, S0 and E galaxies and galaxies in their starburst phase on the basis of their SEDs. It is even possible

to distinguish most of the different post-starburst by their SEDs. From the comparison with observations we find that all observed E+A galaxies from the MORPHS catalog can be matched by our models. However only models with short decline timescales for the star formation rate are possible scenarios for the observed E+A galaxies in agreement with our results from the first paper (see Falkenberg, Kotulla, & Fritze, 2009a).

B.3.3 The First Generation of Virgo Cluster Dwarf Elliptical Galaxies?

Authors: T. Lisker, J. Janz, G. Hensler, S. Kim, S.-C. Rey, S. Weinmann, C. Mastropietro, O. Hielscher, S. Paudel, **R. Kotulla**

published in The Astrophysical Journal Letters, 706, L124–L128 (2009)

In the light of the question whether most early-type dwarf (dE) galaxies in clusters formed through infall and transformation of late-type progenitors, we search for an imprint of such an infall history in the oldest, most centrally concentrated dE subclass of the Virgo cluster: the nucleated dEs that show no signatures of disks or central residual star formation. We select dEs in a (projected) region around the central elliptical galaxies, and subdivide them by their line-of-sight velocity into fast-moving and slow-moving ones. These subsamples turn out to have significantly different shapes: while the fast dEs are relatively flat objects, the slow dEs are nearly round. Likewise, when subdividing the central dEs by their projected axial ratio into flat and round ones, their distributions of line-of-sight velocities differ significantly: the flat dEs have a broad, possibly two-peaked distribution, whereas the round dEs show a narrow single peak. We conclude that the round dEs probably are on circularized orbits, while the flat dEs are still on more eccentric or radial orbits typical for an infalling population. In this picture, the round dEs would have resided in the cluster already for a long time, or would even be a cluster-born species, explaining their nearly circular orbits. They would thus be the first generation of Virgo cluster dEs. Their shape could be caused by dynamical heating through repeated tidal interactions. Further investigations through stellar population measurements and studies of simulated galaxy clusters would be desirable to obtain definite conclusions on their origin.

B.3.4 PHAT: PHoto-z Accuracy Testing

Authors: H. Hildebrandt, S. Arnouts, P. Capak, L. A. Moustakas, C. Wolf, F. B. Abdalla, R. J. Assef, M. Banerji, N. Benítez, G. B. Brammer, T. Budavári, S. Carliles, D. Coe, T. Dahlen, R. Feldmann, D. Gerdes, B. Gillis, O. Ilbert, **R. Kotulla**, O. Lahav, I. H. Li, J.-M. Miralles, N. Purger, S. Schmidt, and J. Singal

submitted to Astronomy & Astrophysics

Context. Photometric redshifts (photo-z's) have become an essential tool in extragalactic astronomy. Many current and upcoming observing programmes require great accuracy of photo-z's to reach their scientific goals.

Aims. Here we introduce PHAT, the PHoto-z Accuracy Testing programme, an international initiative to test and compare different methods of photo-z estimation.

Methods. Two different test environments are set up, one (PHAT0) based on simulations to test the basic functionality of the different photo-z codes, and another one (PHAT1) based on data from the GOODS survey including 18-band photometry and $\approx 2\,000$ spectroscopic redshifts.

Results. The accuracy of the different methods is expressed and ranked by the global photo-z bias, scatter, and outlier rates. While most methods agree very well on PHAT0 there are differences in the handling of the Lyman-α forest for higher redshifts. Furthermore, different methods produce photo-z scatters that can differ by up to a factor of two even in this idealised

case. A larger spread in accuracy is found for PHAT1. Few methods benefit from the addition of mid-IR photometry. The accuracy of the other methods is unaffected or suffers when IRAC data are included. Remaining biases and systematic effects can be explained by shortcomings in the different template sets (especially in the mid-IR) and the use of priors on the one hand and an insufficient training set on the other hand. Some strategies to overcome these problems are identified by comparing the methods in detail. Scatters of $4 - 8\%$ in $\Delta z/(1+z)$ were obtained, consistent with other studies. However, somewhat larger outlier rates ($> 7.5\%$ with $\Delta z = (1+z) > 0.15$; $> 4.5\%$ after cleaning) are found for all codes that can only partly be explained by AGN or issues in the photometry or the spec-z catalogue. Some outliers were probably missed in comparisons of photo-zâĂŹs to other, less complete spectroscopic surveys in the past. There is a general trend that empirical codes produce smaller biases than template-based codes.

Conclusions. The systematic, quantitative comparison of different photo-z codes presented here is a snapshot of the current state-ofthe- art of photo-z estimation and sets a standard for the assessment of photo-z accuracy in the future. The rather large outlier rates reported here for PHAT1 on real data should be investigated further since they are most probably also present (and possibly hidden) in many other studies. The test data sets are publicly available and can be used to compare new, upcoming methods to established ones and help in guiding future photo-z method development.

Bibliography

Adelberger, K. L., Steidel, C. C., Shapley, A. E., Hunt, M. P., Erb, D. K., Reddy, N. A., Pettini, M. 2004, ApJ, 607, 226

Ak, S., Bilir, S., Karaali, S., Buser, R., & Cabrera-Lavers, A. 2007, New Astronomy, 12, 605

Allanson, S. P., Hudson, M. J., Smith, R. J., & Lucey, J. R. 2009, ApJ, 702, 1275

Allard, F., Hauschildt, P. H., & Schwenke, D. 2000, ApJ, 540, 1005

Aller, L. H., ed. 1984, Physics of thermal gaseous nebulae

Aloisi, A., Clementini, G., Tosi, M., Annibali, F., Contreras, R., Fiorentino, G., Mack, J., Marconi, M., et al. 2007, ApJ, 667, L151

Anders, P., Bissantz, N., Boysen, L., de Grijs, R., & Fritze, U. 2007, MNRAS, 377, 91

Anders, P., Bissantz, N., Fritze, U., & de Grijs, R. 2004a, MNRAS, 347, 196

Anders, P., de Grijs, R., Fritze, U., & Bissantz, N. 2004b, MNRAS, 347, 17

Anders, P. & Fritze, U. 2003, A&A, 401, 1063

Andreon, S. 2006, MNRAS, 369, 969

Arnouts, S., Moscardini, L., Vanzella, E., Colombi, S., Cristiani, S., Fontana, A., Giallongo, E., Matarrese, S., et al. 2002, MNRAS, 329, 355

Arnouts, S., Walcher, C. J., Le Fèvre, O., Zamorani, G., Ilbert, O., Le Brun, V., Pozzetti, L., Bardelli, S., et al. 2007, A&A, 476, 137

Ashman, K. M., Conti, A., & Zepf, S. E. 1995, AJ, 110, 1164

Ashman, K. M. & Zepf, S. E. 1992, ApJ, 384, 50

Assef, R. J., Kochanek, C. S., Brodwin, M., Brown, M. J. I., Caldwell, N., Cool, R. J., Eisenhardt, P., Eisenstein, D., et al. 2008, ApJ, 676, 286

Babbedge, T. S. R., Rowan-Robinson, M., Vaccari, M., Surace, J. A., Lonsdale, C. J., Clements, D. L., Fang, F., Farrah, D., et al. 2006, MNRAS, 370, 1159

Bahcall, J. N., Flynn, C., & Gould, A. 1992, ApJ, 389, 234

Balestra, I., Mainieri, V., Popesso, P., Dickinson, M., Nonino, M., Rosati, P., Teimoorinia, H., Vanzella, E., et al. 2010, A&A, 512, A12+

Barger, A. J., Aragon-Salamanca, A., Ellis, R. S., Couch, W. J., Smail, I., Sharples, R. M. 1996, MNRAS, 279, 1

Barmby, P. & Huchra, J. P. 2000, ApJ, 531, L29

Barmby, P., Huchra, J. P., Brodie, J. P., Forbes, D. A., Schroder, L. L., Grillmair, C. J. 2000, AJ, 119, 727

Barnes, J. E. & Hernquist, L. 1996, ApJ, 471, 115

Bastian, N. 2008, MNRAS, 390, 759

Bastian, N. & Goodwin, S. P. 2006, MNRAS, 369, L9

Beasley, M. A., Baugh, C. M., Forbes, D. A., Sharples, R. M., & Frenk, C. S. 2002, MNRAS, 333, 383

Beasley, M. A., Bridges, T., Peng, E., Harris, W. E., Harris, G. L. H., Forbes, D. A., Mackie, G. 2008, MNRAS, 386, 1443

Becker, R. H., Fan, X., White, R. L., Strauss, M. A., Narayanan, V. K., Lupton, R. H., Gunn, J. E., Annis, J., et al. 2001, AJ, 122, 2850

Beckwith, S. V. W., Caldwell, J., Clampin, M., de Marchi, G., Dickinson, M., Ferguson, H., Fruchter, A., Hook, R., et al. 2003, in Bulletin of the American Astronomical Society, Vol. 35, Bulletin of the American Astronomical Society, 723–+

Bell, E. F. & de Jong, R. S. 2001, ApJ, 550, 212

Bell, E. F., McIntosh, D. H., Barden, M., Wolf, C., Caldwell, J. A. R., Rix, H.-W., Beckwith, S. V. W., Borch, A., et al. 2004, ApJ, 600, L11

Benítez, N. 2000, ApJ, 536, 571

Bergström, S. & Wiklind, T. 2004, A&A, 414, 95

Bershady, M. A., Charlton, J. C., & Geoffroy, J. M. 1999, ApJ, 518, 103

Bertelli, G., Bressan, A., Chiosi, C., Fagotto, F., & Nasi, E. 1994, A&AS, 106, 275

Bertin, E. & Arnouts, S. 1996, A&AS, 117, 393

Bicker, J. & Fritze, U. 2005, A&A, 443, L19

Bicker, J., Fritze, U., & Fricke, K. J. 2002, A&A, 387, 412

Bicker, J., Fritze, U., Möller, C. S., & Fricke, K. J. 2004, A&A, 413, 37

Blain, A. W., Smail, I., Ivison, R. J., & Kneib, J.-P. 1999, MNRAS, 302, 632

Blanc, G. A., Lira, P., Barrientos, L. F., Aguirre, P., Francke, H., Taylor, E. N., Quadri, R., Marchesini, D., et al. 2008, astro-ph/0803.0763, 803

Bohlin, R. C. & Gilliland, R. L. 2004, AJ, 128, 3053

Boissier, S., Gil de Paz, A., Boselli, A., Madore, B. F., Buat, V., Cortese, L., Burgarella, D., Muñoz-Mateos, J. C., et al. 2007, ApJS, 173, 524

Bolzonella, M., Miralles, J.-M., & Pelló, R. 2000, A&A, 363, 476

Bondi, M., Ciliegi, P., Schinnerer, E., Smolčić, V., Jahnke, K., Carilli, C., Zamorani, G. 2008, ApJ, 681, 1129

Bournaud, F., Combes, F., & Jog, C. J. 2004, A&A, 418, L27

Bower, R. G., Benson, A. J., Malbon, R., Helly, J. C., Frenk, C. S., Baugh, C. M., Cole, S., Lacey, C. G. 2006, MNRAS, 370, 645

Brammer, G. B., van Dokkum, P. G., & Coppi, P. 2008, ApJ, 686, 1503

Bressan, A., Chiosi, C., & Fagotto, F. 1994, ApJS, 94, 63

Bressan, A., Chiosi, C., & Tantalo, R. 1996, A&A, 311, 425

Brodie, J. P. & Strader, J. 2006, ARA&A, 44, 193

Brown, J. H., Burkert, A., & Truran, J. W. 1995, ApJ, 440, 666

Brown, M. J. I., Brand, K., Dey, A., Jannuzi, B. T., Cool, R., Le Floc'h, E., Kochanek, C. S., Armus, L., et al. 2006, ApJ, 638, 88

Brown, R. L. & Mathews, W. G. 1970, ApJ, 160, 939

Brusa, M., Comastri, A., Daddi, E., Cimatti, A., Mignoli, M., Pozzetti, L. 2002, ApJ, 581, L89

Brusa, M., Zamorani, G., Comastri, A., Hasinger, G., Cappelluti, N., Civano, F., Finoguenov, A., Mainieri, V., et al. 2007, ApJS, 172, 353

Bruzual, A. G. 1983, ApJ, 273, 105

Bruzual, A. G. & Charlot, S. 1993, ApJ, 405, 538

Bruzual, G. & Charlot, S. 2003, MNRAS, 344, 1000

Bundy, K., Ellis, R. S., Conselice, C. J., Taylor, J. E., Cooper, M. C., Willmer, C. N. A., Weiner, B. J., Coil, A. L., et al. 2006, ApJ, 651, 120

Buta, R., Corwin, Jr., H. G., de Vaucouleurs, G., de Vaucouleurs, A., & Longo, G. 1995, AJ, 109, 517

Buta, R. & Williams, K. L. 1995, AJ, 109, 543

Calzetti, D., Armus, L., Bohlin, R. C., Kinney, A. L., Koornneef, J., Storchi-Bergmann, T. 2000, ApJ, 533, 682

Calzetti, D., Kinney, A. L., & Storchi-Bergmann, T. 1994, ApJ, 429, 582

Cannon, R., Drinkwater, M., Edge, A., Eisenstein, D., Nichol, R., Outram, P., Pimbblet, K., de Propris, R., et al. 2006, MNRAS, 372, 425

Capak, P., Aussel, H., Ajiki, M., McCracken, H. J., Mobasher, B., Scoville, N., Shopbell, P., Taniguchi, Y., et al. 2007, ApJS, 172, 99

Cappelluti, N., Hasinger, G., Brusa, M., Comastri, A., Zamorani, G., Böhringer, H., Brunner, H., Civano, F., et al. 2007, ApJS, 172, 341

Cardelli, J. A., Clayton, G. C., & Mathis, J. S. 1989, ApJ, 345, 245

Carlberg, R. G., Pritchet, C. J., & Infante, L. 1994, ApJ, 435, 540

Castellanos, M., Díaz, Á. I., & Tenorio-Tagle, G. 2002, ApJ, 565, L79

Cenarro, A. J., Cervantes, J. L., Beasley, M. A., Marín-Franch, A., & Vazdekis, A. 2008, ApJ, 689, L29

Chabrier, G. 2003, PASP, 115, 763

Chapman, S. C., Smail, I., Windhorst, R., Muxlow, T., & Ivison, R. J. 2004, ApJ, 611, 732

Chen, Y.-M., Wild, V., Kauffmann, G., Blaizot, J., Davis, M., Noeske, K., Wang, J.-M., Willmer, C. 2009, MNRAS, 393, 406

Cimatti, A., Bianchi, S., Ferrara, A., & Giovanardi, C. 1997, MNRAS, 290, L43

Cimatti, A., Daddi, E., Mignoli, M., Pozzetti, L., Renzini, A., Zamorani, G., Broadhurst, T., Fontana, A., et al. 2002a, A&A, 381, L68

Cimatti, A., Mignoli, M., Daddi, E., Pozzetti, L., Fontana, A., Saracco, P., Poli, F., Renzini, A., et al. 2002b, A&A, 392, 395

Coe, D., Benítez, N., Sánchez, S. F., Jee, M., Bouwens, R., Ford, H. 2006, AJ, 132, 926

Coelho, P., Barbuy, B., Meléndez, J., Schiavon, R. P., & Castilho, B. V. 2005, A&A, 443, 735

Colbert, J. W., Malkan, M. A., & Rich, R. M. 2006, ApJ, 648, 250

Cole, A. A., Smecker-Hane, T. A., & Gallagher, III, J. S. 2000a, AJ, 120, 1808

Cole, S., Aragon-Salamanca, A., Frenk, C. S., Navarro, J. F., & Zepf, S. E. 1994, MNRAS, 271, 781

Cole, S., Lacey, C. G., Baugh, C. M., & Frenk, C. S. 2000b, MNRAS, 319, 168

Coleman, G. D., Wu, C.-C., & Weedman, D. W. 1980, ApJS, 43, 393

Collister, A. A. & Lahav, O. 2004, PASP, 116, 345

Conroy, C., Gunn, J. E., & White, M. 2008, ArXiv e-prints

Conroy, C., White, M., & Gunn, J. E. 2009, ArXiv e-prints

Conselice, C. J., Newman, J. A., Georgakakis, A., Almaini, O., Coil, A. L., Cooper, M. C., Eisenhardt, P., Foucaud, S., et al. 2007, ApJ, 660, L55

Contardo, G., Steinmetz, M., & Fritze, U. 1998, ApJ, 507, 497

Cool, R. J., Eisenstein, D. J., Fan, X., Fukugita, M., Jiang, L., Maraston, C., Meiksin, A., Schneider, D. P., et al. 2008, ApJ, 682, 919

Côté, P., Blakeslee, J. P., Ferrarese, L., Jordán, A., Mei, S., Merritt, D., Milosavljević, M., Peng, E. W., et al. 2004, ApJS, 153, 223

Côté, P., Piatek, S., Ferrarese, L., Jordán, A., Merritt, D., Peng, E. W., Haşegan, M., Blakeslee, J. P., et al. 2006, ApJS, 165, 57

Couture, J., Harris, W. E., & Allwright, J. W. B. 1990, ApJS, 73, 671

Cox, T. J., Dutta, S. N., Di Matteo, T., Hernquist, L., Hopkins, P. F., Robertson, B., Springel, V. 2006, ApJ, 650, 791

Croton, D. J., Springel, V., White, S. D. M., De Lucia, G., Frenk, C. S., Gao, L., Jenkins, A., Kauffmann, G., et al. 2006, MNRAS, 365, 11

Cunow, B. 2001, MNRAS, 323, 130

Cunow, B. 2004, MNRAS, 353, 477

Daddi, E., Cimatti, A., Broadhurst, T., Renzini, A., Zamorani, G., Mignoli, M., Saracco, P., Fontana, A., et al. 2002, A&A, 384, L1

Daddi, E., Cimatti, A., Pozzetti, L., Hoekstra, H., Röttgering, H. J. A., Renzini, A., Zamorani, G., Mannucci, F. 2000, A&A, 361, 535

Daddi, E., Cimatti, A., Renzini, A., Fontana, A., Mignoli, M., Pozzetti, L., Tozzi, P., Zamorani, G. 2004, ApJ, 617, 746

Daddi, E., Dannerbauer, H., Elbaz, D., Dickinson, M., Morrison, G., Stern, D., Ravindranath, S. 2008, ApJ, 673, L21

Daddi, E., Dickinson, M., Chary, R., Pope, A., Morrison, G., Alexander, D. M., Bauer, F. E., Brandt, W. N., et al. 2005, ApJ, 631, L13

Daddi, E., Dickinson, M., Morrison, G., Chary, R., Cimatti, A., Elbaz, D., Frayer, D., Renzini, A., et al. 2007, ApJ, 670, 156

Davis, M., Guhathakurta, P., Konidaris, N. P., Newman, J. A., Ashby, M. L. N., Biggs, A. D., Barmby, P., Bundy, K., et al. 2007, ApJ, 660, L1

De Angeli, F., Piotto, G., Cassisi, S., Busso, G., Recio-Blanco, A., Salaris, M., Aparicio, A., Rosenberg, A. 2005, AJ, 130, 116

de Grijs, R. & Anders, P. 2006, MNRAS, 366, 295

de Grijs, R., Fritze, U., Anders, P., Gallagher, J. S., Bastian, N., Taylor, V. A., Windhorst, R. A. 2003a, MNRAS, 342, 259

de Grijs, R., Lee, J. T., Mora Herrera, M. C., Fritze, U., & Anders, P. 2003b, New Astronomy, 8, 155

De Lucia, G. & Blaizot, J. 2007, MNRAS, 375, 2

De Lucia, G., Kauffmann, G., & White, S. D. M. 2004, MNRAS, 349, 1101

De Lucia, G., Poggianti, B. M., Halliday, C., Milvang-Jensen, B., Noll, S., Smail, I., Zaritsky, D. 2009, MNRAS, 400, 68

De Lucia, G., Springel, V., White, S. D. M., Croton, D., & Kauffmann, G. 2006, MNRAS, 366, 499

de Mello, D. F., Daddi, E., Renzini, A., Cimatti, A., di Serego Alighieri, S., Pozzetti, L., Zamorani, G. 2004, ApJ, 608, L29

de Vaucouleurs, G. 1959, Handbuch der Physik, 53, 275

de Vaucouleurs, G. 1963, ApJS, 8, 31

de Vaucouleurs, G., de Vaucouleurs, A., Corwin, H. G., Buta, R. J., Paturel, G., Fouque, P. 1995, VizieR Online Data Catalog, 7155, 0

Dey, A., Graham, J. R., Ivison, R. J., Smail, I., Wright, G. S., Liu, M. C. 1999, ApJ, 519, 610

Dieball, A., Knigge, C., Zurek, D. R., Shara, M. M., Long, K. S., Charles, P. A., Hannikainen, D. 2007, ApJ, 670, 379

Doherty, M., Bunker, A. J., Ellis, R. S., & McCarthy, P. J. 2005, MNRAS, 361, 525

Doi, M., Tanaka, M., Fukugita, M., Gunn, J. E., Yasuda, N., Ivezić, Ž., Brinkmann, J., de Haars, E., et al. 2010, AJ, 139, 1628

Dopita, M. A., Groves, B. A., Fischera, J., Sutherland, R. S., Tuffs, R. J., Popescu, C. C., Kewley, L. J., Reuland, M., et al. 2005, ApJ, 619, 755

Dotter, A., Chaboyer, B., Jevremović, D., Baron, E., Ferguson, J. W., Sarajedini, A., Anderson, J. 2007, AJ, 134, 376

Dressler, A., Oemler, A. J., Poggianti, B. M., Smail, I., Trager, S., Shectman, S. A., Couch, W. J., Ellis, R. S. 2004, ApJ, 617, 867

Dressler, A., Smail, I., Poggianti, B. M., Butcher, H., Couch, W. J., Ellis, R. S., Oemler, A. J. 1999, ApJS, 122, 51

Dye, S., Eales, S. A., Aretxaga, I., Serjeant, S., Dunlop, J. S., Babbedge, T. S. R., Chapman, S. C., Cirasuolo, M., et al. 2008, MNRAS, 386, 1107

Eggen, O. J., Lynden-Bell, D., & Sandage, A. R. 1962, ApJ, 136, 748

Eisenstein, D. J., Annis, J., Gunn, J. E., Szalay, A. S., Connolly, A. J., Nichol, R. C., Bahcall, N. A., Bernardi, M., et al. 2001, AJ, 122, 2267

Eisenstein, D. J., Hogg, D. W., Fukugita, M., Nakamura, O., Bernardi, M., Finkbeiner, D. P., Schlegel, D. J., Brinkmann, J., et al. 2003, ApJ, 585, 694

Eisenstein, D. J., Zehavi, I., Hogg, D. W., Scoccimarro, R., Blanton, M. R., Nichol, R. C., Scranton, R., Seo, H.-J., et al. 2005, ApJ, 633, 560

Elston, R., Rieke, G. H., & Rieke, M. J. 1988, ApJ, 331, L77

Elston, R., Rieke, M. J., & Rieke, G. H. 1989, ApJ, 341, 80

Erb, D. K. 2008, ApJ, 674, 151

Erb, D. K., Shapley, A. E., Pettini, M., Steidel, C. C., Reddy, N. A., Adelberger, K. L. 2006a, ApJ, 644, 813

Erb, D. K., Shapley, A. E., Steidel, C. C., Pettini, M., Adelberger, K. L., Hunt, M. P., Moorwood, A. F. M., Cuby, J.-G. 2003, ApJ, 591, 101

Erb, D. K., Steidel, C. C., Shapley, A. E., Pettini, M., Reddy, N. A., Adelberger, K. L. 2006b, ApJ, 646, 107

Ercolano, B., Barlow, M. J., Storey, P. J., & Liu, X.-W. 2003, MNRAS, 340, 1136

Ercolano, B. & Storey, P. J. 2006, MNRAS, 372, 1875

Eskridge, P. B., Frogel, J. A., Pogge, R. W., Quillen, A. C., Berlind, A. A., Davies, R. L., DePoy, D. L., Gilbert, K. M., et al. 2002, ApJS, 143, 73

Faber, S. M. & Gallagher, J. S. 1979, ARA&A, 17, 135

Faber, S. M., Willmer, C. N. A., Wolf, C., Koo, D. C., Weiner, B. J., Newman, J. A., Im, M., Coil, A. L., et al. 2007, ApJ, 665, 265

Falkenberg, M. A., Kotulla, R., & Fritze, U. 2009a, MNRAS, 397, 1940

Falkenberg, M. A., Kotulla, R., & Fritze, U. 2009b, MNRAS, 397, 1954

Fan, X., Carilli, C. L., & Keating, B. 2006, ARA&A, 44, 415

Fan, X., Strauss, M. A., Schneider, D. P., Gunn, J. E., Lupton, R. H., Becker, R. H., Davis, M., Newman, J. A., et al. 2001, AJ, 121, 54

Feldmann, R., Carollo, C. M., Porciani, C., Lilly, S. J., Capak, P., Taniguchi, Y., Le Fèvre, O., Renzini, A., et al. 2006, MNRAS, 372, 565

Ferguson, A. M. N., Gallagher, J. S., & Wyse, R. F. G. 1998a, AJ, 116, 673

Ferguson, A. M. N., Wyse, R. F. G., Gallagher, J. S., & Hunter, D. A. 1998b, ApJ, 506, L19

Ferguson, A. M. N., Wyse, R. F. G., Gallagher, III, J. S., & Hunter, D. A. 1996, AJ, 111, 2265

Ferland, G. J., Korista, K. T., Verner, D. A., Ferguson, J. W., Kingdon, J. B., Verner, E. M. 1998, PASP, 110, 761

Fernández-Soto, A., Lanzetta, K. M., Chen, H., Pascarelle, S. M., & Yahata, N. 2001, ApJS, 135, 41

Fernández-Soto, A., Lanzetta, K. M., & Chen, H.-W. 2003, MNRAS, 342, 1215

Fernández-Soto, A., Lanzetta, K. M., & Yahil, A. 1999, ApJ, 513, 34

Ferrarese, L., Côté, P., Jordán, A., Peng, E. W., Blakeslee, J. P., Piatek, S., Mei, S., Merritt, D., et al. 2006, ApJS, 164, 334

Finoguenov, A., Guzzo, L., Hasinger, G., Scoville, N. Z., Aussel, H., Böhringer, H., Brusa, M., Capak, P., et al. 2007, ApJS, 172, 182

Fioc, M. & Rocca-Volmerange, B. 1997, A&A, 326, 950

Fontanot, F., De Lucia, G., Monaco, P., Somerville, R. S., & Santini, P. 2009, MNRAS, 397, 1776

Forbes, D. A., Brodie, J. P., & Grillmair, C. J. 1997, AJ, 113, 1652

Förster-Schreiber, N. M., Franx, M., Labbé, I., Rudnick, G., van Dokkum, P. G., Illingworth, G. D., Kuijken, K., Moorwood, A. F. M., et al. 2006, AJ, 131, 1891

Förster-Schreiber, N. M., van Dokkum, P. G., Franx, M., Labbé, I., Rudnick, G., Daddi, E., Illing-worth, G. D., Kriek, M., et al. 2004, ApJ, 616, 40

Franx, M., Labbé, I., Rudnick, G., van Dokkum, P. G., Daddi, E., Förster Schreiber, N. M., Moorwood, A., Rix, H.-W., et al. 2003, ApJ, 587, L79

Franx, M., Moorwood, A., Rix, H., Kuijken, K., Röttgering, H., van der Werf, P., van Dokkum, P., Labbe, I., et al. 2000, The Messenger, 99, 20

Frei, Z. & Gunn, J. E. 1994, AJ, 108, 1476

Fritze, U. 2004, A&A, 414, 515

Fritze, U. & Bicker, J. 2006, A&A, 454, 67

Fritze, U. & Burkert, A. 1995, A&A, 300, 58

Fritze, U. & Gerhard, O. E. 1994a, A&A, 285, 751

Fritze, U. & Gerhard, O. E. 1994b, A&A, 285, 775

Fritze, U., Krüger, H., Fricke, K. J., & Loose, H.-H. 1989, A&A, 224, L1

Fritze, U. & Lilly, T. 2007, in Astronomical Society of the Pacific Conference Series, Vol. 374, From Stars to Galaxies: Building the Pieces to Build Up the Universe, ed. A. Vallenari, R. Tantalo, L. Portinari, & A. Moretti, 341–+

Fritze, U., Papaderos, P., Anders, P., Lilly, T., Cunow, B., Gallagher, J. 2006, in IAU Symposium, Vol. 232, The Scientific Requirements for Extremely Large Telescopes, ed. P. Whitelock, M. Dennefeld, & B. Leibundgut, 241–247

Galilei, G. 1610, Sidereus Nuncius (???)

Ganda, K., Peletier, R. F., McDermid, R. M., Falcón-Barroso, J., de Zeeuw, P. T., Bacon, R., Cappellari, M., Davies, R. L., et al. 2007, MNRAS, 380, 506

Garcia Vargas, M. L. & Diaz, A. I. 1994, ApJS, 91, 553

Gauba, G., Parthasarathy, M., Nakada, Y., & Fujii, T. 2001, A&A, 373, 572

Gavazzi, G., Bonfanti, C., Sanvito, G., Boselli, A., & Scodeggio, M. 2002, ApJ, 576, 135

Gebhardt, K. & Kissler-Patig, M. 1999, AJ, 118, 1526

Geha, M., Guhathakurta, P., & van der Marel, R. P. 2005, AJ, 129, 2617

Georgakakis, A., Hopkins, A. M., Afonso, J., Sullivan, M., Mobasher, B., Cram, L. E. 2006, MNRAS, 367, 331

Gerola, H. & Seiden, P. E. 1978, ApJ, 223, 129

Giacconi, R., Rosati, P., Tozzi, P., Borgani, S., Hasinger, G., Bergeron, J., Gilmozzi, R., Nonino, M., et al. 2000, in Bulletin of the American Astronomical Society, Vol. 32, Bulletin of the American Astronomical Society, 1562–+

Giavalisco, M. 2002, ARA&A, 40, 579

Gil de Paz, A., Boissier, S., Madore, B. F., Seibert, M., Joe, Y. H., Boselli, A., Wyder, T. K., Thilker, D., et al. 2007, ApJS, 173, 185

Gil de Paz, A., Madore, B. F., Boissier, S., Swaters, R., Popescu, C. C., Tuffs, R. J., Sheth, K., Kennicutt, Jr., R. C., et al. 2005, ApJ, 627, L29

Girardi, L., Bressan, A., Bertelli, G., & Chiosi, C. 2000, A&AS, 141, 371

Glassman, T. M. & Larkin, J. E. 2000, ApJ, 539, 570

Gorgas, J., Faber, S. M., Burstein, D., Gonzalez, J. J., Courteau, S., Prosser, C. 1993, ApJS, 86, 153

Goto, T. 2007, MNRAS, 381, 187

Grazian, A., Fontana, A., de Santis, C., Nonino, M., Salimbeni, S., Giallongo, E., Cristiani, S., Gallozzi, S., et al. 2006, A&A, 449, 951

Grebel, E. K. 1997, in Reviews in Modern Astronomy, Vol. 10, Reviews in Modern Astronomy, ed. R. E. Schielicke, 29–60

Greve, T. R., Bertoldi, F., Smail, I., Neri, R., Chapman, S. C., Blain, A. W., Ivison, R. J., Genzel, R., et al. 2005, MNRAS, 359, 1165

Guhathakurta, P., Tyson, J. A., & Majewski, S. R. 1990, ApJ, 357, L9

Guiderdoni, B. & Rocca-Volmerange, B. 1987, A&A, 186, 1

Gunn, J. E., Carr, M., Rockosi, C., Sekiguchi, M., Berry, K., Elms, B., de Haas, E., Ivezić, Ž., et al. 1998, AJ, 116, 3040

Gunn, J. E. & Peterson, B. A. 1965, ApJ, 142, 1633

Harris, G. L. H. & Harris, W. E. 2000, AJ, 120, 2423

Harris, G. L. H., Harris, W. E., & Poole, G. B. 1999, AJ, 117, 855

Harris, W. E. 1996, AJ, 112, 1487

Hartwick, F. D. A. 2004, ApJ, 603, 108

Hasinger, G., Cappelluti, N., Brunner, H., Brusa, M., Comastri, A., Elvis, M., Finoguenov, A., Fiore, F., et al. 2007, ApJS, 172, 29

Hayashi, M., Motohara, K., Shimasaku, K., Onodera, M., Uchimoto, Y. K., Kashikawa, N., Yoshida, M., Okamura, S., et al. 2009, ApJ, 691, 140

Heavens, A., Panter, B., Jimenez, R., & Dunlop, J. 2004, Nature, 428, 625

Hempel, M., Hilker, M., Kissler-Patig, M., Puzia, T. H., Minniti, D., Goudfrooij, P. 2003, A&A, 405, 487

Hempel, M., Zepf, S., Kundu, A., Geisler, D., & Maccarone, T. J. 2007, ApJ, 661, 768

Heyl, J. S., Hernquist, L., & Spergel, D. N. 1994, ApJ, 427, 165

Hibbard, J. E. & Mihos, J. C. 1995, AJ, 110, 140

Hibbard, J. E. & van Gorkom, J. H. 1996, AJ, 111, 655

Hibbard, J. E. & Yun, M. S. 1999, ApJ, 522, L93

Hildebrandt, H., Arnouts, S., Capak, P., Moustakas, L., Wolf, C., Abdalla, F., Assef, R., Banerji, M., et al. 2010, A&A, submitted

Hopkins, A. M., Miller, C. J., Nichol, R. C., Connolly, A. J., Bernardi, M., Gómez, P. L., Goto, T., Tremonti, C. A., et al. 2003, ApJ, 599, 971

Howell, J. H. 2005, AJ, 130, 2065

Hubble, E. 1929a, Proceedings of the National Academy of Science, 15, 168

Hubble, E. & Humason, M. L. 1931, ApJ, 74, 43

Hubble, E. & Humason, M. L. 1934, Proceedings of the National Academy of Science, 20, 264

Hubble, E. P. 1926, ApJ, 64, 321

Hubble, E. P. 1929b, ApJ, 69, 103

Humason, M. L., Mayall, N. U., & Sandage, A. R. 1956, AJ, 61, 97

Hummer, D. G. 1988, ApJ, 327, 477

Ilbert, O., Arnouts, S., McCracken, H. J., Bolzonella, M., Bertin, E., Le Fèvre, O., Mellier, Y., Zamorani, G., et al. 2006, A&A, 457, 841

Ilbert, O., Capak, P., Salvato, M., Aussel, H., McCracken, H. J., Sanders, D. B., Scoville, N., Kartaltepe, J., et al. 2009, ApJ, 690, 1236

Inoue, A. K., Iwata, I., Deharveng, J.-M., Buat, V., & Burgarella, D. 2005, A&A, 435, 471

Ivezić, Ž., Sesar, B., Jurić, M., Bond, N., Dalcanton, J., Rockosi, C. M., Yanny, B., Newberg, H. J., et al. 2008, ApJ, 684, 287

Iye, M., Ota, K., Kashikawa, N., Furusawa, H., Hashimoto, T., Hattori, T., Matsuda, Y., Morokuma, T., et al. 2006, Nature, 443, 186

Izotov, Y. I. & Thuan, T. X. 1998, ApJ, 500, 188

Izotov, Y. I., Thuan, T. X., & Lipovetsky, V. A. 1994, ApJ, 435, 647

Izotov, Y. I., Thuan, T. X., & Lipovetsky, V. A. 1997, ApJS, 108, 1

Jansen, R. A., Franx, M., & Fabricant, D. 2001, ApJ, 551, 825

Jog, C. J. & Chitre, A. 2002, A&A, 393, L89

Juneau, S., Glazebrook, K., Crampton, D., McCarthy, P. J., Savaglio, S., Abraham, R., Carlberg, R. G., Chen, H.-W., et al. 2005, ApJ, 619, L135

Kalirai, J. S., Hansen, B. M. S., Kelson, D. D., Reitzel, D. B., Rich, R. M., Richer, H. B. 2008, ApJ, 676, 594

Kashikawa, N., Shimasaku, K., Yasuda, N., Ajiki, M., Akiyama, M., Ando, H., Aoki, K., Doi, M., et al. 2004, PASJ, 56, 1011

Kauffmann, G., Colberg, J. M., Diaferio, A., & White, S. D. M. 1999, MNRAS, 303, 188

Kauffmann, G., Heckman, T. M., White, S. D. M., Charlot, S., Tremonti, C., Peng, E. W., Seibert, M., Brinkmann, J., et al. 2003, MNRAS, 341, 54

Kauffmann, G., White, S. D. M., & Guiderdoni, B. 1993, MNRAS, 264, 201

Kay, S. T., Pearce, F. R., Frenk, C. S., & Jenkins, A. 2002, MNRAS, 330, 113

Kennicutt, Jr., R. C. 1983, ApJ, 272, 54

Kennicutt, Jr., R. C. 1992, ApJS, 79, 255

Kennicutt, Jr., R. C. 1998, ARA&A, 36, 189

Kewley, L. J. & Dopita, M. A. 2002, ApJS, 142, 35

Kewley, L. J. & Ellison, S. L. 2008, ApJ, 681, 1183

Kewley, L. J., Geller, M. J., & Jansen, R. A. 2004, AJ, 127, 2002

Kissler-Patig, M., Brodie, J. P., & Minniti, D. 2002, A&A, 391, 441

Kitzbichler, M. G. & White, S. D. M. 2007, MNRAS, 376, 2

Kodama, T., Bell, E. F., & Bower, R. G. 1999, MNRAS, 302, 152

Koekemoer, A. M., Aussel, H., Calzetti, D., Capak, P., Giavalisco, M., Kneib, J.-P., Leauthaud, A., Le Fèvre, O., et al. 2007, ApJS, 172, 196

Komatsu, E., Dunkley, J., Nolta, M. R., Bennett, C. L., Gold, B., Hinshaw, G., Jarosik, N., Larson, D., et al. 2009, ApJS, 180, 330

Kong, X., Daddi, E., Arimoto, N., Renzini, A., Broadhurst, T., Cimatti, A., Ikuta, C., Ohta, K., et al. 2006, ApJ, 638, 72

Korn, A. J., Maraston, C., & Thomas, D. 2005, A&A, 438, 685

Kotulla, R. 2009a, MNRAS submitted (back to the referee with minor revisions)

Kotulla, R. 2009b, MNRAS submitted (back to the referee with minor revisions)

Kotulla, R. & Fritze, U. 2009, MNRAS, 393, L55

Kotulla, R., Fritze, U., & Anders, P. 2008a, MNRAS, 387, 1149

Kotulla, R., Fritze, U., & Gallagher, III, J. S. 2008b, ApJ, 688, L65

Kotulla, R., Fritze, U., Weilbacher, P., & Anders, P. 2009, MNRAS, 396, 462

Kriek, M., van Dokkum, P. G., Franx, M., Förster Schreiber, N. M., Gawiser, E., Illingworth, G. D., Labbé, I., Marchesini, D., et al. 2006, ApJ, 645, 44

Kriek, M., van Dokkum, P. G., Labbé, I., Franx, M., Illingworth, G. D., Marchesini, D., Quadri, R. F. 2009, ApJ, 700, 221

Krist, J. 2004, TinyTim User's Manual, Available at http://www.stsci.edu/software/tinytim, 6th edn.

Kroupa, P. 2001, MNRAS, 322, 231

Krüger, H. & Fritze, U. 1994, A&A, 284, 793

Krüger, H., Fritze, U., Fricke, K. J., & Loose, H.-H. 1992, A&A, 259, L73

Krüger, H., Fritze, U., Fricke, K. J., & Loose, H.-H. 1993, Ap&SS, 205, 57

Krüger, H., Fritze, U., & Loose, H.-H. 1995, A&A, 303, 41

Krüger, H., Fritze, U., Loose, H.-H., & Fricke, K. J. 1991, A&A, 242, 343

Krumholz, M. R. & McKee, C. F. 2008, Nature, 451, 1082

Kundu, A. & Whitmore, B. C. 2001a, AJ, 121, 2950

Kundu, A. & Whitmore, B. C. 2001b, AJ, 122, 1251

Kurth, O. M., Fritze, U., & Fricke, K. J. 1999, A&AS, 138, 19

Kurucz, R. L. 1992, in IAU Symposium, Vol. 149, The Stellar Populations of Galaxies, ed. B. Barbuy & A. Renzini, 225–+

Kučinskas, A., Hauschildt, P. H., Brott, I., Vansevičius, V., Lindegren, L., Tanabé, T., Allard, F. 2006, A&A, 452, 1021

Labbé, I., Franx, M., Rudnick, G., Schreiber, N. M. F., Rix, H.-W., Moorwood, A., van Dokkum, P. G., van der Werf, P., et al. 2003, AJ, 125, 1107

Labbé, I., Huang, J., Franx, M., Rudnick, G., Barmby, P., Daddi, E., van Dokkum, P. G., Fazio, G. G., et al. 2005, ApJ, 624, L81

Lacey, C. G., Baugh, C. M., Frenk, C. S., Silva, L., Granato, G. L., Bressan, A. 2008, MNRAS, 385, 1155

Laine, S., van der Marel, R. P., Rossa, J., Hibbard, J. E., Mihos, J. C., Böker, T., Zabludoff, A. I. 2003, AJ, 126, 2717

Lamers, H. J. G. L. M., Gieles, M., & Portegies Zwart, S. F. 2005, A&A, 429, 173

Larsen, S. S. 1999, A&AS, 139, 393

Larsen, S. S. 2002, AJ, 124, 1393

Larsen, S. S., Brodie, J. P., & Strader, J. 2005, A&A, 443, 413

Lawrence, A., Warren, S. J., Almaini, O., Edge, A. C., Hambly, N. C., Jameson, R. F., Lucas, P., Casali, M., et al. 2007, MNRAS, 379, 1599

Le Borgne, D., Abraham, R., Daniel, K., McCarthy, P. J., Glazebrook, K., Savaglio, S., Crampton, D., Juneau, S., et al. 2006, ApJ, 642, 48

Le Borgne, D. & Rocca-Volmerange, B. 2002, A&A, 386, 446

Le Fèvre, O., Abraham, R., Lilly, S. J., Ellis, R. S., Brinchmann, J., Schade, D., Tresse, L., Colless, M., et al. 2000, MNRAS, 311, 565

Lee, H., Skillman, E. D., Cannon, J. M., Jackson, D. C., Gehrz, R. D., Polomski, E. F., Woodward, C. E. 2006, ApJ, 647, 970

Leitherer, C., Schaerer, D., Goldader, J. D., Delgado, R. M. G., Robert, C., Kune, D. F., de Mello, D. F., Devost, D., et al. 1999, ApJS, 123, 3

Lejeune, T., Cuisinier, F., & Buser, R. 1997, A&AS, 125, 229

Lejeune, T., Cuisinier, F., & Buser, R. 1998, A&AS, 130, 65

Li, Y., Mac Low, M.-M., & Klessen, R. S. 2004, ApJ, 614, L29

Lilly, S. J., Le Fèvre, O., Renzini, A., Zamorani, G., Scodeggio, M., Contini, T., Carollo, C. M., Hasinger, G., et al. 2007, ApJS, 172, 70

Lilly, T. & Fritze, U. 2005a, astro-ph/0507305

Lilly, T. & Fritze, U. 2005b, astro-ph/0507303

Lilly, T. & Fritze, U. 2006, A&A, 457, 467

Lilly, T. & Fritze, U. 2008, submitted to A&A

Lindner, U., Fritze, U., & Fricke, K. J. 1999, A&A, 341, 709

Loh, Y.-S. & Strauss, M. A. 2006, MNRAS, 366, 373

Lonsdale, C. J., Smith, H. E., Rowan-Robinson, M., Surace, J., Shupe, D., Xu, C., Oliver, S., Padgett, D., et al. 2003, PASP, 115, 897

Mackey, A. D. & Gilmore, G. F. 2003, MNRAS, 338, 85

Madau, P. 1995, ApJ, 441, 18

Madau, P., Ferguson, H. C., Dickinson, M. E., Giavalisco, M., Steidel, C. C., Fruchter, A. 1996, MNRAS, 283, 1388

Madau, P., Pozzetti, L., & Dickinson, M. 1998, ApJ, 498, 106

Marigo, P., Girardi, L., Bressan, A., Groenewegen, M. A. T., Silva, L., Granato, G. L. 2008, A&A, 482, 883

Marín-Franch, A., Aparicio, A., Piotto, G., Rosenberg, A., Chaboyer, B., Sarajedini, A., Siegel, M., Anderson, J., et al. 2009, ApJ, 694, 1498

Marks, M. & Kroupa, P. 2010, MNRAS, 872

Martin, C. L. & Kennicutt, Jr., R. C. 2001, ApJ, 555, 301

Matteucci, F. & Padovani, P. 1993, ApJ, 419, 485

Matteucci, F. & Tornambe, A. 1987, A&A, 185, 51

Mei, S., Blakeslee, J. P., Côté, P., Tonry, J. L., West, M. J., Ferrarese, L., Jordán, A., Peng, E. W., et al. 2007, ApJ, 655, 144

Meurer, G. R., Wong, O. I., Kim, J. H., Hanish, D. J., Heckman, T. M., Werk, J., Bland-Hawthorn, J., Dopita, M. A., et al. 2009, ApJ, 695, 765

Mezger, P. O. 1978, A&A, 70, 565

Mihos, J. C. & Hernquist, L. 1996, ApJ, 464, 641

Miyazaki, M., Shimasaku, K., Kodama, T., Okamura, S., Furusawa, H., Ouchi, M., Nakata, F., Doi, M., et al. 2003, PASJ, 55, 1079

Mobasher, B., Capak, P., Scoville, N. Z., Dahlen, T., Salvato, M., Aussel, H., Thompson, D. J., Feldmann, R., et al. 2007, ApJS, 172, 117

Möllenhoff, C., Popescu, C. C., & Tuffs, R. J. 2006, A&A, 456, 941

Möller, C. S., Fritze, U., Fricke, K. J., & Calzetti, D. 2001, Ap&SS, 276, 799

Morrissey, P., Conrow, T., Barlow, T. A., Small, T., Seibert, M., Wyder, T. K., Budavári, T., Arnouts, S., et al. 2007, ApJS, 173, 682

Moster, B. P., Somerville, R. S., Newman, J. A., & Rix, H. 2010, ArXiv e-prints

Moustakas, L. A., Casertano, S., Conselice, C. J., Dickinson, M. E., Eisenhardt, P., Ferguson, H. C., Giavalisco, M., Grogin, N. A., et al. 2004, ApJ, 600, L131

Munari, U., Sordo, R., Castelli, F., & Zwitter, T. 2005, A&A, 442, 1127

Murphy, Jr., T. W., Soifer, B. T., Matthews, K., & Armus, L. 2001, ApJ, 559, 201

Nagamine, K., Cen, R., Hernquist, L., Ostriker, J. P., & Springel, V. 2005, ApJ, 627, 608

Nagao, T., Maiolino, R., & Marconi, A. 2006, A&A, 459, 85

Newberry, M. V., Boroson, T. A., & Kirshner, R. P. 1990, ApJ, 350, 585

Noeske, K. G., Faber, S. M., Weiner, B. J., Koo, D. C., Primack, J. R., Dekel, A., Papovich, C., Conselice, C. J., et al. 2007a, ApJ, 660, L47

Noeske, K. G., Weiner, B. J., Faber, S. M., Papovich, C., Koo, D. C., Somerville, R. S., Bundy, K., Conselice, C. J., et al. 2007b, ApJ, 660, L43

Nomoto, K. & Hashimoto, M. 1988, Phys. Reports, 163, 13

Nomoto, K., Iwamoto, K., Nakasato, N., Thielemann, F.-K., Brachwitz, F., Tsujimoto, T., Kubo, Y., Kishimoto, N. 1997, Nuclear Physics A, 621, 467

Nussbaumer, H. & Schmutz, W. 1984, A&A, 138, 495

O'Connell, R. W. 1976, ApJ, 206, 370

O'Connell, R. W. 1980, ApJ, 236, 430

Oey, M. S. & Kennicutt, Jr., R. C. 1993, ApJ, 411, 137

Oey, M. S. & Kennicutt, Jr., R. C. 1997, MNRAS, 291, 827

Oke, J. B. 1974, ApJS, 27, 21

Oke, J. B. & Sandage, A. 1968, ApJ, 154, 21

Opik, E. 1922, ApJ, 55, 406

Osterbrock, D. E. & Ferland, G. J. 2006, Astrophysics of gaseous nebulae and active galactic nuclei, 2nd. ed (University Science Books, Sausalito, CA)

Pannella, M., Carilli, C. L., Daddi, E., Mc Cracken, H. J., Owen, F. N., Renzini, A., Strazzullo, V., Civano, F., et al. 2009, ArXiv:0905.1674

Papovich, C., Moustakas, L. A., Dickinson, M., Le Floc'h, E., Rieke, G. H., Daddi, E., Alexander, D. M., Bauer, F., et al. 2006, ApJ, 640, 92

Parmentier, G. & Fritze, U. 2009, ApJ, 690, 1112

Pasquali, A. & Castangia, P. 2008, MNRAS, 385, 468

Pavlovsky, M., Biretta, J., Bohlin, R., Chiaberge, M., Cox, C., Dressel, L., Fruchter, A., Giavalisco, M., et al. 2005, ACS Data Handbook, Version 4.0 (Baltimore: StScI)

Pei, Y. C. 1995, ApJ, 438, 623

Peng, E. W., Jordán, A., Côté, P., Blakeslee, J. P., Ferrarese, L., Mei, S., West, M. J., Merritt, D., et al. 2006, ApJ, 639, 95

Persson, S. E., Aaronson, M., Cohen, J. G., Frogel, J. A., & Matthews, K. 1983, ApJ, 266, 105

Persson, S. E., Murphy, D. C., Krzeminski, W., Roth, M., & Rieke, M. J. 1998, AJ, 116, 2475

Pettini, M., Shapley, A. E., Steidel, C. C., Cuby, J.-G., Dickinson, M., Moorwood, A. F. M., Adelberger, K. L., Giavalisco, M. 2001, ApJ, 554, 981

Pickles, A. J. 1985a, ApJS, 59, 33

Pickles, A. J. 1985b, ApJ, 296, 340

Pickles, A. J. & Visvanathan, N. 1985, ApJ, 294, 134

Piovan, L., Tantalo, R., & Chiosi, C. 2006a, MNRAS, 366, 923

Piovan, L., Tantalo, R., & Chiosi, C. 2006b, MNRAS, 370, 1454

Pipino, A. & Matteucci, F. 2004, MNRAS, 347, 968

Poggianti, B. M. 1997, A&AS, 122, 399

Poggianti, B. M., Bridges, T. J., Komiyama, Y., Yagi, M., Carter, D., Mobasher, B., Okamura, S., Kashikawa, N. 2004, ApJ, 601, 197

Poggianti, B. M., Smail, I., Dressler, A., Couch, W. J., Barger, A. J., Butcher, H., Ellis, R. S., Oemler, A. J. 1999, ApJ, 518, 576

Popescu, C. C., Misiriotis, A., Kylafis, N. D., Tuffs, R. J., & Fischera, J. 2000, A&A, 362, 138

Portinari, L., Chiosi, C., & Bressan, A. 1998, A&A, 334, 505

Pozzetti, L., Bolzonella, M., Lamareille, F., Zamorani, G., Franzetti, P., Le Fèvre, O., Iovino, A., Temporin, S., et al. 2007, A&A, 474, 443

Prantzos, N., Vangioni-Flam, E., & Chauveau, S. 1994, A&A, 285, 132

Prochaska, J. X., Chen, H.-W., Dessauges-Zavadsky, M., & Bloom, J. S. 2007, ApJ, 666, 267

Prochaska, J. X., Gawiser, E., Wolfe, A. M., Castro, S., & Djorgovski, S. G. 2003, ApJ, 595, L9

Puzia, T. H., Zepf, S. E., Kissler-Patig, M., Hilker, M., Minniti, D., Goudfrooij, P. 2002, A&A, 391, 453

Quadri, R., Marchesini, D., van Dokkum, P., Gawiser, E., Franx, M., Lira, P., Rudnick, G., Urry, C. M., et al. 2007a, AJ, 134, 1103

Quadri, R., van Dokkum, P., Gawiser, E., Franx, M., Marchesini, D., Lira, P., Rudnick, G., Herrera, D., et al. 2007b, ApJ, 654, 138

Ramírez, S. V., Stephens, A. W., Frogel, J. A., & DePoy, D. L. 2000, AJ, 120, 833

Rauch, T. 2003, A&A, 403, 709

Read, J. I. & Trentham, N. 2005, Royal Society of London Philosophical Transactions Series A, 363, 2693

Reddy, N. A., Erb, D. K., Steidel, C. C., Shapley, A. E., Adelberger, K. L., Pettini, M. 2005, ApJ, 633, 748

Reddy, N. A., Steidel, C. C., Erb, D. K., Shapley, A. E., & Pettini, M. 2006, ApJ, 653, 1004

Reddy, N. A., Steidel, C. C., Pettini, M., Adelberger, K. L., Shapley, A. E., Erb, D. K., Dickinson, M. 2008, ApJS, 175, 48

Reuland, M., van Breugel, W., de Vries, W., Dopita, M. A., Dey, A., Miley, G., Röttgering, H., Venemans, B., et al. 2007, AJ, 133, 2607

Rich, R. M., Minniti, D., & Liebert, J. 1993, ApJ, 406, 489

Richards, G. T., Strauss, M. A., Fan, X., Hall, P. B., Jester, S., Schneider, D. P., Vanden Berk, D. E., Stoughton, C., et al. 2006, AJ, 131, 2766

Rocha-Pinto, H. J. & Maciel, W. J. 1998a, A&A, 339, 791

Rocha-Pinto, H. J. & Maciel, W. J. 1998b, A&A, 339, 791

Rocha-Pinto, H. J., Scalo, J., Maciel, W. J., & Flynn, C. 2000, A&A, 358, 869

Roche, N. D., Almaini, O., Dunlop, J., Ivison, R. J., & Willott, C. J. 2002, MNRAS, 337, 1282

Roche, N. D., Dunlop, J., & Almaini, O. 2003, MNRAS, 346, 803

Roche, N. D., Dunlop, J., Caputi, K. I., McLure, R., Willott, C. J., Crampton, D. 2006, MNRAS, 370, 74

Roseboom, I. G., Pimbblet, K. A., Drinkwater, M. J., Cannon, R. D., de Propris, R., Edge, A. C., Eisenstein, D. J., Nichol, R. C., et al. 2006, MNRAS, 373, 349

Ross, N. P., da Ângela, J., Shanks, T., Wake, D. A., Cannon, R. D., Edge, A. C., Nichol, R. C., Outram, P. J., et al. 2007, MNRAS, 381, 573

Ross, N. P., Shanks, T., Cannon, R. D., Wake, D. A., Sharp, R. G., Croom, S. M., Peacock, J. A. 2008, MNRAS, 387, 1323

Rossa, J., Laine, S., van der Marel, R. P., Mihos, J. C., Hibbard, J. E., Böker, T., Zabludoff, A. I. 2007, AJ, 134, 2124

Rothberg, B. & Joseph, R. D. 2004, AJ, 128, 2098

Rudnick, G., Franx, M., Rix, H.-W., Moorwood, A., Kuijken, K., van Starkenburg, L., van der Werf, P., Röttgering, H., et al. 2001, AJ, 122, 2205

Sadler, E. M., Rich, R. M., & Terndrup, D. M. 1996, AJ, 112, 171

Salaris, M. & Weiss, A. 2002, A&A, 388, 492

Salim, S., Charlot, S., Rich, R. M., Kauffmann, G., Heckman, T. M., Barlow, T. A., Bianchi, L., Byun, Y.-I., et al. 2005, ApJ, 619, L39

Salpeter, E. E. 1955, ApJ, 121, 161

Sandage, A. 1961, ApJ, 134, 916

Sandage, A. 1986, A&A, 161, 89

Sandage, A. 1988, ARA&A, 26, 561

Sandage, A., Binggeli, B., & Tammann, G. A. 1985a, AJ, 90, 1759

Sandage, A., Binggeli, B., & Tammann, G. A. 1985b, AJ, 90, 395

Schaerer, D. & de Barros, S. 2009, ArXiv:0905.0866

Schaerer, D. & de Koter, A. 1997, A&A, 322, 598

Schawinski, K., Thomas, D., Sarzi, M., Maraston, C., Kaviraj, S., Joo, S.-J., Yi, S. K., Silk, J. 2007, MNRAS, 382, 1415

Schaye, J. 2004, ApJ, 609, 667

Schechter, P. 1976, ApJ, 203, 297

Schiavon, R. P., Faber, S. M., Konidaris, N., Graves, G., Willmer, C. N. A., Weiner, B. J., Coil, A. L., Cooper, M. C., et al. 2006, ApJ, 651, L93

Schiavon, R. P., Rose, J. A., Courteau, S., & MacArthur, L. A. 2004, ApJ, 608, L33

Schinnerer, E., Carilli, C. L., Capak, P., Martinez-Sansigre, A., Scoville, N. Z., Smolčić, V., Taniguchi, Y., Yun, M. S., et al. 2008, ApJ, 689, L5

Schinnerer, E., Carilli, C. L., Scoville, N. Z., Bondi, M., Ciliegi, P., Vettolani, P., Le Fèvre, O., Koekemoer, A. M., et al. 2004, AJ, 128, 1974

Schinnerer, E., Smolčić, V., Carilli, C. L., Bondi, M., Ciliegi, P., Jahnke, K., Scoville, N. Z., Aussel, H., et al. 2007, ApJS, 172, 46

Schlegel, D. J., Finkbeiner, D. P., & Davis, M. 1998, ApJ, 500, 525

Schmidt, M. 1968, ApJ, 151, 393

Schmidt, M., Schneider, D. P., & Gunn, J. E. 1995, AJ, 110, 68

Schulz, J., Fritze, U., & Fricke, K. J. 2003, A&A, 398, 89

Schulz, J., Fritze, U., Möller, C. S., & Fricke, K. J. 2002, A&A, 392, 1

Schweizer, F. 1982a, ApJ, 252, 455

Schweizer, F. 1982b, ApJ, 252, 455

Schweizer, F. 1996, AJ, 111, 109

Scorza, C. & van den Bosch, F. C. 1998, MNRAS, 300, 469

Scoville, N., Abraham, R. G., Aussel, H., Barnes, J. E., Benson, A., Blain, A. W., Calzetti, D., Comastri, A., et al. 2007a, ApJS, 172, 38

Scoville, N., Aussel, H., Brusa, M., Capak, P., Carollo, C. M., Elvis, M., Giavalisco, M., Guzzo, L., et al. 2007b, ApJS, 172, 1

Seiden, P. E. & Gerola, H. 1979, ApJ, 233, 56

Sekiguchi, K. & et al. 2004, in Astrophysics and Space Science Library, Vol. 301, Astrophysics and Space Science Library, ed. M. Plionis, 169–+

Shapley, A. E., Erb, D. K., Pettini, M., Steidel, C. C., & Adelberger, K. L. 2004, ApJ, 612, 108

Shapley, A. E., Steidel, C. C., Adelberger, K. L., Dickinson, M., Giavalisco, M., Pettini, M. 2001, ApJ, 562, 95

Shapley, A. E., Steidel, C. C., Erb, D. K., Reddy, N. A., Adelberger, K. L., Pettini, M., Barmby, P., Huang, J. 2005, ApJ, 626, 698

Siana, B., Teplitz, H. I., Colbert, J., Ferguson, H. C., Dickinson, M., Brown, T. M., Conselice, C. J., de Mello, D. F., et al. 2007, ApJ, 668, 62

Silk, J. & Rees, M. J. 1998, A&A, 331, L1

Silva, L., Granato, G. L., Bressan, A., & Danese, L. 1998, ApJ, 509, 103

Sirianni, M., Jee, M. J., Benítez, N., Blakeslee, J. P., Martel, A. R., Meurer, G., Clampin, M., De Marchi, G., et al. 2005, PASP, 117, 1049

Skillman, E. D., Kennicutt, R. C., & Hodge, P. W. 1989, ApJ, 347, 875

Skrutskie, M. F., Cutri, R. M., Stiening, R., Weinberg, M. D., Schneider, S., Carpenter, J. M., Beichman, C., Capps, R., et al. 2006, AJ, 131, 1163

Smail, I., Owen, F. N., Morrison, G. E., Keel, W. C., Ivison, R. J., Ledlow, M. J. 2002, ApJ, 581, 844

Smecker-Hane, T. A., Cole, A. A., Gallagher, III, J. S., & Stetson, P. B. 2002, ApJ, 566, 239

Smith, G. P., Treu, T., Ellis, R., Smail, I., Kneib, J.-P., Frye, B. L. 2001, ApJ, 562, 635

Smith, L. J., Norris, R. P. F., & Crowther, P. A. 2002, MNRAS, 337, 1309

Soifer, B. T., Matthews, K., Neugebauer, G., Armus, L., Cohen, J. G., Persson, S. E., Smail, I. 1999, AJ, 118, 2065

Spergel, D. N., Bean, R., Doré, O., Nolta, M. R., Bennett, C. L., Dunkley, J., Hinshaw, G., Jarosik, N., et al. 2007, ApJS, 170, 377

Springel, V. & Hernquist, L. 2005, ApJ, 622, L9

Springel, V., Wang, J., Vogelsberger, M., Ludlow, A., Jenkins, A., Helmi, A., Navarro, J. F., Frenk, C. S., et al. 2008, MNRAS, 391, 1685

Springel, V., White, S. D. M., Jenkins, A., Frenk, C. S., Yoshida, N., Gao, L., Navarro, J., Thacker, R., et al. 2005, Nature, 435, 629

Stasińska, G. 1984, A&AS, 55, 15

Steidel, C. C., Adelberger, K. L., Giavalisco, M., Dickinson, M., & Pettini, M. 1999, ApJ, 519, 1

Steidel, C. C., Adelberger, K. L., Shapley, A. E., Pettini, M., Dickinson, M., Giavalisco, M. 2003, ApJ, 592, 728

Steidel, C. C. & Hamilton, D. 1992, AJ, 104, 941

Steidel, C. C. & Hamilton, D. 1993, AJ, 105, 2017

Steidel, C. C., Shapley, A. E., Pettini, M., Adelberger, K. L., Erb, D. K., Reddy, N. A., Hunt, M. P. 2004, ApJ, 604, 534

Stockton, A., McGrath, E., & Canalizo, G. 2006, ApJ, 650, 706

Strickland, D. K., Heckman, T. M., Colbert, E. J. M., Hoopes, C. G., & Weaver, K. A. 2004, ApJ, 606, 829

Taniguchi, Y., Scoville, N., Murayama, T., Sanders, D. B., Mobasher, B., Aussel, H., Capak, P., Ajiki, M., et al. 2007, ApJS, 172, 9

Temporin, S. & Fritze, U. 2006, A&A, 447, 843

Tepper-García, T. & Fritze, U. 2008, MNRAS, 383, 1671

Thilker, D. A., Bianchi, L., Boissier, S., Gil de Paz, A., Madore, B. F., Martin, D. C., Meurer, G. R., Neff, S. G., et al. 2005, ApJ, 619, L79

Thilker, D. A., Bianchi, L., Meurer, G., Gil de Paz, A., Boissier, S., Madore, B. F., Boselli, A., Ferguson, A. M. N., et al. 2007, ApJS, 173, 538

Thomas, D., Maraston, C., & Bender, R. 2003, MNRAS, 339, 897

Tinsley, B. M. 1968, ApJ, 151, 547

Tinsley, B. M. 1970, Ap&SS, 6, 344

Tinsley, B. M. 1972, ApJ, 178, 319

Tinsley, B. M. H. 1967, PhD thesis, AA(THE UNIVERSITY OF TEXAS AT AUSTIN.)

Tojeiro, R., Heavens, A. F., Jimenez, R., & Panter, B. 2007, MNRAS, 381, 1252

Tonry, J. L., Dressler, A., Blakeslee, J. P., Ajhar, E. A., Fletcher, A. B., Luppino, G. A., Metzger, M. R., Moore, C. B. 2001, ApJ, 546, 681

Toomre, A. & Toomre, J. 1972, ApJ, 178, 623

Trager, S. C., Faber, S. M., & Dressler, A. 2008, MNRAS, 386, 715

Trager, S. C., Faber, S. M., Worthey, G., & González, J. J. 2000, AJ, 120, 165

Trager, S. C., Worthey, G., Faber, S. M., Burstein, D., & Gonzalez, J. J. 1998, ApJS, 116, 1

Tran, K.-V. H., Franx, M., Illingworth, G., Kelson, D. D., & van Dokkum, P. 2003, ApJ, 599, 865

Tremonti, C. A., Heckman, T. M., Kauffmann, G., Brinchmann, J., Charlot, S., White, S. D. M., Seibert, M., Peng, E. W., et al. 2004, ApJ, 613, 898

Treu, T., Ellis, R. S., Liao, T. X., & van Dokkum, P. G. 2005, ApJ, 622, L5

Truran, J. W. & Cameron, A. G. W. 1971, Ap&SS, 14, 179

Valencic, L. A., Clayton, G. C., & Gordon, K. D. 2004, ApJ, 616, 912

van den Bosch, F. C. & Emsellem, E. 1998, MNRAS, 298, 267

van den Bosch, F. C., Jaffe, W., & van der Marel, R. P. 1998, MNRAS, 293, 343

van den Hoek, L. B. & Groenewegen, M. A. T. 1997, A&AS, 123, 305

van Dokkum, P. G., Förster Schreiber, N. M., Franx, M., Daddi, E., Illingworth, G. D., Labbé, I., Moorwood, A., Rix, H.-W., et al. 2003, ApJ, 587, L83

van Dokkum, P. G., Franx, M., Förster Schreiber, N. M., Illingworth, G. D., Daddi, E., Knudsen, K. K., Labbé, I., Moorwood, A., et al. 2004, ApJ, 611, 703

van Zee, L., Salzer, J. J., Haynes, M. P., O'Donoghue, A. A., & Balonek, T. J. 1998, AJ, 116, 2805

Wake, D. A., Nichol, R. C., Eisenstein, D. J., Loveday, J., Edge, A. C., Cannon, R., Smail, I., Schneider, D. P., et al. 2006, MNRAS, 372, 537

Wake, D. A., Sheth, R. K., Nichol, R. C., Baugh, C. M., Bland-Hawthorn, J., Colless, M., Couch, W. J., Croom, S. M., et al. 2008, MNRAS, 387, 1045

Wehner, E. H., Gallagher, J. S., Papaderos, P., Fritze, U., & Westfall, K. B. 2006, MNRAS, 371, 1047

Weidemann, V. 2000, A&A, 363, 647

Weidner, C. & Kroupa, P. 2006, MNRAS, 365, 1333

Weil, M. L. & Hernquist, L. 1996, ApJ, 460, 101

Weilbacher, P. M., Duc, P.-A., & Fritze, U. 2003a, A&A, 397, 545

Weilbacher, P. M. & Fritze, U. 2001, A&A, 373, L9

Weilbacher, P. M., Fritze, U., & Duc, P.-A. 2003b, Ap&SS, 284, 639

Weilbacher, P. M., Fritze, U., Duc, P.-A., & Fricke, K. J. 2002, ApJ, 579, L79

Weiss, A., Peletier, R. F., & Matteucci, F. 1995, A&A, 296, 73

West, M. J., Côté, P., Marzke, R. O., & Jordán, A. 2004, Nature, 427, 31

Westmoquette, M. S., Smith, L. J., & Gallagher, J. S. 2008, MNRAS, 383, 864

White, S. D. M. & Frenk, C. S. 1991, ApJ, 379, 52

Williams, R. E., Blacker, B., Dickinson, M., Dixon, W. V. D., Ferguson, H. C., Fruchter, A. S., Giavalisco, M., Gilliland, R. L., et al. 1996, AJ, 112, 1335

Williams, R. J., Quadri, R. F., Franx, M., van Dokkum, P., & Labbé, I. 2009, ApJ, 691, 1879

Willmer, C. N. A., Faber, S. M., Koo, D. C., Weiner, B. J., Newman, J. A., Coil, A. L., Connolly, A. J., Conroy, C., et al. 2006, ApJ, 647, 853

Wilson, A. 1952, Trans. I.A.U., 8, 335

Wise, J. H. & Cen, R. 2009, ApJ, 693, 984

Wolfe, A. M., Gawiser, E., & Prochaska, J. X. 2005, ARA&A, 43, 861

Woodley, K. A., Harris, W. E., Puzia, T. H., Gómez, M., Harris, G. L. H., Geisler, D. 2010, ApJ, 708, 1335

Woosley, S. E. & Weaver, T. A. 1995, ApJS, 101, 181

Worthey, G., Faber, S. M., Gonzalez, J. J., & Burstein, D. 1994, ApJS, 94, 687

Worthey, G. & Ottaviani, D. L. 1997, ApJS, 111, 377

Wright, G. S., James, P. A., Joseph, R. D., & McLean, I. S. 1990, Nature, 344, 417

Wuyts, S., Labbé, I., Schreiber, N. M. F., Franx, M., Rudnick, G., Brammer, G. B., van Dokkum, P. G. 2008, ApJ, 682, 985

Xin, Y. & Deng, L. 2005, ApJ, 619, 824

Xin, Y., Deng, L., & Han, Z. W. 2007, ApJ, 660, 319

XXX missing reference XXX. 2035, A&AS, 123, 305

Yamauchi, C., Yagi, M., & Goto, T. 2008, MNRAS, 390, 383

Zabludoff, A. I., Zaritsky, D., Lin, H., Tucker, D., Hashimoto, Y., Shectman, S. A., Oemler, A., Kirshner, R. P. 1996, ApJ, 466, 104

Zamojski, M. A., Schiminovich, D., Rich, R. M., Mobasher, B., Koekemoer, A. M., Capak, P., Taniguchi, Y., Sasaki, S. S., et al. 2007, ApJS, 172, 468

Zaritsky, D. & Christlein, D. 2007, AJ, 134, 135

Zaritsky, D., Kennicutt, Jr., R. C., & Huchra, J. P. 1994, ApJ, 420, 87

Zaritsky, D., Smith, R., Frenk, C., & White, S. D. M. 1997, ApJ, 478, 39